University of BRISTOL

Magneto-responsive Surfactants

Paul Brown

ssertation submitted to the University of Bristol in accordance with the requirements of the degree of Doctor of Philosophy in the School of Chemistry, Faculty of Science

Word count: 42,447

ORIGINAL COPY TIGHTLY BOUND

Author's Declaration

I declare that the work in this dissertation was carried out in accordance with the requirements of the University's Regulations and Code of Practice for Research Degree Programmes and that it has not been submitted for any other academic award. Except where indicated by specific reference in the text, the work is the candidate's own work. Work done in collaboration with, or with the assistance of, others, is indicated as such. Any views expressed in the dissertation are those of the author.

SIGNED Paul Brown.....

DATE 20/12/2012.....

Acknowledgements

Firstly, I would like to thank "The Boss", Julian Eastoe for all his help and support. Each time I spoke to you I never failed to be inspired. Thank you.

I have been lucky enough to have two supervisors and I am indebted to Craig Butts for all his patience and advice. No matter how busy you were you always had an open door. Thank you.

I would like to thank Isabelle, Richard and Sarah at the large-scale scattering facilities who have always gone to extremes to help run and analyze experiments. I appreciate all you efforts and have enjoyed being in your company.

A big part of my life has been spent with the members of W302 and the colloid group past and present and I would like to thank them for fun conversations, accompanying me to the pub, and helping with sleepless nights in Oxford and Grenoble running experiments. In no particular order, Adam, Rodrigo, Kieran, Azwan, Azmi, Grace, Steve, Asad, Craig, Marios, David, Greg, Asma, Masa, Benoit, Beatrice, Phil, Cathy, Wiebe, Shirin, Francesca, Katie, Ian, Jindee, Charlotte, Bea, Jing Cheng, Tim, Panithi, Beth, Jusef, Christa, Daniela, Bo, David P and Stuart, thank you.

Finally, to my mother and brother the biggest thank you.

Abstract

Surfactants comprise one of the largest volume commodity chemicals in the world and have multifarious uses from pharmaceuticals, agrochemicals, food, fuel and lubricant additives, paints and inks as well as detergents and cleaning agents. The ability to control surfactants once they are in solution is of great importance not only for scientific reasons but also because of environmental and economic interest. To this end, surfactants sensitive to changes in pH, temperature, CO_2, light and redox have already been developed. This thesis investigates a new class of surfactants designed to be magnetically active, whereby the composition and physico-chemical properties of a system may be perturbed simply by the switching "on" and "off" of a magnetic switch and with no significant energy input.

The thesis demonstrates that these new magneto-responsive surfactants behave like conventional surfactants but are now bifunctional allowing for new magnetic approaches where previously magnetic nanoparticles have been employed. For example, the magnetic properties makes it easier to round up and remove the surfactant from a system once it has been added. By developing the first nanoparticle-free magnetic emulsions the potential for further applications in environmental clean ups (e.g. oil spills), water treatment or drug delivery have been demonstrated. In addition to this, the combination of surfactant adsorption and intrinsic magnetism has allowed for the control and manipulation of biomolecules without the need for magnetic nanoparticles.

This work explores both the fundamental properties of these novel surfactants and also takes significant steps to optimize the surfactants for potential applications.

Project Overview

Project aim

There is a huge push for both economical and environmental reasons to develop new surfactants and solvents that not only reduce waste and are less toxic than before, but also that allow for new chemistry and applications. The work presented in this thesis has aimed to design and study systematically ionic liquids and surfactants with this in mind. One approach was to consider molecular deisgn to produce ionic liquid surfactants (SAILs) that are more environmentally friendly than current ionic liquids, while making an effort to retain any important physico-chemical and electrochemical properties suitable for application. In addition to this, by making these SAILs magnetically responsive a surfactant system was created with great potential for various applications.

Project Overview

Chapter 1 gives a background to the field of surfactant and colloid science. With relevant concepts including surfactants and microemulsions.

Chapter 2 is a literature review on ionic liquid surfactants covering micellar catalysis, ionic liquid design and applications and the development of surfactant ionic liquids (SAILs).

Chapter 3 investigates the design of environmentally friendly SAILs based on commodity surfactants and how their properties compare to conventional surfactants.

Chapter 4 investigates imidazolium based SAILs focussing on their physico-chemical properties and how they may be tuned for potential applications.

Chapter 5 introduces the first magnetic surfactants and their characterization using small-angle neutron scattering and magnetometry.

Chapter 6 describes the first nanoparticle-free magnetic emulsions and explores their potential "out of the laboratory" applications from oil recovery to drug delivery.

Chapter 7 focuses on novel magnetic properties of magnetic microemulsions and how they may be considered as tuneable nanomagnets

Chapter 8 details the magnetization of DNA and other biomolecules simply through surfactant binding and the switching on and off of a magnetic field.

Chapter 9 comprises a summary of results, conclusions and recommendations for further work.

List of Publications

1. **Paul Brown**, Craig Butts, Julian Eastoe, "*Surfactant* Ionic Liquids: potential reaction media?", *Accepted* as book chapter in *Surfactant Science and Technology: Retrospects and Prospects* (Taylor Francis, Editor: Prof. L. Romsted).

2. **Paul Brown**, Craig Butts, Robert Dyer, Julian Eastoe, Isabelle Grillo, Frédéric Guittard, Sarah Rogers, and Richard Heenan, Anionic Surfactants and Surfactant Ionic Liquids with Quaternary Ammonium Counterions, *Langmuir*, 2011, *27*, 4563–4571.

3. **Paul Brown**, Craig P. Butts, Julian Eastoe, David Fermin, Isabelle Grillo, Huai-Chin Lee, David Parker, Daniela Plana, and Robert M. Richardson, Anionic Surfactant Ionic Liquids with 1-Butyl-3-methyl-imidazolium Cations: Characterization and Application. *Langmuir*, 2012, *28*, 2502–2509.

4. **Paul Brown**, Alexey Bushmelev, Craig P. Butts, Jing Cheng, Julian Eastoe, Isabelle Grillo, Richard K. Heenan and Annette M. Schmidt, Magnetic Control over Liquid Surface Properties with Responsive Surfactants, Angew. Chem. Int. Ed., 2012, 51, 2414–2416.

5. **Paul Brown**, Craig P. Butts, Jing Cheng, Julian Eastoe, Christopher A. Russell and Gregory N. Smith, Magnetic emulsions with Responsive Surfactants, *Soft Matter*, **2012**, DOI: 10.1039/C2SM26077H.

6. **Paul Brown**, Asad Khan, James Armstrong, Adam Perriman, Craig Butts, Julian Eastoe, Magnetizing DNA and Proteins using Magnetic Surfactants, *Adv. Mat.*, DOI: 10.1002/adma.201202685.

7. **Paul Brown**, Craig Butts, Julian Eastoe, Stefan Glatzel, Isabelle Grillo, Simon Hall, Sarah Rogers and Kieran Trickett, Magnetic Microemulsions as Tunable Nanomagnets, DOI: 10.1039/C2SM26827B.

8. M. Carmen Galan, Anh Tuan Tran, Julien Boisson, David Benito, Craig Butts, Julien Eastoe and **Paul Brown**, [RN4] [AOT]: A surfactant ionic liquid as a mild glycosylation promoter, *J. Carbohydr. Chem.* 2011, 30, 486-497.

9. **Paul Brown**, Julian Eastoe, Isabelle Grillo and Tim Harrison, Magnetic science: developing a new surfactant, *Science in Schools*, 2012, Issue 25, 22.

10. **Paul Brown**, Craig Butts, Julian Eastoe, Isabelle Grillo, Craig James and Asad Khan, New Catanionic Surfactants with Ionic Liquid Properties, Accepted by *J. Coll. Int. Sci.*, 2012, JCIS-12-2930R1.

11. **Paul Brown**, Craig Butts, Julian Eastoe, Stimuli-responsive Surfactants, Accepted by *Soft Matter*, 2012.

12. **Paul Brown**, Alexey Bushmelev, Craig P. Butts, Jean-Charles Eloi, Julian Eastoe, Isabelle Grillo, Annette M. Schmidt, Properties of New Magnetic Surfactants, Submitted to *Langmuir*, 2012.

Chapter 1

General Introduction

This thesis is concerned primarily with the development of new magneto-responsive surfactant molecules and how they may be designed for various applications ranging from ionic liquid synthesis to the manipulation of colloidal systems. It is therefore important to introduce some background theory on surfactants and the colloidal systems of interest as well as magnetism.

1.1 Colloids

Colloids are ubiquitous both in industrial processes and in nature, and are a stable heterogeneous mixtures of one phase dispersed in another phase. There are no strict boundaries on the size of colloidal particles, but their upper size is limited dependent on the balance between thermal (3/2 k_BT) and potential energy. For this reason they tend to vary between 1 nm to 10 μm in size[1]. One important group of colloidal systems are called *association colloids*[2] which contain amphiphilic molecules that associate in solution to produce aggregates of colloidal dimensions. These amphiphilic molecules are commonly termed *surfactants*.

1.1.0 Surfactants

The term *surfactant* is an abbreviation for surface active agent, and, as the name suggests, is a compound that adsorbs at an interface (whether liquid/air interface, liquid/liquid or even the surface of a biomolecule). Adsorption occurs due to the dual nature (amphiphilic) of the surfactant, where one part of the molecule is hydrophilic (headgroup) and the other hydrophobic (tailgroup). This can be achieved in a number of ways as detailed below.

1.1.1 Surfactant structure and classification

There are many possible surfactant configurations, however, surfactants may be broadly divided up into four main categories depending on the type of head group (Table 1). Anionic surfactants have negatively charged headgroups such as caboxylic acid salts, alkyl phosphates or sulfates (e.g. sodium dodecyl sulfate).

Cationic surfactants have positively charged headgroups and are usually nitrogen based quarternary ammonium compounds (e.g. dodecyltrimethylammonium bromide). Zwitterionic surfactants combine both a positive and a negative group and are often biologically important (e.g. phosphatidylcholine) and finally non-ionic surfactants have no headgroup charge but are amphiphilic due to the presence of strongly polar groups (e.g. decyl glucoside).

Structure	Name
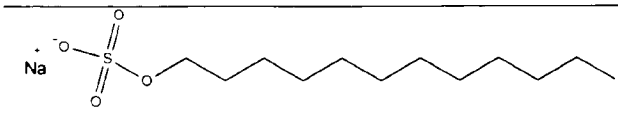	Sodium dodecylsulfate
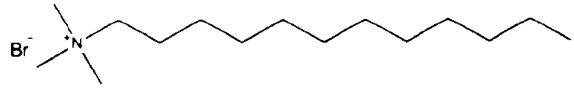	Dodecyltrimethylammonium bromide
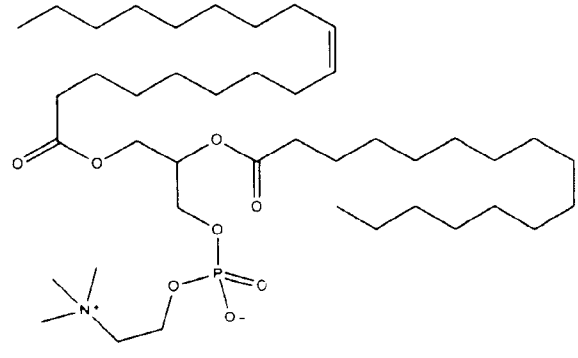	palmitoyl-oleyl-*sn*-phosphatidylcholine
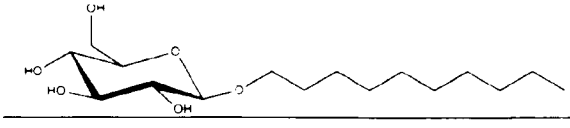	Decyl glucoside

Table 1.1: Examples of typical surfactant structures.

Many other types of surfactants do exist, such as Gemini (effectively two surfactants but made into one by bridging the headgroups), catanionic (mixture of cationic and anionic surfactant which act as counterions to each other) and bolaform (a head group at each end) and surfactant properties may further be enhanced for specific purposes, for example including fluorinated carbon tails for solubility in $scCO_2$[3] or producing surfactant ionic liquids (surfactants with melting points below 100 °C) as detailed in this thesis for potential application in controlling reaction pathways.

In addition to conventional surfactants that are responsive to pH, temperature and electrolyte, stimuli-responsive surfactants may also be prepared containing light-sensitive groups[4], redox groups[5], CO_2[6] responsive groups and magneto-responsive groups (arising from work in this thesis).

1.1.2 Adsorption and aggregation

There is a thermodynamic imperative for amphiphilic molecules to adsorb at an interface. At the air/water interface surfactants orientate themselves so that their hydrophobic tails minimize contact with water due to the hydrophobic effect. By doing this the surfactant molecules disrupt the surface forces between the water molecules increasing the free energy thereby lowering the surface tension.

Once the solubility in the bulk is reached aggregation can take place. The concentration at which this occurs is known as the critical micelle concentration (cmc). The formation of micelles provides a way for hydrocarbon tails to minimize unfavourable contact with water and lowers the systems free energy. These micelles are equilibrium structures, with surfactant unimers exchanging between micelles on a microsecond timescale, and the micelles form and disintegrate on a millisecond scale[7].

The cmc can be determined by measuring a number of physical properties such as electrical conductivity, surface tension, turbidity and osmotic pressure.

Micelle aggregates vary greatly in size and shape dependent on the packing parameter[8] of the surfactant molecules but typically consist of between 50 and 200 molecules. The packing parameter (Eq. 1.1) may be calculated from the optimum headgroup area, a_0, the critical chain length, l_c, and the volume of the hydrocarbon chain, v.

$$P_c = \frac{v}{A_h l_c} \qquad \text{Eq. 1.1}$$

The optimum headgroup area arises from the balance of energetic contributions to the free energy of the system. Headgroup electrostatic repulsions force the surfactants apart while the hydrophobic effect drives them together. This property is easily altered through the addition of electrolyte and control of pH. The critical chain length and volume of the hydrocarbon chains varies substantially with the number of hydrophobic groups, chain branching and chain saturation. It is possible to derive mathematical conditions

under which certain shapes may be formed. For example, a spherical micelle of radius R_{mic} consisting of a number of surfactant molecules, N, will occupy a volume $4\pi/3R_{mic}^3 = N_m v$ and have a surface area $4\pi R_{mic}^2 = N_m A_h$, suggesting that $R_{mic} = 3v/A_h$. In order for the micelle to be spherical this radius must be smaller than or equal to the critical chain length, l_c. The conditions for various micellar shapes are listed in Table 1.2.

P_c	General surfactant type	Extended aggregate structure
< 0.33	Single chain surfactant with large headgroup	Spherical or ellipsoidal micelles
0.33 – 0.50	Single chain surfactant with small headgroup	Cylindrical or rod-like micelles
0.5 – 1.0	Double chain surfactant with large headgroup or flexible chains	Vesicles and bilayers
1.0	Double chain surfactants with small headgroups or rigid chains	Planar extended bilayers
>1.0	Double chain surfactants with bulky hydrophobic groups	Reverse or inverted micelles

Table 1.2: Expected aggregate shapes predicted from packing parameter, P_c.

1.2 Microemulsions

Microemulsions are clear, thermodynamically stable, isotropic mixtures of two immiscible liquids and surfactant (and sometimes a co-surfactant) that form spontaneously[1, 9]. Microemulsion droplets are usually in the size range 5 – 50 nm in radius (much smaller than emulsion droplets, > 0.10 μm).

The spontaneity and thermodynamic stability of microemulsion formation is a direct result of strong adsorption of surfactants at the interface between the two liquids and the lowering of interfacial tension. The droplet formation can be understood in terms of the free energy of the system. The configurational entropy change on forming a dispersed phase of small droplets can be described by equation 1.2:

$$\Delta S_{conf} = -nk_B[ln\phi + \left\{\frac{(1-\phi)}{\phi}\right\} ln\,(1-\phi)] \qquad \text{Eq. 1.2}$$

where n is the number of droplets and ϕ is the volume fraction of the dispersed phase. The associated free energy change in forming a final microemulsion state (Eq. 1.3) is then a combination of this configurational entropy plus the energy required to create a new interfacial area A with an interfacial tension γ.

$$\Delta G = \Delta A \gamma_{o/w} - T\Delta S_{conf} \qquad \text{Eq. 1.3}$$

Microemulsions were classified by Winsor into four main types[10] (Figure 1.1):

Type 1: Surfactant is preferentially soluble in water and o/w microemulsions form (Winsor I). Surfactant-rich water phase co-exists with the oil phase where surfactant is only present as monomers at small concentration.

Type 2: Surfactant is mainly in oil phase and w/o microemulsions form. Surfactant-rich oil phase co-exists with the surfactant-poor aqueous phase (Winsor II).

Type 3: A three phase system where a surfactant-rich middle phase coexists with both excess water and oil surfactant poor phases (Winsor III).

Type 4: a single-phase (isotropic) micellar solution forms upon the addition of a sufficient quantity of amphiphile.

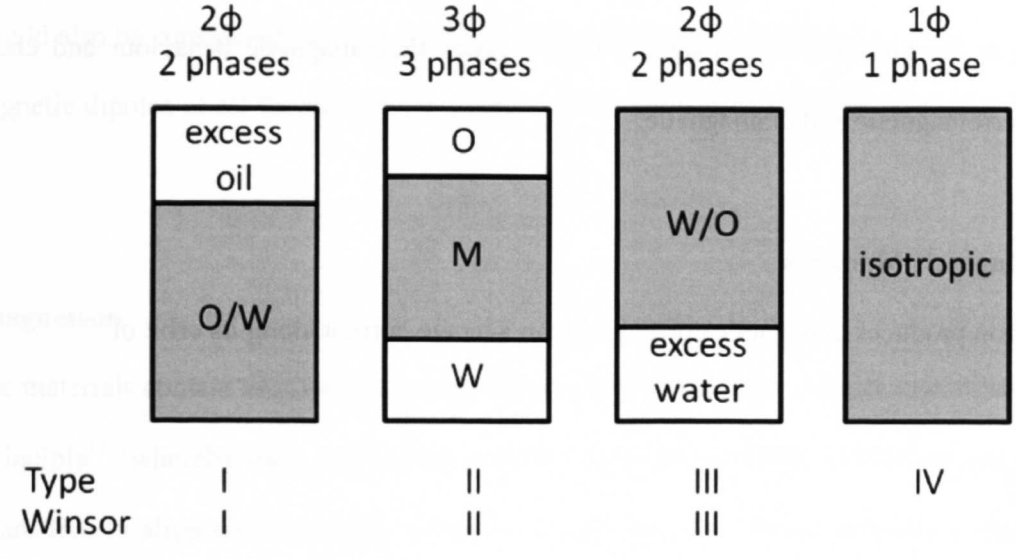

Figure 1.1: Classification of microemulsions. In the three phase system the middle-phase microemulsion (M) in equilibrium with both excess oil (O) and water (W).

By changing the relative components of the system microemulsion droplet size can be altered. One important quantity is the w value (for water-in-oil microemulsions) which can be defined in terms of the molar concentrations of surfactant and water in the system, and is effectively the stabilization efficiency:

$$w = \frac{[H_2O]}{[surfactant]} \qquad \text{Eq. 1.4}$$

The approximate droplet size can be calculated from this w value.

$$R = \frac{3wv_w}{a_0} + l_c \qquad \text{Eq. 1.5}$$

where R is the radius of the spherical microemulsion droplet, v_w is the volume of a water molecule (≈ 30 Å). The range of accessible w values are dependent on the surfactant as well as the solvent combination.

1.3 Magnetism

Electrons orbit around a nucleus and protons orbit around each other inside the nucleus. These orbital motions may be regarded as flowing electric currents within the atom and these currents generate magnetic fields.[11] The orbital motions may be described in terms of magnetic dipole moments and how these dipoles respond (align) in the presence of a magnetic field dictates their magnetic behaviour and classification; paramagnetic, ferromagnetic and diamagnetic.

1.3.1 Atomic Magnetic Moments

A orbiting electron produces a magnetic current with an average current along its orbit of

$$I = \frac{e}{2\pi r/v} = \frac{e}{2\pi r} \qquad \text{Eq. 1.6}$$

where e is the charge moved, r is the radius of the circular orbit (strictly speaking the calculation requires quantum mechanics and not simply classical mechanics but for simplicity is not included here) and v is the speed. This circulating current gives rise to a magnetic moment:

$$\mu = I \times [area] = \frac{ev}{2\pi r} \times \pi r^2 = \frac{evr}{2} \qquad \text{Eq. 1.7}$$

The magnetic moment can also be expressed in terms of angular momentum

$$\mu = \frac{e}{2m_e} L \qquad \text{Eq. 1.8}$$

where $L = m_e vr$. Importantly Equation 1.8 remains valid when using quantum mechanics.[11] In quantum mechanics the magnitude of the orbital angular momentum must be an integer multiple of $\hbar$ (Planck's constant, h divided by 2π); this means it is quantized.

In addition to orbital angular momentum the magnetic moment generated by the rotation (spin) of an electron must also be considered. This has a fixed value of 9.27 x 10^{-24} A m^2 and defines a unit called the Bohr magneton (B. M.). The net magnetic moment of an atom is the combination of all orbital and spin moments of all the electrons, taking into account the directions of these moments. The nuclear magnetic moments should also be considered but are relatively small and usually neglected.

How the magnetic dipoles of all the atoms in a system interact then determines the materials bulk magnetic behaviour.

1.3.2 Paramagnetism

Paramagnetic materials contain unpaired electrons. These unpaired electrons are not constrained by the Pauli exclusion principle[12] (whereby their spins must point in opposite directions cancelling out any magnetic fields), and are free to align their magnetic moments in any direction. When an external magnetic field is applied, the magnetic moments tend to align themselves in the same direction as the applied field, causing

the material to become magnetized and contributing to an extra magnetic field which increases the original magnetic field.

1.3.3 Ferromagnetism

Just like paramagnetic materials, ferromagnets have unpaired electrons. However, in these materials not only do the magnetic moments of the electrons align parallel to the applied field but also align themselves parallel to each other to maintain a lower energy state. This increases the magnetic field significantly, and, importantly, due to this spin-coupling, ferromagnetic materials, unlike paramagnetic materials, remain magnetized even when not immersed in an external magnetic field.

Ferromagnetic materials are always magnetized above the Curie temperature (T_c, the point above which ferromagnetism is lost due to thermal tendency to disorder). However, this is not always evident for systems containing large numbers of molecules. Here, small domains form, within which all magnetic dipoles align, but where the direction of alignment varies from one domain to the next. Hence, on a large scale there is no discernible alignment.

When a ferromagnet is small enough it acts like a single magnetic spin, whose magnetization can flip direction due to thermal effects. Superparamagnetic material are magnetized just like paramagnets in an external magnetic field. However, their magnetic susceptibility is much larger than the one of paramagnets.

1.3.4 Diamagnetism

Diamagnetism appears in all materials and occurs when an alteration in the orbital velocity of electrons around their nuclei is induced by an external magnetic field, thus changing their magnetic dipole moment[11]. The effect of diamagnetism is quite small and masked when paramagnetism or ferromagnetism is present.

1.4 References

1. T. Cosgrove, ed., *Colloid Science Principles, Methods and Applications*, 2 Ed., Wiley, London, 2010.
2. D. F. Evans and H.Wennerström, *The Colloidal Domain*, Wiley-VCH, New York, 1999.
3. J. Eastoe, A. Dupont and D. C. Steytler, *Curr. Opin. Colloid Interface Sci.*, 2003, 8, 267-273.
4. J. Eastoe and A. Vesperinas, *Soft Matter*, 2005, 1, 338-347.
5. B. S. Gallardo, K. L. Metcalfe and N. L. Abbott, *Langmuir*, 1996, 12, 4116-4124.
6. J. Zhang, Y. Zhao, J. Li, G. Yang, B. Han, Z. Wu and Z. Li, *Soft Matter*, 2010, 6, 6200-6205.
7. B. Jönsson, B. Lindman, K. Holmberg and B. Kronberg, *Surfactants and Polymers in Aqueous Solution*, Wiley, New York, 1998.
8. J. N. Israelachvili, D. J. Mitchell and B. W. Ninham, *J. Chem. Soc., Faraday Trans.*, 1976, 72, 1525-1568.
9. I. Danielsson and B. Lindman, *Colloids Surf. A*, 1981, 3, 391.
10. P. A. Winsor, *Trans. Faraday Soc.*, 1948, 44, 376.
11. H. C. Ohanian, *Ohanian Physics* W.H. Norton and Company, New York, 1989.
12. P. Atkins and J. de Paula, *Atkins' Physical Chemistry*, 7 Ed., Oxford University Press, Oxford, 2002.

Chapter 2

Surfactant ionic liquids: potential structured reaction media?

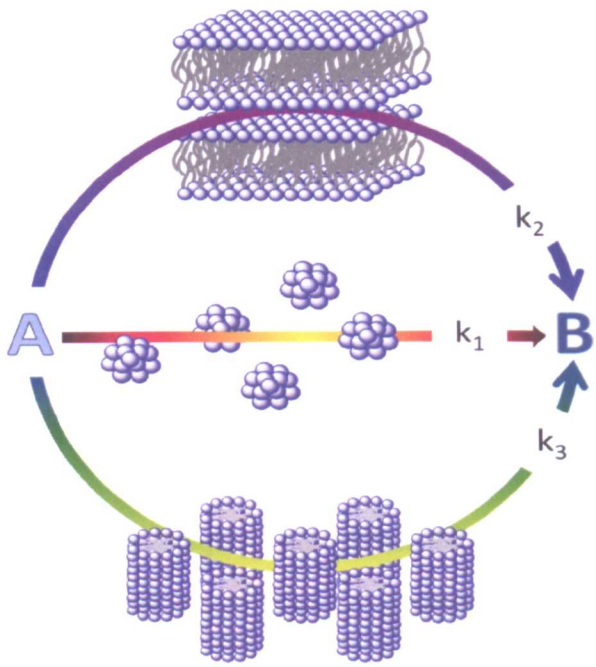

This chapter is a literature review concerning the recent growth of interest in ionic liquids (ILs). As such the chapter serves as a justification for the research in this thesis, exploring further developments in ionic liquids and surfactants. This stems mainly from their unique solvent properties, and the huge permutation of different possible ionic liquids which can result in strong solvent effects when ILs are used as reaction media. It has been known for some years that reaction rates and outcomes can also be influenced by the presence of micellar aggregates formed by common surfactants, as well as by the more concentrated surfactant lyotropic liquid crystalline (LC) mesophases. Considering these two branches of physical and organic chemistry leads to the intriguing question: Can the properties of both ionic liquids and surfactants be combined to generate tuneable and highly selective reaction media? This review addresses the question with reference to both IL and surfactant literature, and points the way to new directions in the field of structured reaction solvents.

2.0 Introduction

Ionic liquids (ILs) and surfactant micelles or mesophases, are two inter-related fields of modern solution phase physical chemistry. An aim of this review is to describe the behaviour of long chain ionic liquid surfactants as compared to normal surfactants, and to explore potential applications of such structured media as phase tunable solvents for chemical reactions.

Ionic liquids are low melting point organic salts, as a result of extreme packing frustrations owing to sizes and shapes of the constituent cations and anions: As such, the common perception is that ILs are themselves weakly structured solvents owing to local electrostatic interactions. There is a vast matrix of possible IL structures, some comprising long alkyl chains coupled to much smaller counterions; these compounds are structural relatives of common surfactants (see below) and have been coined surfactant ionic liquids (SAILs).

Surfactants are an important chemical class with multifarious applications and an industrial production exceeding 10M tonnes per year. Common surfactants possess two moieties with dissimilar properties, linked together (either covalently or ionically) in the same molecule, and these have been termed "amphiphiles". It is traditional to classify these units as hydrophobic, normally long chain hydro- or fluorocarbons; or hydrophilic, being separate ions in the case of ionic surfactants, or zwitterionic and uncharged oligomers in the case of neutral ampholytic or non-ionic surfactants. Charged ionic surfactants bear the closest structural relationship to ILs and SAILs. In aqueous solution common surfactant and SAIL molecules self-assemble to generate micelles above a critical micelle concentration (cmc), which is typically $10^{-6} - 10^{-2}$ mol dm^{-3} for most common compounds. This aggregation is driven by the hydrophobic effect, where the appropriate ions aggregate to minimize (hydrophobic ions) or maximize (hydrophilic ions) interactions with the polar water solvent. Micelles are dynamic aggregates showing rates of monomer uptake/exchange that are close to those of diffusion control[1]. The polar head groups residing at the micellar interface with the aqueous phase are highly hydrated, and in the case of ionic surfactants form a Stern layer. This local region, typically of nanometric dimensions, has important consequences for reagent solubilisation, and consequently "catalysis" as it influences the local concentrations and solvent environments of added reagents.

With increasing concentration the amphiphile aggregate packing density increases, and in an attempt to minimise unfavourable interactions between surfactant aggregates a range of lyotropic liquid crystalline (LC) mesophases may form: examples of mesophase structures can be seen in Figure 2.1.

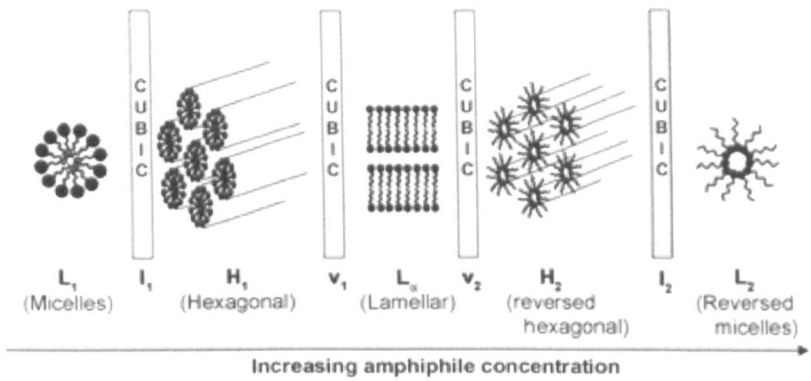

Figure 2.1: The "ideal" sequence of phases as a function of amphiphile concentration (subscripts 1 and 2 refer to "normal" and reversed" phases, respectively). Lamellar phases can be found in different phase states, including: lamellar crystalline (L_c), lamellar gel (L_β), and lamellar fluid (L_α)[2] (from ref. 2 reproduced by permission of The Royal Society of Chemistry).

For common surfactants, mesophase formation, structures and properties have been extensively studied[3,4]. Interestingly it is now appreciated that certain ILs and especially SAILs can also stabilize mesophases[5], as explored in more detail below.

2.1 Solubilization

Hydrophobic compounds solubilise more readily in aqueous surfactant solutions than in pure water, as they can be accommodated into hydrophobic micellar cores[6]. The solvent penetrates to some extent into the micelles, so it can interact with both the hydrophilic head groups and the non-polar alkyl chains, which is believed to be an important feature in "micellar catalysis". Duynstee and Grunwald[7] first demonstrated the catalytic effect of surfactant micelles, and since then much work has been done on investigating micellar effects on both rate and selectivity of different chemical reactions. There are in fact a number of comprehensive reviews[6,8] on the subject, so only key aspects will be covered here.

2.3 Micellar catalysis kinetics

There is indeed a vast literature in this field, and it is now appreciated that the major factor influencing rate enhancement in "micellar catalysis" is increased local concentration of the reactants relative to the surrounding aqueous phases, owing to localized partitioning into the interface/micelles. The field is dominated by studies with certain common surfactants (e.g. anionic such as sodium dodecylsulfate, SDS, or cationic such as cetylmethylammonium bromide, CTAB). Substrates are solubilised into different regions of micellar structures through electrostatic and hydrophobic interactions[8]. This behaviour has certain parallels with that typified by enzymes[9]; both enzymatic and micellar catalysis involve "pre-assembly" of reagents owing to a balance of hydrophobic and hydrophilic interactions. Both also exhibit substrate specificity, with kinetic activity proportional to catalyst and substrate saturation. There are distinctions however; generally rate and regioselectivity enhancements are weaker for micelles compared to enzymes.

The ways in which micellar media alter reaction pathways and kinetics have been accounted for by a pseudophase model[10]. This approach regards the micellar and the aqueous medium as discrete reaction pseudophases in which substrates exist in thermodynamic equilibrium. For uni-molecular reactions the catalytic effect is accounted for by considering local properties of the aqueous micelles. On the other hand, for bi-molecular (or higher order) reactions the local concentration of the reacting substrates is also important.

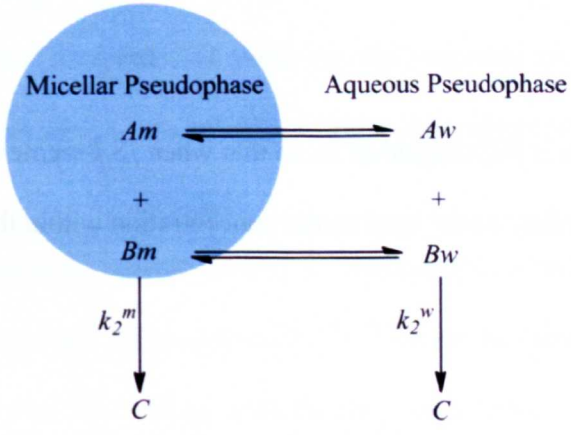

Scheme 2.1: Kinetic model for a typical $A + B \rightarrow C$ bi-molecular reaction in a micellar solution. Where A and B are substrates, located in the external water (w), or internal micellar (m) pseudophases respectively.

For a generic bi-molecular reaction, the observed micellar kinetics can be accounted for with reference to Scheme 2.1, and a Michaelis-Menten type equation for the observed rate constant (Equation 2.1):

$$k_{obs} = \frac{k_2^w[B_w] + k_2^m K_s N_m [S_m]}{1 + K_s[S_m]} \qquad \text{Eq. 2.1}$$

k_2^w and k_2^m are rate constants for reactions in aqueous (w) and micellar (m) pseudophases, respectively. The other terms are: K_s the substrate-micelle binding constant (see Equation 2.2 below); with S_m representing the concentration of micellised surfactant (Equation 2.3), and N_m the local molar concentration within the pseudophases (Equation 3.4). The equilibrium constant, K_s, describes the extent of substrate partitioning, via

$$K_s = \frac{[A_m]}{[A_w][S_m]} \qquad \text{Eq. 2.2}$$

and for hydrophobic substrates it is found to increase with increasing surfactant hydrophobicity (alkyl chain length). Therefore, it can be appreciated that the chemical nature and structure of the amphiphile are of utmost importance for determining solubility and penetration of solute and substrate molecules into the micellar pseudophase.

$$[S_m] = [S_t] - \text{cmc} \qquad \text{Eq. 2.3}$$

The total surfactant concentration is $[S_t]$ (Equation 3), so that when $[S_t] >> \text{cmc}$ then $[S_m] \approx [S_t]$.

The other terms in Equation 2.1 relate to the local molar concentration within the pseudophase, N_m

$$N_m = \frac{[B_m]}{[S_m]V_m} \qquad \text{Eq. 2.4}$$

Where $[B_m]$ is the concentration of reactant ions in the micellar pseudophase, V_m is the micellar molar volume and $[S_m]V_m$ is the fractional volume in which the reaction occurs.

In the case of bimolecular reactions, competition of the incoming reactant for the surfactant counterion X must be taken into account, which is done by introducing a term for the ion-exchange equilibrium.

$$K_B^X = \frac{[B_w][X_m]}{[N_m][X_w]} \qquad \text{Eq. 2.5}$$

This modification is called the pseudo-ion exchange (PIE) model[11], requiring assumptions about B_m: firstly a continual coverage of the micelle surface by counterions, expressed by the mole fraction, β, where $\beta = 1 - \alpha$ with α the fractional free charge at the micelle surface; secondly it treats the micellar surface as a selective ion exchanger with competition between inert counterions X and reactive ions B.

For ionic bimolecular reactions, the second-order rate constant is generally quite similar to that for the pure aqueous phase reaction. This suggests a water-like medium for the majority of micelle catalysed bimolecular reactions, and therefore indicates that any rate enhancement results mainly from an increase in local reactant concentrations in the micellar pseudophase[12].

2.4 Reactions in micelles and lyotropic mesophases

A good example of micellar enhanced reactivity is that of the metalation of picket fence porphyrins toward Cu^{2+} and Zn^{2+} [13]. A wide rate range is observed in aqueous anionic surfactant solutions, up to a factor of 3.5 x 10^4 greater compared to normal homogeneous solutions. Rate depends on alkyl chain length because the mechanism is a function of the location of the solubilised molecules within micelles[14].

An example demonstrating reaction control owing to electrostatic effects is the basic hydrolysis of nitrophenyl esters of carboxylic acids[15]. In the presence of CTAB the substitution of a thiol for a nitro group was increased by a factor of 4 x 10^5, and in addition the concentration enhancement was affected by increased local effects on the acid-base relationship of the nucleophilic thiolation reaction as shown in Figure 2.2:

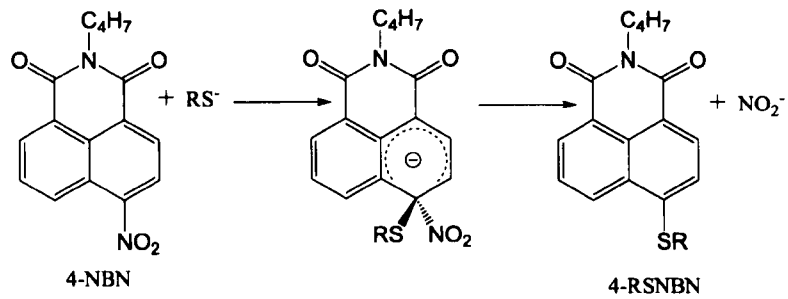

Figure 2.2: Thiol substitution for a nitro group where 4-NBN represents 4-nitro-*N*-n-butyl-1,8-naphthalimide and 4-RSNBN represents 4-heptanothiolate-*N*-n-butyl-1,8-naphthalimide[15].

Micellar systems can also act as phase mediators[8] bringing together insoluble or gaseous reagents such as in the case of hydroformylation. This process is normally carried out in aqueous systems[15], which present limitations since many higher olefin substrates suffer from low solubility. For example, Li and co-workers used a water soluble $[RhCl(CO)(tppts)_2]$ (tppts = tris(m-sulfonatophenyl)phosphine) complex to hydroformylate 1-dodecene in water, in the presence of surfactants such as SDS, resulting in enhancements in both yield and regioselectivity[16].

Lyotropic liquid crystal mesophases can also have a profound effect on chemical reactivity as they can exert a strong control over the orientation of reactants. Reactions performed in surfactant mesophases are sensitive to phase type, with the more ordered mesophases less able to solubilise guest molecules, limiting somewhat the potential for higher ordering effects on reactivity[17]. At the time of writing, studies of kinetics and reaction outcomes in LCs were only very limited. This is surprising because the analogous dilute micellar systems which are known to confer remarkable effects on catalysis and stereoselectivity, have been much studied. Ahmed and Friberg[18] reported the first reaction (p-nitrophenyl laurate hydrolysis) in a lyotropic LC phase (CTAB – water – hexanol). They reported that the reactions proceeded readily in isotropic, L_α and "middle" (hexagonal) phases. Interestingly, changes in the reaction rate caused by composition variation within each phase were also noted e.g. 'an increase of factor of 3...' when the hexanol-CTAB ratio was raised from 0.2 to 0.7% w/w. However, they did not simultaneously analyse the mesophase structure, leaving doubts to the origin of this rate enhancement.

Bakeeva and co-workers[19] noted an increase in rate up to ten-fold for an alkaline hydrolysis when carried out in a micellar phase as compared to water. The kinetics was faster with increasing surfactant concentration. The same reaction in the hexagonal phase resulted in only a two-fold rate enhancement but, interestingly, it was explained by a change in substrate orientation within the hexagonal cylinders, rather than a change in mobility (diffusion) as seen within the micellar phase. Clearly mesophases and related structures have interesting and potentially useful roles to play as media in control of reaction outcomes, though systematic studies combining kinetics and structural effects are sorely lacking.

2.5 Ionic Liquids

Ionic compounds are typically solids with high melting points, however, as early as 1914 Waldon[20] described neutralization of ethylamine with concentrated nitric acid to create an ionic liquid (ethylammonium nitrate EAN) having an unusually low melting point of around 13 °C. Today ionic liquids (ILs) are classed as salts that form stable liquids below (arbitrarily) 100 °C. These salts are poorly coordinated, where at least one ion has a delocalized charge preventing stable crystal lattice formation.

Barrer[21] synthesized the first imidazolium IL, on which most of today's ILs are still based (see Figure 2.3). However it was not until much later when the first imidazolium halogenoaluminate salts were synthesized[22], that ionic liquids really became of interest both academically and commercially. The field advanced in the early 1980s with the introduction of a homologous series of 1,3-dialkylimidazolium chlorides (Figure 2.3, a-c), and studies of the properties of mixtures of these salts[23].

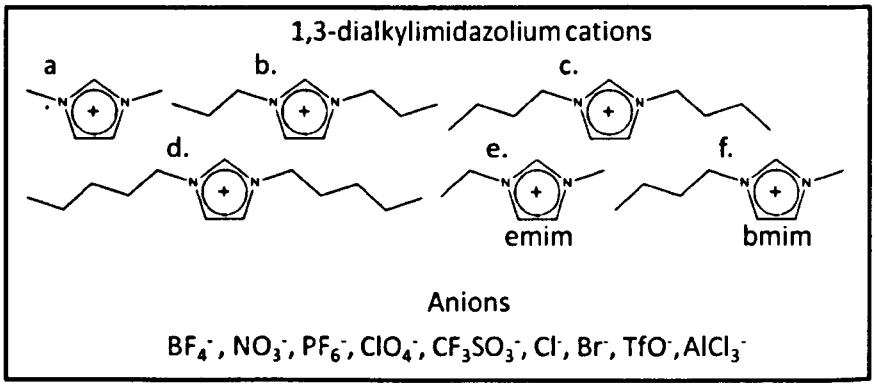

Figure 2.3: Various 1,3-dialkylimidazolium cation-anion combinations.

It was found that reacting $AlCl_3$ with 1,3-dialkylimidozalium halides gave rise to a series of equilibria to generate Cl^-, $AlCl_4^-$, $Al_2Cl_7^-$, $Al_3X_{10}^-$, etc.[24] and that by adjusting the mixing ratios of imidazolium halide to the halogenaluminate, properties such as viscosity, acidity and refractive index were affected[25]. It was also shown that by changing the anions and cations, other physicochemical properties of ILs, such as solubility, density and melting point, could be controlled[26]. The chloroaluminate melt prepared from 1–methyl-3-ethylimidazolium chloride [emim]Cl, had the most favourable physical properties (large liquidus range and electrochemical window) and was easy to prepare[27]. These imidazolium salts (Figure 2.3) were used in organic synthesis[28] and proved to be an ideal starting point for the development of other ILs[24].

Inert anions such as toluenesulfonate[29], tetrafluoroborate[23] and hexafluorophosphates[30] were used with 1,3-dialkylimidozalium cations to create the first air and moisture stable room temperature ILs (RTILs). These compounds are, however, quite expensive, being often difficult to prepare in high purity, have unknown toxicity, and so fluorine-free (halogen-free) and hydrophobic anions that are more environmentally friendly such as tetraalkylborates and tetraphenylborates are currently being reinvestigated[31, 32].

The range of potential cations is also vast, with not only imidazolium, but also pyridinium, ammonium, phosphonium, thiazolium, sulfonium and pyrrolidinium salts (and more). These ILs are thermally stable[33] and have low saturated vapour pressures; in fact for a long time it was thought that distillation of these liquids was impossible until work by Earle[34]. Because there is such a huge number of permutations ($\sim 10^9$)[35] ILs are highly tuneable and many have been developed for specific synthetic purposes, replacing molecular solvents for greener chemistry and earning the designation "designer solvents[36]".

2.6 Customizing ionic liquids

By modifying the cations and anions of ILs their properties can be dramatically altered: for example, [bmim]CH_3COO^- is miscible with water whereas [bmim][PF_6] is not[37]. The size, charge, and charge distribution and separation are acknowledged as major factors influencing the melting point[38, 39] and viscosity[40]. In accordance with the Kapustinskii equation[41] (Equation 2.6) increasing the cation size and/or

decreasing that of the anion decreases the lattice energy (U_L) of the salt (for example, NaCl has mp 803 °C, whereas for 1-propyl-3-methylimidazolium chloride mp ~ 60 °C)[42].

$$U_L = -K \cdot \frac{v \cdot |z^+| \cdot |z^-|}{r^+ \cdot r^-} \cdot \left(1 - \frac{d}{r^+ + r^-}\right) \qquad \text{Eq. 2.6}$$

Here z^+ and z^- and r^+ and r^- represent the elementary charges and the anion and cation radii, respectively, and v is the number of ions in the empirical formula. The terms K and d are salt-specific constants. Attractive Coulombic and van der Waals interactions decrease the energy of the salt, while repulsive Pauli forces increase it[43]. by minimizing this cohesive energy the glass transition (T_g) is lowered; also, due to higher degrees of freedom, more asymmetric cations result in lower melting points by disrupting crystal packing[44], as shown in Figure 2.4. There is an optimum chain length asymmetry for lowering the melting point showing that organic chemical structure can have profound effects on physicochemical properties of ILs.

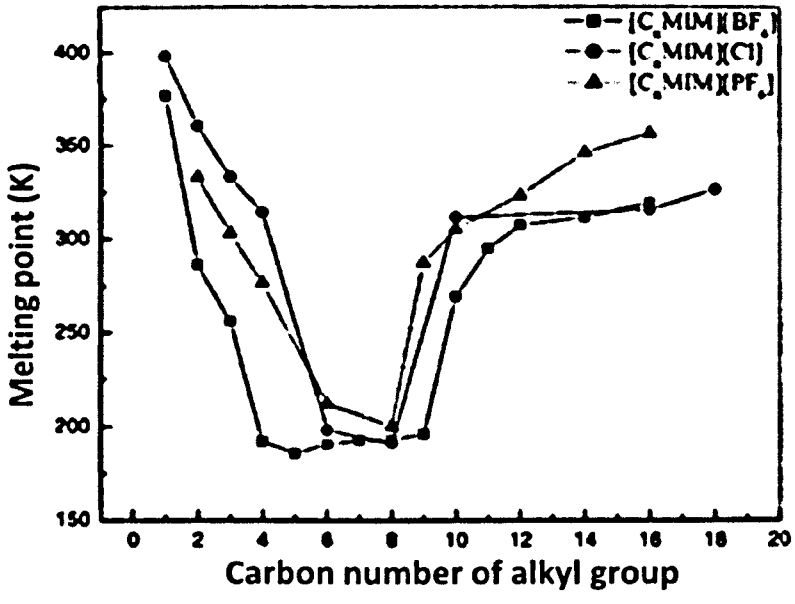

Figure 2.4: Observed melting points for a series of imidazolium based ionic liquids with increasing carbon chain length on the cation[45] (modified and reproduced with permission of The American Institute of Physics).

Commonly used anions in ILs include hexafluorophosphates [PF_6^-], tetrafluoroborates [BF_4^-], tetrachloroaluminates [$AlCl_4^-$], bistriflate imides [Tf_2N^-] and halides, as they are symmetrical and pseudo-spherical. However, there are a whole host of possible anions, leading to a huge number of low melting point salts.

There are also other interesting characteristics of ILs including density which does not show much sensitivity to variations in temperature[46] but does depend greatly on structure. For example, increasing alkyl chain length decreases density of 1,3-methylimidazolium hexafluorophosphates (Figure 2.5)[47].

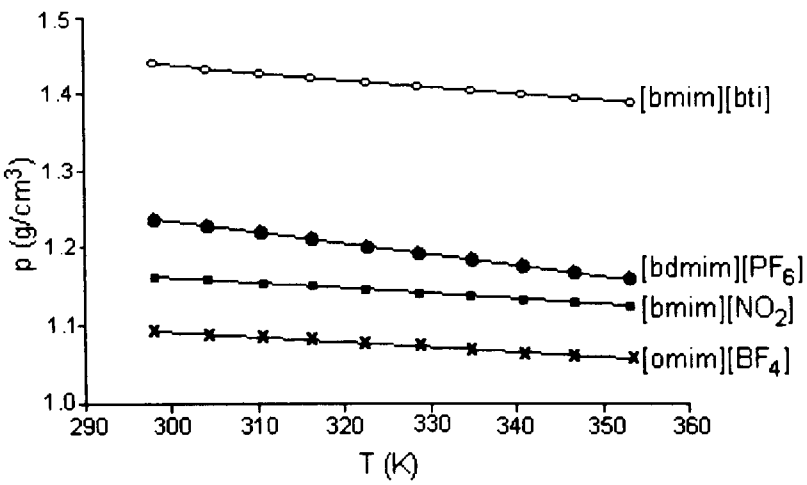

Figure 2.5: Apparent linear dependence of the density as a function of the temperature for ionic liquids[48]. [bmim][bti]: 1-butyl-,3-methylimidazolium bis(trifluoromethylsulfonyl)imide; [bdmim][PF_6]: 1-butyl-2,3-dimethylimidazolium hexafluorophosphate; [omim][BF_4]: 1-octyl-,3-methylimidazolium tetrafluoroborate (modified and reproduced with permission from Elsevier).

Unsurprisingly, there are also strong effects on vapour pressure, often considered advantageous[38]. For many years it was thought that ILs did not exhibit a measurable vapour pressure[49], however new generations of ILs can be reversibly vapourised at sufficiently high temperatures, and re-condensed on cooling[34].

2.7Reactions using ionic liquids

In the mid 1980s, Fry and Pienta[50] and Boon *et al.*[51] realized that ionic liquids could act as solvents for organic synthesis. ILs are often suitable as reaction media as they are thermally stable, having large liquidus ranges, for example [emim]Cl/[emim]$AlCl_3$ (Figure 2.3, b) mixtures are liquid between -90 °C and 300 °C compared to 0 - 100 °C for water or -114 - 78 °C for ethanol[52, 53]. In addition ILs are able to dissolve a wide range of organic, inorganic and organometallic compounds, as well as gases such as H_2, CO and O_2. All of these features make ILs attractive solvents for catalytic hydrogenations, carbonylations, hydroformylations, and aerobic oxidations, and because they can be polar but non-coordinating so they have rate enhancing effects on reactions involving cationic intermediates[54]. It has also been noted that they can facilitate reaction stereoselectivity, not possible in normal molecular solvents[55-57].

The unusual effects of ILs on reactions cannot be explained through traditional theories of polarity and Lewis acid-base properties, though they still exhibit hydrogen bonding, dispersion, electrostatic, dipolar and hydrophobic interactions[24]. As with all solvents, altering IL functional groups affects solvent properties. Bartsch and Dzyuba[58] proposed that the polarity difference (based on the Dimroth-Reichardt $E_T(30)$ parameter) between the alcohol and ether functionalized imidazolium salts of [Tf_2N^-] influences the *endo/exo* ratio of Diels-Alder products formed between cyclopentadiene and methyl methacrylate (Figure 2.6).

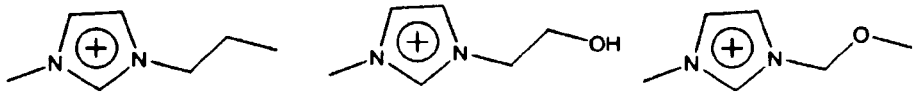

$E_T(30)$	52.0	60.8	61.4
endo/exo ratio	4.3	6.1	5.7

Figure 6: Diels-Alder product ratios for the reaction between cyclopentadiene and methyl methacrylate in IL media with different polarities.

ILs are also useful for precious metal catalysis as the organic products can be removed without aqueous workup, the catalyst often remains in the IL, so that it can be directly reused[59]. There are different systems for catalysis in/by ILs where the catalyst and substrate are dissolved in the IL, those where the IL acts as both solvent and catalyst, and those whereby the IL acts as a ligand for the catalyst[60, 61], including bi-[62, 63] and triphasic[64] systems.

2.7.1 Hydroformylation

Hydroformylation is an important process in catalysis, and the first example with an IL was Pt-catalysed hydroformylation of ethane[65]. Since then much work has been done to improve product separation, catalyst recovery, stability[66], and selectivity. To increase alkene solubility and selectivity for the linear aldehyde, imidazolium triflate IL was used with a Rh catalyst in a biphasic system with organic solvents (Figure 2.7)[67], giving evidence that all catalytic activity occurred in the ionic phase.

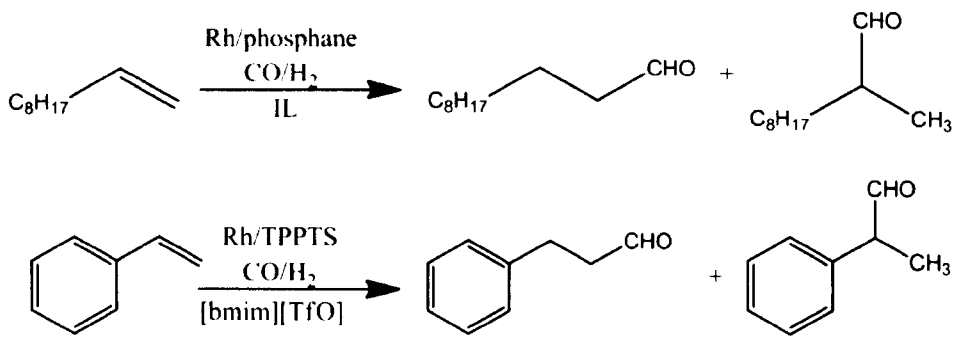

Figure 2.7: Hydroformylation of 1-decene and styrene in IL-biphasic systems[67].

2.7.2 Cross coupling reactions

Heck couplings in [bmim][PF_6] were demonstrated by Carmichael *et al.*[61] using $Pd(OAc)_2$-Ph_3P as catalyst to couple 4-bromoanisole with ethylacrylate, which gave a yield of 98% ethyl 4-methoxycinnamate (Figure 2.8). Since the IL is virtually insoluble in water and alkenes, but dissolves the transition meal catalyst, simple extraction and recycling of the expensive palladium catalyst becomes possible.

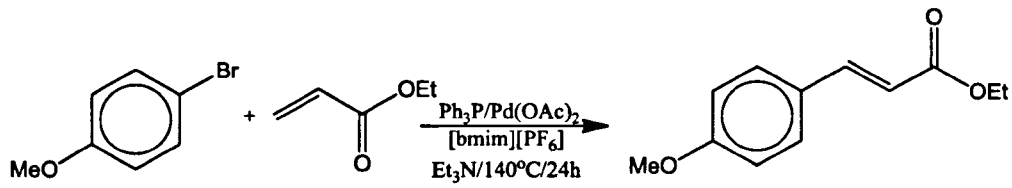

Figure 2.8: Heck reaction to couple 4-bromoanisole with ethylacrylate.

Another example is Heck coupling of 1-bromonaphthalene to butyl vinyl ether: in regular solvents such as toluene or dimethylsulfoxide a mixture of isomers is formed, however Xiao *et al.*[68] showed that in [bmim][PF_6] >99% selectivity to the α-arylation product occurs (Figure 2.9).

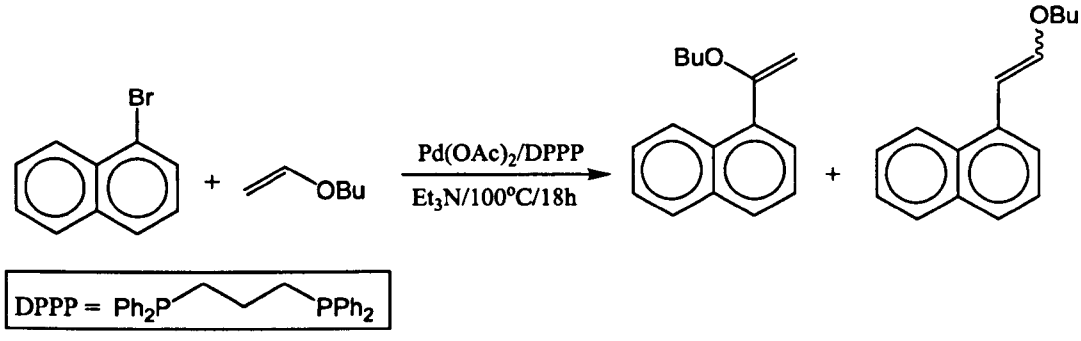

Solvent	Conv. %	α/β
[bmim][PF_6]	50	>99%
Toluene	23	46/54
Acetonitrile	36	69/31
DMF	100	60/40
DMSO	100	75/25

Figure 2.9: Coupling of 1-bromonaphthalene to butyl vinyl ether in different solvents[68].

α/β is the isomer ratio.

In Suzuki coupling reactions [bmim][BF_4] afforded good yields[69, 70], and a phosphonium ionic liquid allowed nanofiltration and recovery of the solvent and catalyst[71]. There were problems with Negeshi cross-coupling reactions though; by using an imidazolium salt with a phosphine ligand the problems of cation deprotonation with amine base could be avoided. Interestingly, where [bmim]-based ILs met with failure, [bdmim][BF_4]/toluene biphasic solvents gave high yields (~90%)[72]. This IL was also used for a copper-

catalysed, ligand-free Sonogashira reaction, however ultrasonic irradiation had to be used to assist the reaction[73].

Although it has been shown that ILs can enhance the activity and stability of catalysts in cross-coupling reactions as well as stereoselectivity, there are sometimes drawbacks to using ionic liquids in synthesis. In particular, ILs may have high viscosities compared with conventional molecular solvents, which can slow heat and mass transfer, thereby lowering reaction rates. For example, Diels-Alder[74] reactions occur faster in water than IL media due to the absence of hydrophobic interactions, and weaker hydrogen bonding, so it is important to realize that conventional solvents still offer the best media for certain reactions.

2.7.3 Other reactions

The first reports of hydrogenation in ILs showed the rhodium catalysed hydrogenation of pent-1-ene with reaction rates up to five times higher than in acetone solvent and Rh losses below detection[75]. Regioselective hydrogenation in ILs has also been reported[76]. Two other industrially important processes include aromatic substitution reactions, for which selectivity, reaction time and yields can be improved by ILs[77]. For olefin dimerisations, Ni-catalysed dimerisation of propene in [bmim][$AlCl_4$] was the first to be reported[75]. Many catalysed oxidations such as epoxidation, dehydroxylation and the oxidation of alcohols[78], thio compounds[79], oximes[80] and alkanes, amongst others, have made use of ionic liquids. A good example of aromatic aldehyde oxidation to the corresponding acid was that studied by Howarth[81]. Nickel II acetylacetonate catalyst was employed in [bmim][PF6] at 60 °C with oxygen; and the reaction was repeated three times using the recovered IL/Ni system without a decrease in yield.

Recently biocatalytic reactions in ionic liquids have also been investigated as, unlike organic solvents of comparable polarity, they often do not deactivate enzymes, which simplifies reactions involving polar substrates such as sugars[82]. IL solvents permit faster rates and enantioselectivity which can be advantageous[83]; work on amino acid/peptide chemistry shows not only that the polar nature of ionic liquids is particularly suitable for synthesis, but also that amino acids can be used as starting materials for the generation of chiral ILs[84-86]. Ionic liquids also offer new possibilities as buffers in non-aqueous systems

which is especially exciting for the optimization of acid-base conditions and enzymatic reactions[87], an area recently reviewed by Rantwijk and Sheldon[88].

2.8 Ionic liquid applications and industrial processes

Initial optimism about potential industrial utilization of ionic liquids was perhaps misplaced; however, there are numerous real-life applications. There may still be an "ionic liquid revolution", especially since current as well as proposed applications of ILs are no longer limited to solvent replacement, but diverse applications ranging from catalysis, separations, data storage[89], photochemistry[90], CO_2 capture[91], hazardous gas storage[92], lubrication[93] and rocket propulsion[94, 95] to name just a few. Commercial, as well as up and coming applications are reviewed below.

2.8.1 The BASIL process

The Basil process (Scheme 2.2) (Biphasic Acid Scavenging using Ionic Liquids) was first introduced by BASF in 2002 and is used commercially in the preparation of alkoxyphenylphosphines. The improved process uses a 1-methylimidazole to scavenge acid, the resulting salt is an IL which forms a discrete phase, and is much more easily removed from the reaction mixture than traditional solid by-products[36].

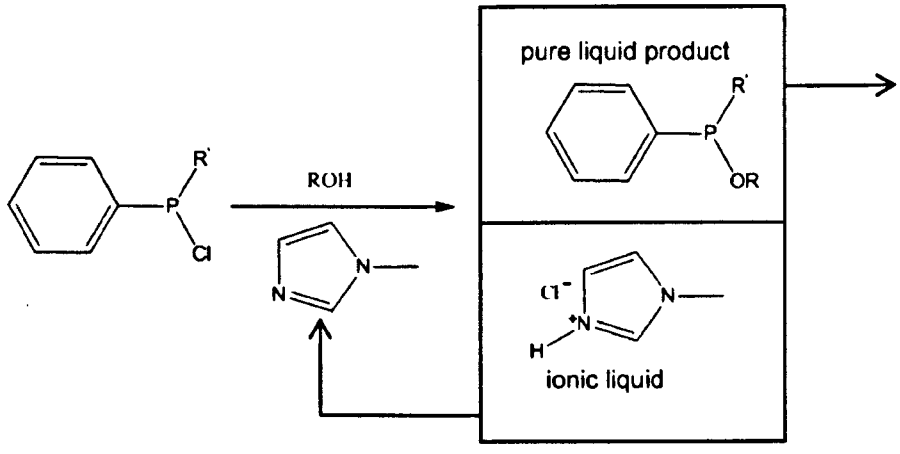

Scheme 2.2: The BASIL™ process.

Compared to the conventional liquid process the space-time yield (mass of product formed per volume of the reactor and time, kg m^{-3} s^{-1}) is increased by a factor of over 8.5 x 10^4, and yield increases from 50% to

98% have been possible. The ionic liquid produced is also recycled via base decomposition of the 1-H-3-imidazolium chloride[96].

2.8.2 Cellulose processing

Rogers and co-workers[97] found that technically useable concentrations of cellulose could be produced by using ILs. This shows great potential as it prevents the disposal of huge quantities of waste water as well as various other compounds such as CS_2. Now their techniques are being commercially developed by BASF to make cellulose-polymer blends as novel plastics.

2.8.3 Nuclear fuel waste disposal

ILs exhibit good stability against radiation and hence can be used in solvent extraction systems as alternate non-aqueous electrolyte media for high temperature pyrochemical processing of spent nuclear fuel[98]. Recovery of uranium[99], and other useful fission products such as palladium[100], using ILs have been reported. In a further development uranyl ions in nitric acid has been extracted by using [bmim][Tf_2N] and transferred to supercritical CO_2[101], because ILs do not dissolve in CO_2 so their recycling and repeated use should be possible.

2.8.4 Plastic recycling

Although not yet an economical approach, recycling of thermosetting plastics has been demonstrated by depolymerising nylon in ILs at 300 °C to regenerate the cycloprolactam feedstock[102]. This is especially exciting as up until now most thermosetting plastics are simply unrecyclable.

2.8.5 Ionikylation[103]

This process, developed by Petrochina (Beijing, China), employs aluminium chloride based ILs in place of sulfuric acid catalysts for alkylation of isobutene, which is a key step in gasoline generation. This process is employed on an industrial scale with 65,000 tonnes produced per year, being the largest commercialization of ILs to date. They are also employed as the transport medium for reactive gases at sub-ambient pressures, and as paint additives to enhance the drying properties and finish of paint[104, 105].

2.8.6 Other applications

ILs exhibit high thermal stability and thus show potential for use in solar energy thermal power plants[106]. Furthermore, owing to low volatility they can be used for safer microwave synthesis, as they reduce sudden pressure surges. The dipolar characteristics of ILs also facilitate rapid excitation by microwaves, and consequently faster reactions[24].

2.9 Micellisation and lyotropic mesophases of SAILs

In the early 1980s Evans and coworkers described micelle formation by added surfactants in EAN[107, 108], being the first reported case of self-assembly in ILs. For typical cationic amphiphiles the cmcs determined in EAN were 5-10 times larger than in water[109], and it was proposed this was due to enhanced solubility of the surfactant hydrocarbon chains in the IL[108].

Unlike water and other molecular solvents capable of supporting amphiphile self-assembly, ILs themselves consist of cations and anions which can obviously undergo ion exchange with surfactants[110]. ILs can also be mixed with other solvents, as either the major or minor constituent. The first systems studied were IL:H_2O systems because ILs are often very hygroscopic, and physico-chemical properties and reactivity should be dependent on water content. Reverse micelles with IL polar cores and reverse microemulsions with nano-sized IL droplets dispersed in cyclohexane (continuous phase) by non-ionic Triton X 100 surfactant were first reported by Han and coworkers in 2004[111]. Since then much work has continued concerning ILs both as the dispersed and continuous phase.

Some ILs can also act as amphiphiles, not just solvents, and interestingly, if the IL molecules comprise long alkyl chains, which are termed surfactant ionic liquids (SAILs), then they have additional thermotropic properties, forming liquid crystals[112]. Examples of such IL amphiphiles include 1-alkylimidazolium nitrates or chlorides[113], which form LCs in water, acidic water, or tetrahydrofuran (THF). The lyotropic phases of SAILs based on 1-alkyl-3-methylimidazolium cations (Figure 2.3) have been investigated by Firestone and co-workers[114] and then Bowers and co-workers[115]. These systems showed aggregation in aqueous solution, yielding micellar-like structures just above the cmc. In 2007 Inoue and co-workers[116] showed evidence of

both lamellar ($L\alpha$) and hexagonal (H_1) phases for the SAIL 1-dodecyl-3-methylimidazolium bromide with water in the range 10-50% v/v (Figure 2.10). In fact relatively short alkyl chain ILs (C_8) have been shown to form mesophases[115], which was further confirmed by ^{2}H-NMR and X-ray diffraction[117]. Recently, El Seoud and co-workers[118] and Eastoe and co-workers[119] have clearly demonstrated that the IL nature of SAILS has no notable effect on aggregation properties. Nevertheless, the development of SAILs is advantageous as it presents the opportunity to combine the catalytic properties of surfactant systems with those unique to ILs, especially for separations and extractions. Furthermore, this also offers the possibility to switch between a "pure" IL solvent, with favourable solvating properties, and an IL mesophase which may confer different selectivity and kinetics.

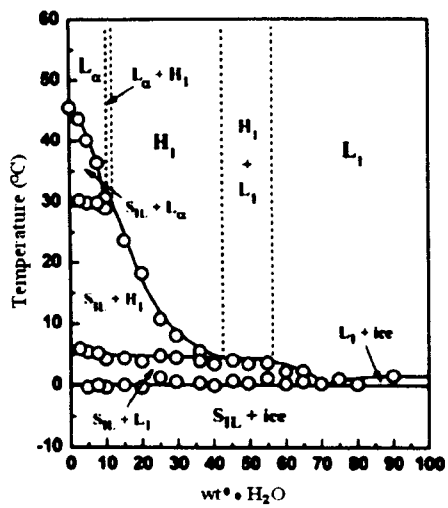

Figure 2.10: Temperature–concentration phase diagram for C_{12}mimBr/H_2O mixtures. S_{IL} (solid phase of C_{12}mimBr), L_α (lamellar phase), H_1 (hexagonal phase), L_1 (micellar solution)[116] (reproduced with permission from Elsevier).

2.10 Reactions in IL mesophases

Many studies on 1-alkyl-3-methylimidazolium salts have been undertaken[120] showing self-organization[121] and tendency to supercool to a glassy state. Bowlas and co-workers[122] produced imidazolium salts with long alkyl chain lengths (C_n = 12-18) that exhibited mesophases over large temperature ranges, showing promise as a solvent with catalytic ability[114]. Through using N-alkylimidazolium ILs (Figure 2.11) Lin and co-

workers[115] demonstrated stereoselectivity of a Diels-Alder reaction, a condensation reaction of cyclopentadiene with diethyl maleate. In ethanol the *endo* product was favoured 88:12, whereas in the L_α LC phase the *endo* product was favoured 46:54.

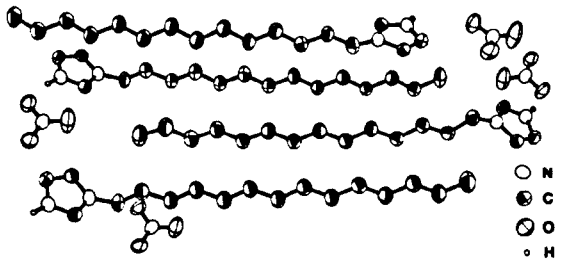

Figure 2.11: Bilayer lamellar structure of $[C_{14}H_{29}\text{-imH}][NO_3]$ used as a solvent to enhance *endo* selectivity in a Diels Alder reaction[115] (reproduced with permission of The Royal Society of Chemistry).

This thermotropic LC result is extremely promising and leads to intriguing questions about the possible combined effect of ionic liquid solvent properties and mesophase structure on organic reactions. Savelli and co-workers[123] demonstrated, through an accelerated decarboxylation in an imidazolium-based SAIL, that microenvironment properties vary with SAIL concentration as well as modifications of SAIL structure, such as anion type or alkyl chain length, with results a consequence of the system's structural conformation in water. This presents tantalizing possibilities for control over reaction outcomes, owing to changes in the nature of the ILs and the solvent employed to induce the mesophases, as well as the composition of IL:solvent mixtures. Then it would be possible to consider the entire mesophase as being the "supporting solvent" for any reaction under investigation.

2.11 Conclusions and future prospects

This review has explored how rate, stereoselectivity and mechanism of reactions can be altered by performing them in structured reaction media, comprising surfactants, mesophases as well as less well ordered ionic liquids. It has also been shown that certain ILs self-assemble opening up the possibility of new

ordered, tunable solvents. With a dearth of systematic studies in ordered ionic solvent systems interesting questions can be posed.

- How does substrate partitioning, orientation and reactivity in micelles compare to that in the pure structured IL solvent?
- Is there a balance between increased local concentrations and limited diffusion in more ordered mesophases?
- Where do reactions occur in a given mesophase? Could reactions pathways be switched during a reaction by modulating the solvent structural environment?

Reactions in ILs will continue to be studied due to often facile extraction and separation, but by simultaneously investigating control of the underlying solvent structure to manipulate reaction behaviour, exciting new potential applications may be found.

2.12 References

1. J. Rassing, P.J. Sams and E. Wyn-Jones, Chem. Phys. Lett., 1972, 13, 233-236.
2. C.J. Drummond and T. Kaasgaard, Chem. Phys. Chem., 2006, 8, 4957-4975.
3. K. Holmberg, B. Jönsson, B. Kronberg and B. Lindman, *Surfactants and Polymers in Aqueous solution*, 2nd ed., Wiley, Weinheim, p. 39-95, 2003.
4. T.F. Tadros, *Applied Surfactants: Principles and Applications*, 1st ed., Wiley, Weinheim, p. 19-71, 2005.
5. T.L. Greaves and C.J. Drummond, Chem. Soc. Rev., 2008, 37, 1709-1726.
6. S. Tascioglu, Tetrahedron, 1996, 34, 11113-11152.
7. E.F.J. Duynstee and E. Grunwald, J. Am. Chem. Soc., 1959, 81, 4540.
8. T. Dwars, E. Paetzold and G. Oehme, Angew. Chem. Int. Ed., 2005, 44, 7174-7199.
9. R.B. Dunlap and E.H. Cordes, J. Am. Chem. Soc., 1968, 90, 4395.
10. G. Savelli R. Germani and L. Brinchi, *Reactions and Synthesis in Surfactant Systems*, 1st Ed., CRC Press, New York, 2001.
11. M.N. Khan and E. Ismail, J. Chem. Soc. Perkin 2, 2001, 1346.
12. C.A. Bunton, Catal. Rev. Sci. Eng., 1979, 20, 1.
13. D.C. Barber T.E. Woodhouse and D.G. Whitten, J. Phys. Chem., 1992, 96, 5106-5114.
14. H. Al-Lohedan, C.A. Bunton and M.M. Mhala, J. Am. Chem. Soc., 1982, 104, 6654-6660.
15. B. Cornils and E.G. Kuntz, *Aqueous-phase organometallic catalysis: Concepts and Applications*, 2nd ed., Wiley, Weinheim. p. 351, 2004.
16. H. Chen, Y.E. He, M. Li, X.J. Li and Y.Z. Li, J. Mol. Catal. A, 2003, 194, 13.
17. W.J. Leigh and M.S. Workentin, *Liquid crystals as solvents for spectroscopic chemical reactions, and gas chromatographic applications*, in *Handbook of Liquid Crystals*, Wiley, Weinheim, p. 849, 1998.
18. S.I. Ahmad and S. Freiberg, J. Am. Chem. Soc., 1972, 94, 5196-5199.
19. R.F. Bakeeva, L.A. Kudryavtseva, G. Eme, E.M. Kosacheva, V.E. Bel'skii, D.B. Kudryavstev, R.R. Shagidullin, V.F. Sopin, Russ. Chem. Bull., 1998, 47, 1454-1459.
20. P. Waldon, Bull. Acad. Sci. (St. Petersberg), 1914, 6, 405-442.

21. R.M. Barrer, Trans. Farad. Soc., 1943. 39, 59-67.

22. H.L. Chum, V.R. Koch, L.L. Miller and R.A. Osteryoung, J. Am. Chem. Soc., 1975, 97, 3264.

23. M.L. Druelinger, C.L. Hussey, J.A. Levisky and J.S. Wilkes, Proc. Int. Symp. Molten Salts, 1980, 81, 245-255.

24. P. Keim and P. Wasserscheid, Angew. Chem. Int. Ed., 2000, 39, 3772-3789.

25. R.J. Gale and R.A. Osteryoung, Inorg. Chem., 1979, 18, 1603.

26. S. Chauhan, S.M.S. Chauhan, N. Jain and A. Kumar, Tetrahedron, 2005, 61, 1015-1060.

27. C.L. Hussey, J.A. Levisky, J.S. Wilkes and R.A. Wilson, Inorg. Chem., 1982, 21, 1263-1264.

28. H. Olivier, J. Mol. Catal. A, 1999, 146, 285-289.

29. E. Cooper, Elec. Chem. Soc. Proceeding Series, 6, 386, Pennington NJ, 1992.

30. C.M. Gordon, J.D. Holbrey, A.R. Kennedy and K.R. Seddon, J. Mater. Chem, 1998, 8, 2627-2636.

31. W.T. Ford, D.J. Hart and R.J. Hauri, J. Org. Chem., 1973, 38, 3916-3918.

32. T. Kakiuchi, T. Kawakami, N. Nishi, F. Shigematsu and M. Yamamoto, Green Chem.,2006, 8, 349-355.

33. N.J. Audic, J. Am. Chem. Soc., 2003, 125,9248-9249.

34. M. Earle, Nature, 2006, 439, 831-834.

35. M.J. Earle and K.R. Seddon, Pure Appl. Chem., 2000, 72, 1391-1398.

36. N.V. Plechkova and K.R. Seddon, Chem. Soc. Rev., 2008, 37, 123-150.

37. M. Koel, Proc. Est. Acad. Sci. Chem, 2000, 49, 145-155.

38. P. Wasserscheid and T. Welton, *Ionic liquids in synthesis*, Wiley, Weinheim, p. 364, 2002.

39. E. Burello, P.N. Davey, I. Lopez-Martin, G. Rothenberg and K.R. Seddon, Chem. Phys. Chem., 2000, 8, 690-695.

40. A. Bagno, C.P. Butts, C. Chiappe, F. D'Amico, J.C.D. Lord, D. Pieraccini and F. Rastrelli, Org. Biomol. Chem., 2005, 3 1624-1630.

41. A.F. Kapustinskii, Q. Rev. Chem. Soc, 1956, 10, 283.

42. K.R. Seddon, Kinet. Katal., 1996, 37, 743-748.

43. C.A. Angell, E.I. Cooper and W. Xu, J. Phys. Chem. B., 2003, 107, 6170-6178.

44. A.K. Abdul-Sada, A.M. Greenway, P.B. Hitchcock, J.M. Thamer, K.R. Seddon and J.A. Zora, J. Chem. Soc. Chem. Commun., 1986, 1753-1754.

45. X. He, X. Lu, and X. Zhang, J. Phys. Chem. Ref. Data, 2006, 35, 1475-1517.

46. R.A. Mantz and P.C. Truelove, *Viscosity and density of ionic liquids*, in *Ionic Liquids in Synthesis*, Wiley, Weinheim, p. 56-68, 2002.

47. J.A. Boxall, R. Lichtenhalter and K.N. Marsh, Fluid Phase Equilibria, 2004, 219, 93-98.

48. J.O. Valderrama and K. Zarricueta, Fluid Phase Equilibria, 2009, 275, 145-151.

49. A.V. Blokhin, M. Frenkel, G.J. Kabo, J.W. Magee, Y.U. Paulechka and O.A. Vydrov, J. Chem. Eng. Data, 2003, 48, 457.

50. S.E. Fry and N.J. Pienta, J. Am. Chem. Soc., 1986, 107, 6399-6400.

51. J.A. Boon, J.A. Levisky, J.L. Plug and J.S. Wilkes, J. Org. Chem., 1986, 51, 480-483.

52. C.L. Hussey, J.A. Levisky, J.A.Wilkes and R.A. Wilson, Inorg. Chem., 1982, 21, 1263,.

53. A.A. Fannin, D.A. Floreani, L.A. King, J.S. Landers, B.J. Piersma, D.J. Stech, R.L. Vaughn, J.S. Wilkes and J.L Williams, J. Phys. Chem., 1984, 88, 2614.

54. R. Sheldon, Chem. Commun., 2001, 2399-2407.

55. M.S. Rao, B.V.S. Reddy, P.N. Reddy and J.S. Yadav, Synthesis, 2003, 9, 1387.

56. Z.C. Chen, Y. Hi, Z.G. Le and Q.G. Zheng, *S*ynthesis, 2004, 12, 1951-1954.

57. Z. Hou, Y. Hu and B. Feng, Catalysis Commun., 2009, 10, 1903-1907.

58. R.A. Bartsch and S.V. Dzyuba, Tetrahedron Lett., 2002, 43, 4657-4659.

59. R. Bernini, A. Coratti, G. Fabrizi and A. Goggiamani, Tetrahedron Lett., 2003, 44, 8991-8994.

60. A. Ahosseini, W. Ren and A.M. Scurto, Ind. Eng. Chem. Res., 2009, 48, 4254-4265.

61. A.J. Carmichael, M.J. Earle, D.J. Holbrey, P.B. McCormac and K.R. Seddon, Org. Lett., 1999. 1, 997-1000.

62. G.W. Parshall, J. Am. Chem. Soc., 1972, 94, 8716-8719.

63. C.M. Gordon, Applied Catalysis A, 2001, 222, 101-117.

64. J. Dupont, R.F. de Souza and P.A.Z. Suarez, Chem. Rev., 2002, 102, 3667-3692.

65. R. Fehrmann, M. Haumann, A. Riisager and P. Wassersheid, *Catalytic SILP materials*. Topics in Organomtallic Chemistry, Springer, Heidelberg, Vol. 23, p. 149-161, 2008.

66. R. Fehrmann, M. Haumann, A. Riisager and P. Wassersheid, Ind. Eng. Chem. Res, 2005, 44, 9853-9859.

67. L. Leclercq, I. Suisse and F. Agnossu-Niedercorn, Chem. Commun, 2008, 311.

68. W. Chen, J. Ross, J. Xiao and L. Xu, Org. Lett., 2001, 3, 295-297.

69. C. J. Mathews, P.J. Smith, T. Welton, A.J.P. White and D.J. Williams, Organometallics, 2001, 20, 3848-3850.

70. C.J. Mathews, F. McLachlan, P.J. Smith and T. Welton, Organometallics, 2003, 22, 5350-5357.

71. F.C. Ferreria, G. Livingston, J.P. Pink and H. Wong, Green Chem., 2006, 8, 373-379.

72. B. Betzemeier, P. Knochel, M. Ossberger and J. Sirieix, Synlett, 2000, 1613-1615.

73. A.R. Gholap, K. Venkatesan, R. Pasricha, T. Daniel, R.J. Lahoti and K.V. Srinivasan, J. Org. Chem., 2005, 70, 4869-4872.

74. S. Tiwari and A. Kumar, Angew. Chem. Int. Ed., 2006, 118, 4824-4825.

75. Y. Chauvin, B. Gilbert and I. Guibard, J. Chem. Soc. Chem. Commun., 1990, 1715-1757.

76. J. Arras, P. Claus, Y. Shayeghi and M. Steffan, Chem. Commun., 2008, 2348-2349.

77. N. Llewellyn Lancaster and V. Llopis-Mestre, Chem. Commun., 2003, 2812-2813.

78. N. Jiang and J. Ragauskas, J. Org. Chem., 2007, 72, 7030-7033.

79. S.M.S. Chauhan, A. Kumar and K.A. Srinivas, Chem. Commun., 2003, 2348.

80. S.M.S. Chauan, A. Jain and A. Kumar, Tetrahedron Lett., 2005, 46, 2599-2602.

81. J. Howarth, Tetrahedron Lett., 2000, 41, 6627-6629.

82. S. Park and R.J. Kazlauskas, Curr. Opin. Biotechnol., 2003, 14, 432-437.

83. N. Kaftzik, U. Kragl, S.H. Schoefer and P. Wassersheid, Chem. Commun., 2001,425.

84. A.D. Headley and B. Ni, Aldrichimica Acta, 2007, 40, 107-117.

85. A. Gaumont, F. Guillan, C. Malhaic, J. Levillain and J. Plaquevent, Chem. Rev., 2008, 108, 5035-5060.

86. C. Chiappe, G. Imperato and B. Koenig, Eur. J. Org. Chem., 2007, 1049-1058.

87. G. Ou, J. She, Y. Yuan and H. Zhou, Chem. Commun, 2006, 4626-4628.

88. F.R. Rantwijk and R.A. Sheldon, Chem. Rev., 2007, 107, 2757-2785.

89. P. Licence, F.J.M. Rutten and H. Tadesse, Angew. Chem., 2007, 46, 4163-4165.

90. C.M.Gordon and A.J. McClean, Chem. Commun., 2000, 1395-1396.

91. E.D. Bates, J.H. Davis Jr, R.D. Mayton and I. Ntai, J. Am. Chem. Soc., 2002, 124, 926.

92. J.R. Brozozowski, H. Cheng, P.B. Henderson, R.M. Pearlstein and D.J. Tempel, J. Am. Chem. Soc., 2008, 130, 400-401.

93. Y. Chen, W. Liu, C. Ye and L. Yu, Chem. Commun., 2001, 2244.

94. G. Gamero-Catano and V. Hruby , J. Prop. Power, 2001, 17, 977.

95. C. M. Jin, C. Ye, B.S. Phillips, J.S. Zabinski, X. Liu, W. Liu, J.M. Shreeve, J. Mater. Chem., 2006, 16, 1529-1535.

96. M. Maase, K. Massonne, K. Halbritter, R. Noe, M. Bartsch, W. Siegel, V. Stegmann, M. Flores, O. Huttenloch and M. Becker, Wo. Pat., 062171, 2003.

97. J.D. Holbrey, R.D. Rogers, S.K. Spear and R.P. Swatloski, J. Am. Chem. Soc., 2002, 124, 4974-4975.

98. S. Mekki, C.M. Wai, I.Billard, G. Moutiers, J. Burt, B. Yoon, J.S. Wang, C. Gaillard, A. Ouadi and P. Hesemann, Chem. Eur. J., 2006, 12, 1760-1766.

99. P. Giridhar, T.G. Srinivasan, P.R. Vasudeva, and K.A. Venkatesan, Electrochimica Acta, 2007, 52, 3006-3012.

100. M. Jayakumar, T.G. Srinivasav and K.A. Venkatesan, Electrochimica Acta, 2007, 52, 7121-7127.

101. J. S. Wang, C.N. Sheaff, B. Yoon, R.S. Addleman and C.M. Wai, Chem. Eur. J., 2009, 15, 4458-4463.

102. A. Kamimura and S. Yamamoto, Org. Lett., 2007, 9, 2533-2535.

103. Z.C. Liu, R.G. Xia, C.M. Xu and R. Zhang, Oil Gas J., 2006, 104, 52-56.

104. A. Hoff, C. Jost, A. Prodi-Schwab, F.G. Schmidt and B. Weyershausen, *Ionic Liquids: New designer compounds for more efficient chemistry, Elements,* Degussa Science Newsletter, 9, 10-15, 2004.

105. K. Lehmann and B. Weyerhausen, Green Chem., 2005, 7, 15-19.

106. B. Wu, R.G. Reddy and R.D. Rogers, *Solar energy: the power to choose*, Proc. Solar Forum, Washington DC, 445-451, 2001.

107. D.F. Evans, S.H. Chen, G.W. Schriver and E.M. Arnett, J. Am. Chem. Soc., 1981, 103,481-482.

108. W.J. Benton, D.F. Evans and E.W. Kaler, J. Phys. Chem., 1983, 87, 533.

109. E.Z. Casassa, D.F. Evans, R. Roman and A. Yamauchi, J. Coll. Int. Sci., 1982, 88, 89.

110. C.J. Drummond and T.L. Greaves, Chem. Rev., 2008, 108, 206.

111. H.X. Gao, J.C. Li, B.X. Han, W.N. Chen, J.L. Zhang, R. Zhang and D.D. Yan, Phys. Chem. Chem. Phys., 2004, 6, 2914-2916.

112. K. Binnemans, Chem. Rev., 2005, 105, 4148-4204.

113. H.W. Huang, C.K. Lee and I. Lin, Chem. Commun., 2000, 1911.

114. M.A. Firestone, J.A. Dzielawa, P. Zapol, L.A. Curtiss, S. Seifert and M.L. Dietz, Langmuir, 2002, 18, 7258-7260.

115. J. Bowers, C.P. Butts, P.J. Martin and M.C. Vergara-Gutierrez, Langmuir, 2004, 20, 2191-2198.

116. B. Dong, T. Inoue and L.Q. Zheng, J. Coll. Int. Sci., 2007, 307, 578-581.

117. I. Goodchild, L. Collier, S.L. Millar, I. Prokes, J.C.D. Lord, C.P. Butts, J. Bowers, R.P. Webster and R.K. Heenan, J. Coll. Int. Sci., 2007, 307, 455-468.

118. P.D. Galgano and O.A. El Seoud, J. Coll. Int. Sci., 2010, 345, 1-11.

119. P. Brown, C.P. Butts, R. Dyer, J. Eastoe, I. Grillo, F. Guittard, S. Rogers and R.K. Heenan, *Langmuir*, 2011, *27*, 4563–4571.

120. C.M. Paleos and D. Tsiourvas, Liq. Cryst., 2001, 28, 1127.

121. K.M. Lee, Y.T. Lee and I.J.B. Lin, J. Mater. Chem., 2003, 13, 1079-1084.

122. C.J. Bowlas, C.J. Bruce and K.R. Seddon, Chem. Commun., 1996, 1625-1626.

123. L. Brinchi, R. Germani, E. Braccalenti, N. Spreti, M. Tiecco and G. Savelli, J. Coll. Int. Sci., 2010, 348, 137–145.

Chapter 3

SURFs and SAILs: anionic surfactants and ionic liquids with quaternary ammonium counterions

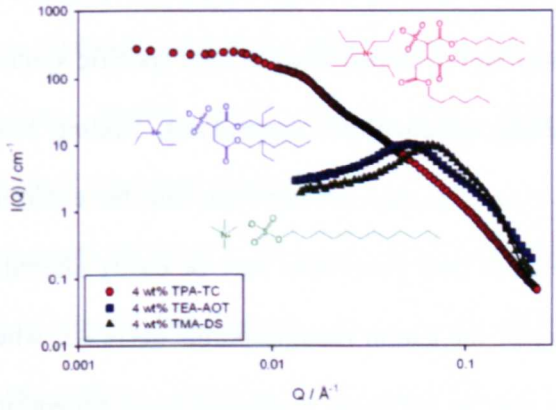

In this chapter small-angle neutron scattering (SANS) and surface tension were used to characterize a class of surfactants (SURFs), including surfactant ionic liquids (SAILs). These SURFs and SAILs are based on organic surfactant anions (single tail dodecylsulfate (DS), double chain AOT and the tri-chain TC) with substituted quaternary ammonium cations. This class of surfactants can be obtained by straightforward chemistry, being cheaper and more environmentally benign than standard cationic SAILs. A surprising aspect of the results is that, broadly speaking, physico-chemical properties of these SURFs and SAILs are dominated by the nature of the surfactant anion, and that chemical structure of the added cation plays only a secondary role.

3.0 Introduction

There is ever increasing interest in applications of ionic liquids (ILs). One area of live interest is in reaction control, as ILs have a drastic effect on rates and stereoselectivity of certain organic reactions, due to the different microenvironments and solvent properties compared to conventional molecular solvents[1]. They have also been touted as environmentally benign solvents due to extremely low vapour pressures and their potential for recyclability. Because there is such a huge number of possible ILs ($\sim 10^9$)[2] these "designer solvents" are highly tuneable and may be developed to overcome specific synthetic problems. Wilkes *et al.*[3] were the first to investigate 1,3-dialkylimidazolium electrolytes, finding lower melting points than for analogues 1-alkylpyridium cations: ever since then imidazolium salts have dominated IL research.

Imidazolium salts have proved useful as their properties may be easily altered, for example, on increasing the alkyl chain length and symmetry of the cation melting points decrease, whereas on changing the anion, hydrophobicity may be controlled due to differing hydrogen-bond accepting ability. In fact 1-alkyl-3-methylimidazolium salts were used in the first studied surfactant ionic liquids (SAILs), these ILs showing aggregation in aqueous solution[4]. Just like for normal surfactants, Inoue *et al.*[5] showed evidence of both lamellar (L_α) and hexagonal (H_1) lyotropic mesophases in mixtures of the SAIL 1-dodecyl-3-methylimidazolium bromide with water over a concentration range 10-50% v/v. The use of ILs as solvents, also capable of self-assembly and nanostructuring, may allow the generation of a new class of highly tuneable and highly selective reaction media, offering unique opportunities for controlling solvent properties in localized self-assembled nanodomains (tuneable nanostructured solvents).

El Seoud *et al.*[6] have shown that the main difference between micellization in imidazolium-based SAILs and conventional cationic surfactants is down to the chemical structure of the head group. For imidazolium-based SAILs H-bonding of the heterocyclic-ring compensates for the hydrophilic character of the head group, promoting aggregation. Apart from this they suggest there is nothing particularly special about imidazolium-based SAILs (aside structural versatility) or, in fact, any cationic SAILS in terms of physico-chemical properties of micellar solutions.

The attraction of imidazolium cations as components in ILs and SAILs is twofold. Firstly, the positive charge is delocalized over the heterocycle conferring high cation stability. Secondly, when the C-2 position bears a proton substituent the imidazolium moiety is also able to act as a catalyst, ligating to metal atoms

(planar geometry may also be an important factor for future catalyst design) or simply provide an acidic medium appropriate for other types of reaction (for example Diels-Alder or Friedel-Crafts)[7].

However, imidazolium salts also suffer from numerous drawbacks, including relative expense; only a limited range of commercially available N-substituted imidazoles; often unknown toxicity and environmentally hazardous starting materials, finally there are well documented problems with purification[8]. In addition, because of the acidity of the C-2 proton, imidazolium ILs are also unsuitable for reactions involving basic salts (e.g. silver (I) oxide) and active metals (Na, K, etc.)[9] or in reactions involving strong bases (Grignards, organolithiums, $NaBH_4$ etc)[10]. Indeed, even with weaker bases such as NR_3, decomposition of the imidazolium IL has been observed[11].

In this work a new class of surfactants (SURFs) is presented, which includes ILs and SAILs, comprising the well known homologous series of tetraalkylammonium cations (TAA) and common surfactant anions, as alternatives to imidazolium-based systems. The new SURFs and SAILs are shown below in Figure 3.1, being derived from dodecylsulfate (DS) (a), Aerosol-OT (AOT) (b), and a novel Aerosol-OT trichain (TC) analogue (c).

The advantages of this group of anionic SURFs and SAILs being they are synthesised from cheap, environmentally benign, commercially available starting materials by a simple ion exchange process. In addition purification is easier than for imidazoliums, importantly with no halide contamination.

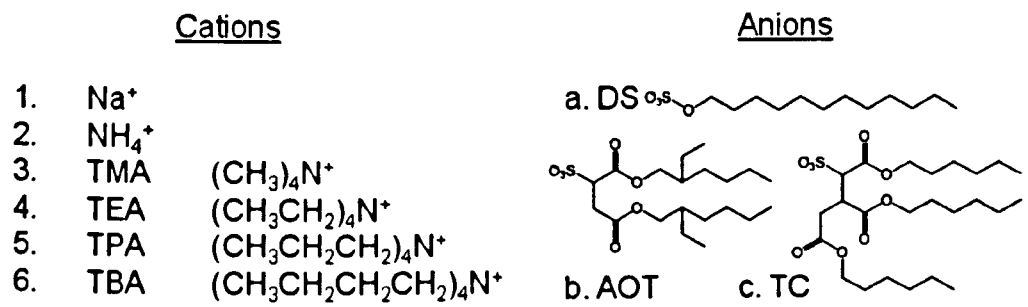

Figure 3.1: Surfactants studied.

Interestingly, the results show that properties of these SURFs and SAILs depend strongly on the chemical structure of the surfactant anion, but only weakly on the cation type, despite the obvious fact that there are significant changes in the organic substituents. This suggests that symmetrical highly substituted TAA cations are merely of secondary importance for the global physico-chemical properties.

3.1 Experimental

3.1.1 Surfactant Synthesis

SDS was purchased from Sigma-Aldrich and purified by recrystallization using methanol as solvent. AOT was purchased from Sigma-Aldrich and purified by Soxhlet extraction using dry acetone as the solvent followed by dissolving in the minimum amount of dry acetone and subjecting to repeat centrifugation[12]. TAA hydroxide solutions and D_2O were used as purchased (Sigma-Aldrich) without further purification.

The synthesis, purification and chemical characterization of TAA-AOT[13] and TAA-DS[14] compounds were synthesized according to literature, whereby purified Na-AOT and SDS were converted into the surfactants bearing different counterions by an ion-exchange technique using strong ion exchange resin (Amberlite IR 120 H^+ form) by dissolving 1 eq. in $EtOH/H_2O$ (1:1 v/v) and passing through a column (30 cm x 1 cm^2) of the ion exchange resin. The column was first of all rinsed with pure water. The free sulfonic acid formed on passing the Na^+ salt through the resin was then immediately neutralized with an aqueous solution of tetraalkylammonium hydroxide of the desired counterion. These tetraalkylammonium hydroxide solutions were bought from Sigma Aldrich and not purified further. The solvent was then removed by evaporation and drying *in vacuo* for 36hrs.

The TC analogue was synthesized following a method previously reported[15]: Transaconitic acid (5 g, 28.75 mmol) and hexanol (3.2 eq., 9.39 g, 92 mmol) was dissolved in toluene (100 ml) and *p*-toluene sulfonic acid (0.99 g, 5.75 mmol) added. The reaction mixture was heated to 110 °C for 15 h and the water generated removed via Dean and Stark apparatus. The reaction mixture was washed repeatedly with saturated $NaHCO_3$ (aq.) solution, the organic phase dried over $MgSO_4$ and solvent removed to give an off-white oil. Purification was achieved via flash column chromatography over SiO_2 using 10% Et_2O/petroleum ether. The resulting triester (9.57 g, 22.4 mmol), was dissolved in ethanol (100 ml) and water added up to saturation. $Na_2S_2O_5$ (2.2 eq., 9.37 g, 49.3 mmol), Na_2SO_3 (1.8 eq., 5 g, 40.3 mmol) was then added and the mixture was allowed to heat under reflux for 6 h. Solvent was completely removed to give white solid product which underwent crude purification via Soxhlet extraction using dry distilled AcOEt. Further purification was achieved by dissolving in the minimum amount of dry MeOH and centrifuging at 6,000 rpm for 30 min. The supernatant solution was decanted from residual salts and solvent removed to yield white solid.

The synthesized surfactants were characterized by elemental analysis and NMR all being consistent with experimental chemical structures.

Figure 3.2 shows the ^{1}H-NMR spectrum of Na-TC after purification. The spectrum was recorded (as were all NMR spectra reported here) on a Varian 400-MR machine at 25 °C in $CDCl_3$. Details of peak assignments and integrations are as follows: (δ=0.88-0.92) (a, 9H), (δ=1.21-1.40) (a, 18H), (δ=1.53-1.69) (c, 6H), (δ=2.75-3.19) (d, 2H), (δ=3.67-3.89) (e, 1H), (δ=3.95-4.24) (f, 6H), (δ=4.30-4.48) (g, 1H).

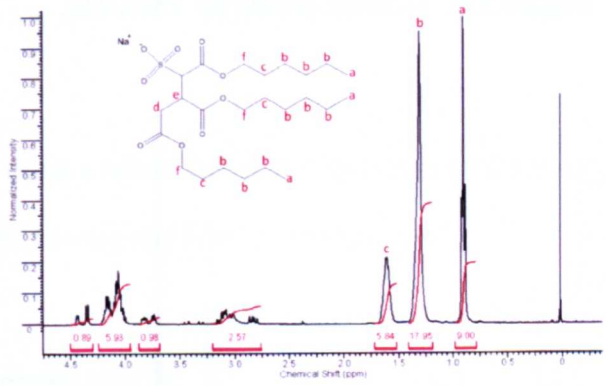

Figure 3.2: ^{1}H-NMR profile for Na-TC.

The ^{1}H-NMR spectra of the TMA containing compounds are recorded below (Figure 3.3 – 3.5). Other TAA surfactants have spectra consistent with molecular structure and were treated in the same way). Integrals are as follows: TMA-DS (δ=0.81-0.95) (a, 3H), (δ=1.16-1.40) (b, 18H), (δ=1.56-1.71) (c, 2H), (δ=3.31-3.42) (d, 12H), (δ=3.93-4.04) (e, 2H); TMA-AOT (δ=0.77-0.92) (a, 12H), (δ=1.15-1.43) (b, 16H), (δ=1.46-1.66) (c, 2H), (δ=3.00-3.24) (d, 2H), (δ=3.29-3.38) (e, 12H), (δ=3.85-4.12) (f, g, 5H); TMA-TC (δ=0.80-0.95) (a, 9H), (δ=1.18-1.41) (b, 18H), (δ=1.49-1.71) (c, 6H), (δ=3.00-3.19) (d, 2H), (δ=3.19-3.31) (e, 12H), (δ=3.49-3.77) (f, 1H), (δ=3.93-4.20) (g, 6H), (δ=4.21-4.44) (h, 1H).

Elemental analysis was obtained for each compound with good agreement between experimental and theoretical values (Table 3.1).

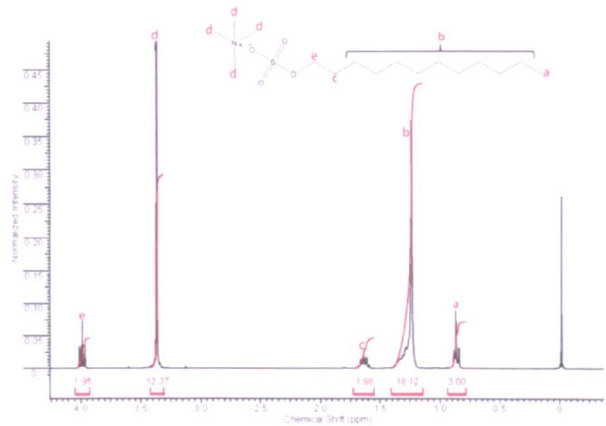

Figure 3.3: ^{1}H-NMR profile for TMA-DS.

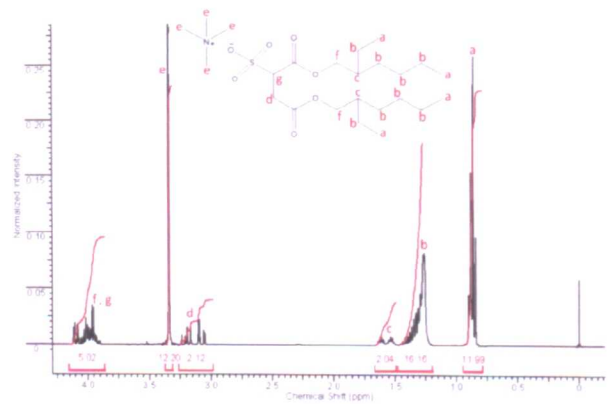

Figure 3.4: ^{1}H-NMR profile for TMA-AOT.

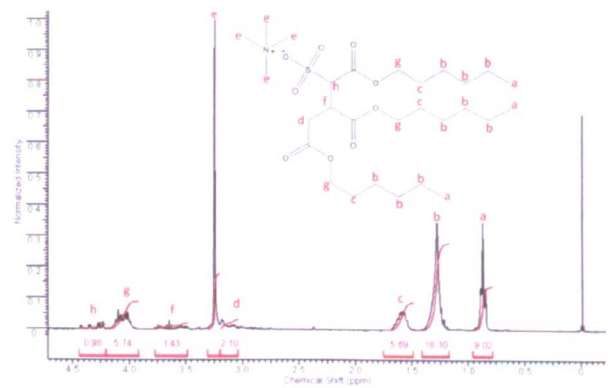

Figure 3.5: ^{1}H-NMR profile for TMA-TC.

Compound	C	H	N	S
TMA-DS	58.3 (58.1)	9.8 (9.9)	2.5 (2.8)	6.7 (6.5)
TMA-AOT	58.3 (58.2)	9.8 (9.9)	3.1 (2.8)	6.5 (6.5)
TMA-TC	61.0 (61.2)	10.1 (10.0)	3.1 (2.6)	5.4 (5.8)

Table 3.1: Elemental analysis results, experimental and theoretical (brackets), for TMA-compounds.

Elemental analysis was obtained for each compound with good agreement between experimental and theoretical values (Table 3.1).

3.1.2 Melting Points

Melting points were recorded using a Nikon Optiphot-2 optical microscope combined with a Linkam TH600 controller comprising a THS 91 heating and LNP 1 cooling stage.

3.1.3 Polarizing Light Microscopy (PLM)

A Nikon Optiphot-2 microscope fitted with polarizing filters and Linkam heating/cooling stage was used. Images were captured on a PC via a video camera and colour processor connected to the microscope. The liquid crystal phase progression of each surfactant was investigated by the solvent penetration method (i.e. phase cut). A small amount of surfactant was placed on a microscope slide, under a cover slip. The slide was mounted on the cover slide and heated until fluid and completely isotropic. After slowly cooling (1.0 °C min^{-1}) to 25 °C a drop of water was added at the edge of the cover slip. As the water penetrated the surfactant, a concentration gradient was established, from water at one side to pure surfactant at the other, enabling the entire range of mesophases to be observed in the field of view.

3.1.4 Surface Tension

Surface tensions were taken using the Wilhelmy plate method on a Krüss K11 or K100 instrument. Glassware was pre-washed with 50% nitric acid solution and then rinsed thoroughly with distilled water. The Pt plate was cleaned with distilled water and dried in a blue Bunsen flame before each measurement. The cleanliness of the glassware and plate were tested by checking the surface tension of pure water (Elga 18 MΩ cm). All measurements were carried out at 25 °C. For the standard sodium forms of AOT and TC

surfactants measurements below the cmc were carried out using low levels of the chelating agent EDTA (99.5% tetrasodium salt hydrate, Sigma-Aldrich) at constant surfactant to EDTA ratio in order to sequester trace impurities of divalent cationic species M^{2+}. This is standard practice for obtaining reliable surface tensions with these classes of surfactants[12, 16].

Measurements were repeated at appropriate time intervals to ensure equilibrium had been reached between the bulk phase and the surface. Furthermore, where there was overlap with literature data[14, 17] the new measurements were in very good agreement. The cmc was taken as the intersection of the two branches of behaviour describing the steep tension decreases, and higher concentration plateaux, respectively.

3.1.5 Small-Angle Neutron Scattering (SANS)

Scattering was measured on the LOQ and SANS2D diffractometers at the ISIS Facility, Rutherford Appleton Laboratory, UK, and the D22 diffractometer at ILL, Grenoble, France. LOQ and SANS2D are both time-of-flight instruments SANS2D uses neutrons with an incident wavelength $2.2 < \lambda < 14$ Å, and with the $1m^2$ detector offset sideways and vertically by 150mm, the resulting Q-range was $0.006 < Q < 0.7$ $Å^{-1}$. For LOQ the incident wavelengths were $2.2 < \lambda < 10$ Å giving $0.006 < Q < 0.24$ $Å^{-1}$. D22 is a reactor-based diffractometer, and a neutron wavelength of $\lambda = 10$ Å was employed at two different detector distances giving $0.0024 < Q < 0.37$ $Å^{-1}$. Appropriate normalization using site-specific procedures gave the absolute cross section $I(Q)$ (cm^{-1}) as a function of momentum transfer Q ($Å^{-1}$). Measurements of the dilute aqueous systems ranged from 0.25-4 wt% in D_2O (scattering length density $\rho = 6.33 \times 10^{10}$ cm^{-2}) to provide the necessary contrast, and were placed in Hellma fused silica cuvettes with a path length of 2 mm, which allow an incident beam diameter of 12 mm (on SANS2D and 8 mm LOQ). Raw SANS data were normalized by subtracting the scattering of the empty cell and a solvent background, using appropriate transmission measurements. Any low level of residual incoherent scattering was accounted for by a flat background term during the fitting process. Details on data analysis and scattering laws employed in the model fitting are presented in Appendix B1. Data analyzed were in absolute units, with the scale factors being consistent with expectations based on the sample compositions.

One model employed was for an ellipsoid form factor (P(Q)) multiplied by a Hayter-Penfold charge repulsion S(Q) explicitly declaring molecular fragment sizes and scattering lengths, giving the effective

structure factor for charged micelles[18]. To constrain the model, the alkyl tail lengths, and the head group and counterion volumes were input as constants (anionic headgroup volumes determined by SPARTAN, see below, cation volumes based on radii in Tables 3.1 and 3.2), as well as the sums of scattering lengths Σb_i of these fragments. The hydration numbers were; headgroup 4, cation 6 (for TAA ions). The fit parameters were: ellipsoid $P(Q)$, aggregation number N, principal radius R_1, aspect ratio X; S(Q), micellar charge z, and volume fraction, ϕ, Debye length, κ^{-1}, and the effective radius of the charged micelle, $R_{S(Q)}$. The fractional charge of micellized surfactant $\beta = z/N$. Other systems showing a Q^{-2} regime were fitted with a multilayer stack model[19].

3.1.6 Molecular modelling for packing parameter determinations

The hydrocarbon chain volumes and lengths were determined by SPARTAN (Wavefunction Inc., Irvine, CA) molecular modelling program. The molecules were created with all bonds in the *trans* configuration, with energy minimization calculations using a Merck molecular force field (MMFF).

3.2 Results and discussion

3.2.1 Phase behaviour and physical properties

For inorganic salts an increase in ionic radius leads to a marked decrease in melting point (mp), consistent with the Kaputinskii equation (Eq. 3.1).[20]

$$U_L = -K \cdot \frac{v \cdot |z^+| \cdot |z^-|}{r^+ \cdot r^-} \cdot \left(1 - \frac{d}{r^+ + r^-}\right) \qquad \text{Eq. 3.1}$$

Here z and r represent ion charges and radii respectively with v the stoichiometric coefficient, the terms K and d are salt-specific constants. This effect of ion size on mp can also be seen with organic salts, however in these cases r^+ and r^- are more difficult to determine owing to non-symmetrical structure and smaller polarization effects, especially there for larger TAA salts. Furthermore, with organic ions structural effects can become dominant: branching or lengthening of substituent tails will lead to disruption of crystal packing, generally decreasing mps. Figure 6 shows melting points for the three different classes of surfactant anions (melting points below -50 °C were not measured), with common cations, and a boundary line of 100 °C

which is commonly recognized as defining "ionic liquid"[21]. The x-axis has been ordered in line with cation radius (values given in Table 3.2) and it is clear that the melting point falls substantially with only a small increase in organic cation size. This behaviour is also consistent with deviations from Eq. 3.1, as expected for organic salts. As can be seen all surfactants with the most highly substituted cations TPA and TBA (see Figure 3.1 for structures) can be classified as ionic liquids and surfactant ionic liquids (SAILs). Interestingly, except for the sodium and ammonium (NH_4^+) materials, all the tri-chain (TC) compounds are ILs.

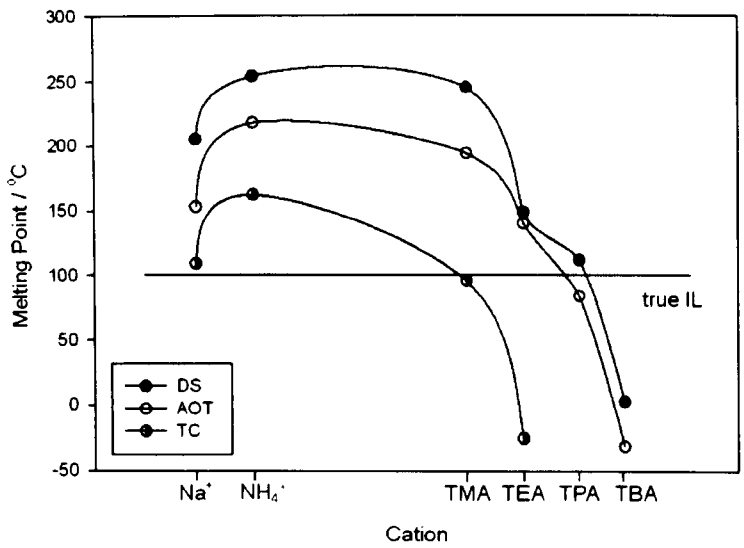

Figure 3.6: Melting points of surfactants given in Figure 1 with x-axis scaled to the cation radius (Table 3.2). Melting points below -50 °C were not measured.

The effect of cation type on the physical properties of the neat surfactants, and concentrated phases with water was investigated using PLM to seek evidence of mesophase formation. This is most obvious when looking at the mesophase structure of the AOT compounds (Figure 3.7, other PLM textures may be found in supporting information). Studies of mesophase behaviour were limited to visual observation, with shown textures spanning a steep concentration gradient with water. The transition from fluid micellar to liquid crystalline phases can be explained due to a competition between the increase in free energy associated with loss of orientational entropy, and reduction of free energy related to excluded volume and additional interactions.

With no added water Na^+-AOT exhibits a fan-like texture characteristic of hexagonal phases, the phase progression also agrees with previous work[22]: L_1- L_α- V_2- H_2, where L_1 represents a non-birefringent micellar solution, L_α a lamellar phase with parallel streak patterns, V_2, a non-birefringent cubic bi-continuous phase, and finally, H_2, a fan-like mosaic texture representing a reverse hexagonal phase.

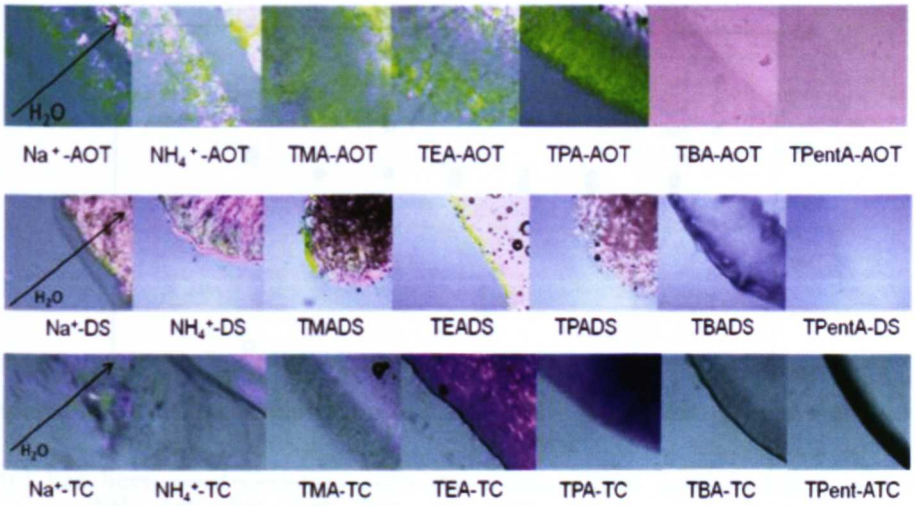

Figure 3.7: Polarising light microscopy textures showing mesophase formation of DS, AOT and TC-based compounds on addition of water at 25 °C.

This progression was also observed as alkyl substitution of the cation was increased up to TPA (tetrapropylammonium), with further substitution of the cation leading to the extinction of mesophases for the butylated analogue.

The phase penetration PLM images for DS and TC series of SURFs and SAILs are shown in Figure 3.7. Because the experiments were done at 25 °C the Na-DS does not show a phase progression which becomes evident >30 °C[23]. All the compounds studied follow broadly the same pattern: the pure dry surfactants are birefringent and mesophase progressions are evident (TC series), but birefringence disappears for butyl and pentyl substituted TAA cations. It is recognised that further work would be needed to correctly assign the mesophase structures (X-rays, ^{2}H-NMR quadrupolar splittings).

3.2.2 Surface tension data and analyses

In the pre-cmc region trace impurities of polyvalent cationic species M^{n+} can give rise to a lowering of the surface tension leading to errors in adsorption isotherm interpretation. To explore if this would be a potential

source of error for the Na^+ surfactants Na_4EDTA (Aldrich) was used as a chelating agent as has previously been reported[12, 16, 24]. The amount of EDTA required was determined by measuring γ at fixed surfactant concentrations as a function of [EDTA], and example data are shown in Figure 3.8 for the surfactants Na^+-DS, Na^+-AOT and Na-TC.

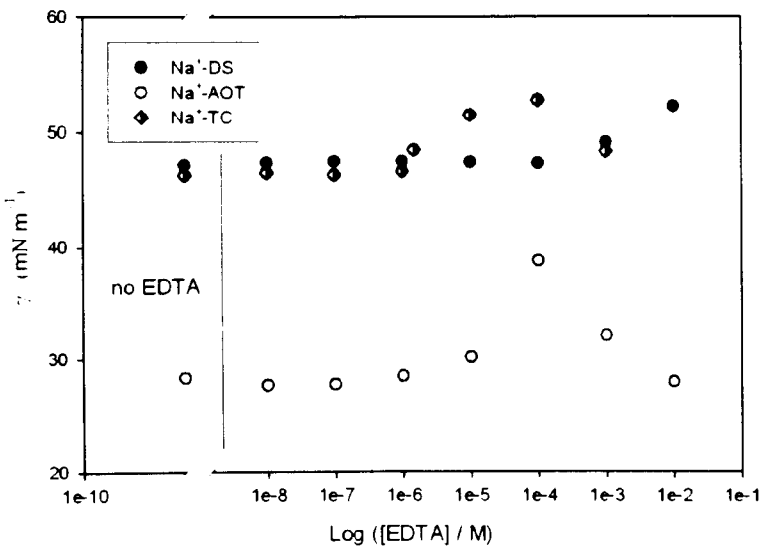

Figure 3.8: Effect of EDTA on surface tensions of surfactant solutions at 25 °C. [Na-DS] = 0.37 mM (1/20 cmc), [Na-AOT] = 0.10 mM (1/30 cmc), [Na-TC] = 0.04 mM (1/30 cmc).

For Na^+-AOT and Na^+-TC a raised γ occurred at 1 x 10^{-4} M of added EDTA; in this region it is expected that all the divalent cationic species are chelated. At higher [EDTA] the tension begins to decrease due to enhanced ionic strength provided by EDTA. Therefore, for the surface tension measurements a constant EDTA to surfactant ratio 1:30 was used representing the lowest concentration needed to give the maximum increase in γ, and recovery of the "pure surfactant" isotherm.

It may expected that forming the TAA compounds adds no extra M^{2+} to the system (Sigma lists no M^{2+} impurities in the quaternary ammonium hydroxide solutions used). However, Na^+-DS and some TAA compounds show no increase in γ until 1 x 10^{-2} M EDTA, so for the reason of enhanced ionic strength EDTA it was not added at such high levels. Instead 1 x 10^{-4} M EDTA was added to all these systems to allow direct comparison between the different Na and TAA systems studied.

Surface tension isotherms were recorded at 25 °C to establish critical micelle concentrations (cmc), identified by sharp break points in the plots, in combination with the parameters derived from fits to

adsorption isotherms (Figure 3.9). The limiting headgroup areas at the cmc (A_{cmc}) were calculated by fitting pre-cmc tensions to quadratics, to generate adsorption isotherms using the Gibbs equation (Eq. 3.2)[12, 24b]. It has been established[12, 24] that when appropriate trace levels of EDTA are used with sodium AOT-type surfactants then the pre-factor $m = 2$, as expected for 1:1 dissociating ionic surfactants.

$$\Gamma = -\frac{1}{mRT}\frac{d\gamma}{\ln c} \qquad \text{Eq. 3.2}$$

$$A_{cmc} = \frac{1}{\Gamma N_a} \qquad \text{Eq. 3.3}$$

To readily compare the different surfactant adsorption isotherms a reduced concentration axis (concentration/cmc) has been used (Figures 3.9b and 3.9d). Table 3.2 lists other adsorption parameters derived from the surface tension curves.

Cation	r^+ / Å	Anion	cmc/mM ± 0.03 experimental	cmc/mM predicted by eq. 4	γ_{cmc}/ (mN m^{-1}) ± 0.5	A_{cmc}/Å^2 ± 10%	Packing Parameter P_c
Na^+	0.95[a]	DS	8.00 (8.3[c])	-	34.9	56 (47.4[f])	0.30
NH_4^+	1.48[a]	DS	5.52 (7.1[d])	5.52	30.6	48	0.35
TMA	3.47[b]	DS	4.21 (5.4[e])	0.345	33.2	65 (52 ± 5[g])	0.26
TEA	4.00[b]	DS	2.76 (3.7[e])	0.022	33.7	78	0.22
TPA	4.52[b]	DS	1.42 (2.2[e])	1.35×10^{-3}	32.7	67	0.25
Na^+	0.95[a]	AOT	2.88 (2.63[h])	-	30.6 (30.8[i])	70 (75[i])	0.65
NH_4^+	1.48[a]	AOT	3.01 (2.70[h])	3.01	28.3	109	0.45
TMA	3.47[b]	AOT	2.48 (2.90[h])	0.188	29.4	96	0.52
TEA	4.00[b]	AOT	2.07 (2.45[h])	0.012	28.7	101	0.49
TPA	4.52[b]	AOT	1.27 (0.97[e])	7.35×10^{-4}	26.1	96	0.52
TBA	4.94[b]	AOT	- (0.80[h])	4.59×10^{-5}	-	-	-
Na^+	0.95[a]	TC	0.11	-	24.9	136	0.39
NH_4^+	1.48[a]	TC	0.07	0.07	25.5	117	0.45
TMA	3.47[b]	TC	0.12	4.38×10^{-3}	24.7	129	0.41
TEA	4.00[b]	TC	0.10	2.73×10^{-4}	25.1	132	0.40
TPA	4.52[b]	TC	0.07	1.71×10^{-5}	25.4	137	0.38

Table 3.2: Parameters derived from surface tension measurements. [a]Data from Pauling[25]. [b]Data from Robinson and Stokes[26]. [c]Data from Mukerjee[27]. [d]Data from Bales[14a]. [e]Data from Benrraou[14b]. [f]Data from Thomas[28], [g]Data from Thomas[29]. [h]Data from Chakraborty[17]. [e]Data from Eastoe[12].

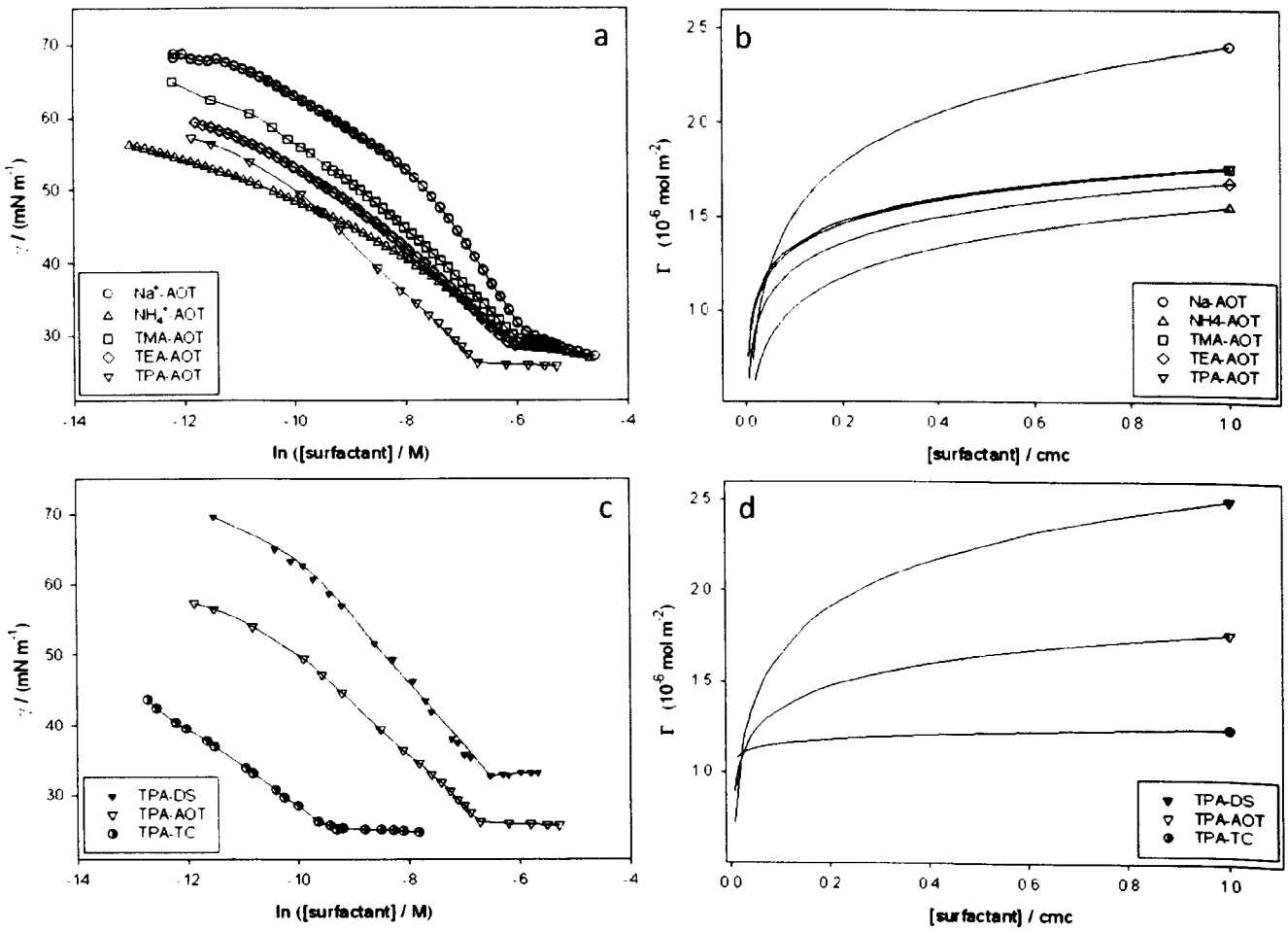

Figure 3.9: Surface tension data and derived adsorption isotherms for homologous SURFs and SAILs

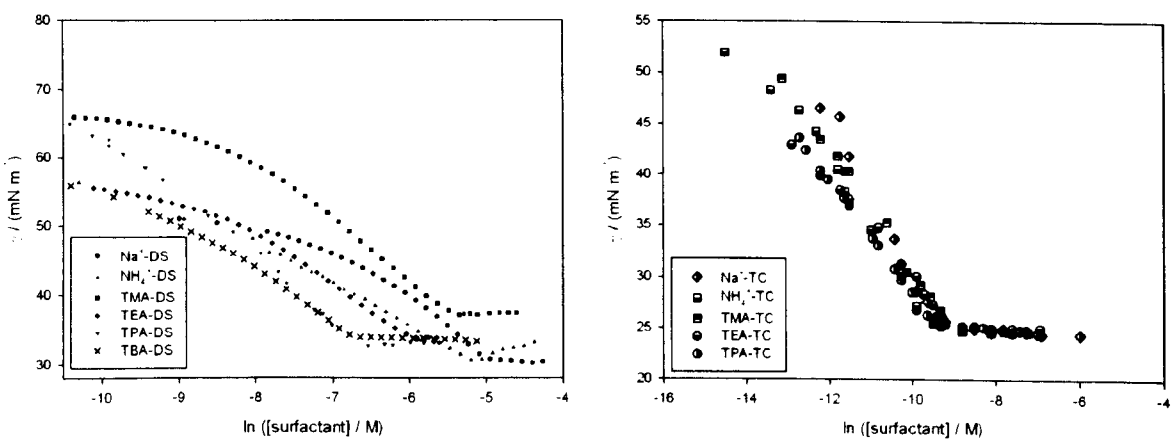

Figure 3.10: Surface tension data for homologous SURFs and SAILs recorded at 25 °C

Previous studies show that the free energy of micellization becomes increasingly negative with increasing counterion size, indicating that micellization is favoured by increasing counterion hydrophobicity[14b]. The work presented here is in agreement, and with that of Chakraborty[17] who reported the effect of TAA size on

AOT micellization. Importantly, however, the data reported here also includes the effect of varying the anion on micellization and reveals some unexpected trends and findings in that respect.

It is well known that cmcs are dependent on the nature of the counterion[30]. This effect can be seen with the homologous series of AOT compounds (Figure 3.9, Table 3.2) where the cmc decreases NH_4^+>Na^+>TMA>TEA>TPA. As the hydrated radius decreases from NH_4^+ to Na^+ so should the degree of dissociation, promoting micellization (3.01 mM for NH_4^+, and 2.88 mM for Na^+). However, this effect is weak and for organic counterions can be overshadowed by hydrophobic interactions: this appears to be the case here since the cmc decreases only a little for TAA compounds, even though hydrophobicity increases greatly down the homologous series. The arguments of Whitten[31] and later Bonilha *et al.*[32] are consistent with this. They showed that binding strength increases with additional methylene groups to the surfactant chain, independent of the spatial distribution of the alkyl groups attached to the nitrogen. The binding affinities were considerably lower than might have been expected from the total chain hydrophobicity.

For a series of linear single-chain surfactants the cmc decreases logarithmically with alkyl chain carbon number. This relationship usually fits the Klevens equation[33] (Eq. 3.4).

$$lg(\text{cmc}) = A - Bn_c \qquad \text{Eq. 3.4}$$

where A and B are constants and, for paraffin chain salts having a single ionic head group, B is approximately equal to lg 2 and n_c is the number of carbon atoms in the chain, C_nH_{2n+1} (i.e. reducing the cmc to approximately one-half per each additional CH_2 group). Applying this equation to symmetrical TAA chain substitutions is not very accurate but gives an idea of the region the cmc might be found. The total carbon number n_c^{tot} of these compounds increases greatly from NH_4^+ to TPA (an increase of 12 carbons) and so a significant decrease in cmc is expected based on equation 3.4, if it is assumed each carbon added to the entire surfactant (including the hydrophobic cation) contributes equally to the cmc (Table 3.2, column 5): in fact TPA-AOT would be essentially insoluble. However, nothing so dramatic is seen. Surprisingly the experimental decrement in cmc (column 4) from NH_4^+-AOT to TPA-AOT is merely a factor of 2. This highlights a very interesting observation "not all carbons are thermodynamically equivalent" in these systems.

Methylene groups added to the surfactant anions decrease cmc in line with Klevens behaviour (this kind of anion effect has been reported before for a similar series of compounds with a sodium cation)[34], whereas methylene groups added to organic TAA cations pack a weaker thermodynamic punch, and exert only a minor influence on the cmc value.

Benrraou[14b] discusses the possibility of TAA counterions penetrating into micelles, thus lowering the free energy of micellization. This is supported by neutron reflection experiments by Lu *et al.*[29], who showed TMA did indeed penetrate into DS monolayers at the air-solution interface. Also by Bain *et al.*[35] who showed that for hexadecylammonium-tosylate the methyl groups of the p-tosylate anion point away from the aqueous sub-phase, and that the tosylate aromatic rings locate in the hydrophobic region of the monolayer. There have also been reports in the literature alluding to TPA and TBA self association in solution[36]. All of this points to only minor effects of TAA structure on the most fundamental surfactant property, the cmc.

The effective area per head group at the respective cmc increases significantly with increasing anion size due to the effect of the tail volume on the packing parameter, whereas for cations the values are hardly effected. This may be due to the anion dominating in size, but might also lend support to a model where a single alkyl chain of TAA penetrates into the micelles, rather than one where the face of a TAA tetrahedron is present at one of the fatty patches at the micelle surface[14b].

A further point of interest is the effectiveness of the tri-chain surfactants at reducing surface tension (expressed by γ_{cmc}). The values in the range 24.7 – 25.5 mN m^{-1}, are very low for hydrocarbon surfactants and are comparable to some fluorocarbon surfactants.[37] The TC compounds bear linear hexyl chains, hence the effective limit for γ_{cmc} would be γ_{hexane} = 18.43 mNm^{-1} at 25 °C[38]. Therefore, hydrocarbon surfactants of this type of structure are beginning to approach the physical limit of surface tension reduction. This is likely due to hydrocarbon tail packing efficiency being balanced against electrostatic headgroup repulsions, and an increase in the number of low energy methyl groups per head group. It is, however, remarkable that straight chain anions have produced such an effect and at such low concentrations.

3.2.3 Micellar structures by SANS

SANS data were collected as a function of concentration for all the water soluble surfactants, but not for the insoluble compounds TBA-AOT and TBA-TC (Figure 3.11). Most of the scattering profiles were indicative

of charged micelles, showing an obvious charge repulsion S(Q) peak, others bore logarithmic Q^{-2} scattering, signatures of sheet-like structures.

The scattered intensity $I(Q)$ is a product of the size and shape of the aggregates (form factor, $P(Q)$) and the interaction between these aggregates (structure factor, $S(Q)$),

$$I(Q) \propto P(Q,R)S(Q) \qquad \text{Eq. 3.5}$$

where R is the particle radius. Data have been fitted with different models using FISH[39] interactive fitting program, which can be found online (http://www.small-angle.ac.uk).

The main model employed was for an ellipsoid form factor ($P(Q)$) multiplied by a Hayter-Penfold charge repulsion $S(Q)$, explicitly declaring molecular fragment sizes and scattering lengths, giving the effective structure factor for charged micelles[18, 40].

There are three structural dimensions in the ellipsoidal form factor model used, and these are the radius of the principal axis, R_1, the axial ratio, X, and the radius of the secondary axis, R_3. X is 1 for a spherical, < 1 for an oblate and > 1 for a prolate structure. To constrain the model, the alkyl tail lengths, and the head group and counterion volumes were input as constants (anionic headroup volumes determined by SPARTAN, see below, cation volumes based on radii in Tables 1 and 2 in the main paper), as well as the sums of scattering lengths Σb_i of these fragments. The hydration numbers were; headgroup 4, cation 6 (for TAA ions). Fit parameters: ellipsoid $P(Q)$, aggregation number N, principal radius R_1, aspect ratio X; $S(Q)$, micellar charge Z, and volume fraction, ϕ, Debye length, κ^{-1}, and the effective radius of the charged micelle, $R_{S(Q)}$. Note the fractional charge $\beta = Z/N$.

For $S(Q)$ the value of ϕ is known based on composition and κ^{-1} can be estimated to a first approximation using

$$\kappa = \left(\frac{2F^2\rho I}{\varepsilon_0\varepsilon_r RT}\right)^{1/2} \qquad \text{Eq. 3.6}$$

where F is the Faraday constant, ρ is the solvent density, I the ionic strength, ε_0 is the permittivity of free space and ε_r is the dielectric constant of the solvent. κ^{-1} has the dimensions of length and is a measure of the extent of the electric double layer.

Other systems (certain AOT and TC surfactants) were fitted with form factors for scattering from a thin interface combined with a one dimensional para-crystalline stack model[19]:

$$I(Q) \rightarrow N(\Delta\rho)^2 V^2 \left(\frac{\sin(QT_1/2)}{(QT_1/2)}\right)^2 \qquad \text{Eq. 3.7}$$

with N a concentration in cm^{-3}, $\Delta\rho$ the scattering length difference between solvent and surfactant sheet and T the planar sheet thickness. A modified Lorentz factor allows for Gaussian distribution of surface normals around the Q vector. The model approximates the local extent of planarity, R^*, the mean layer thickness L, number of layers M, planar spacing D and the Gaussian distribution of L and D as σ_L and σ_D respectively (Table 3.4).

For all the single chain DS surfactants the scattering shown on Figures 3.11 and 3.12 is consistent with charged ellipsoidal micelles, and a ($P(Q)$) with principal axis R_1 and aspect ratio X multiplied by an electrostatic interparticle structure factor $S(Q)$[18]. At 1 wt% Na-DS the fitted micellar dimensions R_1 = 22 Å and X = 1.4 (Table 3.3), are similar to literature[41]. On moving to NH_4^+-DS this micellar dimension is not greatly affected (R_1 = 22 Å, X = 1.1). For the TAA cations R_1 shows no variation and the aspect ratio changes only slightly (1.5 to 1.7). It might be expected that for strong binding of TAA to DS at the micellar surface, the plane of contrast between hydrocarbon chains and D_2O would move out from the micellar core, hence the cross section dimension seen by SANS would increase concomitantly (the hydrocarbon micelles would get fatter). In the extreme case of TPA-DS the cross sectional dimension should have increased by over 9 Å (SANS profiles for aggregates around 20 Å and 30 Å being notably different, crossing in the high Q region). However, this is not the case (Figure 3.11) therefore a model of strong association (complexing) of TAA and DS at the surface must be ruled out. This is supported by the degree of ionization, β, which is, on the whole, constant with increasing cation size, indicating 20-30% ion dissociation at the micellar surface.

In an earlier study Zana *et al.*[42] assumed enhanced penetration of TAA into DS micelles, this would also be inconsistent with the apparent constant micellar size seen by SANS for this series of compounds. In addition, they calculated that for the case of TBA the maximum number of cations that can be packed in contact with the micellar surface is limited, and so a second layer of TBA ions was predicted to form. That idea is again inconsistent with SANS data reported here (SANS profiles almost invariant, no obvious increases in R_1 or X).

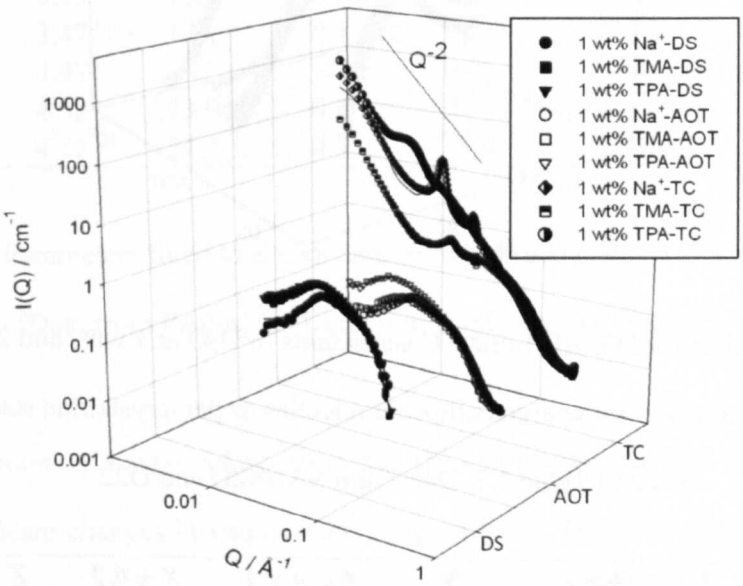

Figure 3.11: SANS profiles for DS, AOT and TC surfactants in D_2O at 1 wt% and 25 °C. Lines through data points are fits using a model for charged ellipsoid micelles or paracrystalline stacks, with parameters listed in Table 3.3. Data from SANS2D and D22.

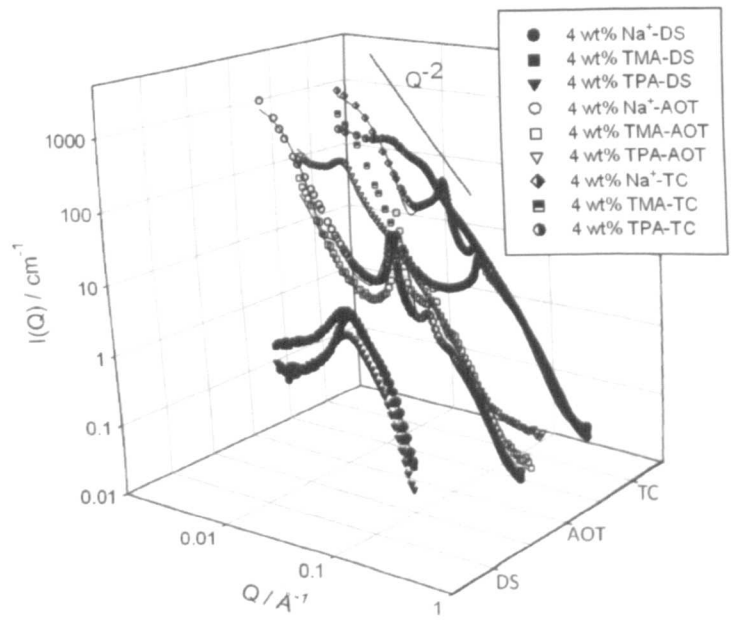

Figure 3.12: SANS profiles for DS, AOT and TC surfactants in D_2O at 4 wt% and 25 °C. Lines through data points are fits using a model for charged ellipsoid micelles or paracrystalline stacks, with parameters listed in Table 3.3. Data from SANS2D and D22.

Surfactant	r^+ / Å	*Shape*	*N*	R_1/ Å ± 1	*X* ± 0.2	*Z*	$\beta = Z/N$
Na^+-DS	0.95[a]	ellipsoid	68 (64)[c]	22 (17[c])	1.4 (1.3[c])	14	0.21 (0.24[c])
NH_4^+-DS	1.48[a]	ellipsoid	79	23	1.1	14	0.18
TMA-DS	3.47[b]	ellipsoid	106	25 (19[d])	1.5 (1.6[d])	22	0.21
TEA-DS	4.00[b]	ellipsoid	78	23	1.5	21	0.27
TPA-DS	4.52[b]	ellipsoid	76	23	1.7	16	0.21
TBA-DS	4.94[b]	ellipsoid	81	23	1.7	17	0.21
Na^+-AOT	0.95[a]	ellipsoid	55	21	2.1	21	0.37
TMA-DS	3.47[b]	ellipsoid	106	25	1.5	22	0.21
TMA-AOT	3.47[b]	ellipsoid	55	20	2.0	18	0.32
TMA-TC	3.47[b]	biphasic	-	-	-	-	-

Table 3.3: Parameters fitted to SANS using the model for charged ellipsoid micelles. Samples dispersed in D_2O at 1 wt% and 25 °C. [a]Data from Pauling[25]. [b]Data from Robinson and Stokes[26]. [c]Data from Griffiths[43]. [d]Data from Paul[44] at 11.5 wt% with Hayter Penfold method[40c].

Surfactant	wt %	r^+ / Å	$L \pm 0.5$	$\sigma_L \pm 0.05$	$R^* \pm 10$	$M \pm 0.5$	$D \pm 10$	$\sigma_D \pm 0.05$
Na^+-AOT	4	0.95[a]	11.4	0.2	240	4.9	188	0.2
NH_4^+-AOT	4	1.48[a]	15.2	0.2	247	1.7	330	0.2
TMA-AOT	4	3.47[b]	14.1	0.3	310	32.6	134	0.1
TPA-AOT	4	4.52[b]	25.1	0.4	439	12.8	498	0.2
NH_4^+-AOT	1	1.48[a]	15.2	0.1	173	1.2	191	0.2
Na^+-TC	1	0.95[a]	14.3	0.1	317	2.9	307	0.1
Na^+-TC	4	0.95[a]	15.9	0.1	270	2.1	301	0.1
TMA-TC	1	3.47[b]	17.1	0.1	289	2.5	297	0.2
TMA-TC	4	3.47[b]	-	-	-	-	190	-
TPA-TC	1	4.52[b]	23.9	0.3	1014	1.7	609	0.3
TPA-TC	4	4.52[b]	24.2	0.3	356	32.9	603	0.5

Table 3.4: Parameters fitted to SANS data from biphasic systems in water at 25 °C

[a]Data from Pauling[25]. [b]Data from Robinson and Stokes[26].

At the higher concentration of 4 wt% SANS from the DS compounds are still similar across the series; analyses show no significant changes in shape or size (Figure 3.12). This is in good agreement with Paul *et al.*[44] who reported constant micellar shape and size for TMA-DS over a much wider concentration range. (For example at 11.5 wt% the literature fit parameters[44] are essentially the same as those reported here at lower concentrations of 1 and 4 wt%). The other TAA-DS compounds also show concentration invariance of the overall micellar structures of the range 1 – 4 wt%. If the cation and anion were strongly bound, forming a 1:1 complex, then the micellar radius would increase because the plane of contrast against the D_2O solvent would move out from the micellar centre. Notably, this does not happen and so it is to be assumed that the TAA surface binding is only very weak in the case of single chain DS surfactant anions.

Moving to the other chemical structural extreme, the tri-chain compounds at 1 and 4 wt% all give Q^{-2} regimes of scattering consistent with disk/lamellar like structures, and also show strong undulations at lower Q regions, dependant on concentration, suggesting longer range ordering. This scattering is consistent with stacked lamellar phase fragments of repeat distances ~300 Å ($=2\pi/Q_{max}$) for Na^+-TC up to ~600 Å for TPA-TC. This SANS behaviour is analogous to common AOT, which is known to exhibit a mixed structure (L_l + L_α) under these conditions[22,45], giving striking SANS profiles such as seen here. SANS curves from the TC series could be adequately fit by a model for multi-lamellar stacks[19], with parameters R^* the local extent of

planarity, L a mean layer thickness of M layers, spaced by D with a superimposed Gaussian distribution of L and D as σ_L and σ_D respectively. Now the principal dimension, the layer thickness L is consistent with the sum of molecular fragment sizes (anion + cation), and also does increment in line with increased counterion size. Hence, it appears that ion association can be detected in these extended 2-D systems with triple-chain surfactants, in contrast to single tail DS surfactants. However, none of the other fitted parameters show any obvious trend down the counterion series, making it difficult to draw firm conclusions about relationships between cation structure and aggregation. Taking all of these results and fitted parameters together for the TC series it is clear multi-lamellar dispersions are present, but that beyond that the results cannot be interpreted further.

The case of the twin-tailed AOT-based compounds is a little more complicated, being more strongly concentration and cation dependent. At the lower concentration of 1 wt% Na^+-AOT in this Q-range SANS is consistent with the charged ellipsoid model, having R_1 = 21, X = 2.1 (Figure 3.13 and Table 3.5). For the TAA-AOT compounds at 1 wt% the SANS profiles are also consistent with this model, reporting increasing micellar size and aggregation number, N, with increasing cation size, consistent with cation-anion association at the micellar surfaces. Furthermore, the degree of dissociation β decreases with increased alkyl substitution of the ammonium cation, suggesting enhanced surface binding.

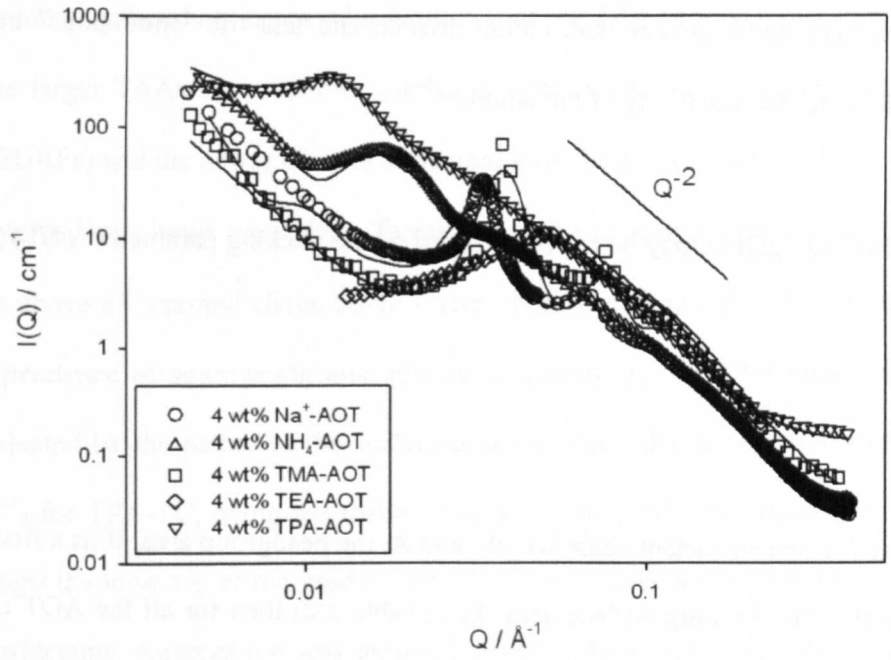

Figure 3.13: SANS profiles for AOT surfactants in D_2O at 4 wt% and 25 °C. Lines through data points are fits using a model for charged ellipsoid micelles (TEA-AOT only) or paracrystalline stacks (other systems). Data from D22 and LOQ (restricted Q-range).

Surfactant	wt %	r^+ / Å	N	R_1 / Å ± 2	X ± 0.2	Z	$\beta = Z/N$
Na^+-AOT	1	0.95[a]	55	21	2.1	21	0.37
TMA-AOT	1	3.47[b]	55	20	2.0	18	0.32
TEA-AOT	1	4.00[b]	78	23	2.3	23	0.29
TPA-AOT	1	4.52[b]	131	27	5.5	10	0.08
TEA-AOT	4	4.00[b]	139	28	2.6	14	0.10

Table 5: Parameters fitted to SANS data from ellipsoidal micelles of the AOT series in water at 25 °C. [a]Data from Pauling[25]. [b]Data from Robinson and Stokes[26].

Now at 4 wt% for the AOT series (Figure 3.13) both surfactant concentration and cation type affect aggregation. Here Na^+-AOT, NH_4^+-AOT and TMA-AOT (4 wt%) have scattering profiles consistent with mixed systems ($L_1 + L_\alpha$)[45], whereas in contrast TEA-AOT forms small charged ellipsoidal micelles ($R_1 = 28$, $X = 2.6$, Table 5). Finally, the largest counterion system TPA-AOT displays strong Q^{-2} scattering, again consistent with extended disk-like micelles. Obviously counterion radius strongly impacts the shape of aggregates[46], and these AOT-based systems appear to sit in an interesting position, where even small changes in cation size and shape cause structural differences. However, the overall picture still shows that

surfactant anion effects are much greater than cation effects, and that the "anomalous" behaviour of the AOT compounds is down to the sensitivity of the anion.

These broad changes in aggregation may be expected based on the packing parameter[47], (P_c) (Eq. 3.8).

$$P_c = \frac{V}{A_h \cdot l_c} \qquad \text{Eq. 3.8}$$

where V is the volume l_c is the surfactant chain length, and A_h the headgroup area. If as a first approximation A_h is taken to be equal to the limiting surface area A_{cmc} (Table 3.2) then for all the AOT compounds $P_c >$ 0.33 ruling out purely spherical micelles, as observed by SANS. Furthermore, this simple model is clearly consistent with the evolution from small ellipsoidal micelles to the more extensive sheet-like structures, seen on increasing hydrophobic volume V from single to double to triple chain compounds. However, the packing parameter model breaks down when applied to the alkyl substituted cation systems with the different surfactant anions, being unable to predict the concentration dependent structural changes seen with AOT. This is likely owing to limitations of the P_c model with regard to specific cation-anion interactions at the micellar surface.

Certainly, comparing all these results with the phase behaviour from section 1, there is no threshold delineating aggregation of regular solid surfactants (SURFs) from the ionic liquid analogues (SAILs). The indications are there is nothing unusual about a surfactant which is also an ionic liquid, supporting the findings of El Soeud *et al.* for a range of cationic SAILs[6].

3.3 Conclusions

The synthesis and characterization of physico-chemical properties of new surfactants (SURFs) and surfactant ionic liquids (SAILs) with wide variations in chemical structure have been presented. Although some compounds have been previously reported[14b, 17, 34] others are new (especially the tri-chain TC series).

Melting points become depressed on increased substitution of the TAA cation so that true ionic liquids could be formed with the larger TAAs. As such these series of compounds span the threshold between standard solid surfactants (SURFs) and the newer class of surfactant ionic liquids (SAILs).

Polarizing light microscopy shows mesophase formation which disappears once alkyl substitution on the TAA ion increases above a C_3 propyl chain. Surface tension measurements reveal some surprising findings: firstly, a weak dependence of aggregation and adsorption parameters on TAA structure, these properties being largely dominated by the nature of the surfactant anion; secondly, a very low surface tension at the cmc ($\gamma \approx 25$ mNm^{-1}) for TPA-TC, being the triple chain anion coupled with tetrapropylammonium cation. This value is amongst the lowest ever reported for a hydrocarbon surfactant, being typical of fluorocarbon[37, 48] rather than H-surfactants. Aggregation was studied by SANS showing a strong dependence on surfactant anion structure, whereas cation structure had only a secondary effect.

The different roles played by the surfactant anion and associated cation in governing aggregation were strongly evident, single chain anions and double chain anions at low concentrations result in (broadly) ellipsoidal micelles, but increasing the hydrophobic bulk by introducing a third surfactant chain induced a transition to extended sheet-like micellar aggregates and/or dispersed lamellar phases. This structural evolution is consistent with packing parameter arguments commonly used to account for micellar shapes[47]. there does appear to be a shift in the tendency from cation-anion complexation as a function of the surfactant anion type: no evidence for that was found for the single tail DS system, in contrast to both of the double and triple tailed surfactants.

Taking all these results together it can be seen there is no magic switch in behaviour as traditional crystalline solid surfactants (SURFs) are transformed into surfactant ionic liquids (SAILs) by chemical structure modification. Similar conclusions were presented recently by El Seoud *et al.*[6], but for imidazolium SURFs and SAILs. Hence, the findings appear quite general, casting a shadow of doubt over frequent claims that the ionic liquid nature confers special properties on SAILs.

The study has revealed another (quite surprising) finding, in surfactants bearing highly substituted organic cations, not all methylene groups and methyl groups contribute equally to the net hydrophobicity. In the compounds investigated here methylene groups added to the TAA counterions have only a minor effect on adsorption parameters and cmcs, much less so than if these were added to the carbon framework of the

surfactant anion. Thus, it appears that these common symmetrically substituted alkyl ammonium ions act as "spectators" in the underlying physical chemistry of these amphiphiles.

3.4 References

1. Sheldon, R., *Chem. Commun.*, 2001, 2399.
2. Earle, M. J.; Seddon, K. R., *Pure Appl. Chem.*, 2000, *72*, 1391.
3. Wilkes, J. S.; Levisky, J. A.; Hussey, C. L.; Druelinger, M. L., *Proc. Int. Symp. Molten Salts* 1980, *81*, 245.
4. (a) Firestone, M. A.; Dzielawa, J. A.; Zapol, P.; Curtiss, L. A.; Seifert, S.; Dietz, M. L., *Langmuir*, 2002, *18*, 7258; (b) Bowers, J.; Butts, C. P.; Martin, P. J.; Vergara-Gutierrez, M. C.; Heenan, R. K., *Langmuir*, 2004, *20* (6), 2191.
5. Inoue, T.; Dong, B.; Zheng, L. Q., *J. Coll. Int. Sci.*, 2007, *307*, 578.
6. (a) El Seoud, O. A.; Pires, P. A. R.; Abdel-Moghny, T.; Bastos, E. L., *J. Coll. Int. Sci.*, 2007, *313*, 296; (b) Galgano, P. D.; El Seoud, O. A., *J. Coll. Int. Sci.*, 2010, *345*, 1.
7. (a) Yeung, K.-S.; Farkas, M. E.; Qiu, Z.; Yang, Z., *Tetrahedron Lett.*, 2002, *43*, 5793; (b) Janus, E.; Goc-Maciejewska, I.; Lozynski, M.; Pernak, J., *Tetrahedron Lett.*, 2006, *47*, 4079; (c) Lee, C. K.; Huang, H. W.; Lin, I. J. B., *Chem. Commun.*, 2000, 1911.
8. Wasserscheid, P.; Welton, T., *Ionic Liquids in Synthesis*. Wiley Weinheim, 2003; p 364.
9. Gorodetsky, B.; Ramnial, T.; Branda, N. R.; Clyburne, J. A. C., *Chem. Commun.*, 2004, 1972.
10. (a) Arduengo, A. J., *Acc. Chem. Res.*, 1999, *32*, 913; (b) Handy, S. T., *J. Org. Chem.*, 2006, *71*, 4659.
11. Aggarwal, V. K.; Emme, I.; Mereu, A., *Chem. Commun.*, 2002, 1612.
12. Nave, S.; Eastoe, J.; Penfold, J., *Langmuir*, 2000, *16*, 8733.
13. Eastoe, J.; Robinson, B. H.; Heenan, R. K., *Langmuir*, 1993, *9*, 2820.
14. (a) Tcacenco, C. M.; Zana, R.; Bales, B. L., *J. Phys. Chem. B*, 2005, *109* (33), 15997; (b) Benrraou, M.; Bales, B. L.; Zana, R., *J. Phys. Chem. B*, 2003, *107*, 13432.
15. Gold, S.; Eastoe, J.; Grilli, R.; Steytler, D. C., *Colloid Polym. Sci.*, 2006, *284*, 1333.
16. Nave, S.; Eastoe, J.; Heenan, R. K.; Steytler, D.; Grillo, I., *Langmuir*, 2000, *16*, 8741.
17. Chakraborty, A.; Saha, S.; Chakraborty, S., *Colloid Polym. Sci.*, 2008, *286*, 927.
18. Hayter, J. B.; Penfold, J., *J. Colloid. Polym. Sci.* 1983, *261*, 1022.
19. Kotlarchyk, M.; Ritzau, S. M., *J.Appl. Crystallogr.*, 1991, *24*, 753.
20. Kapustinskii, A. F., *Q. Rev. Chem. Soc.*, 1956, *10*, 283.

21. Ionic Liquids in Synthesis. Wasserscheid, P.; Welton, P., Eds. Wiley-VCH: Weinheim, 2002; p 1.

22. Rogers, J.; Winsor, P. A., *J. Coll. Int. Sci.*, 1969, *30*, 247.

23. Kekicheff, P.; Cabane, B., *J. Physique*, 1987, *48*, 1571.

24. (a) Eastoe, J.; Paul, A.; Downer, A.; Steytler, D. C.; Rumsey, E., *Langmuir*, 2002, *18*, 3014; (b) Eastoe, J.; Downer, A.; Paul, A.; Steytler, D. C.; Rumsey, E.; Penfold, J.; Heenan, R. K., *Phys. Chem. Chem. Phys.*, 2000, *2*, 5235; (c) Li, Z. X.; Lu, J. R.; Thomas, R. K., *Langmuir*, 1997, *13*, 3681.

25. Pauling, L., The nature of the chemical bond and the structure of molecules and crystals. Cornell Univ. Press, Ithica, 1960.

26. Robinson, R. A.; Stokes, R. H., *Electrolyte solutions, 2nd Ed.* 2nd ed.; Butterworths, London: 1970.

27. Mukerjee, P., *Adv. Coll. Int. Sci.*, 1967, *1*, 242.

28. Lu, J. R.; Marrocco, A.; Su, T. J.; Thomas, R. K.; Penfold, J., *J. Coll. Int. Sci.*, 1993, *158*, 303.

29. Su, T. J.; Lu, J. R.; Thomas, R. K.; Penfold, J., *J. Phys. Chem. B*, 1997, *101*, 937.

30. Mukerjee, P.; Mysels, K.; Kapauan, P., *J. Phys. Chem.*, 1967, *71*, 4166.

31. Schmehl, R. H.; Whitesell, L. G.; Whitten, D. G., *J. Am. Chem. Soc.*, 1981, *103*, 3761.

32. Bonilha, J. B. S.; Georgetto, R. M. Z.; Abuin, E.; Lissi, E.; Quina, F., *J. Coll. Int. Sci.*, 1990, *135*, 238.

33. Klevens, H., *J. Am. Oil Chem. Soc.*, 1953, *30*, 4.

34. Mohamed, A.; Trickett, K.; Chin, S. Y.; Cummings, S.; Sagisaka, M.; Hudson, L.; Nave, S.; Dyer, R.; Rogers, S. E.; Heenan, R. K.; Eastoe, J., *Langmuir*, 2010, *26*, 13861.

35. (a) Bell, G. R.; Bain, C. D.; Li, Z. X.; Thomas, R. K.; Duffy, D. C.; Penfold, J., *J. Am. Chem. Soc.*, 1997, *119*, 10227; (b) Bell, G. R.; Li, Z. X.; Bain, C. D.; Fischer, P.; Duffy, D. C., *J. Phys. Chem. B*, 1998, *102*, 9461.

36. (a) Wirth, H. E.; Lo Surdo, A., *J. Phys. Chem.*, 1968, *72*, 751; (b) LoSurdo, A.; Wirth, H. E., *J. Phys. Chem.*, 1972, *76*, 130.

37. Pitt, A. R.; Morley, S. D.; Burbidge, N. J.; Quickenden, E. L., *Colloids Surf. A*, 1996, *114*, 321.

38. Atkins, P., *Physical Chemistry*, W. H. Freeman and Company: New York, 1988.

39. Heenan, R. K. *Fish Data Analysis Program*; Rutherford Appleton Laboratory Report: 1989; pp RAL.

40. (a) Hansen, J.-P.; Hayter, J. B., *Mol. Phys.*, 1982, *46*, 651 ; (b) Hayter, J. B.; Penfold, J., *Colloid Polym. Sci.*, 1983, *261*, 1022; (c) Hayter, J. B.; Penfold, J., *Mol. Phys.*, 1981, *42*, 109

41. Yurekli, K.; Mitchell, C. A.; Krishnamoorti, R., *J. Am. Chem. Soc.*, 2004, *126*, 9902.

42. Zana, R.; Benrraou, M.; Bales, B. L., *J. Phys. Chem. B*, 2004, *108*, 18195.

43. Griffiths, P. C.; Paul, A.; Khayat, Z.; Heenan, R. K.; Ranganathan, R.; Grillo, I., *Soft Matter*, 2005, *1*, 152.

44. Paul, A.; Griffiths, P. C.; Pettersson, E.; Stilbs, P.; Bales, B. L.; Zana, R.; Heenan, R. K., *J. Phys. Chem. B*, 2005, *109*, 15775.

45. Li, Z. X.; Weller, A.; Thomas, R. K.; Rennie, A. R.; Webster, J. R. P.; Penfold, J.; Heenan, R. K.; Cubitt, R., *J. Phys. Chem. B*, 1999, *103*, 10800.

46. Eastoe, J.; Towey, T. F.; Robinson, B. H.; Williams, J.; Heenan, R. K., *J. Phys. Chem.*, 1993, *97*, 1459.

47. Israelachivilli, J., *J. Chem. Soc. Faraday Trans. 2*, 1976, *72*, 1525.

48. Ferrer, M.; Comelles, F.; Plou, F. J.; Cruces, M. A.; Fuentes, G.; Parra, J. L.; Ballesteros, A., *Langmuir*, 2002, *18*, 667.

Chapter 4

Anionic surfactant ionic liquids with 1-butyl-3-methyl-imidazolium cations: characterization and application

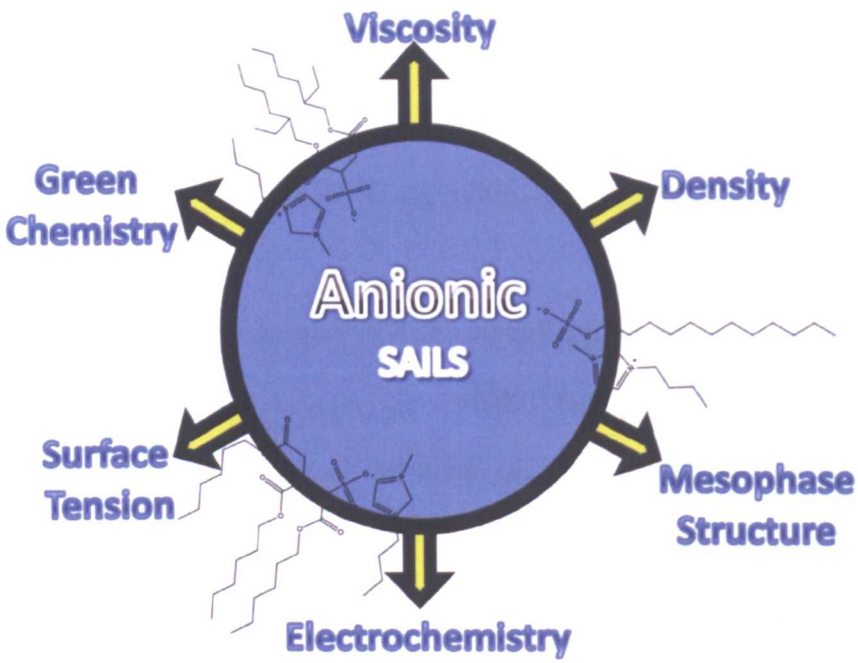

This chapter deals with a series of anionic surfactant ionic liquids (SAILs) based on organic surfactant anions and imidazolium cations. These compounds are more environmentally friendly and chemically tuneable as compared to other common ionic liquids. A detailed investigation of physico-chemical properties, studies into aqueous aggregation behaviour, structuring in the pure ILs, as well as electrochemical investigations has been conducted. The results suggest potential applications in electrochemistry, battery design and catalytic reaction control.

4.0 Introduction

As mentioned in chapter 2 ionic liquids (ILs), commonly thought of as liquid salts below 100 °C, are of immense interest as they have physico-chemical properties different from conventional molecular solvents[1]. Typical ILs are 1-butyl-3-methyl imidazolium halides (bmim X), and the bmim moiety is a common component in many ILs. Ionic liquids are often considered to be environmentally benign due to low vapour pressure; with up to 10^9 cation-anion combinations[2] they are highly tunable and may be designed for specific chemical and synthetic applications.

It soon became appreciated that long chain analogues of the common cationic imidazolium based ILs could self-assemble to form micelles in aqueous solutions[3], these systems were then dubbed "surfactant ionic liquids" (SAILs)[4]. Since then catanionic SAILs have been reported[5], these are novel systems being composed of cations and anions both having an amphiphilic character. Initial studies of cationic SAILs were limited in scope, with only minor chemical variations centred around substituted imidazolium analogues[6]. In this chapter a systematic study of catanionic SAILs is undertaken, comprising the 1-butyl-3-methyl-imidazolium (bmim) cation and common anionic surfactant anions, which also bear bulky hydrophobic chains (Figure 4.1).

The results in Chapter 3 have shown that the ionic liquid nature confers no special properties in terms of surfactant properties or aggregation behaviour of SAILs: essentially they behave just like regular surfactants. Nonetheless, the development of these SAILs is advantageous as it presents interesting opportunities to combine the properties of surfactants with those of imidazolium-based ILs, and this dual nature may well be beneficial in applications such as separation, condensation and extraction. Recently[7], it was shown that hydrophobic analytes, such as hydrocarbons, partition strongly into micellized SAILs, suggesting advantages in aqueous phase transfer catalysis, being also appropriate liquid media for extraction and recycling of reagents.

The SAILs reported here are appealing for various reasons. Firstly, aggregation is controlled by the chemical structures of the anions, being more tailorable than the chemically limited sub-set of imidazolium cations commonly employed: in these new systems small structural changes feed through to significant effects on aggregation properties such as critical micelle concentration (cmc), mesophase behaviour, and also on bulk physico-chemical properties such as melting point and solvent miscibility. Secondly, since the compounds

contain imidazolium heterocycles it is probable that these SAILs could act as catalysts, either ligating to metal atoms or providing an acidic medium appropriate for certain chemistries (for example Diels-Alder or Friedel-Crafts reactions)[8]. Thirdly, since they are halogen-free the compounds are more environmentally friendly than traditional imidazolium-based SAILs. In addition to this, the intrinsic nature/properties of the cations and anions selected are also important. For example, anions such as AOT (Figure 3.1) have antibiotic and pesticidic properties[9], and imidazolium cations are also known to have antibacterial properties[9]. Another reason for selecting a short alkyl chained imidazolium group is that aquatic toxicity is reduced compared to longer chain analogues[10].

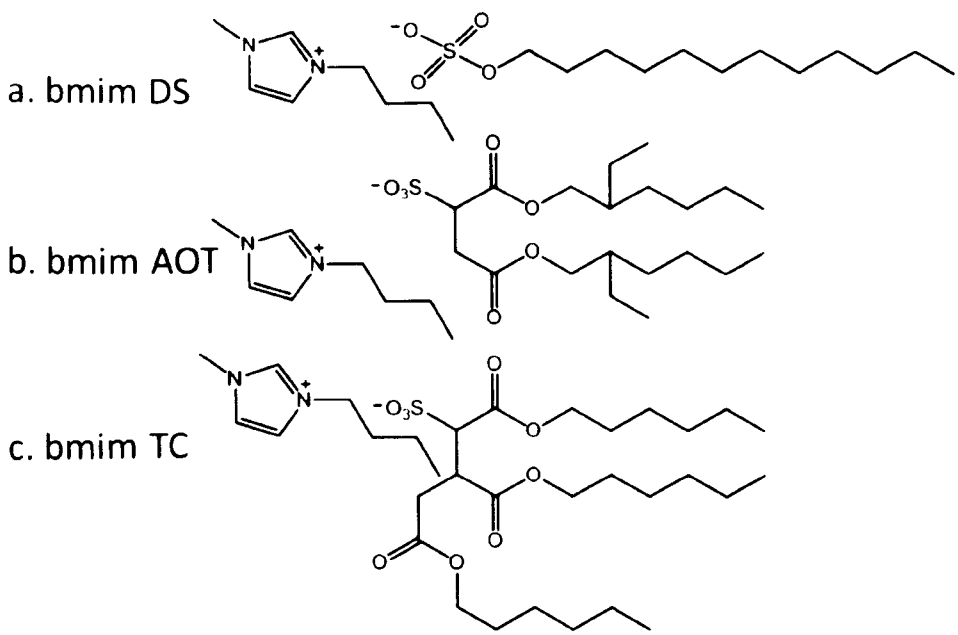

Figure 4.1: Surfactant ionic liquids (SAILs) studied here.

This chapter describes the synthesis, chemical characterization, and physico-chemical properties of neat ILs (viscosity, density, melting point, etc.) as well as for aqueous solutions (surface tensiometry, small-angle neutron scattering). Furthermore, a potential application of the SAILs in electrochemistry is explored. Aqueous phase studies are important to learn how self-assembly structure is related to the IL molecular architecture, useful for example in applications where the underlying phase structure can be tuned to provide a new dimension for control over outcomes of organic reactions. Densities are important when considering electrochemical and battery applications, where weight is a concern. In addition, low density may also be advantageous for phase separation of immiscible liquids. Knowledge of viscosity η is important for

chemical engineering applications, but is also fundamental for uses as chemical reaction media, since η affects reactant diffusion coefficients.

Ionic liquids were originally conceived as electrochemical solvents[11] and are industrially important because they are effective at moderate temperatures, being also less corrosive than classical molten salts. The electrochemical windows of ILs are often > 4 V[12], which permits deposition of elements that cannot be delivered from normal aqueous solutions, such as elemental and compound semi-conductors.

Halogen-free ILs are attractive not only for environmental reasons (F^- can react with water, giving off HF, for example) but also because the presence of Cl^- or Br^- can affect electrochemical behaviour. In addition, by introducing large organic anions, the hydrophobicity of the ILs may increase, limiting water uptake that can also be detrimental to electrochemical applications. In contrast to variable cathodic potential limits, generally there is little variation in the anodic edge of the potential window, with the most common anions (BF_4^-, PF_6^-, $N(Tf)_2^-$) lying within a 0.5 V range[11]. However, this is not the case with the compounds presented here, allowing the possibility to fine tune the anion chemical structure and properties to achieve a much wider electrochemical window than for other available solvent media.

Although, there have been reviews in the field of micellar electrochemistry[13], the use of SAILs as electrochemical solvents has so far not been investigated. In addition, the combination of surface active IL properties presents intriguing material properties, offering advantages to using microheterogeneous fluids as electrochemical media. Ionic surfactants above the cmc form full coverage aggregates on metal and carbon electrodes with structures (bilayers, surface micelles) depending on the applied potential, electrode surface and surfactant type[14], which allows manipulation of surface electrode properties and surface structures. The surfactants solubilise reactants in these structures allowing penetration to the electrode while also excluding water. Hence, the development of SAILs may give rise to both the large potential windows seen for normal ILs and increased surface selectivity fund with surfactants, but now in the same medium. Finally, extremely high capacitances of these new ILs have been determined, which may prove of interest for the future design of supercapacitors and batteries[15].

4.1 Experimental

4.1.1 Materials

1-butyl-3-methyl-imidazolium chloride (≥ 99%) was purchased from Sigma-Aldrich and used as received. Sodium dodecylsulfate (SDS) was purchased from Sigma-Aldrich and purified by recrystallization from methanol. Aerosol-OT (AOT) was purchased from Sigma-Aldrich and purified by Soxhlet extraction using dry acetone and subjected to repeated centrifugation[16]. D_2O and ethyl acetate (≥ 99.5%) were purchased from Sigma-Aldrich and used without further purification.

4.1.2 Synthesis

Synthesis of the precursor triple-chain Na-TC surfactant (Figure 4.1) followed the method reported in Chapter 3[17]. Bmim AOT and bmim TC were synthesized by adding 1.0 mol. eq. of 1-butyl-3-methyl-imidazolium chloride and Na-AOT or Na-TC in a round-bottom flask and stirring in dichloromethane for 6 hours, the resulting NaCl precipitate was then filtered off and solvent removed under reduced pressure. The ILs were then dissolved in dry ethyl acetate and centrifuged at 6000 rpm for 1 hour. The pure solution was separated from excess salt, solvent was removed under reduced pressure, and the ILs were then dried *in vacuo* at 70 °C for 24 hours. A similar procedure using methanol as solvent was employed to make bmim DS. Bmim AOT and bmim TC were clear liquids, whereas bmim DS was an opaque viscous liquid/solid (depending on cooling rates due to polymorphism). The synthesized surfactant ionic liquids were characterized by NMR (Figures 4.2 – 4.4) and elemental analysis (Table 4.2), all being consistent with expected values. ^{1}H-NMR spectra of the ILs were recorded on a Varian 400-MR machine at 25 °C in $CDCl_3$. Details of peak assignments and integrals are as follows: bmim DS (δ=0.86-0.89, 0.94-0.98) (a, 6H), (δ=1.25-1.42) (b, 20H), (δ=1.64-1.71)(c, 2H), (δ=1.83-1.91) (d, 2H), (δ=4.03-4.07) (e, f, 5H), (δ=4.23-4.26) (g, 2H), (δ=7.28-7.29) (h, 1H), (δ=7.37-7.38)(i, 1H), (δ=9.68) (j, 1H); bmim AOT (δ=0.84-0.98) (a, 15H), (δ=1.27-1.45) (b, 18H), (δ=1.51-1.64) (c, 2H), (δ=1.82-1.90) (d, 2H), (δ=3.11-4.27) (e, f, g, h, i, 12H), (δ=7.23-7.24) (j, 1H), (δ=7.31-7.32) (k, 1H), (δ=9.65) (l, 1H); bmim TC (δ=0.83-0.95) (a, 12H), (δ=1.21-1.39) (b, 20H), (δ=1.50-1.67) (c, 6H), (δ=1.77-1.87) (d, 2H), (δ=2.80-4.35) (e, f, g, h, i, j, 15H), (δ=7.27-7.28) (k, 1H), (δ=7.38-7.40) (l, 1H), (δ=9.56) (m, 1H).

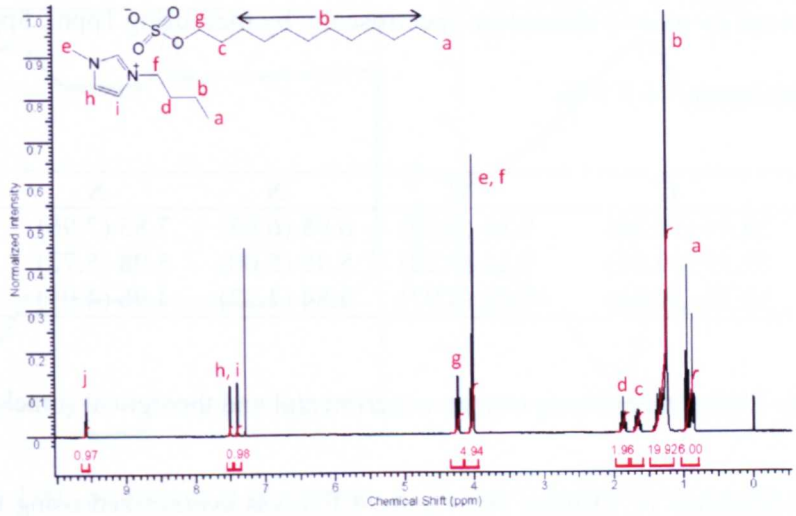

Figure 4.2: ^{1}H-NMR profile for bmim DS.

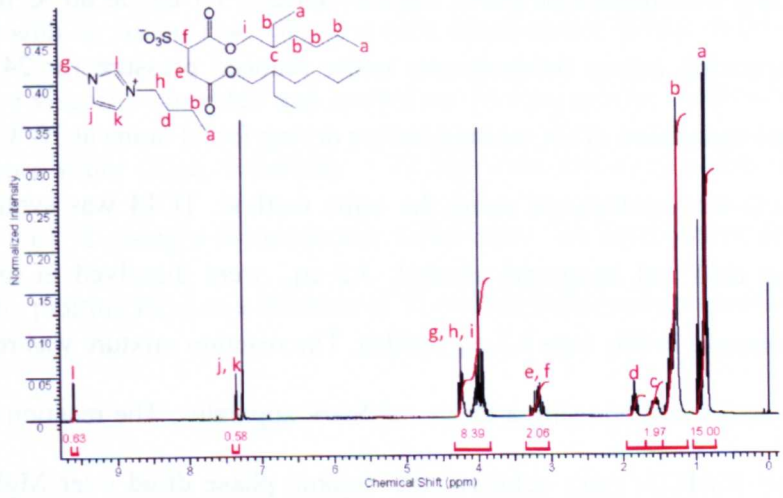

Figure 4.3: ^{1}H-NMR profile for bmim AOT.

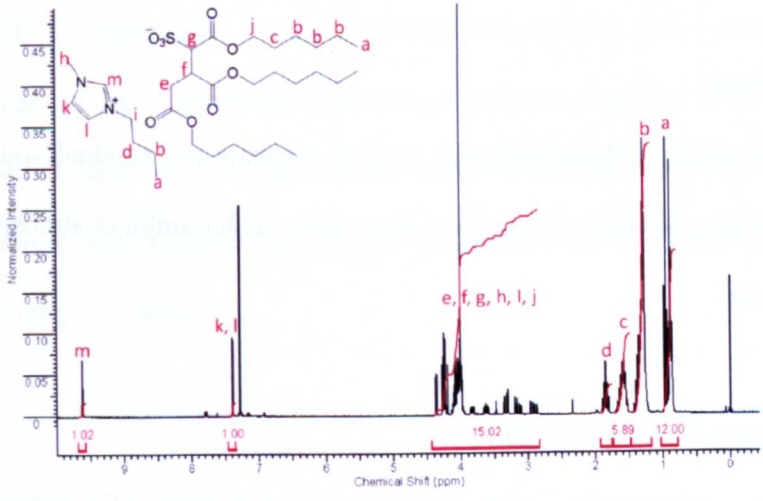

Figure 4.4: ^{1}H-NMR profile for bmim TC.

Sodium content was obtained by atomic absorption spectroscopy by measuring 1ppm, 5ppm and 10ppm samples. The error in calculation is ± 0.3 %.

Compound	C	H	N	S	Na
bmim DS	59.49 (59.38)	9.86 (9.89)	6.98 (6.93)	7.83 (7.96)	0.0 (0)
bmim AOT	59.39 (60.01)	9.14 (9.28)	5.49 (5.00)	5.98 (5.72)	0.0 (0)
bmim TC	58.79 (59.46)	9.02 (8.97)	4.54 (4.33)	4.96 (4.91)	0.0 (0)

Table 4.1: Elemental analysis results, experimental and theoretical (brackets).

Synthesis of 1-hexyl-imidazolium TC (Hmim TC, Figure 4.13) was synthesized using the same method as for the other ILs. 1-hexyl-3-methyl-imidazolium chloride was synthesized by refluxing 1-methylimidazole (≥99%, Sigma-Aldrich) and 1-bromohexane (98%, Sigma-Aldrich), 1.1 eq., at 80 °C for 48 hours. The salt was then purified by removing excess bromodecane under reduced pressure for 24 hours and repeated washing with ethyl acetate (minimum of six washes) before drying for 24 hours at 70 °C[18].

Bmim-TC14 (Figure 4.13) was synthesized using the same method. TC14 was synthesized according to literature[19]. Transaconitic acid and neopentyl alcohol, 3.2 eq., were dissolved in toluene and *p*-toluene sulfonic acid (catalytic amount, in this case 0.2 eq.) added. The reaction mixture was refluxed at 110 °C for 12 h and the water generated removed using a Dean and Stark apparatus. The reaction mixture was washed repeatedly with saturated $NaHCO_3$ (aq.) solution, the organic phase dried over $MgSO_4$ and the solvent removed to give an off-white oil. Purification was achieved via flash column chromatography over SiO_2 using 10% Et_2O/petroleum ether.

4.1.3 Karl Fischer Analysis

Karl Fischer coulometric titration (Metrohm) was used to measure the residual water content of the ILs: analyses were conducted as a function of time over three days, under ambient atmospheric conditions, until no more water was detected.

4.1.4 Differential Scanning Calorimetry (DSC)

The melting points and thermal behaviour of the ILs were measured using a TA instruments DSC Q200. The heating and cooling ramp for each sample was 10 °C min^{-1} and cyclic profiles were repeated three times. Example profiles can be seen in Figure 4.5. Bmim DS is not included for reasons explained below.

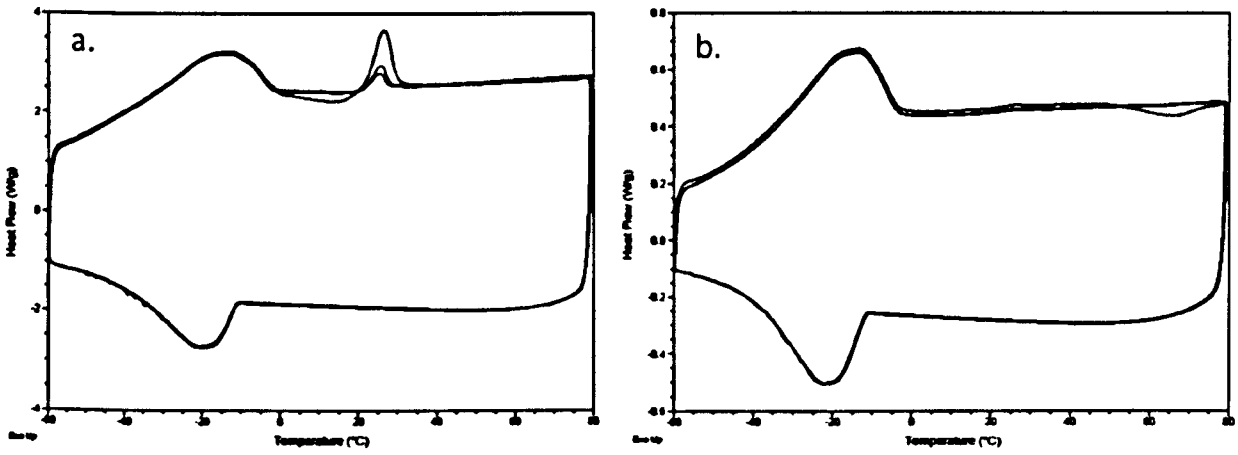

Figure 4.5: Cyclic DSC profiles (x3) of a) bmim AOT and b) bmim TC at a scan rate of 10 °C min^{-1}.

4.1.5 Density Measurements

Density was measured with an Anton Paar vibrating tube densitometer (DMA 4100), from 25 °C to 90 °C. The measurements were viscosity corrected and carried out in atmospheric conditions. The instrument was calibrated using ultrapure water (Elga, resistivity = 18 MΩ cm) and atmospheric air, temperatures were controlled to within ± 0.01 °C using a thermostatted water bath. The temperature dependence fit a simple linear regression, and by plotting $\ln(\rho)$ as a function of T, the thermal expansion coefficient ($d\ln(\rho)/dT = -\alpha_p$) was calculated.

4.1.6 Viscosity Measurements

A Bohlin CVO (Malvern Instruments), fitted with a cone and plate (4° / 20 mm), was used to determine viscosities between 25-70 °C (water bath). First, repeat scans of viscosity as a function of shear stress (10-1000 Pa) at 25 °C were carried out to ensure the materials gave linear responses with no shear history. Scans were then repeated at 40 °C and 70 °C (Figure 4.8). Once Newtonian behaviour was verified, plots of viscosity against temperature were recorded at constant shear stress (50 Pa) The experiments for bmim DS are not included for reasons given below.

4.1.7 Small-Angle X-Ray Scattering (SAXS)

Samples were simply placed onto a thin film of mica and measurements recorded with home-built SAXS (Physics Department, University of Bristol), using a sealed-tube CuK_{α} source with a wavelength of 1.54 Å. The scattering pattern covered scattering vectors ranging from 0.01-0.5 $Å^{-1}$.

4.1.8 Polarizing Light Microscopy (PLM)

A Nikon Optiphot-2 microscope fitted with polarizing filters was used, and images were captured on a PC via a video camera and colour processor connected to the microscope. The liquid crystal phase progression of each SAIL was investigated by the solvent penetration method (i.e. phase cut)[17].

4.1.9 Surface Tensions

Surface tensions γ were measured at 25 °C using the Wilhelmy plate method, on a Krüss K100 instrument as described in chapter 3. Glassware was pre-washed with 50% nitric acid solution and then rinsed thoroughly with distilled water. The Pt plate was cleaned with distilled water and dried in a blue Bunsen flame before each measurement. The cleanliness of the glassware and plate were tested by checking the surface tension of pure water (Elga, resistivity = 18 MΩ cm). For all SAILs, measurements below the cmc were carried out using low levels of the chelating agent EDTA (99.5% tetrasodium salt hydrate, Sigma-Aldrich), at constant surfactant to EDTA ratio, in order to sequester trace impurities of divalent cationic species (M^{2+}). This is standard practice for obtaining reliable γ values with these classes of surfactants (c.f. Chapter 3)[16, 20].

Measurements were repeated at appropriate time intervals to ensure equilibrium. The cmc was taken as the intersection of the two branches of behaviour describing the steep tension decreases, and higher concentration plateaux, respectively. Limiting surface tensions (γ_{cmc}) were also measured by shape analysis of a pendant drop on a DSA10-MK2 instrument (Krüss, Germany), by fitting pendant drop spatial coordinates to the Laplace-Young equation. Interfacial tension measurements between *n*-dodecane and water were made by shape analysis of a pendant drop of water (~40 µL) in 4 mL of *n*-dodecane using the DSA10 MK2.

4.1.10 Small-Angle Neutron Scattering (SANS)

Scattering was measured on the D22 diffractometer at ILL, Grenoble, France. A model for multilayer stacks[21] was employed (see Chapter 3 for more detail).

4.1.11 Electrochemical studies

Measurements of potential windows were carried out at room temperature on pre-dried SAIL samples (vacuum oven). An Autolab PGSTAT-30 potentiostat (Metrohm, Switzerland) was used and the IL medium was contained in a custom built electrochemical cell, designed to accommodate small sample volumes (0.5 mL). A silver wire was used as a quasi-reference electrode, with a platinum coil as a counter electrode, and a 25 μm diameter gold micro-electrode as the working electrode.

4.2. Results and discussion

4.2.1 Physico-chemical properties

Karl Fischer analyses revealed that bmim DS contained the highest water levels, with bmim AOT and bmim TC considerably drier (Table 4.2). The value for bmim AOT is lower than that for pure dry Na-AOT (~4052 ppm)[22], possibly due to the larger counterion limiting hydration around the sulfonate group. These values are comparable to that found for a dried standard IL, bmim BF_4 (4538 ppm)[23].

It has been established that residual water content can have a major effect on physico-chemical properties of ionic liquids[24], however most previous work either fails to mention this or goes to the extreme of carrying out experiments under rather difficult to establish moisture-free conditions[25]. Although the latter is necessary for fundamental research, it does not prove useful for practical applications of ILs. It is in fact impractical to exclude water from the compounds used in this chapter owing to water being very difficult to remove in the starting materials (for example, Na-AOT cannot be easily dried to less than 10 mol % water)[22]: on the other hand, this structured water may actually be beneficial for certain applications. Recently, Fujita *et al.*[26] showed that small amounts of water strongly affect protein solubility in ILs, while retaining the properties of the IL. This is because the water is strongly solvated to the ions, thus limiting its chemical activity.

Compound	Melting point / °C	Water content / ppm	Density at 25 °C / (g cm^{-3})	Viscosity at 25 °C / (mPa s)
bmim DS	-	11790	-	-
bmim AOT	-19	3367	1.08	3916
bmim TC	-22	5232	1.08	3639

Table 4.2: Bulk physico-chemical properties of SAILs studied

The melting points of both bmim AOT and bmim TC are far below room temperature, being -19 °C and -22 °C respectively, as expected due to the asymmetry and large size of the anions in such ILs. For bmim AOT, a liquid crystal phase is seen up to 25 °C, which melted to yield an isotropic liquid. Other imidazolium-based ILs with straight chain sulfonate anions have shown this behaviour[5]. It has been suggested that the C2 proton is essential to promote liquid crystal stabilization[6b]. For the largest anion studied here, the triple-chain, TC, no liquid crystal phases were observed within the operating range of the DSC (>-60 °C) (Figure 4.5). Profiles for bmim DS were measured with vastly different melting points recorded, probably due to polymorphism and so no firm conclusions could be made about that compound. This is not uncommon behaviour: for example, bmim Cl has two possible non-interconvertable crystal structures (and melting points) due to the various possible *trans gauche* arrangements of the cation[27]. Crystallization is promoted when two different local structures (*trans* and *gauche* conformers) with different enthalpies of melting transition can coexist. However, for those with similar enthalpies, crystallization is hindered and lower melting are points observed. This may explain the results seen here, and also implies the possibility of polymorphism in the bmim AOT and bmim TC should not be ruled out.

The density ρ values (Table 4.3) agree with those previously reported for cationic ILs, for which ρ decreases with increasing alkyl chain length substituent on the cation (methylene groups are less dense than imidazole)[23].

	bmim AOT	bmim TC
	α_p = 7.40 x 10^{-4} °C^{-1}	α_p = 7.17 x 10^{-4} °C^{-1}
T / (°C)	ρ / (± 0.001 g cm^{-3})	ρ / (± 0.001 g cm^{-3})
25.0	1.082	1.079
30.0	1.078	1.075
40.0	1.071	1.067
50.0	1.063	1.059
60.0	1.055	1.052
70.0	1.047	1.044
80.0	1.039	1.037
90.0	1.032	1.030

Table 4.3: Experimental values of density, ρ, as a function of temperature. Also included is the thermal expansion coefficient, α_p.

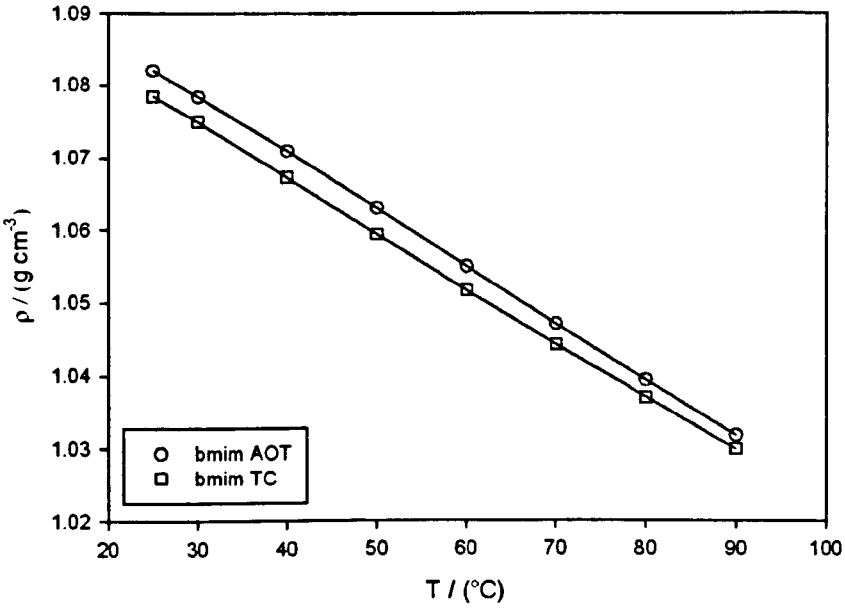

Figure 4.6: Variation of density ρ with temperature.

Interestingly, bmim AOT and bmim TC contain high methylene contents so that that their densities ($\rho \approx$ 1.08 g cm^{-3}) are much lower than most other ILs. For example, the densities of bmim based ILs have the following densities[23] (units in g cm^{-3}):

$$TC\ (1.08) \approx AOT\ (1.08) \approx Cl^-\ (1.08) < BF_4^-\ (1.12) < PF_6^-\ (1.36) < Tf_2N\ (1.43) < I^-\ (1.44)$$

Small-angle x-ray scattering was carried out on the neat SAILs (Figure 4.7). Even though the bmim DS sample was isotropic during the experiment, DSC showed that the system was polymorphic around this

temperature (25 °C). A broad diffraction band is centred around Q = 0.2745 $Å^{-1}$ ($2\pi/Q$ = 22.88 Å). This peak becomes broader for bmim AOT and bmim TC, suggesting a more disordered structure.

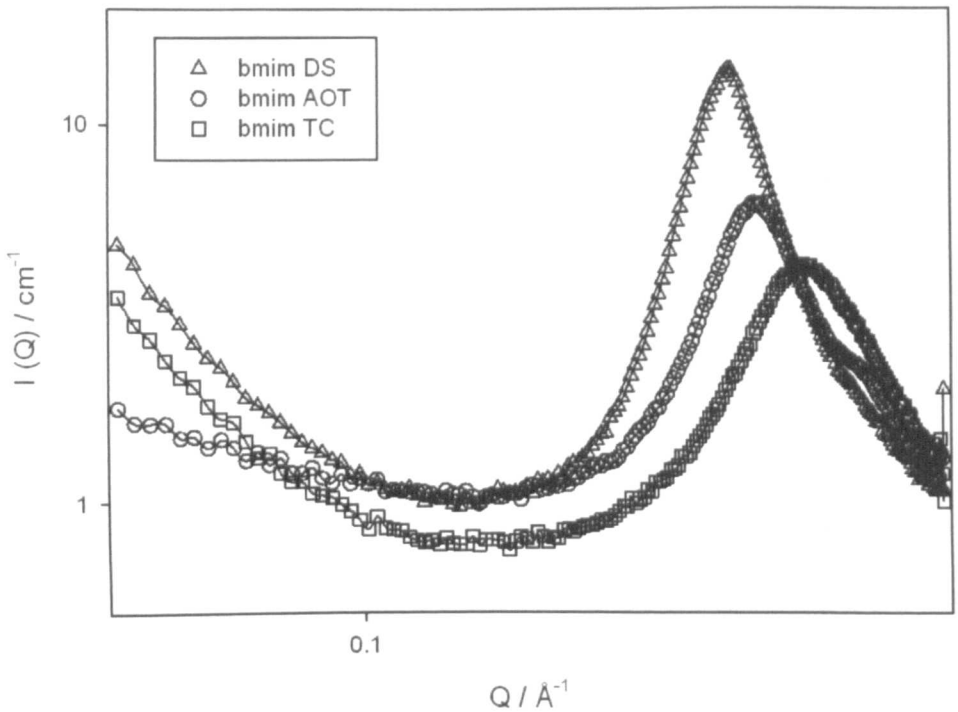

Fig. 4.7: SAXS profiles for neat bmim DS, bmim AOT and bmim TC at 25 °C.

The peaks also lower in intensity and shift to higher Q values (bmim AOT = 21.47 Å, bmim TC = 18.83 Å), consistent with reducing anion lengths DS>AOT>TC. Further investigation would be required to determine exactly how the anion/cation pair orient relative to each other. However, X-ray data reveal ordering present even in the isotropic liquid phase, which may be important for explaining electrochemical properties such as capacitance (discussed later). Investigation of the structure of "neat" SAILs may also be important for possible applications controlling stereoselective outcomes of organic reactions.

4.2.2 Viscosity measurements

For bmim DS, shear thinning was observed, possibly due to a structural change (as previously mentioned various polymorphs may be possible). Measurements for bmim DS were not reproducible and so an analogous straight chain surfactant from the literature (bmim C_8SO_4) was included in Figure 4.9 for comparison. The common IL Bmim PF_4 was also selected for a more detailed comparison.

Viscosity measurements for the other compounds (bmim AOT and bmim TC) were taken at temperatures ranging from 25 – 70 °C, with a maximum viscosity of 3640 mPa s reducing to 295 mPa s (Figure 4.9, Table 4.4).

Most ionic liquids[23] may be classed as Newtonian fluids as viscosity remains constant as shear rate increases. This was observed for the most highly branched IL surfactant, bmim TC, even after multiple hystereses of shear stresses had been repeated at increasing temperatures (Figure 4.8, bottom).

bmim AOT	E_a = 49.46 kJ mol^{-1}	**bmim TC**	E_a = 47.08 kJ mol^{-1}
T / (°C)	**η / (± 2% mPa s)**	**T / (°C)**	**η / (± 2% mPa s)**
25.0	3916.3	25.0	3639.2
29.9	2719.8	30.0	2506.3
35.0	1881.4	35.0	1793.6
40.0	1343.2	40.0	1308.1
44.9	995.48	45.0	976.58
49.9	745.22	50.0	741.03
55.0	568.94	55.0	585.28
60.0	442.97	60.0	451.38
65.1	347.54	65.0	359.87
70.1	279.93	70.0	294.69

Table 4.4: Experimental values of viscosity, η (mPa s), and the associated activation energies for viscous flow, E_a.

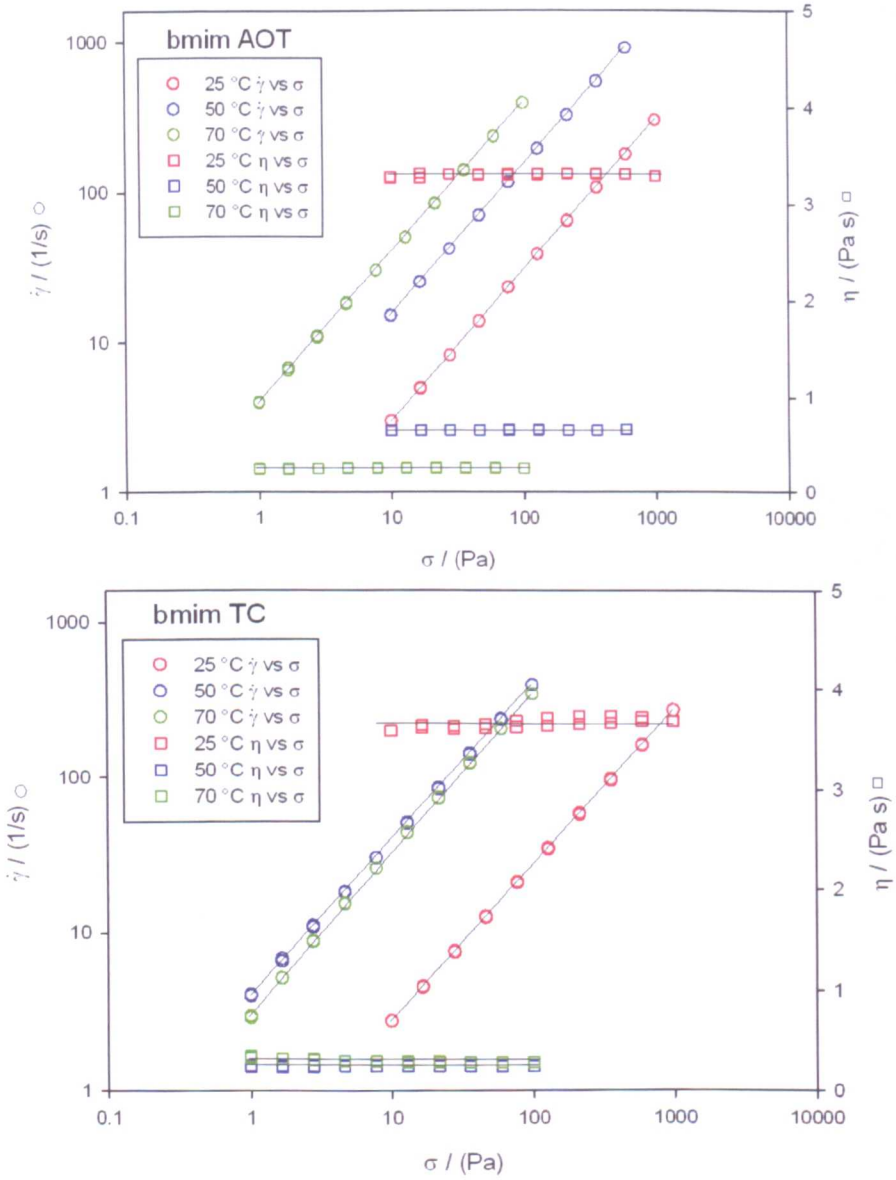

Figure 4.8: Shear rate ($\dot{\gamma}$) *vs* shear stress (σ) and viscosity (η) *vs* shear stress (σ) for bmim AOT and bmim TC at different temperatures (solid lines are a guide for the eye only). Plots clearly describe Newtonian behaviour where viscosity is independent of shear rate. Each measurement was repeated three times with no shear history observed.

Seddon[28] reported that ILs of the imidazolium BF_4 family (cationic surfactants) with longer alkyl chains (typically n >12) exhibit non-Newtonian behaviour. Surprisingly however, the anionic compounds studied here, with more alkyl carbons than compounds in the previous study[27], are still Newtonian. For bmim AOT Newtonian behaviour is also seen with the viscosity ranging from 3920 mPa s to 280 mPa s over the temperature range examined (Figure 8, left). Astonishingly, the viscosity falls by over 50% between 25 °C

and 35 °C. These values indicate that branching of the anion causes similar behaviour to that reported in literature, whereby increasing alkyl content on the anion slightly increases viscosity. However, the viscosities are around an order of magnitude higher than similar alkylsulfate based ILs, perhaps owing to an increase in van der Waals interactions owing to long branched alkyl chains, competing with electrostatic terms[29].

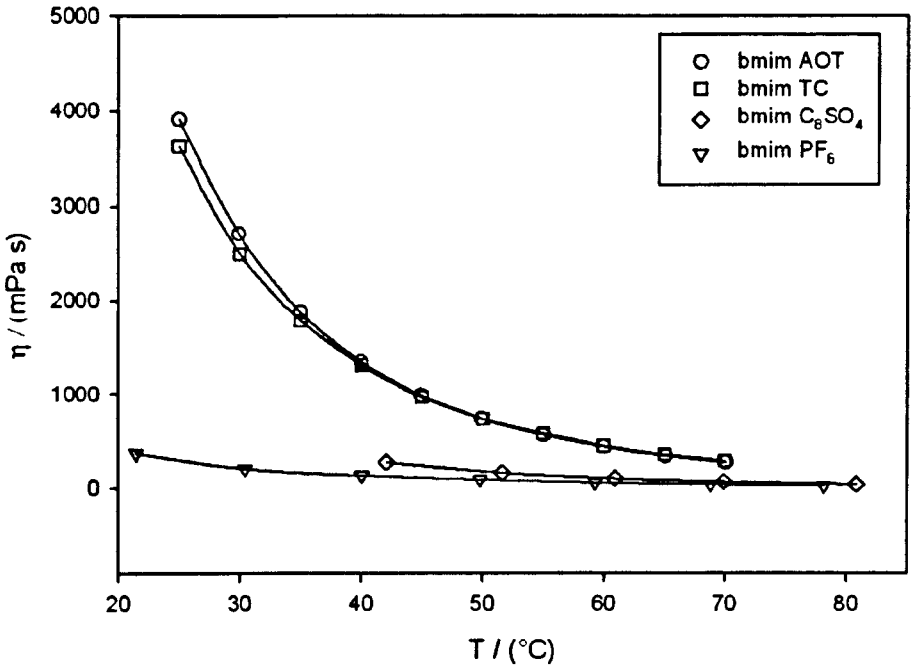

Figure 4.9: Effect of temperature on viscosity.

Literature data for bmim PF_4[30] and bmim C_8SO_4[31] have been included for comparison.

In order to calculate the activation energies for viscous flow from Equation 4.1, semi-logarithmic Arrhenius-like plots were made. Plots of bmim AOT and bmim TC deviate slightly from the Arrehnius-like expression at higher temperatures.

An extra factor affecting bulk viscosity may also be hydrogen bonding between the C2 proton and the anionic sulfonate group. An interesting observation is that anion chain branching opens up a much wider window of viscosity, and that this should be tunable depending on the anion chemical architecture. Such control over viscosity may be useful in chemical engineering applications involving reaction kinetics and heat transfer.

The experimental viscosities were calculated from the integrated form of an Arrhenius-like expression (Equation 4.1), which is more appropriate than the comparative Vogel-Fulcher-Tammann (VFT) equation, due to the asymmetry and bulk of the anions[28].

$$\eta = \eta_{\infty} exp\left(\frac{E_a}{RT}\right) \qquad \text{Eq. 4.1}$$

η_{∞} is the apparent viscosity at infinite temperature and E_a is the viscosity activation energy (the semi-logarithmic plots can be seen in Figure 4.10, results in Table 4.5).

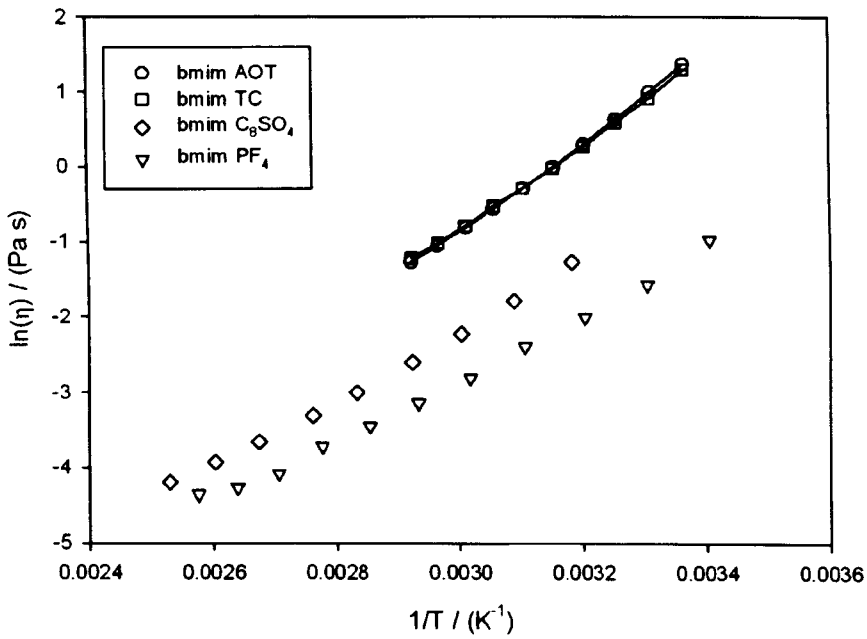

Figure 4.10: Semi-logarithmic Arrhenius-like plots.

Data for plots of bmim C_8SO_4 and bmim-PF_4 from Jacquemin *et al.*[30-31]

Compound	E_a / (kJ mol^{-1})	η_{∞} / (10^{-6} mPa s)
bmim AOT	49.5	7.413
bmim TC	47.1	18.00
bmim C_8SO_4	38.0	179.3
bmim PF_4	34.1	271.9

Table 4.5: Correlation parameters (η_{∞}, E_a) for the Arrhenius equation for viscosity for ILs as a function of temperature. Data for 1-butyl-3-methylimidazolium octyl sulfate (bmim C_8SO_4) and bmim PF_4 from Jacquemin *et al.*[30-31]

The magnitude of E_a is an indication of the difficulty of transfer of molecules through the liquid matrix. The value for E_a with bmim AOT is a little higher than that for bmim TC (49.46 and 47.08 kJ mol^{-1}, respectively), suggesting more order in the bmim AOT system. The activation energies are also higher (approx. 30%) than those of bmim PF_4 (dry = 34.1 kJ mol^{-1}, and saturated with H_2O = 29.0 kJ mol^{-1})[30] and much higher than for typical molecular solvents (c.f. H_2O (20°C) = 17.0 kJ mol^{-1}, benzene = 10.4 kJ mol^{-1}, and acetone = 7.1 kJ mol^{-1})[32]. Addition of co-solvents has also been shown to reduce viscosity[33], and this might be used to provide finer control still. For example, small additions of solvent could affect mesophase formation resulting in larger viscosity changes.

4.2.3 Phase behaviour by polarizing light microscopy (PLM)

The phase penetration PLM method was used to seek evidence of mesophase formation with added water (Figure 4.11): different mesophase optical textures appear across the steep concentration gradient set up against water. The transition from fluid micellar to liquid crystalline phases can be explained by a competition between increase in free energy associated with loss of orientational entropy, and reduction of free energy related to excluded volume and additional interactions.

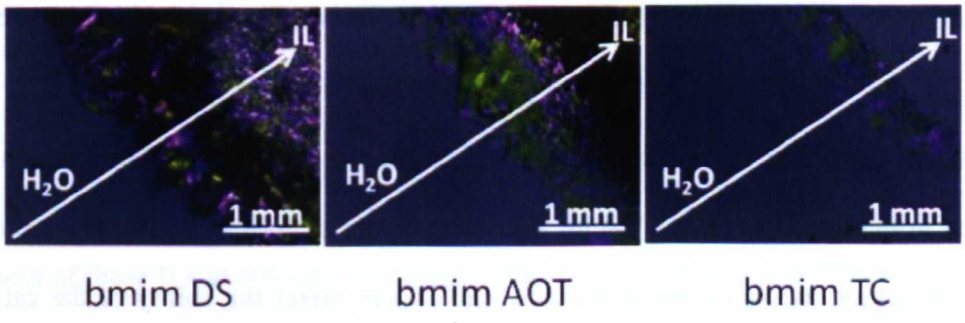

Figure 4.11: Optical textures of SAILs in phase penetration experiments (T = 25 °C).

As mentioned above, the single chained SAIL (bmim DS) exhibits irreproducible properties, possibly because of polymorphism. All batches produced, whether liquid or solid at 25 °C, showed birefringence as neat ILs, evidence of liquid crystalline ordering and mesophase formation in the presence of water. Both bmim AOT and bmim TC showed evidence of mesophase formation on addition of water, but no birefringence in the neat sample, consistent with findings from DSC and SAXS analysis.

4.2.4 Surface tensiometry and analysis

Surface tensions as a function of concentration in dilute aqueous solutions were recorded at 25 °C to establish critical micelle concentrations (cmc) (Figure 4.12, Table 4.6), and generate adsorption parameters. Although the self-aggregation behaviour of SAILs has recently attracted much attention, it now appears that in this respect they behave just like regular ionic surfactants[17, 34]. For example, the cmcs of the SAILs decrease with increasing carbon numbers on the anion tails, n_c in broad accordance to the Klevens equation[35]:

$$log(\text{cmc}) = A - Bn_c \qquad \text{Eq. 4.2}$$

where A and B are constants and, for paraffin chain salts having a single ionic headgroup, B is approximately equal to log 2 (i.e., reducing the surface tension to approximately half per each additional CH_2 group). It is known that chain branching in hydrocarbon surfactants gives higher cmc values than comparable straight-chain surfactants[36].

The cmcs for bmim DS and bmim AOT lie lower than their respective normal sodium forms (Table 4.6)[17]. This may be because the bmim cation is more effective at screening intramicellar electrostatic repulsions compared to Na^+ [6c], but also because bmim is more hydrophobic, thus reducing the free energy of micellization.

The tri-chain SAIL (bmim TC) has a cmc a little higher than that of its sodium analogue. There are contrasting reports in the literature to how bmim ions might order at an interface[37]. This ordering may be influenced by the structural nature of the anion tails, and in turn affect the ability of the cation to screen headgroup repulsions.

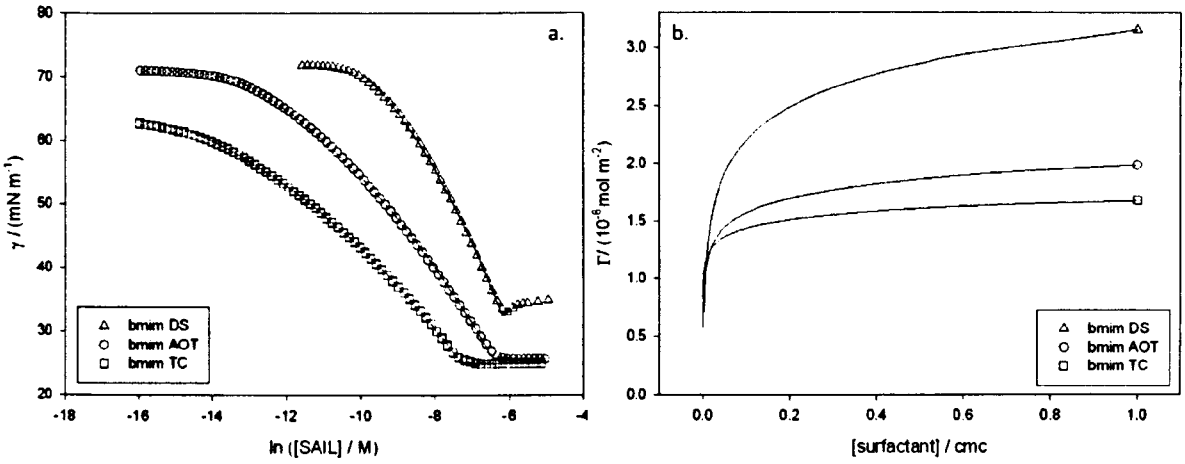

Figure 4.12: Surface tension data (with quadratic fits to pre-cmc data) and derived adsorption isotherms.

SAIL	cmc / mM ± 0.3	γ_{cmc} / (mN m^{-1}) ± 0.5 (Wilhelmy plate)	A_{cmc} / Å^2 ± 10%
Na-DS	8.00	34.9	56
Na-AOT	2.88	30.6	70
Na-TC	0.11	24.9	136
bmim DS	2.30	32.9	56
bmim AOT	1.78	25.7	86
bmim TC	0.55	24.8	111
hmim TC	0.76	24.7	116
bmimTC14	9.48	24.7	95

Table 4.6: Parameters derived from surface tension measurements.

Data for sodium analogues taken from Eastoe *et al.*[17]

The effectiveness of these ILs at reducing limiting surface tensions is very interesting. It has been observed before that for such SAILs with bulky organic cations, aggregation properties are dominated by anion structure[17]. The single chained bmim DS has a surface tension lower than its sodium analogue (32.9 mN m^{-1} c.f. 34.9 mN m^{-1})[17], as does bmim AOT (25.7 mN m^{-1} *c.f.* 30.6 mN m^{-1} for Na-AOT)[17], with values comparable to those of these anions with tetrapropylammonium cations. However, with bmim TC a lower limiting surface tension is reached, having what is believed to be the lowest surface tension for any imidazolium containing compound. Furthermore, these values are as low as any hydrocarbon surfactant, being comparable to some fluorocarbon surfactants[38], possibly representing the physical limit of surface

tension reduction for such compounds. It is instructive to compare these γ_{cmc} values with those for linear alkanes such as hexane (γ_{cmc} = 18.4 mN m^{-1} at 25 °C)[39].

It has been suggested that the lowest surface tensions are reached when the cation and anion tails are similar in size[5], and although this may be true for single chain compounds, for these SAILs there is no further reduction in surface tension (because hydrophobic bulk of the anion governs micellization). This was concluded by combining the TC anion with a cation with a comparatively long alkyl chain (1-hexyl-3-methyl imidazolium, hmim, Figure 4.13 and 4.14). No further reduction in γ_{cmc} was observed (Table 4.6). Another approach was to use a branched tri-chain anion, TC14 (Figure 4.13 and 4.14), as the sodium form has been show to exhibit very low γ_{cmc} (27.0 mN m^{-1})[40]. Again, for bmim TC14 no further decrease in γ_{cmc} was observed, lending support to the claim of reaching the physical limit for this type of surfactants.

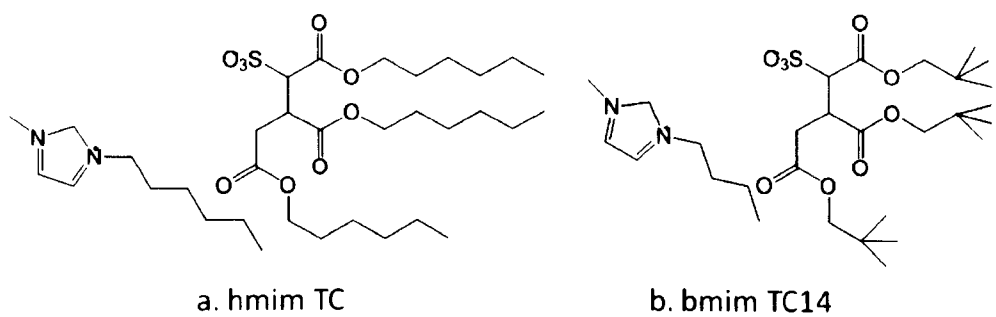

Figure 4.13: Compounds studied for comparison of surface tension

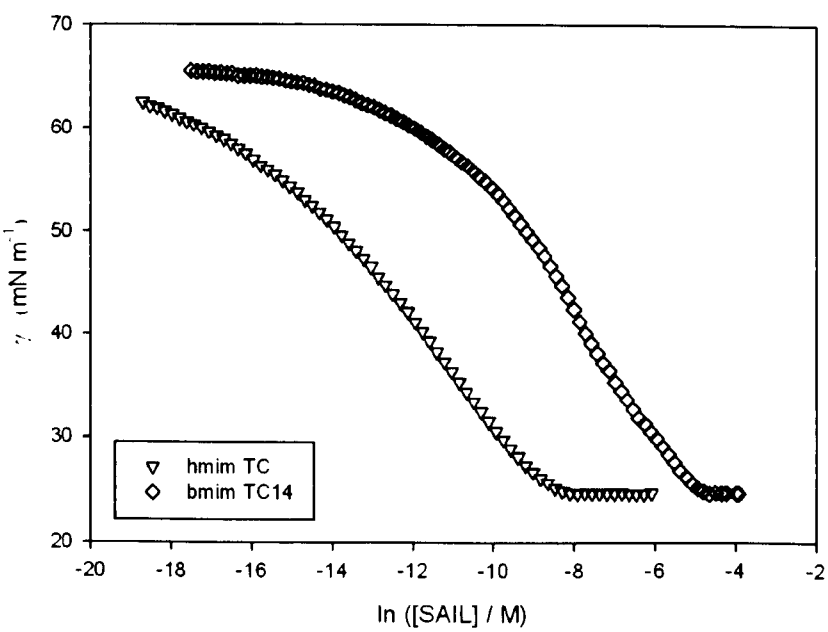

Figure 4.14: Surface tension data for SAILs at 25°C.

The limiting headgroup areas at the cmc (A_{cmc}) were calculated by fitting pre-cmc tension data to quadratics to generate adsorption isotherms using the Gibbs equation (Equations 4.3 and 4.4)[16,41]. A prefactor of $m = 2$ is expected for 1:1 dissociating ionic surfactants[17].

$$\Gamma = -\frac{1}{mRT}\frac{d\gamma}{\ln c} \qquad \text{Eq. 4.3}$$

$$A_{cmc} = \frac{1}{\Gamma N_A} \qquad \text{Eq. 4.4}$$

Previous studies have shown that for the parent surfactants (Na-DS, Na-AOT, Na-TC)(Table 4.6), A_{cmc} increases dramatically, consistent with expectations based on packing parameter arguments[17]. The same studies also showed that on replacing the Na^+ with large bulky tetraalkylammonium cations, A_{cmc} was still dominated by the identity of anion, appearing to also be the case with the bmim cation used here. The A_{cmc} value for Na-TC is larger than that for the bmim TC but, as mentioned above, this may be a result of ordering of the bmim cation at the air-water interface.

4.2.5 Micellar structure by SANS

SANS data were collected as a function of concentration in dilute aqueous phases, with all bmim compounds exhibiting strong Q^{-2} scattering (Figure 4.15). This scattering is consistent with stacked lamellar phase fragments, and curves could be adequately fit by a model for multilamellar stacks[21].

The SANS profiles were fitted with form factors for scattering from a thin interface combined with a one dimensional para-crystalline stack model[21]:

$$I(Q) \rightarrow N(\Delta\rho)^2V^2\left(\frac{\sin(QL_1/2)}{(QL_1/2)}\right)^2 \qquad \text{Eq. 4.5}$$

With N a concentration in cm^{-3}, $\Delta\rho$ the scattering length difference between solvent and surfactant sheets and L the planar sheet thickness. A modified Lorentz factor allows for a Gaussian distribution of surface normals around the Q vector. The model approximates the local extent of planarity, R^*, the mean layer thickness L,

number of layers M, planar spacing D and the Gaussian distribution of L and D as σ_L and σ_D respectively. The properties for 2 wt% bmim AOT and 0.5 - 1 wt% bmim TC could not be fitted, perhaps evidence for polymorphism. (Figure 4.16, Table 4.7).

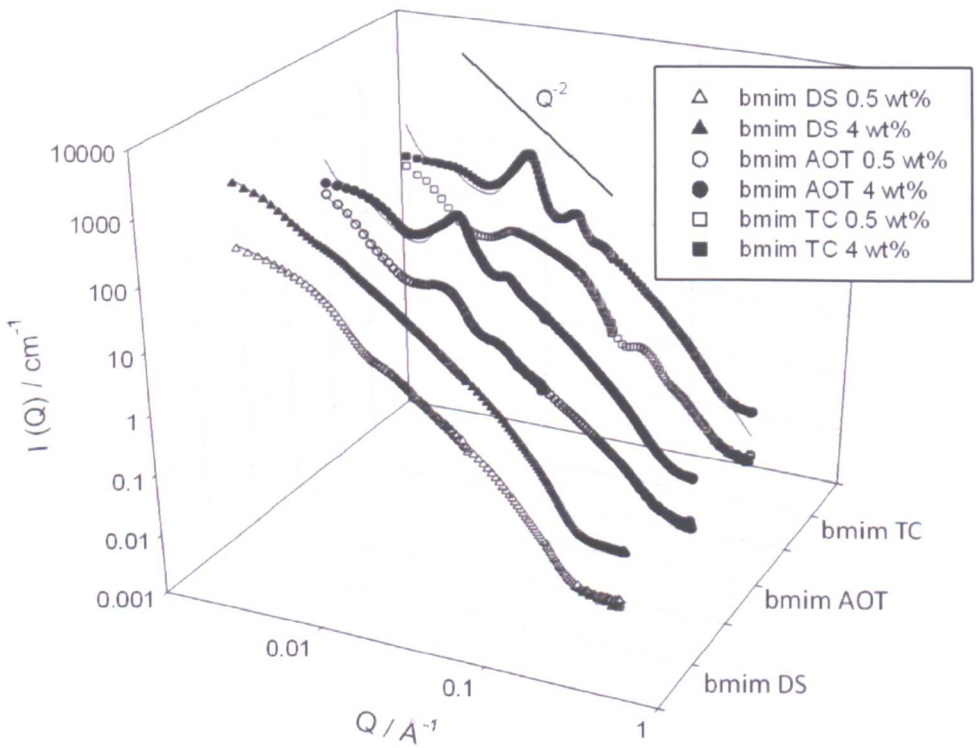

Figure 4.15: SANS profiles for bmim DS, bmim AOT and bmim TC surfactants in D_2O at 0.5 and 4 wt% at 25 °C. Lines through the data are fits using the model for paracrystalline stacks, with the parameters listed in Table 4.3.

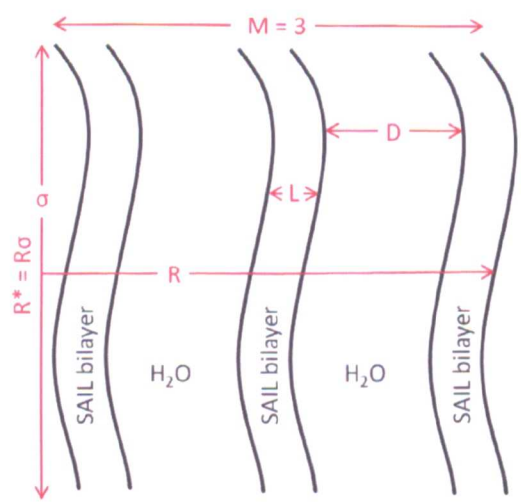

Figure 4.16: Schematic of paracrystalline stack structure.

SAIL	wt%	L / Å	R^*	M	D / Å
bmim DS	0.5	27.3	415	2.39	136
bmim DS	1.0	30.8	223	3.47	82
bmim DS	2.0	29.2	150	13.8	55
bmim DS	4.0	28.4	154	15.1	68
bmim AOT	0.5	12.6	676	1.9	559
bmim AOT	1.0	17.9	625	1.9	559
bmim AOT	2.0	-	-	-	(537)
bmim AOT	4.0	19.0	555	6.1	462
bmim TC	0.5	-	-	-	-
bmim TC	1.0	-	-	-	(659)
bmim TC	2.0	21.2	529	1.8	679
bmim TC	4.0	20.5	312	5.1	489

Table 4.7: Parameters fitted to SANS data using the model for polycrystalline stacks[25]. Values in brackets estimated using (2π/Q).

Bowers *et al.*[3] showed that bmim BF_4 aggregates above the "cmc" form spherical micelles around 13 Å in radius. It is known that SDS forms spherical micelles[17, 42], and even when substituting sodium for bulky tetraalkylammonium cations the micellar size and shape is maintained[17, 42]. Mislkolczy investigated bmim C_8SO_4 by turbidity and conductivity measurements, and also observed micelles[6c]. Surprisingly, however, at 0.5 wt% in water this longer C_{12} chain analogue, bmim DS, forms multilayer stacks where the bilayer thickness (L) is approximately twice the DS^- anion length. Increasing the concentration increases the layer rigidity (R^*), whilst also increasing the number of bilayers (M). This SANS behaviour for bmim AOT is analogous to other AOT containing ILs[17], which are known to exhibit a mixed structure ($L_l + L_a$) under these conditions[43]. In comparison to bmim DS, the decrease in bilayer separation is less pronounced, as is the extent of bilayer aggregation, M, and the stiffness parameter, R^*. On increasing the anion size from straight chain to double and triple chain, it appears that the bilayer separation, D, increases substantially. However, none of the other fitted parameters show any obvious trend down the anion series, making it difficult to draw firm conclusions about relationships between anion structure and aggregation.

4.2.6 Electrochemical properties

Cyclic voltammograms of bmim AOT and bmim TC employing an Au microelectrode at scan rate of 100 mV s^{-1} are displayed in Figure 4.7. Taking an arbitrary scale of 100 nA, it could be estimated that the

potential windows of both SAILs are approximately 4 V. This potential window is significantly wider than those found in aqueous solutions (water ~ 2 V[44]) and comparable to those reported in conventional 1-butyl-3-methyl-imidazolium containing ILs. For example, using a platinum microelectrode, Schröder *et al.*[45] reported potential windows of 4.15 V and 4.10 V for dry samples of bmim BF_4 and bmim PF_6 respectively, and Suarez *et al.*[46] recorded potential windows of 4.0 V and 5.0 V. It is also noteworthy that these new ILs have beneficial electrochemical properties, even under anaerobic conditions. Continuous potential cycling of bmim AOT showed progressive passivation of the electrode at high positive potentials (results not shown). This can be observed from the relatively slow rate of current increase at the anodic potential limit (Figure 4.17). The greater anodic/cathodic current of the bmim TC as compared to bmim AOT could be a result of the lower viscosity (*c.f.* Figure 4.9).

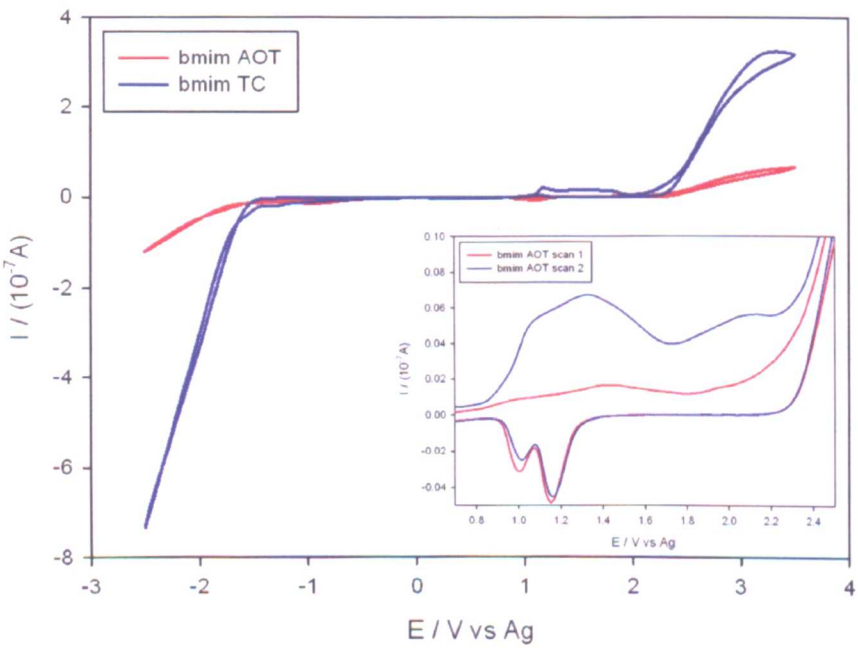

Figure 4.17: Cyclic voltammograms for bmim AOT and bmim TC on an Au microelectrode at a scan rate of 100 mV s^{-1} at room temperature.

The anodic responses observed between 1 and 3 V are linked to the formation of Au oxide, as well as oxidation of products generated at the negative end of the potential window. As shown in the inset of Figure 4.7, part of the current responses observed around 1 V disappear when the potential window is restricted to -1.5 V. The fact that the reduction products of the imidazolium ring can be oxidised in the reverse scan is

likely linked to the high viscosity of the SAILs. Indeed, the hemispherical geometry of the diffusion profiles characteristic of microelectrodes tends to enhance the rate of product diffusion away from the electrode. In this case, the diffusion coefficients are expected to be low, allowing the oxidation of products in the reverse scan. It should also be mentioned that the presence of impurities, such as water, may also be connected to some of the smallest features observed in the voltammograms. A key issue to be investigated in the future is the solubilisation of metal precursors, which could be electrodeposited upon negative polarisation. It is envisaged that structural ordering (Figure 4.6) could be translated in to the structure of the electrodeposits.

Ionic liquids exhibiting large capacitances offer potential for the development of supercapacitors, which are presently considered to be energy storage devices of choice. The capacitances of these SAILS have been estimated at the ionic liquid-electrode interface using the following formula:

$$C = \frac{\int_{E_1}^{E_2} I dt}{(E_2 - E_1)} \qquad \text{Eq. 4.6}$$

where E_1 and E_2 represent electrode potentials and I is the current. Integration was carried out between 0.1 V and 0.5 V, this region being well within the potential window for both bmim AOT and bmim TC.
Values obtained were 260 ± 97 μF cm^{-2} and 34 ± 12 μ F cm^{-2} for bmim AOT and bmim TC respectively. The electric double layer capacitances for bmim BF_4 and bmim PF_6 have been determined in a detailed study by Lockett *et al.*[47] and showed strong potential dependence, with maximum capacitances in the order of 10 μF cm^{-2}; significantly less than the capacitances obtained here. Unlike aqueous electrolytes or high-temperature molten salts the ions in ILs are often more complex, with delocalised charges, hydrogen bonding capability and high ion polarizability, leading to microstructuring at the IL-electrode interface. The high capacitances observed here are most probably due to increased amphiphilic nature of the anions, leading to more regular ionic domains (*c.f.* X-ray scattering data) and shifting the potential of zero charge (pzc). Conventionally, large anions lead to lower capacitance[48], but here the anions account for most of the hydrophobic bulk which seems to further increase capacitance.

4.3 Conclusions

This chapter reports the synthesis and characterization of physico-chemical properties of new SAILs with wide variations in chemical structure, and potential applications have been explored. The advantages of these compounds over existing ILs and SAILs are facile synthesis: they can also be readily generated from commercially available, cheap starting materials, with lower potential environmental hazards (halogen free) and toxicity (short imidazolium alkyl chain) than normal imidazolium based SAILs. Interestingly, the experimental data obtained under atmospheric conditions suggest suitability of these ILs for electrochemical applications, without the need for excluding air or water, which is a limitation of other common ILs. For example, low densities have been recorded which could be ideal for producing lightweight batteries, and the 50% drop in viscosity over 10 °C shows that these ILs may be useful transport media at convenient temperatures.

Polarizing light microscopy shows evidence for mesophase formation, and surface tension measurements show that cmc can be controlled by hydrophobic bulk of the anion. These SAILs have also been shown to promote very low air-water surface tensions: bmim TC promotes what appears to be the lowest surface tension of any imidazolium based IL, and also of any normal hydrocarbon surfactant, this γ_{cmc} of ~ 25 mN m^{-1} is equivalent to values of typical low surface energy fluorocarbon analogues[38]. This could potentially lead to replacement of hazardous fluorinated surfactants, with cheaper more benign hydrocarbon compounds, such as reported in this chapter.

In dilute aqueous phases SANS data indicate sheet-like structures for all compounds in dilute aqueous phases, with parameters such as interlayer distances, *D*, controlled by concentration and anion structure, all consistent with packing parameter arguments[49]. Particularly interesting is how bmim DS follows this trend, deviating from the spherical aggregates seen for other dodecylsulfate anions with large organic counterions, such as the tetraalkylammonium dodecylsulfates[17].

These results suggest that the ionic liquid nature of bmim SAILs confers no special properties on their aggregation behaviour[17, 34]. The unique combination of ionic liquid with surfactant properties may pave the way to the development of novel reaction media, where the possibility of mesophase catalysis may be combined with subsequent separation and extraction from an IL phase. Furthermore, these novel SAILs may find applications in electrochemistry, since the accessible potential window is influenced by the intrinsic

ionic liquid nature, with partitioning of reactants at electrodes influenced by the inherent surface active properties. Electrochemical results also indicate that these compounds, although containing trace water, still have relatively large potential windows and that this may be further increased through anion substitution. Other possible applications include templating electrodeposition, and due to large capacitances and low densities, in batteries and supercapacitors.

4.4 References

1. K. N. Marsh; J. A. Boxall; R. Lichtenthaler, *Fluid Phase Equilibria*, 2004, *219*, 93.
2. M. J. Earle; K. R. Seddon, *Pure Appl. Chem.*, 2000, *72*, 1391.
3. J. Bowers; C. P. Butts; P. J. Martin; M. C. Vergara-Gutierrez; R. K. Heenan, *Langmuir*, 2004, *20*, 2191.
4. O. A. El Seoud; P. A. R. Pires; T. Abdel-Moghny; E. L. Bastos, *J. Coll. Int. Sci.*, 2007, *313*, 296.
5. M. Blesic; M. Swadzba-Kwasny; J. D. Holbrey; J. N. Canongia Lopes; K. R. Seddon; L. P. N. Rebelo, *Phys. Chem. Chem. Phys.*, 2009, *11*, 4260.
6. (a) P. Wasserscheid; R. v. Hal; A. Bosmann, *Green Chem.*, 2002, *4*, 400; (b) T. Mukai; M. Yoshio; T. Kato; H. Ohno, *Chem. Lett.*, 2004, *33*, 1630; (c) Z. Miskolczy; K. Sebok-Nagy; L. Biczók; S. Göktürk, *Chem. Phys. Lett.*, 2004, *400*, 296.
7. C. Yao; V. Pino; J. L. Anderson, *J. Chromatogr. A* 2009, *1216*, 948.
8. (a) K.-S. Yeung; M. E. Farkas; Z. Qiu; Z. Yang, *Tetrahedron Lett.*, 2002, *43*, 5793; (b) E. Janus; I. Goc-Maciejewska; M. Lozynski; J. Pernak, *Tetrahedron Lett.*, 2006, *47*, 4079; (c) C. K. Lee; H. W. Huang; I. J. B. Lin, *Chem. Commun.*, 2000, 1911.
9. W. L. Hough; M. Smiglak; H. Rodriguez; R. P. Swatloski; S. K. Spear; D. T. Daly; J. Pernak; J. E. Grisel; R. D. Carliss; M. D. Soutullo; J. J. H. Davis; R. D. Rogers, *New J. Chem.*, 2007, *31*, 1429.
10. C.-W. Cho; T. P. T. Pham; Y. C. Jeon; K. Vijayaraghavan; W. S. Choe; Y. S. Yun, *Chemosphere*, 2007, *69*, 1003.
11. M. C. Buzzeo; R. G. Evans; R. G. Compton, *Chem. Phys. Chem.*, 2004, *5*, 1106.
12. E. I. Rogers; B. S[illegible]ljukić; C. Hardacre; R. G. Compton, *J. Chem. Eng. Data*, 2009, *54*, 2049.
13. (a) R. A. Mackay; J. Texter, *Electrochemistry in Colloids and Dispersions*. VHC: New York, 1992; (b) A. J. Bard; M. Stratmann, *Interfacial Kinetics and Mass Transport*. Wiley-VCH: Weinheim, 2003; Vol. 2, p 553; (c) J. F. Rusling, *Acc. Chem. Res.*, 1991, *24*, 75.
14. J. F. Rusling, *Colloids Surf. A*, 1997, *123-124*, 81.
15. A. Balducci; U. Bardi; S. Caporali; M. Mastragostino; F. Soavi, *Electrochem. Commun.*, 2004, *6*, 566.
16. S. Nave; J. Eastoe; J. Penfold, *Langmuir*, 2000, *16*, 8733.

17. P. Brown; C. Butts; R. Dyer; J. Eastoe; I. Grillo; F. Guittard; S. Rogers; R. Heenan, *Langmuir,* 2011, 27, 4563.

18. I. Goodchild; L. Collier; S. L. Millar; I. Prokes; J. C. D. Lord; C. P. Butts; J. Bowers; J. R. P. Webster; R. K. Heenan, *J. Coll. Int. Sci.,* 2007, *307*, 455.

19. S. Gold; J. Eastoe; R. Grilli; D. Steytler, *Colloid Polym. Sci.,* 2006, *284*, 1333.

20. S. Nave; J. Eastoe; R. K. Heenan; D. Steytler; I. Grillo, *Langmuir,* 2000, *16*, 8741.

21. M. Kotlarchyk; S. M. Ritzau, *J. App. Crystallogr.,* 1991, *24*, 753.

22. M. Ueda; Z. A. Schelly, *Langmuir,* 1989, *5*, 1005.

23. J. G. Huddleston; A. E. Visser; W. M. Reichert; H. D. Willauer; G. A. Broker; R. D. Rogers, *Green Chem.,* 2001, *3*, 156.

24. K. R. Seddon; A. Stark; M. J. Torres, *Pure Appl. Chem.,* 2000, *72*, 2275.

25. O. O. Okoturo; T. J. VanderNoot, *J. Electroanal. Chem.,* 2004, *568*, 167.

26. K. Fujita; D. R. MacFarlane; M. Forsyth; M. Yoshizawa-Fujita; K. Murata; N. Nakamura; H. Ohno, *Biomacromolecules,* 2007, *8*, 2080.

27. S. Hayashi; R. Ozawa; H. Hamaguchi, *Chem. Lett.,* 2003, *32*, 498.

28. K. R. Seddon; A. S. Stark; M.-J. Torres, Viscosity and Density of 1-alkyl-3-methylimidazolium ionic liquids. In *Ionic Liquids III: Fundamentals, Progress, Challenges, and Opportunities*, Rogers, R. D.; Seddon, K. R., Eds. ACS Symposium Series 901, Washington DC: 2004; Vol. 901.

29. (a) H. Tokuda; K. Hayamizu; K. Ishii; M. A. B. H. Susan; M. Watanabe, *J. Phys. Chem., B* 2005, *109*, 6103; (b) P. Bonhôte; A.-P. Dias; N. Papageorgiou; K. Kalyanasundaram; M. Grätzel, *Inorg. Chem.,* 1996, *35*, 1168.

30. J. Jacquemin; P. Husson; A. A. H. Padua; V. Majer, *Green Chem.,* 2006, *8*, 172.

31. J. Jacquemin; P. Husson; V. Majer; A. A. H. Padua; M. F. Costa Gomes, *Green Chem.,* 2008, *10*, 944.

32. J. R. V. Wazer; J. W. Lyons; K. Y. Kim; R. E. Colwell, *Viscosity and Flow Measurment.* Wiley: New York, 1963; p 406.

33. (a) Q. Liao; C. L. Hussey, *J. Chem. Eng. Data,* 1996, *41*, 1126; (b) U. Domańska; A. Marciniak, *J. Phys. Chem. B,* 2004, *108*, 2376.

34. P. D. Galgano; O. A. El Seoud, *J. Coll. Int. Sci.*, 2010, *345*, 1.

35. H. Klevens, *J. Am. Oil Chem. Soc.*, 1953, *30*, 4.

36. M. J. Rosen, Surfactants and Interfacial Phenomena. John Wiley and Sons, Ltd: USA, 1989.

37. (a) B. L. Bhargava; S. Balasubramanian, *J. Am. Chem. Soc.*, 2006, *128*, 10073; (b) T. J. Gannon; G. Law; P. R. Watson; A. J. Carmichael; K. R. Seddon, *Langmuir*, 1999, *15*, 8429; (c) S. Rivera-Rubero; S. Baldelli, *J. Phys. Chem. B*, 2006, *110*, 4756; (d) S. Rivera-Rubero; S. Baldelli, *J. Phys. Chem. B*, 2006, *110*, 15499; (e) S. Baldelli, *J. Phys. Chem. B*, 2003, *107*, 6148; (f) C. Aliaga; S. Baldelli, *J. Phys. Chem. B*, 2007, *111*, 9733.

38. A. R. Pitt; S. D. Morley; N. J. Burbidge; E. L. Quickenden, *Colloids Surf. A:* 1996, *114*, 321.

39. P. Atkins; J. de Paula, *Atkins' Physical Chemistry*. 7 Ed.; Oxford University Press: Oxford, 2002.

40. A. Mohamed; K. Trickett; S. Y. Chin; S. Cummings; M. Sagisaka; L. Hudson; S. Nave; R. Dyer; S. E. Rogers; R. K. Heenan; J. Eastoe, *Langmuir*, 2010, *26*, 13861.

41. J. Eastoe; A. Downer; A. Paul; D. C. Steytler; E. Rumsey; J. Penfold; R. K. Heenan, *Phys. Chem. Chem. Phys.*, 2000, *2*, 5235.

42. A. Paul; P. C. Griffiths; E. Pettersson; P. Stilbs; B. L. Bales; R. Zana; R. K. Heenan, *J. Phys. Chem. B*, 2005, *109*, 15775.

43. (a) J. Rogers; P. A. Winsor, *J. Coll. Int. Sci.*, 1969, *30*, 247; (b) Z. X. Li; A. Weller; R. K. Thomas; A. R. Rennie; J. R. P. Webster; J. Penfold; R. K. Heenan; R. Cubitt, *J. Phys. Chem. B*, 1999, *103*, 10800.

44. K. Izutsu, *Electrochemistry in Nonaqeous Solutions*. Wiley-VCH: Weinheim, 2002.

45. U. Schroder; J. D. Wadhawan; R. G. Compton; F. Marken; P. A. Z. Suarez; C. S. Consorti; R. F. de Souza; J. Dupont, *New J. Chem.*, 2000, *24*, 1009.

46. P. A. Z. Suarez; V. M. Selbach; J. E. L. Dullius; S. Einloft; C. M. S. Piatnicki; D. S. Azambuja; R. F. de Souza; J. Dupont, *Electrochimica Acta*, 1997, *42*, 2533.

47. V. Lockett; M. Horne; R. Sedev; T. Rodopoulos; J. Ralston, *Phys. Chem. Chem. Phys.*, 2010, *12*, 12499.

48. R. Costa; C. M. Pereira; F. Silva, *Phys. Chem. Chem. Phys.*, 2010, *12*, 11125.

49. J. N. Israelachvili; D. J. Mitchell; B. W. Ninham, *J. Chem. Soc. Faraday Trans.*, 1976, *72*, 1525.

Chapter 5

Magnetic Control Over Liquid Surface Properties with Responsive Surfactants

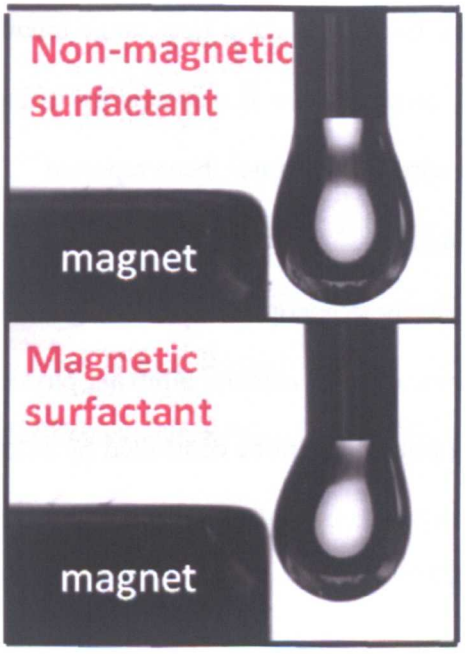

This chapter contains two parts. The first part looks at new magneto-responsive surfactants based on transition metals, their characterisation and potential applications. Part two investigates lanthanide based surfactants, and then considers the possibility of calculating critical micelle concentrations as a function of magnetic susceptibility.

Part One

5.0 Introduction

Surfactants responsive to pH[1], temperature[2], CO_2[3], and light[4] are already known: this chapter reports the first surfactants, which are also ionic liquids (ILs), and magneto-responsive.

Although ILs containing transition metal complexes have been known for some time[5], it had always been assumed that the metallic centers were isolated, lacking long range interactions and communication necessary to be magnetically-active[6]. Only recently have ILs containing magneto-active metal complex anions, such as 1-methyl-3-butylimidazolium tetrachloroferrate[7], been reported[7-8]. These magnetic ILs (mag-ILs) are especially interesting since typical magnetic fluids (ferrofluids) comprise magnetic colloidal particles (≥10 nm) dispersed in a carrier fluid. Whereas these nanoparticle-free mag-IL fluids are themselves paramagnetic; containing high effective concentrations of metal centers, allowing physico-chemical properties (hydrophobicity, electrical conductivity, melting point, etc.) to be controlled by external magnetic fields. Furthermore, because mag-ILs and MILSs, are non-volatile they offer advantages over conventional ferrofluids which often employ flammable organic solvents.

Compound	Anion	Cation
C_{10}mim Cl	Cl^-	
C_{10}mim F	$FeCl_4^-$	
DTAB	Br^-	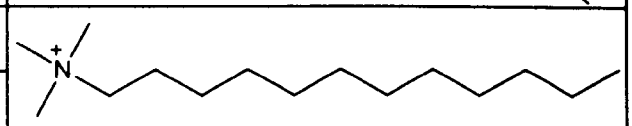
DTAF	$FeCl_3Br^-$	
DDAB	Br^-	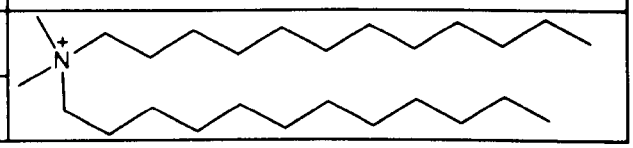
DDAF	$FeCl_3Br^-$	

Table 5.1: Inert (SURFs) and magnetic surfactants (MILS) studied.

Previous work has shown numerous ILs exhibiting magnetic responses[6, 8b]. The compounds introduced here (Table 5.1) extend this approach, but now importantly encompass surface activity, which is a fundamental

property of liquids and solutions. With this, magneto-responsive emulsions become accessible, which to date have exclusively been realized in Pickering emulsions comprising surface active magnetic nanoparticles[9]. Synthesis of the MILSs can be achieved by mixing appropriate metal halides with cationic surfactants. In the "pure" ionic liquid form such compounds also represent progress towards cheaper and more environmentally friendly mag-ILs.

5.1 Experimental

5.1.1Synthesis

1-decyl-3-methyl imidazolium chloride (96%, C_{10}mim Cl), dodecyltrimethylammonium bromide (DTAB,), didodecyltrimethylammonium bromide (DDAB), octaethylene glycol monododecyl ether ($C_{12}E_8$), iron tetrachloride and D_2O were purchased from Sigma Aldrich without further purification. 1-butyl-3-methyl imidazolium tetrachloroferrate ([bmim]$FeCl_4$) was purchased from TCI chemicals and used without further purification.

1-decyl-3-methyl imidazolium tetrachloroferrate (C_{10}mim F) was synthesized similar to previous literature[6], whereby 1 equivalent of iron tetrachloroferrate was added to the imidazolium halide and stirred overnight at 80 °C dehydrating at reduced pressure at 80 °C overnight to yield a viscous brown liquid. DTAF (dodecyltrimethylammonium trichlorobromoferrate) and DDAF (didodecyldimethylammonium trichlorobromoferrate) were synthesized by stirring the appropriate parent surfactant with and equimolar amount of metal halide in methanol overnight. The solvent was removed under reduced pressure and dried *in vacuo* at 80 °C overnight.

5.1.2 Surfactant Characterization

Elemental analysis shows that all the compounds contain the expected molecular ratios.

Compound	C	H	N	Cl
C_{10}mim F	40.0 (40.1)	6.4 (6.5)	6.7 (6.7)	33.7 (33.5)
DTAF	38.3 (38.3)	7.2 (7.2)	3.0 (3.0)	-
DDAF	50.2 (50.0)	8.9 (9.0)	2.0(2.2)	-

Table 5.2: Elemental analysis results, experimental and theoretical (brackets) as % wt.

The visible absorption spectra of the MILS were recorded on a Nicolet Eco 300 UV-Vis spectrometer, in acetonitrile (0.1 M, 500 – 900 nm, Figure 5.1). MILS 1 shows the three characteristic bands of the $[FeCl_4]^-$ ion at 534, 619 and 688 nm and agrees with previous literature for $[bmim]FeCl_4$[10], suggesting that $[FeCl_4]^-$ is the dominant anion in the system. However it is known from the literature that there is probable small quantities of $[Fe_2Cl_7]^-$ species present[11]. The other MILS showed bands for the $[FeCl_3Br]^-$ ion similar to those for the $[FeBr_4]^-$ ion[12].

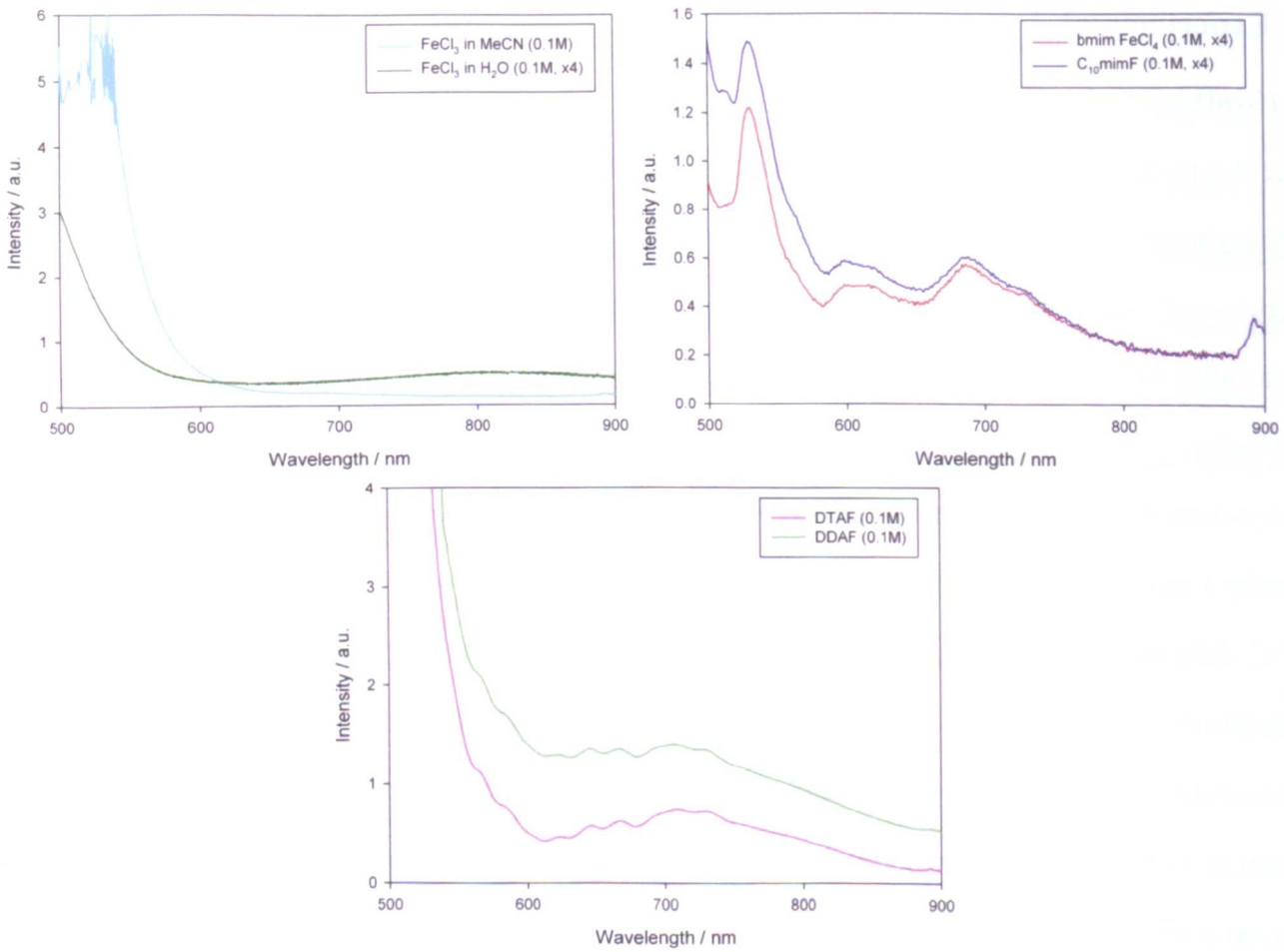

Figure 5.1: Visible spectra of $FeCl_3$ (starting material) and MILS at a concentration of 0.1 M in acetonitrile. The intensity for $FeCl_3$ (in H_2O), $[bmim]FeCl_4$ and DTAF has been scaled up by a factor of 4.

5.1.3 Differential Scanning Calorimetry (DSC)

The melting points and thermal behaviour of the MILS were measured using a TA instruments DSC Q200. The heating and cooling ramp for each sample was 10 °C min^{-1} and cyclic profiles were repeated three times. All the MILS can be classified as ionic liquids as they have melting points below 100 °C and much

lower than their equivalent parent surfactants. C10mim Cl also has many glass transition temperatures[13] which were not observed for C10mim F.

5.1.4 Conductivity

Electrical conductivities were determined using a Jenway Model 4510 Conductivity/TDS conductivity meter with temperature controlled at 25 °C ± 0.1 (thermostatic water bath). Dissociation constants (β), were estimated from the ratio of the slopes of two intersecting lines.

5.1.5 Magnetic susceptibility

Magnetization curves were monitored at room temperature with an ADE Magnetics Vibrating Sample Magnetometer EV7 up to a maximum field strength of 2.2 T (Figure 5.3 and 5.4). A typical experiment consisted of a virgin curve, followed by a full hysteresis loop. Samples were measured in sealed Teflon vessels, placed on a glass sample holder between two poles of an electromagnet, and vibrated at a frequency of 75 Hz.

5.1.6 Polarizing Light Microscopy (PLM)

A Nikon Optiphot-2 microscope fitted with polarizing filters and a Linkam heating/cooling stage was used. Images were captured on a PC via a video camera and colour processor connected to the microscope. The liquid crystal progression of each surfactant was investigated by the solvent penetration method (i.e., phase cut). A small amount of surfactant was placed on a microscope slide under a coverslip. The slide was mounted on the cover slide and heated until fluid and completely isotropic. After slow cooling (1.0 °C min^{-1}) to 25 °C, a drop of water was added to the edge of the coverslip. As the water penetrated the surfactant, a concentration gradient was established, from water at one side to pure surfactant at the other, enabling the entire range of mesophases to be observed in the field of view.

5.1.7 Small-Angle Neutron Scattering (SANS)

Scattering was measured on the reactor-based D22 diffractometer at Institut Laue-Langevin (ILL), Grenoble, France (further details can be found in Chapter 2).

5.1.8 SANS fitting

Scattering intensity $I(Q)$ is a product of the size and shape of the aggregates (form factor, $P(Q)$) and the interaction between these aggregates (structure factor, $S(Q)$).

$$I(Q) \propto P(Q,R)S(Q) \qquad \text{Eq. 5.1}$$

where R is the particle radius.

Different models were employed to fit the raw data using FISH[14] interactive fitting program, which can be found online (http://www.small-angle.ac.uk). C10mim C and DTAB used the model for an ellipsoid form factor ($P(Q)$) multiplied by a Hayter-Penfold charge repulsion ($S(Q)$), giving the effective structure factor for charged micelles[15].

There are three structural dimensions in the ellipsoidal form factor model used, and these are the radius of the principal axis, R_1, the axial ratio, X, and the radius of the secondary axis, R_3. X is 1 for a spherical, < 1 for an oblate and > 1 for a prolate structure. Fit parameters: ellipsoid P(Q), principal radius R_1, aspect ratio X; $S(Q)$, micellar charge Z, volume fraction, ϕ, Debye length, κ^{-1}, and the effective radius of the charged micelle, $R_{S(Q)}$.

For $S(Q)$ the value of ϕ is known based on composition and κ can be estimated to a first approximation using

$$\kappa = \left(\frac{2F^2\rho I}{\varepsilon_0\varepsilon_r RT}\right)^{1/2} \qquad \text{Eq. 5.2}$$

where F is the Faraday constant, ρ is the solvent density, I the ionic strength, ε_0 is the permittivity of free space and ε_r is the dielectric constant of the solvent. κ^{-1} has the dimensions of length and is a measure of the extent of the electric double layer.

For MILS 1 this model was further constrained by inputting the alkyl tail lengths, and the head group and counterion volumes constants (determined by SPARTAN), as well as the sums of scattering lengths Σb_i of these fragments. The hydration numbers were; headgroup 4, anion 8. Fit parameters now also include aggre-

gation number N allowing the calculation of the fractional charge $\beta = Z/N$. And DTAF was fitted using a hard sphere structure factor (HSS(Q)),[16] fitting to parameters of R_1, X, and HSϕ.

DDAF was fitted to rods (disks) of radius, R, and length, L, with the form factor[17] expressed as:

$$P_{rod}(Q) = Vr^2(\Delta\rho)^2 \int_0^{\frac{\pi}{2}} \frac{[sin^2[(QLcos\beta)/2]][4J_1^2(Qrsin\beta)]}{\left[\frac{1}{4}(QL)^2cos^2\beta\right][(Qr)^2sin2\beta]} sin\beta d\beta \quad \text{Eq. 5.3}$$

where V_r is the rod volume, J_1 is the first-order Bessel function of the first kind, and β is the angle between the rod axis and the scattering vector, Q.

DDAB was fitted using the program SansView (http://danse.chem.utk.edu/index.html) and a LamellarPS model.[18] This model provides the scattering intensity for a lyotropic lamellar phase where a random distribution in solution is assumed. The scattering intensity I(Q) is:

$$I(Q) = 2\pi \frac{P(Q)S(Q)}{\delta Q^2} \quad \text{Eq. 5.4}$$

The form factor is:

$$P(Q) = \frac{2\Delta\rho^2}{n^2}(1 - \cos(Q\delta)) \quad \text{Eq. 5.5}$$

and the structure factor is:

$$S(Q) = 1 + 2\sum_1^{N-1}\left(1 - \frac{n}{N}\right)\cos(Qdn)\, exp\left(-\frac{2Q^2d^2\alpha(n)}{2}\right) \quad \text{Eq. 5.6}$$

where

$$\alpha(n) = \frac{\eta_Q}{4\pi^2}(\ln(\pi n) + \gamma_E \quad \text{Eq. 5.7}$$

γ_E=0.577216 = *Euler's const.*

$$\eta_Q = \frac{Q_o^2 k_B T}{8\pi\sqrt{KB}} = Caillé\ const. \qquad \text{Eq. 5.8}$$

Here d is the lamellar periodicity, related to the bilayer thickness, e,($d = e/\varphi$, where φ is the volume fraction), K = smectic bending elasticity, B = compression modulus and N = number of lamellar plates (bilayers).

Fitting parameters include calculation of the scattering length densities of the solvent and headgroup with the assumption of a basic core-shell form factor such that one might imagine a hollow sphere with an inner and outer radius. The model also accounts for smearing of the data due to the instrumental resolution as a result of finite size of the direct beam and of the wavelength spread. Finally, the Caillé parameter, η, introduces bending modulus constants accounting for bilayer displacement around its equilibrium position.

The adjustable parameters in the model include: η, N, and d.

5.1.9 Surface Tensions

Surface tension measurements between aqueous surfactant solutions and air were performed at 25 ± 1 °C, using a Krüss Drop Shape Analysis DSA1 apparatus. This instrument obtains the coordinates of the drop edge (shape and size), which are used in an algorithm to calculate surface tension. Prior to use, the capillary needle (diameter, 1.834 mm) and syringe were rinsed with copious amounts of distilled water. Before being mounted on the dosing dispenser, the syringe was rinsed a few times with the surfactant solution to be measured. An aqueous drop was manually formed at the tip of the capillary. Measurements were acquired until steady values of surface tension were reached. Calibration was carried out by measuring the surface tension of pure water (Elga, 18 MΩ cm) at the air-water interface[19].

Measurements were taken on the same drop (0.2 M for maximum visual effect) with and without a magnet. The magnet was held in position at an approximate distance of 1 mm from the drop. The magnet was a NdFeB magnet (N42, 20 mm x 10 mm with a magnetic field density of 0.44 T on the surface and 0.26 T at 5 mm).

As a control $FeCl_3$ was dissolved in pure water and surface tensions measured. Paramagnetism is common in dilute transition-metal salts as the unpaired electrons interact weakly and their spins, which are randomly orientated at room temperature, align slightly to an external field[20]. It should also be expected for inorganic

salts that the interfacial tension increases. A slight decrease was seen but was assumed to lie within the range of error. On placing the magnet 1mm from the surface tension dropped dramatically due to $FeCl_3$ relocating from the bulk to the surface and reducing the internal pressure of the droplet.

For comparison a non-ionic surfactant (0.2 M), octaethylene glycol monododecyl ether ($C_{12}E_8$), was chosen.

5.2 Results and Discussion

5.2.1 Electrical conductivity

Electrical conductivity measurements of dilute aqueous solutions show that the cmcs (Table 5.3) are not greatly affected by the changes in anion alone. At first sight this is surprising as the larger anions ($[FeCl_3]^-$, $[FeCl_3Br]^-$) should be less effective at screening cation-cation headgroup repulsions, thus increasing the cmc (surfactants become more hydrophilic). However, the $[FeCl_3]^-$ and $[FeCl_3Br]^-$ anions may interact with the hydrophobic moieties, and it is seen that the degree of dissociation, β, increases exchanging halide for the tetrahalogenferrate (III) anion.

Compound	M_w / (g mol^{-1})	Mp / °C	cmc / (mM) ± 0.005	β	χ_{mol} / (m^3 mol^{-1})	μ_{eff} / (B. M.)
C10mim C	258.61	311[13]	37.0 (39[21])	0.55	-	-
DTAB	308.35	246	15.5 (14.5[22])	0.26 (0.25[22])	-	-
DDAB	420.81	161-163	0.05 (0.07[23])	0.53[a]	-	-
C10mim F	462.64	-60	40.6	0.73	1.53×10^{-7}[b]	5.38 (5.66[6])[b]
DTAF	470.55	32	13.6	0.81	1.37×10^{-7}	5.09
DDAF	624.84	40	0.06	0.87	1.31×10^{-7}	4.99

Table 5.3: Properties of surfactants studied. [a]Estimated as 0.5 at low surfactant concentrations[23]. Brackets indicate literature values. [b]For comparison, (C_4) [bmim] $FeCl_4$ (1.77×10^{-7} m^3 kg^{-1}, 5.90 B. M.)[7] and (C_8) [omim] $FeCl_4$ (1.76×10^{-7} m^3 kg^{-1}, 5.78 B. M.)[10b].

5.2.2 Magnetic behaviour

The MILSs investigated here show no saturation magnetization; but do exhibit paramagnetic behavior (Figure 5.3 and 5.4) and the values for magnetic susceptibility, χ, are similar to those reported in the literature (Table 5.2)[7, 10b]. Any discrepancy could be due to either water adsorption or incomplete conversion of $FeCl_3$ to $[FeCl_4]^-$, but is more likely attributable to the structure of the pure ionic liquids. This may perhaps be ex-

plained in the fact that C10mim F has a different level of anion dissociation or that $[FeCl_3Br]^-$ may not be the dominate anion in this system due to a different equilibrium constant for all possible anions, based on Lewis acid arguments[11, 24].

Effective magnetic moments (μ_{eff}), have also been estimated, are similar to literature reported and lie close to that expected for high-spin d^5 Fe^{III} ions (spin-only value: 5.92 B. M.)[25]. χ decreases when moving from C10mim F to DTAF and DDAF. A slight decrease should be expected as Br^- is a larger anion than Cl^- (1.98 Å and 1.81 Å respectively) and more polarisable, occupying an out of plane position forcing the Fe^{2+} ion towards the planes containing Cl^- resulting in smaller contact angle of the spins[26]. It may also be explained in terms of lower ligand field strength (Br is before Cl in the electrochemical series)[10b]. Surprisingly, even micellar solutions of these MILSs demonstrate a field response, leading to the intriguing question of the effect of micellar structuring in comparison to a non-micellizing magnetic IL.

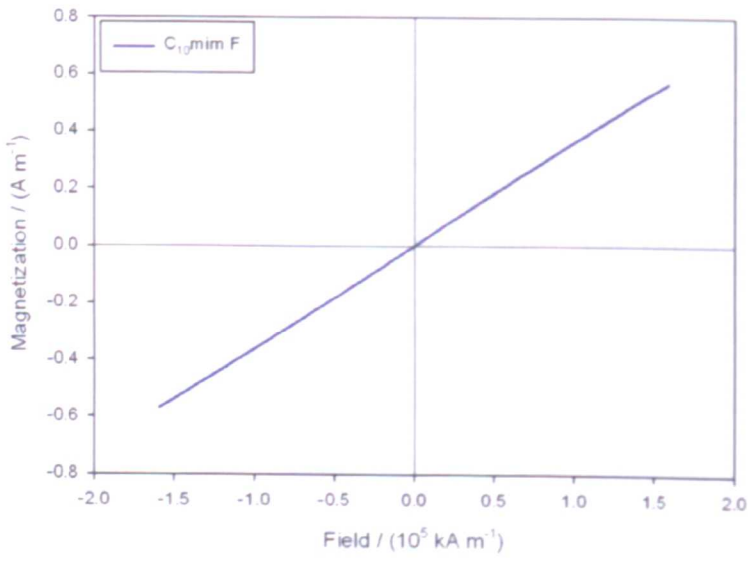

Figure 5.2: Magnetisation curve for C_{10}mim F.

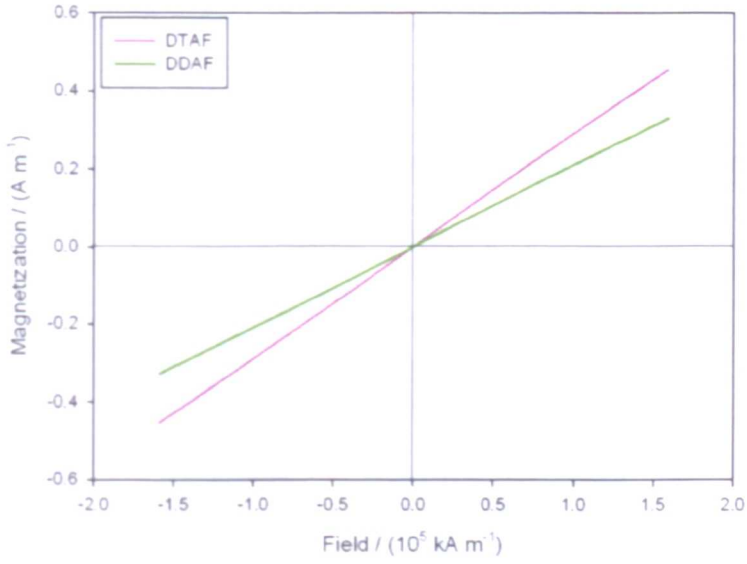

Figure 5.3: Magnetisation curve for DTAF and DDAF.

It has been shown that a homogeneous mixture of [bmim] $FeCl_4$ in water could not be separated by a 1 T magnet[27]. However, concentration was spatially varied in the magnetic field gradient and it is expected that MILSs showing a higher magnetic susceptibility in water could also be created by altering cation-anion structure (lowering molecular weight of cation or changing the paramagnetic anion) or perhaps further increasing alignment of magnetic moieties by creating non-ionic MILS. This may then open up the possibility of combining a magnetic field with other separation techniques such as centrifugation, filtration and adsorption. For example, locally increased concentrations of magnetic ionic liquids can increase the efficiency of ultracentrifugation[28].

5.2.3 Polarizing light microscopy (PLM)

PLM textures (Figure 5.4) clearly show that all the SURFS exhibit transitions from fluid micellar to liquid crystalline phases, understood as due to a competition between the increase in free energy associated with loss of orientational entropy and a reduction of free energy related to the excluded volume and other interactions. With no added water pure C_{10}mim Cl exhibits a fan-like texture characteristic of a hexagonal phase (or focal conic lamellar phase). The phase progressions of DTAB and 3 at 25 °C are consistent with the literature: DTAB[29] L_1-H_α-crystals; DDAB[30303030303030] isotropic-D_1-D_2 (where L_1 represents a non-birefringent micellar solution, H_α a mosaic texture representing a reverse hexagonal phase, D_1 a dilute lamellar phase,

and D_2 a collapsed lamellar phase). Mesophase formation is lost when progressing from C_{10}mim Cl to C. $_{10}$mim F and DTAB to DTAF, though dilute isotropic (micellar) phases are still present. This may possibly be explained by the increased hydrophobicity of the MILS. DDAF still retains mesophase structure (*c.f.* SANS) though less extended than its parent surfactant.

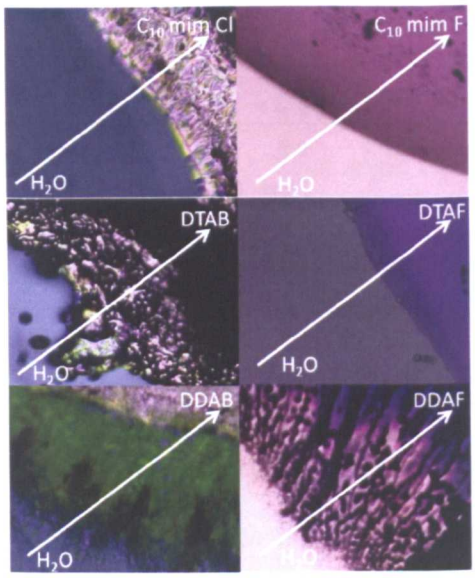

Figure 5.4: PLM textures showing mesophase formation of surfactants studied on addition of water at 25 °C.

5.2.4 Small-angle neutron scattering

SANS conclusively shows that the SURFs and MILSs aggregate at concentrations in excess of their critical micelle concentration (cmcs). Data analyses, through scattering law model fitting, show minor changes in micellar size or shape after exchanging the halide for tetrahalogenferrate (III), and also with concentration. The SANS for C_{10}mim Cl, DTAB, C_{10}mim F and DDAF micelles can be fitted using a model for ellipsoidal micelles with principal radii R_1 11-18 Å and aspect ratio X 1.0 – 2.4 depending on surfactant and concentration (Figure 5.5 and 5.6, Table 5.4 and 5.5)

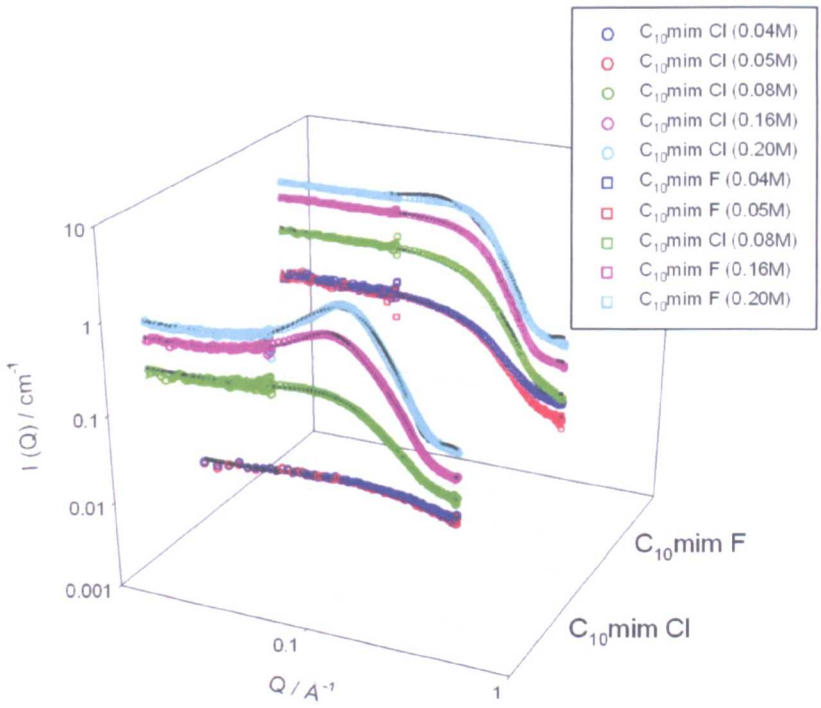

Figure 5.5: SANS profiles for C_{10}mim Cl and C_{10}mim F. Lines through the data are fits using the models listed above with parameters listed in Tables 5.4 and 5.4.

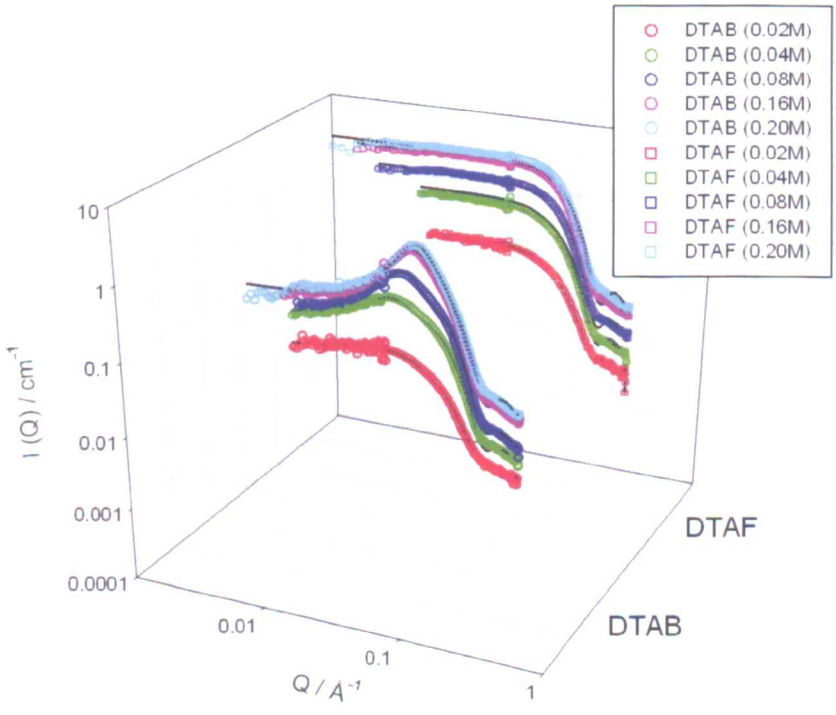

Figure 5.6: SANS profiles for DTAB and DTAF. Lines through the data are fits using the models listed above with parameters listed in Table 5.4.

Compound	Concn / M	Shape	R_l / Å ± 2	X ± 0.2
C_{10}mim Cl	0.040	ellipsoid	11 (10.0[21])	1.0 (1.0[21])
C_{10}mim Cl	0.050	ellipsoid	11 (12.8[21])	1.0 (1.1[21])
C_{10}mim Cl	0.080	ellipsoid	13 (13.7[21])	1.1 (1.1[21])
C_{10}mim Cl	0.160	ellipsoid	13 (13.8[21])[a]	1.4 (1.1[21])[a]
C_{10}mim Cl	0.200	ellipsoid	13 (13.6[21])	1.4 (1.2[21])
DTAB	0.020	ellipsoid	17	1.7
DTAB	0.040	ellipsoid	18[b]	1.4[b]
DTAB	0.080	ellipsoid	18[c]	1.5[c]
DTAB	0.160	ellipsoid	18	1.6
DTAB	0.200	ellipsoid	18	1.8
DTAF	0.020	ellipsoid	-	-
DTAF	0.040	ellipsoid	17	1.7
DTAF	0.080	ellipsoid	18	2.0
DTAF	0.160	ellipsoid	18	2.2
DTAF	0.200	ellipsoid	18	2.4

Table 5.4: Parameters fitted to SANS data using the Hayter-Penfold model for charged ellipsoid micelles. [a]Data recorded at 0.17 M. [b]At 0.05M and for a hard sphere model literature reports R_l = 19.8 Å, X = 1.2.[31] [c]At 0.1M literature reports R_l = 15 Å, X = 1.8.[32]

Compound	Concn / M	Shape	R_l / Å ± 2	X ± 0.2	N	z	$\beta = z/N$
C_{10}mim F	0.040	ellipsoid	12	2.1	27	4.2	0.16
C_{10}mim F	0.050	ellipsoid	12	2.1	27	2.6	0.10
C_{10}mim F	0.080	ellipsoid	13	1.5	35	4.5	0.13
C_{10}mim F	0.160	ellipsoid	14	1.5	43	2.6	0.06
C_{10}mim F	0.200	ellipsoid	14	1.5	45	1.7	0.04

Table 5.5: Parameters fitted to SANS data using the HSS(Q) model for charged ellipsoid micelles.

On the other hand DDAB and DDAF both show strong Q^{-2} scattering, described by a model bilayer micellar disks (thickness ~ 22 Å, radius >900 Å) (Figure 5.7, Table 5.6 and 5.7).

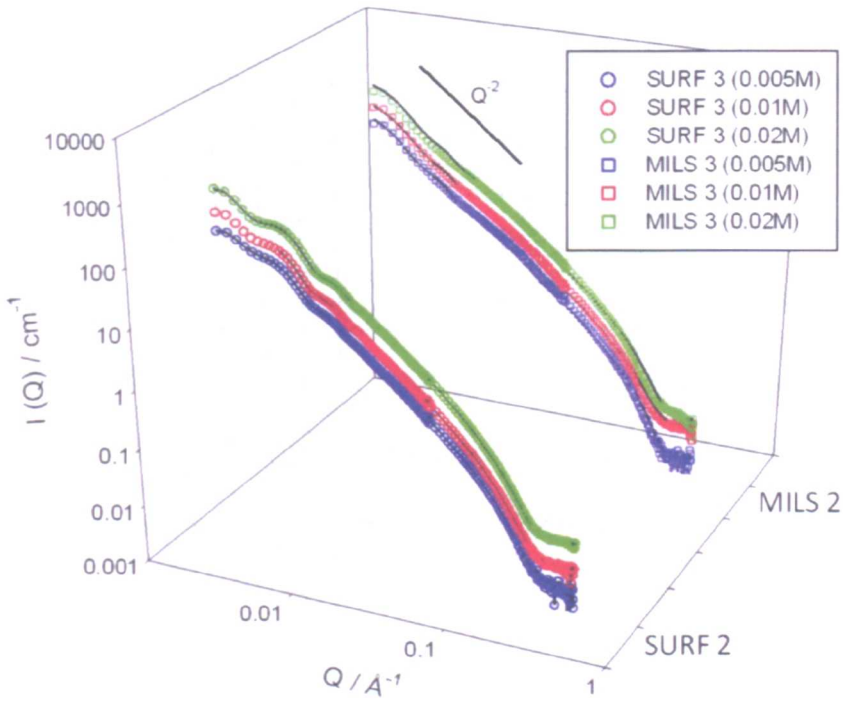

Fig. 7: SANS profiles for DDAB and DDAF. Lines through the data are fits using the models listed above with parameters listed in Tables 5.6 and 5.7.

Compound	Concn / M	Shape	R / Å ± 2	L / Å ± 5
DDAF	0.005	disk	22	953
DDAF	0.010	disk	22	867
DDAF	0.020	disk	21	845

Table 5.6: Parameters fitted to SANS data using the model for rods.

Compound	Concn / M	Shape	e / Å ± 1	d ± 5	η	N
DDAB	0.005	bilayers	24	1096	0.59	3
DDAB	0.010	bilayers	23	1068	0.59	3
DDAB	0.020	bilayers	24	1036	0.59	3

Table 5.7: Parameters fitted to SANS data using the model multilamellar vesicles.

An interesting feature of the profiles for C_{10}mim F and DTAF is the lack any obvious structure factor, (S(Q)), indicating only weak electrostatic interactions. One possible reason for this could be association of metal halide anions around micelles (or even into the micellar core), thereby compressing the electrical double layer as compared to the regular surfactant micelles

5.2.5 Surface tension

In the absence of an applied field, the MILSs are more effective surfactants than their parent surfactants showing greater surface tension γ reduction of water for the same concentration (Figure 5.8, Table 5.8). On placing a magnet (0.4 T) in close proximity (1 mm) to aqueous solutions of the MILS γ reduces even further. The paramagnetic C_{10}mim F and DTAF are bi-functional, being both intrinsically surface active and also showing a magnetically-induced reduction in γ on the order of –4 mN m^{-1} (possibly due to unpaired electrons aligning with the external field and anion partitioning at the interface). The observed magnetic effect decreases with decreasing MILS concentration. On the contrary, for the inert surfactants γ increased by about +2 mN m^{-1} in the magnetic field. This is a surprising result, however, recent reports[33] have shown that strong magnets can indeed affect γ for liquid water due to development of hydrogen-bonding and a weakening of van der Waals forces. For pure water saturated with O_2 large effects on contact angle at the solid-liquid interface have been seen in magnetic fields (6 T).[34]

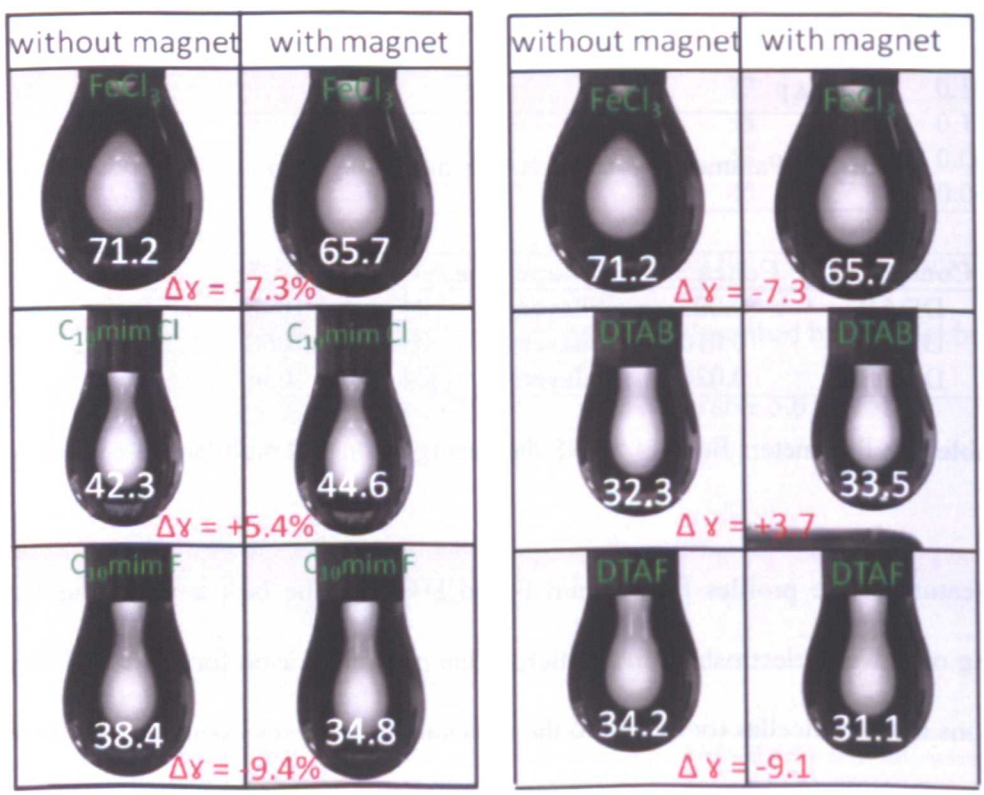

Figure 5.8: Pendant drop profiles of (**left**) C_{10}mim Cl and C_{10}mim F, and (**right**) DTAB and DTAF with and without a magnet. Units are mN m^{-1}.

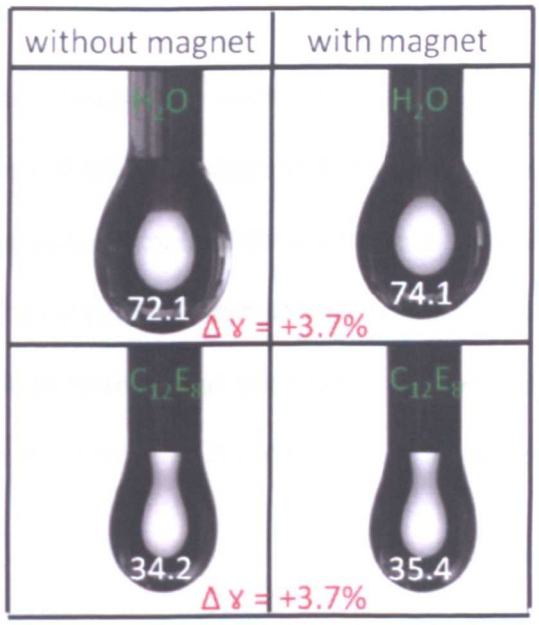

Figure 5.9: Pendant drop profiles of water and non-ionic surfactant $C_{12}E_8$ (0.2 M) with and without a magnet. Units are mN m^{-1}.

Compound	Concn / M	$\gamma_{no\ mag}$ / (mN m^{-1})	γ_{mag} / (mN m^{-1})	$\Delta\gamma$
H_2O	-	72.1 (72.0[19])	74.1	+2.0
C_{10}mim Cl	0.20	42.3	44.6	+2.3
DTAB	0.20	32.3	33.5	+1.2
$C_{12}E_8$	0.20	34.2	35.4	+1.2
$FeCl_3$	0.05	71.7	71.4	-0.3
$FeCl_3$	0.08	71.8	70.2	-1.6
$FeCl_3$	0.16	71.2	67.3	-3.9
$FeCl_3$	0.20	71.2	65.7	-5.5
C_{10}mim F	0.05	40.6	40.5	-0.1
C_{10}mim F	0.08	40.4	39.0	-1.4
C_{10}mim F	0.16	38.9	36.5	-2.4
C_{10}mim F	0.20	38.4	34.8	-3.6
DTAF	0.05	37.9	37.3	-0.6
DTAF	0.08	37.4	36.7	-0.7
DTAF	0.16	35.7	34.5	-1.2
DTAF	0.20	34.2	31.1	-3.1

Table 5.8: Surface tension data from pendant drop experiments at 25 °C, with and without a magnet.

5.2.6 Applications

Figure 5.10 shows an application of C_{10}mim F (20 wt% in H_2O) in biphasic aqueous surfactant solution-organic solvent (dodecane) systems. Using a vertically applied magnet it is possible to perturb the equilibrium, overcoming both gravity and the water-oil interfacial tension, "levitating" the lower polar magnetic liquid and pulling it through the upper organic solvent. This phase inversion is energetically unfavorable since it both increases water-oil interfacial area, and inverts the liquid phases of different density, but occurs due to lowering of the system magnetic energy.

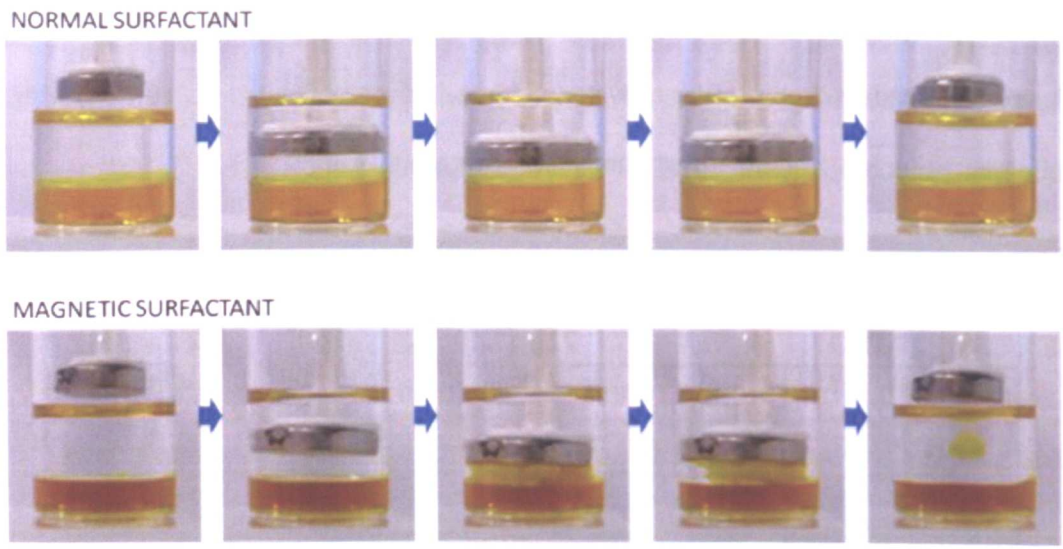

Figure 5.10: Effect of magnetic field through dodecane on 20 wt% aqueous surfactant solutions. Above inert C_{10}mim Cl, below magnetically active C_{10}mim F. The C_{10}mim Cl solution was dyed with trace methyl orange (to aid the eye).

5.3 Conclusions

Materials combining magneto-responsivity with surface activity offer tantalizing possibilities in potential applications. With the exception of photosensitive surfactants[35], in order to alter properties of normal inert surfactant solutions such as cmc, surface tension, aggregate size and shape, or to control phase separation/recovery it is necessary to perturb the composition, such as with electrolyte or pH, or external thermodynamic variables temperature and/or pressure. Disadvantages of these control methods are irreversible

changes in system composition, or significant energy inputs. Now, with the magnetic ionic liquid surfactants (MILSs) reported it is possible to control physico-chemical properties non-invasively and reversibly, simply by switching "on" or "off" the magnetic field. Further to this the potential for controlled orientation of colloidal dispersions, resulting in magnetophoretic effects may also have application, such as in display technology. These MILSs also have the potential to combine partitioning and enrichment of catalysts induced by internal magnetic field effects (due to faster proton transfer) in photochemical reactions[36], or allow clean recovery of expensive products and facile recyclability of the "solvent medium".

Part two

5.4 Introduction

In part two new *f*-block metal based compounds are presented and also uses SQUID magnetometry is employed to provide a detailed investigation into the magnetic properties of these compounds. The use of *f*-block metals is important not just because they have the highest known effective magnetic moments but also because of their interesting magnetic phase behaviour, exhibiting ferro- or antiferromagnetism as well as paramagnetism. Lanthanide metals also have many uses as catalysts[37], superconductors[38], active ions in luminescent materials used in optoelectronics and ceramics[39], and as surfactant counterions they have been used in spectroscopic studies because of their well defined luminescence[40].

It is important to note that the structures of the magnetic materials presented in part two include no covalent bonds between spin sites. As such, they may be considered as a novel and interesting variant of molecular magnets, whereby the organic surfactant moiety provides some control over magnetic behaviour through partitioning of the metal ions.[41] As the organic moiety is also surface active it is interesting to investigate whether self-aggregation might lead to further control of magnetic behaviour.

It has been shown that magnetic water-in-oil microemulsions can be made using magnetic anionic surfactants (based on transition and lanthanide metals). These magneto-responsive microemulsions exhibit superparamagnetism and unprecedented magnetic susceptibilities owing to a lack of bulk anisotropy due to the partitioning of surfactant molecules at the water/oil interface (Chapter 7). This chapter furthers this work by investigating the susceptibility of micellar solutions in order to elucidate whether the formation of micelles at the critical micelle concentration (cmc) leads to ordering which significantly increases any observable magnetic susceptibility.

5.5 Experimental

5.5.1 Materials and Synthesis

Gadolinium chloride hexahydrate (99%), holmium chloride hexahydrate (99.9%) and cerium chloride heptahydrate (99.9%), were purchased from Sigma Aldrich and used without further purification. All compounds were synthesized as mentioned in Part One, whereby 1 eq. of metal trichloride was added to a

methanolic solution of 1 eq. of either DTAB or C_{10}mim Cl and stirred overnight at room temperature, then dehydrated *in vacuo* at 80 °C overnight.

5.5.2 Polarizing Light Microscopy (PLM), Electrical Conductivity Measurements, Surface Tensiometry and Small-angle neutron scattering (SANS) Carried out as detailed in Chapter 5, part one.

5.5.3 Magnetometry

Magnetic susceptibility data were collected for dried surfactant samples, placed in sealed polypropylene tubes and mounted inside a plastic drinking straw for measurements in a magnetometer equipped with a superconducting quantum interference device (SQUID, MPMS XL-5) and reciprocating sample option (RSO). After demagnetizing at 298 K, the samples were cooled in zero field to 5 K. The data were then collected in 500 Oe from 5 to 300 K at 2 K/min.

5.6 Results and Discussion

5.6.1 Characterization

The new magnetic surfactants (Figure 5.11) were readily synthesized by mixing an equivalent of lanthanide metal trihalide with the appropriate cationic surfactant.

Compound	Anion	Cation
DTAB	Br^-	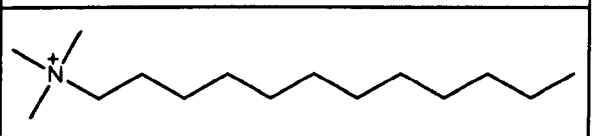
DTAG	$GdCl_3Br^-$	
DTAH	$HoCl_3Br^-$	
DTAC	$CeCl_3Br^-$	
C_{10}mim Cl	Cl^-	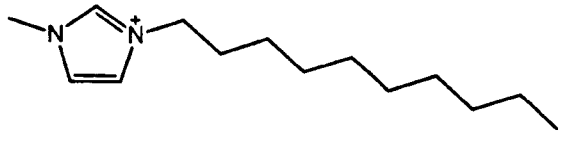
C_{10}mim G	$GdCl_4^-$	
C_{10}mim H	$HoCl_4^-$	
C_{10}mim C	$CeCl_4^-$	

Figure 5.11: Compounds studied (DTAB and [C_{10}mim]Cl are non-magnetic).

Polarizing light microscopy (PLM) textures (Figure 5.12) show that all the compounds exhibit some transition from fluid micellar to liquid crystalline phase. Mesophase formation was lost for the previously reported

Fe(III)-based surfactants (Figure 5.4)[42] but is thought to exist here due to the large hydration numbers (increased hydophilicity) of the metal counterions.

Again, electrical conductivity measurements of dilute aqueous solutions show that the critical micelle concentrations (cmcs, Table 5.1) are not greatly affected by the changes in anion alone. However, this may in part be explained by the increased dissociation constant, β; a result perhaps of partial coordination of the cation-anion pair.

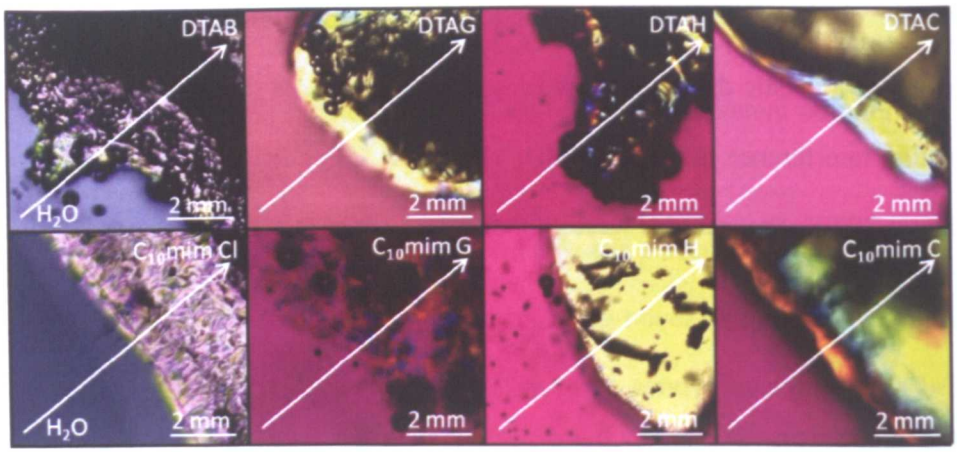

Figure 5.12: PLM textures showing mesophase formation of surfactants studied on addition of water at 25 °C.

Small-angle neutron scattering (SANS) shows unambiguously that these surfactants aggregate above their cmc. Data were collected (Figure 5.13, Table 5.9) for every compound except Gd-based surfactants owing to exceptionally high neutron absorbance. At 0.04 M the inert parent surfactant DTAB formed ellipsoidal aggregates of radius 18 Å and aspect ratio, $X = 1.4$, commensurate with the alkyl chain length and agreeing with literature[31]. On exchanging the counterion almost no change in shape or size was observed and importantly almost all structure factor, (SQ), which represents interparticle interactions between micelles, was lost. A similar result could be seen for the imidazolium based surfactants. However, the Ce- and Ho-based surfactants lead to some larger scale aggregates, indicated by an upturned profile at low Q, and were fitted using an ellipsoid model rather than that for spheres used for the chloride analogue.

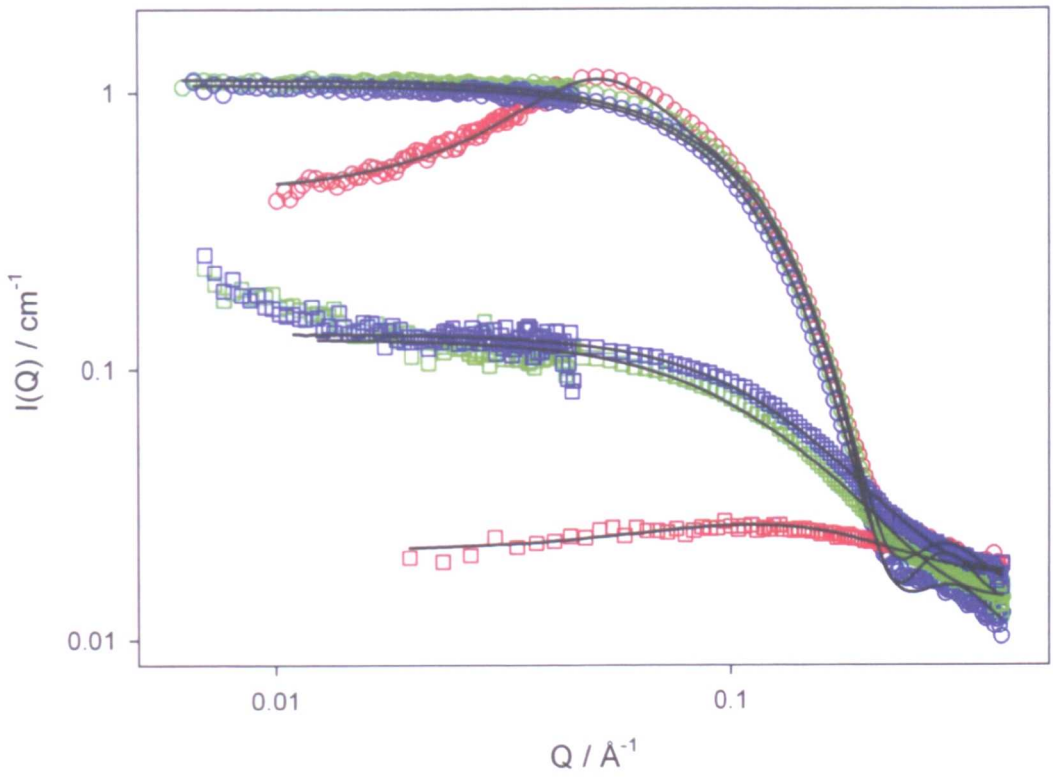

Figure 5.13 : SANS profiles for inert and magnetic surfactants. Lines through data are fits using parameters listed in Table 5.9. C10mimCl 0.04 M (□), C10mimCl 0.04 M (□), C10mimCl 0.04 M (□), DTAB 0.04 M (o),DTAC 0.04 M (o),DTAH 0.04 M (o).

Compound	Shape	R_1 / Å ± 1	X ± 0.2
DTAB	ellipsoid	18.0 (19.8)[31]	1.4 (1.2)[31]
DTAC	ellipsoid	18.0	1.3
DTAH	ellipsoid	17.4	1.6
C10mim Cl	ellipsoid	11.0 (10.0)[21, a]	1.0 (1.0)[21, a]
C10mim C	ellipsoid	10.1	3.3
C10mim H	ellipsoid	10.4	2.4

Table 5.9: Parameters fitted to SANS data using the Hayter-Penfold model for ellipsoid micelles with a hard sphere structure factor (HSSQ). Brackets indicate literature values. [a]Data recorded at 0.05 M.

5.6.2 Magnetic behaviour

All the compounds displayed simple paramagnetic behaviour at room temperature. DTAH had the highest $\chi_m T$ value of all the surfactants (10.15 emu K mol^{-1} Oe^{-1}) corresponding to an effective paramagnetic moment of 9.05 B.M. (Table 5.10), followed by C_{10}mimH (8.55 emu K mol^{-1} Oe^{-1}, 8.30 B.M.). These values are lower than the theoretical spin-only values (Ho^{3+} has the $^5I_8$ electronic ground state, with the predicted

effective magnetic moment, $g[J(J+1)]^{1/2}$ giving 10.61 B.M.). The same pattern is observed for Gd and Ce based surfactants with the respective with the tetraalkylammonium surfactants exhibiting effective magnetic moments above that of the analogous imidazolium surfactant. This is especially surprising as lanthanide metals possess 4f (inner) electrons that are effectively shielded from the influence of external forces by the overlying $5s^2$ and $5p^6$ shells. Therefore they have large spin-orbit couplings resulting in large effective magnetic moments, but only weak ligand field effects thus exhibiting magnetic properties little affected by their chemical surroundings. The result may be due to the DTAB analogues being less amorphous (due to molecular packing arguments) than the imidazolium based surfactants, therefore exhibiting longer range structural ordering, longer range interactions and stronger communication between metal ions. The difference in packing may also influence bulk anisotropy.

It is clear from Figure 5.14 that most of the compounds exhibit magnetic phase transitions. Firstly, for DTAH a reduction of effective magnetic moment ($\chi_m T$) is observed when temperature decreases resulting in a Curie temperature (T_c) at 5.1 K. Only weak ferromagnetic transitions are observed as seen by the positive Curie-Weiss values, θ_p = 4.09 K (Table 1). A Néel temperature, T_N, around 133 K occurs in crystalline Ho[43] but no such transition was observed within the studied range. C_{10}mim H exhibits much the same behaviour as DTAH, however a T_c was not observed above 5 K as indicated by a plot of $1/\chi_m$ as a function of temperature (Figure 5.15), which is linear. Unlike for DTAH, without any obvious magnetic transition, the calculated value of θ_p 2.78 K for C_{10}mimH gives an approximate upper bound on the possible ordering temperature. A full hysteresis of the solid sample at 2K (Figure 5.16) supports this conclusion as no hysteresis was observed. In addition, the curve can be distributed into two components, one having a magnetic moment of 4.6 B.M. and the other 2.7 B.M., both of which are too small to suggest a ferromagnetic state.

The gadolinium compounds showed no sign of a Néel temperature (T_N) (which occurs at 298.4 K in the pure metal[44]) and followed the Curie-Weiss law within the measured regime.

The magnetic behaviour of the Ce compounds was particularly interesting. A plot of $1/\chi_m$ *vs* T (Figure 5.17) suggests a phase transition at 12.2 K (T_N); understood to be the transition from antiferromagnetism to paramagnetism and similar to literature values for crystalline β-Ce.[45] In these compounds ordering is suppressed from the Curie-Weiss constant by a factor of ten, as might be expected for anisotropic systems. The

likelihood is that Ce compounds are antiferromagnetic at lower temperature and paramagnetic at higher temperatures.

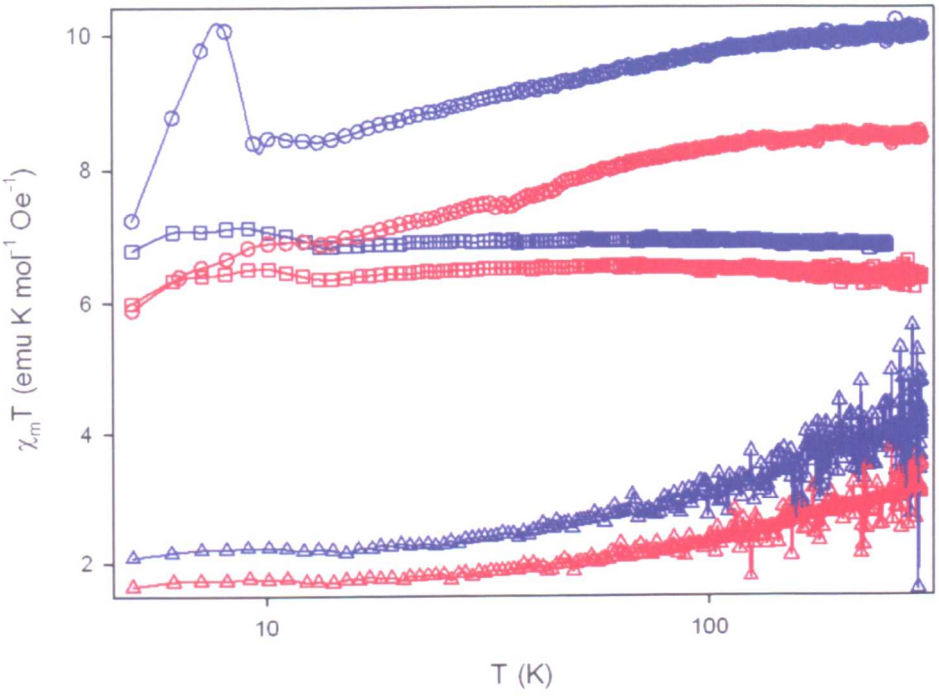

Figure 5.14: Magnetic susceptibility as a function of temperature. DTAH (○), C_{10}mim H (○), DTAG (□), C_{10}mim G (□), DTAC (x 10, Δ), C_{10}mim C (x 10, Δ).

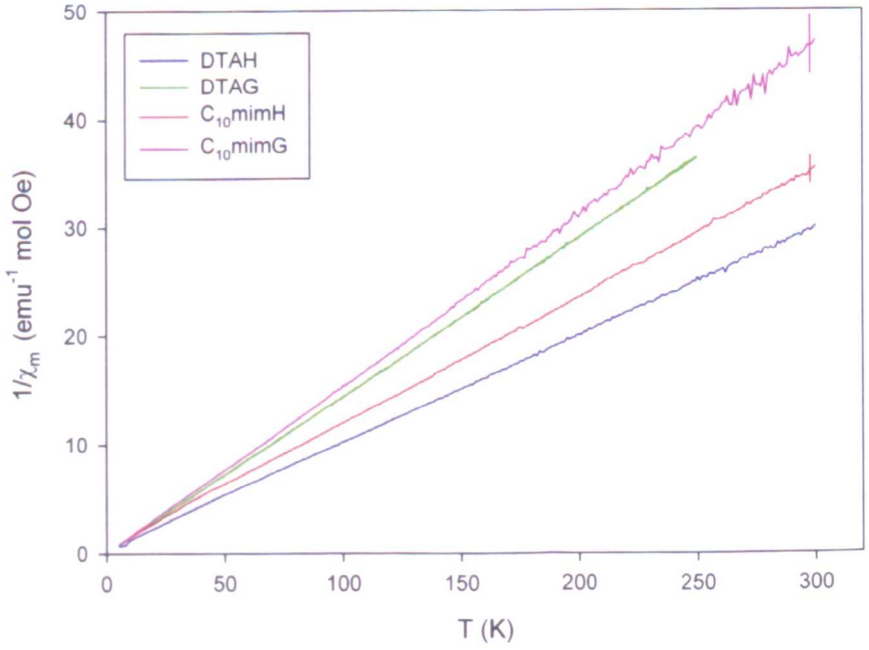

Figure 5.15: Temperature dependence of $1/\chi_m$ for Gd and Ho based compounds, measured under 0.50 kOe.

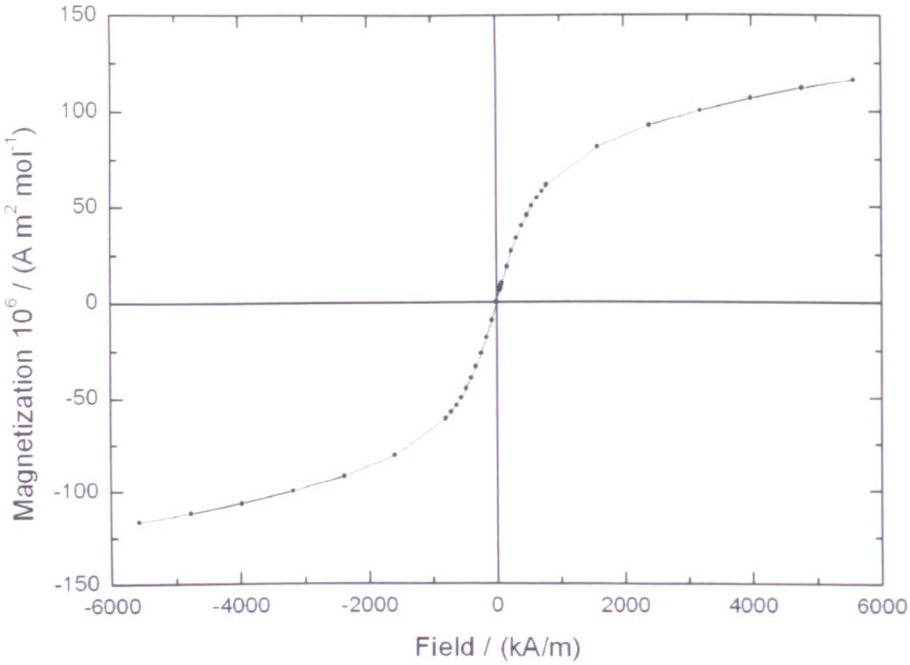

Figure 5.16: SQUID magnetometry data showing full hysteresis slope for C_{10}mimH at 2K.

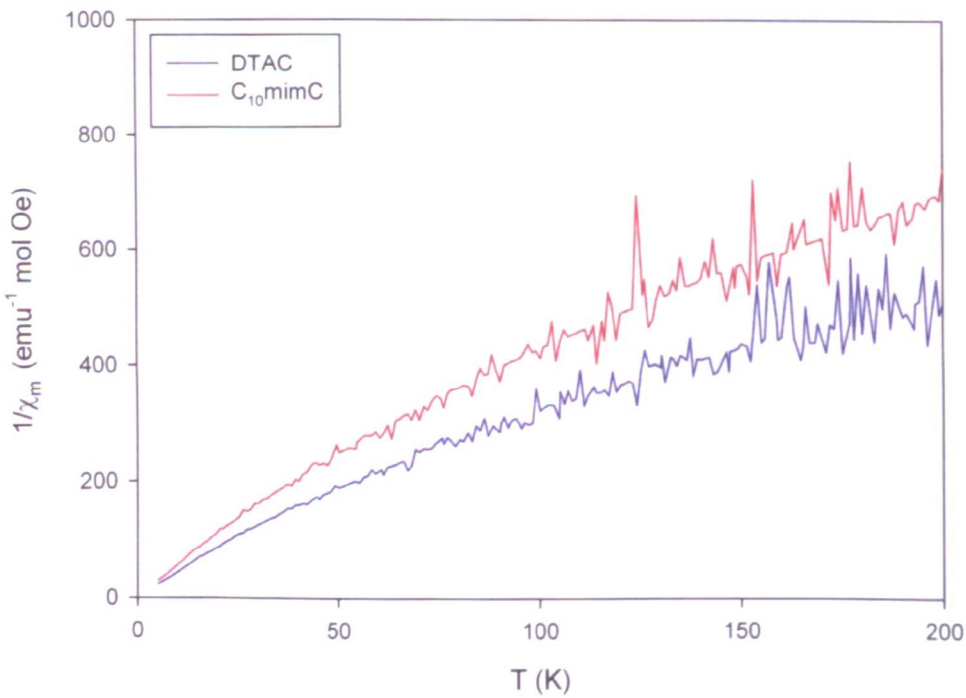

Figure 5.17: Temperature dependence of $1/\chi_m$ for Ce based compounds, measured under 0.50 kOe.

Compound	M_w / (g mol^{-1})	cmc / mM	β	$\chi_m T$/ (emu K mol^{-1} Oe^{-1})	μ_{eff}/ B.M.	θ_p/ K	T_c/ K	T_N/ K
DTAB	308.35	15.5	0.26	-	-	-	-	-
DTAH	579.34	11.6	0.76	10.15	9.05 (10.6[a])	4.09	5.1(85[c])	- (133[c])
DTAG	571.66	11.9	0.59	6.89	7.45*(7.94[a])	0.06	(293.4[b])	-
DTAC	554.53	10.9	0.82	0.43	1.86 (2.54[a])	-60	-	12.2
C10mim Cl	258.61	37.0	0.55	-	-	-	(85[c])	-
C10mim H	529.89	31.3	0.74	8.55	8.30 (10.6[a])	2.78	20	(133[c])
C10mim G	522.21	30.0	0.82	6.41	7.19 (7.94[a])	-0.18	(293.4[b])	-
C10mim C	505.08	27.6	0.75	0.32	1.61 (2.54[a])	-72	-	12.2 (12.5[d])

Table 5.10: Selected physical properties of surfactants. *At 250 K. [a]Brackets indicate spin-only/calculated values[46]. [b]Expected values for Gd[47], [c]Expected values for Ho[48], [d]Expected values for Ce[45].

5.6.3 Surface tension

As in part one, pendant drop measurements were made for each surfactant (Figure 5.18). In the absence of an applied field, the magnetic surfactants behave like conventional inert surfactants and lower the surface tension (γ) at the air-water interface. In fact they show more effective surfactant behaviour than their parent surfactant, showing greater γ reduction of water for the same concentration (Figure 5.18). On placing a magnet (0.4 T) in close proximity (~1 mm) to aqueous solutions of the Gd and Ho based surfactants γ reduces even further. The magnetic surfactants may therefore be considered bi-functional, being both intrinsically surface active and also showing a magnetically induced reduction in γ (possibly due to unpaired electrons aligning with the external field and anion partitioning at the interface). The effect is often quite remarkable. For example, the γ of C_{10}mim H solutions reduces by a further 12 % in a magnetic field.

It is important to note that for the inert surfactants γ increased by about 1 mN m^{-1} in the magnetic field. This is perhaps not so unusual as recent reports[33a, b] have shown that strong magnets can indeed affect γ for liquid water due to development of hydrogen-bonding and a weakening of van der Waals forces. In fact it actually implies that the real magnetic surface reduction is around 1 mN m^{-1} greater than observed for Gd and Ho based surfactants and explains the slight increase observed for the Ce based surfactants.

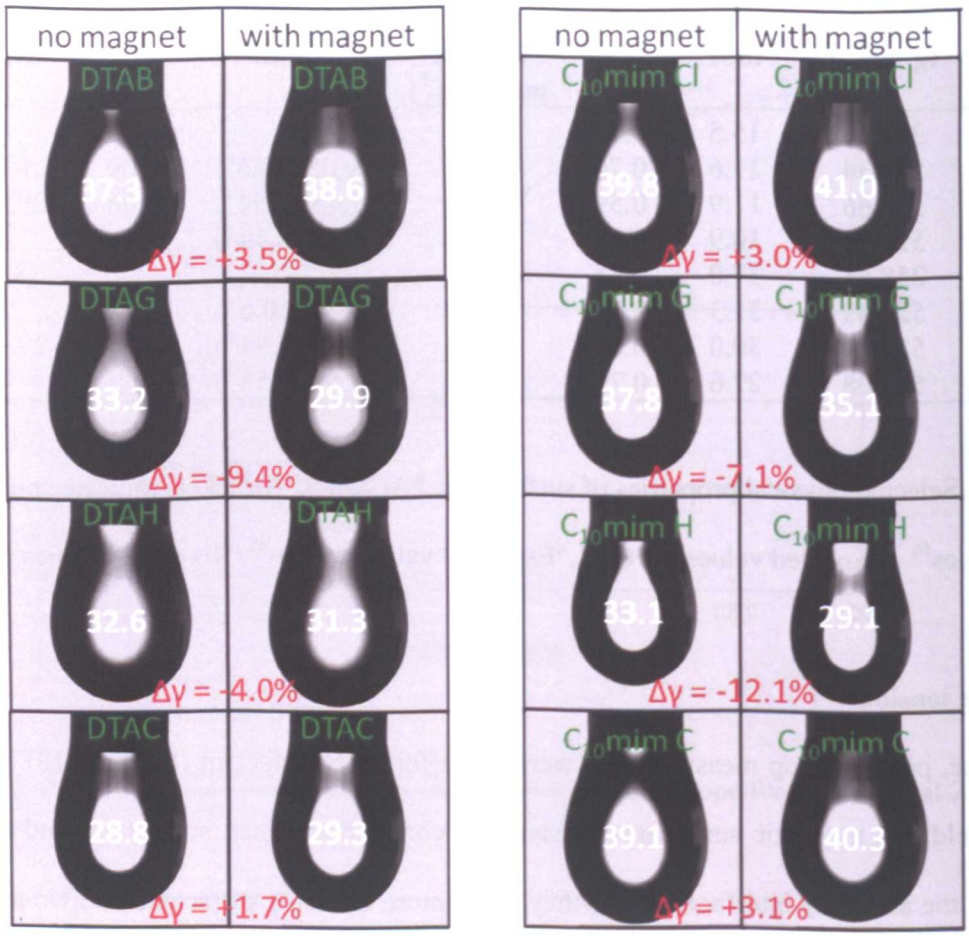

Figure 5.18: Determining pendant drop profiles of magnetic surfactants (0.10 M) with and without a magnet. Units of surface tension are mN m^{-1}.

5.6.4 Effects of Micellar structure on Magnetic Behaviour

It has recently been demonstrated[49] that the formation of microemulsions by magnetic anionic surfactants leads to a large increase in magnetic susceptibility (as compared to solid surfactant samples) and a change in magnetic behaviour (paramagnetic in the solid to superparamagnetic in solution) attributed to a loss of bulk anisotropy, with all the surfactant molecules partitioned at the oil/water interface (Chapter 7). It was therefore considered of interest to ascertain how the formation and structuring of micelles might affect magnetic susceptibility and phase behaviour. In order to test this magnetic susceptibility was calculated (by VSM) as a function of concentration for C_{10}mimH (Figure 5.20). This may be considered analogous to conductivity *vs.* concentration plots where a change in gradient may be observed at the cmc[50].

The corrected magnetization graphs for all concentrations show straight lines with no sign of hysteresis (Figure 5.19). The measured value for the volume susceptibility of water, χ_{water}, is $(-6.78 \pm 1.36)\cdot10^{-6}$ and differs from the literature value of $-9.04\cdot10^{-6}$ by 25%[51]. The relative standard deviation increases with decreasing concentration of C_{10}mim H below 20mM, up to 33.4% for sample for the concentration of 2.5 mM, and no trend can be observed in the plot (Figure 5.20, Table 5.11).

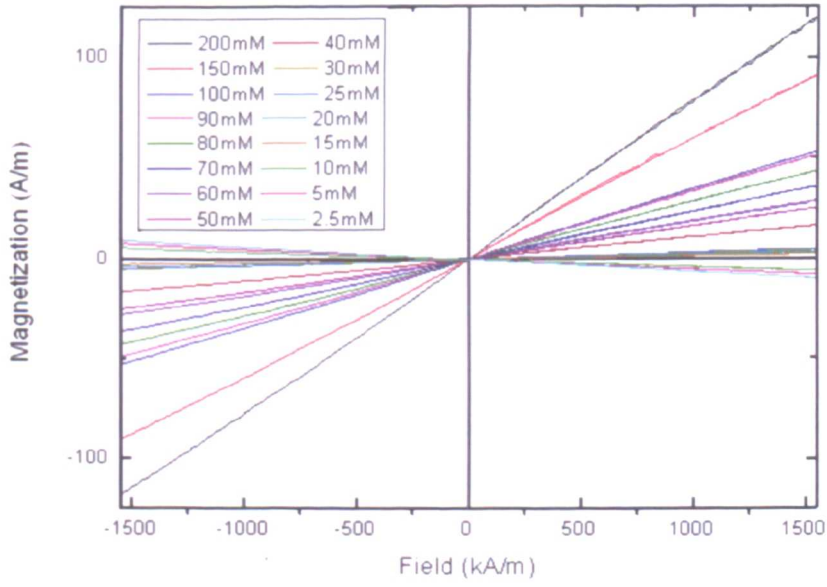

Figure 5.19. VSM curves of the solutions made from C_{10}mim Ho with different concentrations.

C / mM	μ_{eff} / B. M.	$\Delta\mu_{eff}$ / B. M.	$\Delta\mu_{eff}$ / %
200	8.86	0.09	1.04
150	9.09	0.07	0.75
100	8.97	0.08	0.84
90	9.09	0.10	1.12
80	8.96	0.25	2.78
70	9.17	0.40	4.41
60	9.03	0.32	3.52
50	9.45	0.29	3.04
40	9.19	0.57	6.21
30	9.29	0.18	1.98
25	9.16	0.35	3.77
20	9.66	0.44	4.52
15	9.38	1.36	14.5
10	8.50	0.84	9.83
5	9.11	1.87	20,6
2.5	11.9	3.96	33.4

Table 5.11: Calculated mean values for the effective magnetic moment and standard deviation.

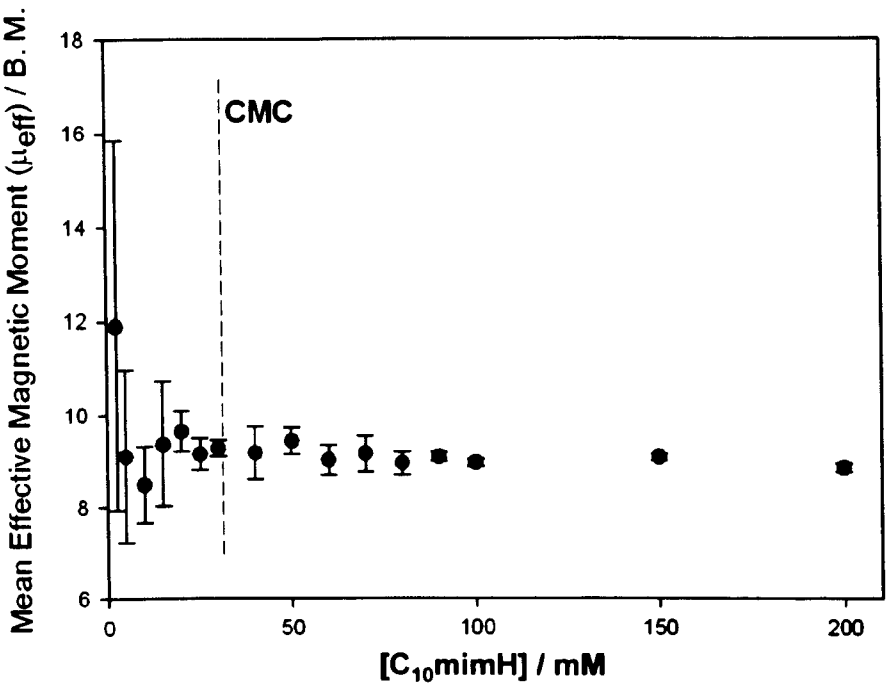

Figure 5.20: The relationship between the mean effective magnetic moment and the concentration of the C_{10}mimH. Red dotted line represents cmc predicted by conductivity.

The most probable reason that no transition was observable is that magnetic counterions in these systems are hghly dissociated (Table 5.10) with as few as ~20% of the magnetic counterions "structured" around the micelles. This is in complete contrast to the microemulsions (inverse micelles) recently studied[49], where, although dissociated, the counterions are partitioned into the small volume of the aqueous droplet and are in close proximity to one another.

5.7 Conclusions

In conclusion part two introduces new magnetic surfactants that have greater magnetic responsivity than previously reported magnetic surfactants.[42] It also looks in detail at their magnetic phase behaviour, which indicates that these systems may be considered as novel molecular magnets,[41] with interspin coupling tunable through careful consideration of molecular architecture, selection of metal ion and now potentially aggregation.

At room temperature, aggregation (micellization) appears to have no effect on molar magnetic susceptibility for the cationic surfactants systems studied here and it was not possible to determine a critical micelle con-

centration through magnetometry. However, a wider range of magneto-surfactants would be needed to be studied to confirm this behaviour more generally. What the study does reveal is that even very dilute systems exhibit magnetic susceptibility which should be controllable given a large enough applied magnetic field.

Finally, magnetic effects on surface tension combined with catalytic and luminescent properties of lanthanide metals suggest diverse potential applications.[37, 40]

5.8 References

1. (a) I. D. Robb, *Specialist Surfactants*. Blackie Academic and Professional: London, 1997; (b) K. Holmberg, *Novel Surfactants*. Marcel Dekker: New York, 1998.
2. K. Meguro; M. Ueno; K. Esumi, *Nonionic Surfactants: Physical Chemistry*. Marcel Dekker: New York, 1987.
3. J. Zhang; Y. Zhao; J. Li; G. Yang; B. Han; Z. Wu; Z. Li, *Soft Matter*, 2010, *6*, 6200.
4. J. Eastoe; A. Vesperinas, *Soft Matter*, 2005, *1*, 338.
5. (a) M. Lipsztajn; R. A. Osteryoung, *Inorg. Chem.*, 1985, *24*, 716; (b) S. A. Bolkan; J. T. Yoke, *J. Chem. Eng. Data*, 1986, *31*, 194.
6. R. E. Del Sesto; T. M. McCleskey; A. K. Burrell; G. A. Baker; J. D. Thompson; B. L. Scott; J. S. Wilkes; P. Williams, *Chem. Commun.*, 2008, 447.
7. S. Hayashi; H. Hamaguchi, *Chem. Lett.*, 2004, *33*, 1590
8. (a) Y. Yoshida; A. Otsuka; G. Saito; S. Natsume; E. Nishibori; M. Takata; M. Sakata; M. Takahashi; T. Yoko, *Bull. Chem. Soc. Jpn* 2005, *78*, 1921 ; (b) M. Li; S. L. De Rooy; D. K. Bwambok; B. El-Zahab; J. F. DiTusa; I. M. Warner, *Chem. Commun.*, 2009, 6922.
9. A. Kaiser; T. Liu; W. Richtering; A. M. Schmidt, *Langmuir*, 2009, *25*, 7335.
10. (a) H. L. Friedman, *J. Am. Chem. Soc.*, 1952, *74*, 5; (b) Y. Yoshida; G. Saito, *J. Mater. Chem.*, 2006, *16*, 1254.
11. M. S. Sitze; E. R. Schreiter; E. V. Patterson; R. G. Freeman, *Inorg. Chem.*, 2001, *40*, 2298.
12. M. Dobbelin; V. Jovanovski; I. Llarena; L. J. Claros Marfil; G. Cabanero; J. Rodriguez; D. Mecerreyes, *Polym. Chem.*, 2011, *2*, 1275.
13. U. Domańska; E. Bogel-Łukasik; R. Bogel-Łukasik, *Chem. Eur. J.*, 2003, *9*, 3033.
14. R. K. Heenan *Fish Data Analysis Program*; Rutherford Appleton Laboratory pp RAL, 1989.
15. (a) J. B. Hayter; J. Penfold, *Molec. Phys.*, 1981, *42*, 109; (b) J.-P. Hansen; J. B. Hayter, *Molec. Phys.*, 1982, *46*, 651; (c) J. B. Hayter; J. Penfold, *Colloid Polym. Sci.*, 1983, *261*, 1022.
16. N. W. Ashcroft; J. Lekner, *Phys. Rev.* 1966, *145*, 83.

17. J. Eastoe; G. Fragneto; B. H. Robinson; T. F. Towey; R. K. Heenan; F. J. Leng, *J. Chem. Soc., Faraday Trans.*, 1992, *88*, 461.

18. (a) J. Berghausen; J. Zipfel; P. Lindner; W. Richtering, *J. Phys. Chem. B*, 2001, *105*, 11081; (b) F. Nallet; R. Laversanne; D. Roux, *J. Phys. II*, 1993, *3*, 487.

19. N. R. Pallas; Y. Harrison, *Colloids Surf.*, 1990, *43*, 169.

20. B. M. Krieger; H. Y. Lee; T. J. Emge; J. F. Wishart; J. E. W. Castner, *Phys. Chem. Chem. Phys.*, 2010, *12*, 8919.

21. I. Goodchild; L. Collier; S. L. Millar; I. Prokes; J. C. D. Lord; C. P. Butts; J. Bowers; J. R. P. Webster; R. K. Heenan, *J. Coll. Int. Sci.*, 2007, *307*, 455.

22. M. del Mar Graciani; M. Muñoz; A. Rodríguez; M. L. Moyá, *Langmuir*, 2005, *21*, 3303.

23. J. F. A. Soltero; F. Bautista; E. Pecina; J. E. Puig; O. Manero; Z. Proverbio; P. C. Schulz, *Colloid Polym. Sci.*, 2000, *278*, 37.

24. A. P. Abbott; G. Capper; D. L. Davies; R. Rasheed, *Inorg. Chem.*, 2004, *43*, 3447.

25. D. Moon; J. Kim; M. S. Lah, *Bull. Korean. Chem. Soc.*, 2006, *27*, 1597.

26. M. A. Semary; M. F. Mostafa; M. A. Ahmed, *Solid State Commun.*, 1978, *25*, 443.

27. S. H. Lee; S. H. Ha; S. S. Ha; H. B. Jin; C. Y. You; Y. M. Koo, *J. App. Phys.*, 2007, *101*, 09J102.

28. S. Lee; S. Ha; C. Y. You; Y.-M. Koo, *Korean J. Chem. Eng.*, 2007, *24*, 436.

29. K. M. McGrath, *Langmuir*, 1995, *11*, 1835.

30. E. F. Marques; O. Regev; A. Khan; M. da Graça Miguel; B. Lindman, *J. Phys. Chem. B*, 1999, *103*, 8353.

31. P. C. Griffiths; A. Paul; Z. Khayat; R. K. Heenan; R. Ranganathan; I. Grillo, *Soft Matter* 2005, *1* (2), 152.

32. R. K. Mahajan; K. K. Vohra; V. K. Aswal, *Colloids Surf. A*, 2008, *326*, 48.

33. (a) R. Cai; H. Yang; J. He; W. Zhu, *J. Molec. Struc.*, 2009, *938*, 15; (b) L. Holysz; A. Szczes; E. Chibowski, *J. Coll. Int. Sci.*, 2007, *316*, 996; (c) H. Inaba; T. Saitou; K. Tozaki; H. Hayashi, *Effect of the magnetic field on the melting transition of H2O and D2O measured by a high resolution and supersensitive differential scanning calorimeter*. AIP: 2004, 96, 6127.

34. (a) S. Ozeki; I. Otsuka, *J. Phys. Chem. B*, 2006, *110*, 20067; (b) I. Otsuka; S. Ozeki, *J. Phys. Chem. B*, 2006, *110*, 1509.

35. R. F. Tabor; R. J. Oakley; J. Eastoe; C. F. J. Faul; I. Grillo; R. K. Heenan, *Soft Matter*, 2009, *5*, 78.

36. Y. Sakaguchi; H. Hayashi, *Chem. Phys.*, 1992, *162*, 119.

37. B. Marciniec, *Hydrosilylation: A Comprehensive Review on Recent Advances*, Springer: New York, 2009.

38. C. H. Booth; E. D. Bauer; J. N. Mitchell, *IOP Conference Series: Materials Science and Engineering* 2010, *9*, 012087.

39. S. Solomon, *Ceramics Int.*, 2012, *38*, 599.

40. A. Beeby; I. M. Clarkson; J. Eastoe; S. Faulkner; B. Warne, *Langmuir*, 1997, *13*, 5816.

41. S. J. Blundell; F. L. Pratt, *J. Phys. Conden. Matter.*, 2004, *16*, R771.

42. P. Brown; A. Bushmelev; C. P. Butts; J. Cheng; J. Eastoe; I. Grillo; R. K. Heenan; A. M. Schmidt, *Angew. Chem. Int. Ed.*, 2012, 2414.

43. D. L. Strandburg; S. Legvold; F. H. Spedding, *Phys. Rev.*, 1962, *127*, 2046.

44. *Handbook of Magnetic Materials*, Elsevier: Amsterdam, 2012.

45. P. Burgardt; K. A. Gschneidner, Jr.; D. C. Koskenmaki; D. K. Finnemore; J. O. Moorman; S. Legvold; C. Stassis; T. A. Vyrostek, *Phys. Rev. B*, 1976, *14*, 2995.

46. J. A. Peters; J. Huskens; D. J. Raber, *Prog. Nucl. Magn. Reson. Spectrosc.*, 1996, *28*, 283.

47. H. E. Nigh; S. Legvold; F. H. Spedding, *Phys. Rev.*, 1963, *132*, 1092.

48. C. Sutter; D. Labergerie; A. Remhof; H. Zabel; C. Detlefs; G. Grübel, *Europhys. Lett.*, 2001, *53*, 257.

49. P. Brown; C. P. Butts; J. Eastoe; S. Glatzel; I. Grillo; S. H. Hall; S. Rogers; K. Trickett, *Soft Matter* 2012, DOI: 10.1039/C2SM26827B.

50. J. Rodríguez; A. González-Pérez; J. L. Del Castillo; J. Czapkiewicz, *J. Coll. Int. Sci.*, 2002, *250*, 438.

51. G. P. Arrighini; M. Maestro; R. Moccia, *J. Chem. Phys.*, 1968, *49*, 882.

Chapter 6

Magnetic Emulsions and Microemulsions

This chapter is split into two parts. In Part One magnetically-responsive emulsions are investigated with special attention being paid to their potential applications. In Part Two magnetically-responsive microemulsions are characterized and their phase and structural behaviour investigated.

Part One

6.0 Introduction

Emulsions are mixtures of two or more immiscible fluids, stabilised by interfacial adsorption of surfactants or particles. As such emulsions are essential components in multifarious processes and products, such as foods, pharmaceutical and agrochemical formulations, paints, inks, lubricants, oils and oil recovery. Stability and structure of responsive colloids and emulsions can be controlled by changes in composition, pH, as well as by external stimuli temperature, pressure and light.

To-date magneto-responsive emulsions (MREs) have only been realized with Pickering emulsions, stabilized by pre-synthesized magnetic nanoparticles[1], and this limits scale up applications. Here it is shown that MREs can be readily generated from water and oil mixtures using surfactants only: the key is to employ magneto-surfactants (MagSurfs, Figure 6.1)[2]. This chapter investigates easy to formulate magnetically-responsive emulsions (MREs), readily generated from water and oil mixtures and stabilized by magnetic surfactants.

Owing to adsorption and aggregation properties of surfactants these MagSurfs allow control of physico-chemical properties non-invasively and reversibly, by simple use of external fields[2], opening up new possibilities for control over interfaces, dispersions, colloids and nanoparticles. The field effects seen on these responsive emulsions suggest applications from environmental cleanup, water treatment, separation and enhanced oil recovery[3], through to emulsion-templating[4], catalysis[5], microfluidics, nanomedicine and targeted drug delivery[6]. In addition, nanoparticle-free magnetic foams, aerosols, gels and microemulsions are accessible for applications in mineral separation by magnetic froth floatation[7], or magnetic drug delivery[8]. Importantly, the MagSurfs are readily recovered, beneficial in environmental remediation and clean-up.

6.1 Experimental

6.1.1 MagSurf Synthesis

Dodecyltrimethylammonium bromide (99%, DTAB), iron (III) trichloride and gadolinium (III) chloride hexahydrate were purchased from Sigma Aldrich and used without further purification. *n*-Dodecane (<99%)

was purchased from Fluka and purified using fuming sulfuric acid to reach surface chemical purity. Dodecyltrimethylammonium trichloro-monobromoferrate (DTAF) was synthesized according to the procedure described in Chapter 5, by mixing equimolar amounts of DTAB with iron trichloride in methanol and stirring overnight at room temperature. The solvent was then removed and the product dried at reduced pressure at 80 °C overnight to yield a viscous brown liquid. Dodecyltrimethylammonium trichloromonobromogadolinate DTAG) was synthesized using a similar procedure, yielding a white solid. MagSurfs were characterized by UV-Vis spectroscopy and elemental analysis.

6.1.2 Elemental Analysis,

Experimental and theoretical (brackets) as % wt. DTAF: C 38.29 (38.31), H 7.22 (7.23), N 2.98 (2.97); DTAG: C 31.45 (31.51), H 6.39 (5.95), N 2.73 (2.45).

6.1.3 UV- Visible Spectroscopy

UV-Vis absorption spectra of 0.10 M MagSurf acetonitrile solutions were recorded on a Nicolet Eco 300 machine (500 – 900 nm). The spectrum for DTAF shows three bands characteristic of the $[FeCl_3Br]^-$ ion, similar to those for the [FeBr4]$^-$ ion, in agreement with Chapter 5, and literature[2, 9]. There is no absorption in the UV-Vis range for $GdCl_3$ or the $[GdCl_3Br]^-$ ion.

6.1.4 Dodecane Purification

n-Dodecane (Fluka >99%), is known to contain surface-active impurities[10]. Prior to making emulsions, dodecane was purified by washing with fuming sulfuric acid, then neutralising with 10 wt% sodium bicarbonate (aq.). Further washing was done with pure water and the dodecane was dried with calcium chloride. The dodecane was then fractioned under reduced pressure with the middle fraction of the distillate collected for experiments[11]. The cleaned dodecane was assessed for surface chemical purity by interfacial tension $\gamma_{o/w}$ measurements as a function of surface age (protocol outlined below): good agreement of $\gamma_{o/w}$ compared with literature[10] was found.

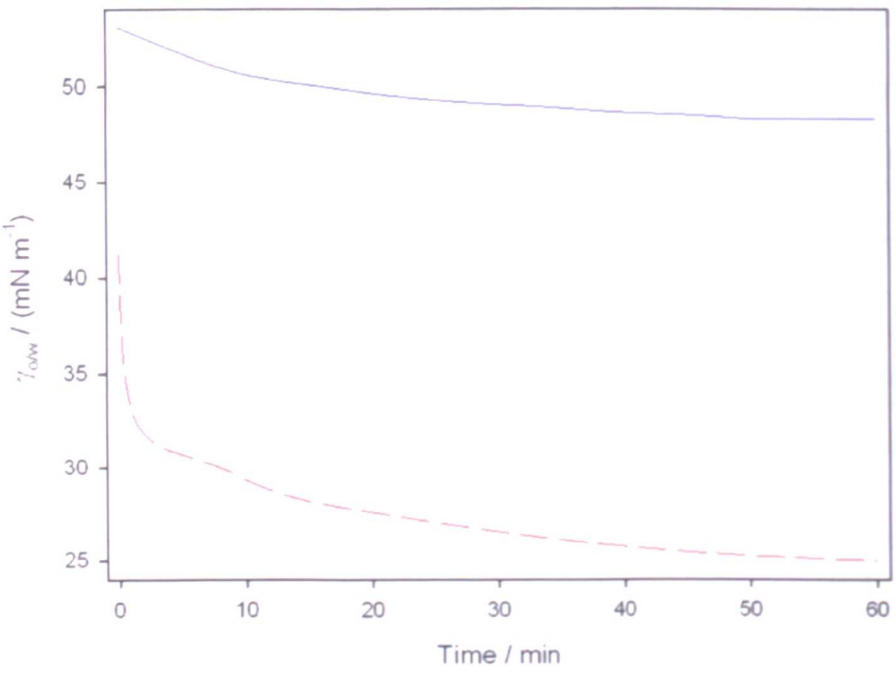

Figure 6.1: Interfacial tensions as a function of surface age determined by drop shape analysis (see below) for dodecane-water interfaces at 25 °C: red-dashed lower curve, as received dodecane; blue upper curve purified dodecane.

To assess the purity of dodecane, interfacial tensions between pure water and either purified or "as purchased" dodecane were performed at 25 ± 1 °C, using a Krüss Drop Shape Analysis DSA1 apparatus. A drop of water was formed at the tip of the capillary, then submerged in a couvette containing dodecane. Measurements were acquired every 5 minutes for 60 minutes using the automatic fitting function on the DSA1 software.

6.1.5 Electrical Conductivity Measurements

Electrical conductivities and critical micelle concentrations (cmcs) were determined as normal, from the break points between the high (low concentration) and lower branches of behaviour (see Chapter 3). Surfactant ionic dissociation constants (β), were estimated using the ratio of the slopes method.[12]

6.1.6 Surface Tensiometry Method

Surface tensions between aqueous surfactant solutions and air were performed at 25 ± 1 °C (see Chapter 5 and Figure 6.4). Measurements of MagSurf aqueous solutions at 0.20 M were taken on the same drop with and without a magnet: NdFeB (N42, 20 mm x 10 mm magnetic field density of 0.44 T on the surface and a gradient of about 36 mT mm^{-2}) and was held in position at an approximate distance of 1 mm from the bottom of the drop surface.

6.1.7 Emulsion preparation and characterization.

Emulsions were prepared with surface chemically pure n-dodecane, a commercial base oil chosen to represent the chief constituent of engine lube oil[13], pure water and also a set of emulsions were made with brine. For this 20 wt% aqueous (or brine) solutions of the appropriate surfactant were used to make up 10.5 wt% Triton-X100 (Sigma Aldrich) solutions. These mixed surfactant/MagSurf+Triton-X100 solutions were vortexed for 5 minutes, before either base oil (Exxonmobil core 150) or pure n-dodecane was added (7.8 wt% with respect to the final emulsion). The resulting emulsions were voretxed for a further 10 minutes and then sonicated (MSE Soniprep 150 (UK), 23 kHz) five times, each time at full power for four minutes with 30 seconds cooling time between successive sonication. The visual appearances of the water, oil, oil + water bi-phasic system, and the resulting MagSurf emulsions are shown in Figure 6.2.

Figure 6.2: Oil and brine do not mix. However on adding a surfactant and sonicating, oil in brine (o/b) emulsions form.

The emulsion droplet sizes were determined using a Brookhaven Instruments Zeta-PALS Dynamic Light Scattering (DLS) apparatus (Brookhaven Instruments Corporation, Holtsville, NY) with the detector set at 90°. Measurements were taken of the neat emulsions, and then at a series of dilutions with pure water or

brine as appropriate. At high concentrations DLS is sensitive to interparticle interactions, in the region of 10 vol% dilution with solvent (water or brine) the DLS particle sizes stabilized to limiting values.

Sizing for neat mixed micellar solutions not containing oil were also carried out. However, very weak scattered intensities owing to the small sizes (~2 nm) gave rise to unreliable analyses of the correlation functions.

6.1.8 Magnets

The magnet used for Figure 6.4 were NdFeB (20 mm x 10 mm) with a field density of 0.44 T on the surface, and a gradient of about 36 mT mm^{-2}. In addition a NdFeB rod magnet (25mm diameter x 50mm) with a maximum field density of ~ 1.0 T, varying along the length was employed. Both magnets were purchased from e-magnets (UK).

6.2 Results and discussion

A Gd(III)-containing surfactant (DTAG) (Figure 6.3) and a related high-spin Fe(III)-based analogue $(DTAF)^2$ were synthesised, UV-Vis spectroscopy for DTAF being consistent with the proposed structure. The DTAG offers greater responsivity owing to a higher effective magnetic moment (spin only) of Gd (III) compared to high-spin Fe (III) (7.94 B.M and 5.92 B.M. respectively[14], Table 6.1).

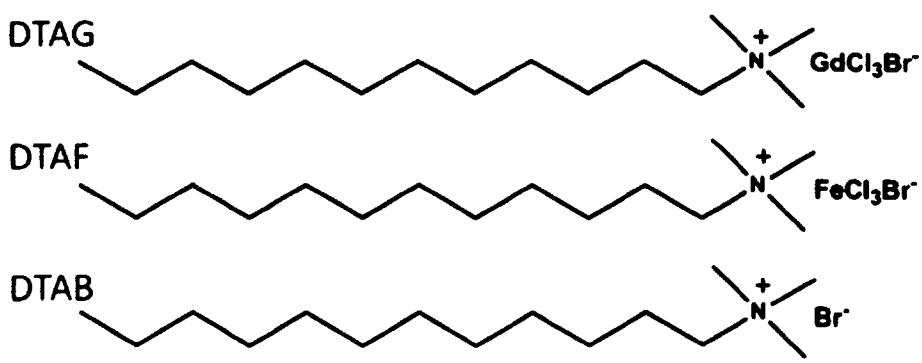

Figure 6.3: Magnetically-responsive surfactants DTAG and DTAF, and the inert analogue DTAB.

Compound	M_w / (g mol^{-1})	Mp / °C	cmc / (mM) ± 0.005	β
DTAG	571.85	-	11.9	0.59
DTAF	470.55	32	13.6 (13.6)	0.81
DTAB	308.35	246	15.5 (14.5)	0.26 (0.25)

Table 6.1: Selected physical properties of surfactants studied.

In dilute aqueous solutions MagSurfs lower surface tension γ, just as for normal surfactants. Interestingly, because these MagSurfs are inherently paramagnetic they exhibit pronounced magnetically-induced reductions in γ, which are not seen for the inert DTAB. Electrical conductivity studies are consistent with charged micelle formation with the MagSurfs.

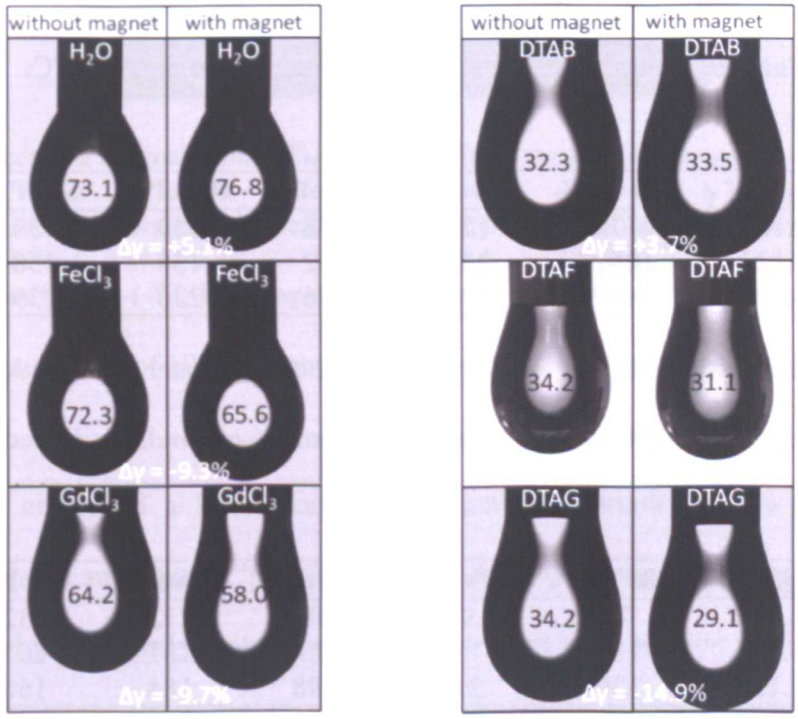

Figure 6.4: Pendant drop profiles of the surfactants studied with and without a magnet. Units of surface tension are mN m^{-1}.

Magneto-responsive emulsions (MREs) were made using the MagSurfs at 16.5 wt% (volume fraction ϕ 0.123) a co-surfactant, TritonX-100 9.7wt% (ϕ = 0.094) and 7.8 wt% pure dodecane (ϕ = 0.104), or a commercial lubricant oil (ϕ = 0.093) (Table 6.2 and 6.3). Emulsions were also made in brine (Table 6.2 and 6.4), therefore demonstrating not only proof of principle but also showing how they may be prepared and implemented for applications involving sea water, outside of the laboratory. Emulsions do form without co-

surfactant, but are less stable separating over hours rather than days. A further benefit of co-surfactant is that MagSurf levels can be minimized, whilst still retaining magnetic responsivity. More concentrated MREs at 41 wt% DTAG (ϕ = 0.34) indicate emulsion stability to composition variation at constant oil (7.8 wt%). Particle sizing by dilution studies with dynamic light scattering (DLS) show average domain sizes of the MREs are commensurate with those stabilized by the inert DTAB.

Compound	Density / (g cm^{-3})	Volume fraction (ϕ)
DTAB / DTAF /DTAG	1.40	0.123
TritonX-100	1.07	0.094
Base oil	0.87*	0.093
dodecane	0.75	0.104
water	1.00	0.690

Table 6.2: Parameters for emulsion characterization. *At 15 °C.

Compound	MagSurf ϕ	100 vol%	50 vol%	25 vol%	10 vol%	5 vol%	1 vol%
DTAG	0.123	21707	159	138	150	154	159
DTAF	0.123	10817	222	172	158	158	136
DTAB	0.123	1308	175	176	220	239	240

Table 6.3: Apparent emulsion size (nm) for emulsions of lube oil in water as a function of concentration determined by DLS: vol% represents the final volume % of emulsion diluted in water.

Compound	MagSurf ϕ	100 vol%	50 vol%	25 vol%	10 vol%	5 vol%	1 vol%
DTAG	0.123	773	93	99	212	232	260
DTAF	0.123	1722	118	75	187	207	209
DTAB	0.123	1307	250	198	184	166	164

Table 6.4: Apparent emulsion size (nm) for emulsions of dodecane in brine as a function of concentration by DLS: vol% represents the final volume % of emulsion diluted in brine

Figure 6.5 shows DTAB and MagSurf emulsions (lower phases) in equilibrium with excess dodecane (upper phases). As can be seen, introducing a small-sized magnet overcomes both gravity and water-oil interfacial tension (ca. 50 mN m^{-1}), pulling the lower MREs through the upper oil phase. Furthermore, Figure 6.2 also shows an MRE being "levitated" through air using a strong rod magnet. The magnet is static, but after ~ 10 s

in the field the emulsion begins to dimple in high flux regions, 10 s later the viscous emulsion has jumped the gap owing to strong magnetic attraction.

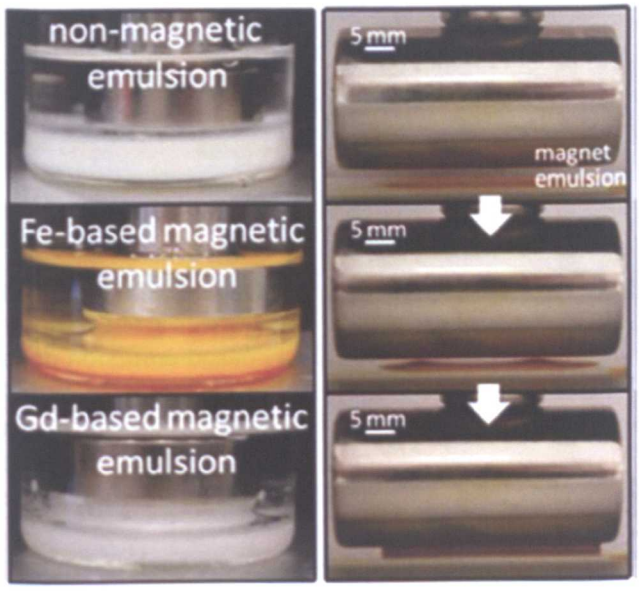

Figure 6.5: (left) Effect of a magnetic field (0.44 T on surface) through dodecane on emulsions. The same results are seen with either pure water or brine in the emulsions. **(right)** An Fe(III)-based emulsion attracted to a magnetic field (max field = 1 T). The magnet is suspended about 1 mm above the emulsion. The arrows represent a time interval of 10 s whereby the viscous emulsion is pulled towards the magnet.

Figure 6.6 shows the control of a DTAG oil in water emulsion droplet with a magnet. This droplet overcomes both gravity and an effective "flow" of solvent. It has been reported that a magnet field strength of 0.2 – 0.7 T is needed to efficiently capture particles and control and emulsion flowing in blood vessels[15]. Here, the magnetic field density on the inside of the tubing is estimated to be in the required range ~0.37 T, indicating the suitability of these systems for nanomedical applications.

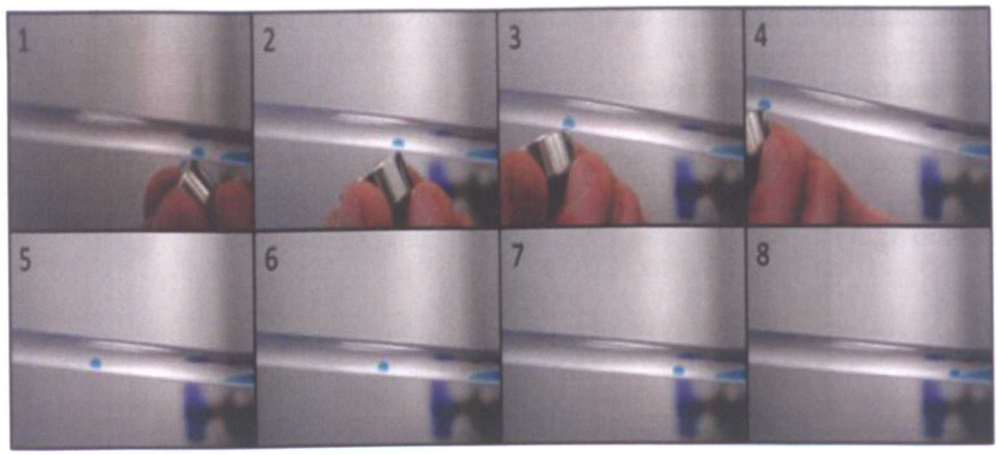

Figure 6.6: Effect of a magnetic field (0.37 T) on a DTAG based emulsion droplet (dyed with methylene blue for visualization) in a dodecane background. DTAG (50 wt%) oil (dodecane, 10 wt%). The droplet is pulled against gravity and viscosity of the dodecane fluid (picture 1 – 4). Once the magnet is removed (picture 5) gravity causes the droplet to flow back down the tube.

6.3 Conclusions

Control of emulsion size and shape, as well as physico-chemical properties through appropriate surfactant selection is well established, these principles can be applied to generate other kinds of MREs from MagSurfs. Compared to nanoparticle-stabilized magnetic emulsions[1] a major advantage of these MagSurfs is the simple synthesis and purification, offering new possibilities for molecular design of specialist surfactants. These MagSurfs, and the responsive MREs represent a new paradigm in materials science, offering a platform for developing responsive systems with spatial control, tailored towards active and recoverable methodologies, industrial processes and high-end applications.

6.4 Introduction

Like emulsions, microemulsions have widespread industrial application, and may be considered as being related to emulsions[16] (i.e. droplet type dispersions either of oil in water (o/w) or of water-in-oil, with a size range in the order of 1 – 50 nm in drop radius). However, unlike emulsions, once the conditions are right, microemulsions form spontaneously and are thermodynamically stable mixtures. The magnetically-responsive microemulsions reported in this chapter are believed to be the first of their kind.

The associated free energy change on forming a microemulsion can be expressed as a sum of the free energy of creating an new area of interface, $\Delta A\gamma_{12}$, and configurational entropy, ΔS_{conf}:

$$\Delta G_{form} = \Delta A\gamma_{12} - T\Delta S_{conf} \qquad \text{Eq. 6.1}$$

where ΔA is the change in interfacial area A (equal to $4\pi r^2$ per droplet of radius r) and γ_{12} is the interfacial tension between phases 1 and 2 (e.g. oil and water) at temperature T (in Kelvin).

During microemulsion formation the increase in interfacial area is very large and so in order to fulfil the condition that $\Delta A\gamma_{12} \leq T\Delta S_{conf}$ the interfacial tension should be very low (approximately 0.01 mN m^{-1}). This is done by the addition of surfactant. In most cases (e.g. ionic single hydrocarbon chain surfactants, DTAB), such low surface tensions are only reached by combining two surface-active species. Microemulsion type is then dependent on surfactant type and structure, composition ratio and water and oil volume fractions. Here, the magnetically-responsive surfactant DTAF has been used with an inert di-chain analogue DDAB (didodecyltrimethlammonium bromide) to form w/o microemulsions. Phase behaviour has been characterized and droplet movement in a magnetic field has been investigated using SANS.

6.5 Experimental

6.5.1 Materials and Synthesis

Dodecyltrimethylammonium tetrachloroferrate was synthesized according to the procedure in Part One. Didodecyltrimethylammonium bromide (99%, DDAB) and n-heptane (<99). Microemulsions were prepared

by weighing the required amounts of DDAB and DTAF (weighed using a four-figure balance with an accuracy of ± 0.1 mg) into clean, 5 ml volumetric flasks, then required volumes of water were added (using a Hamilton microsyringe). Next, a few microlitres of heptane was added and the mixture ultrasonicated until all the surfactant dissolved. Finally, more heptane was added up to the 5 mL mark and samples were shaken thoroughly to attain equilibrium. Samples were then left for 48 hours (owing to phase resolution) and characterized by visual inspection. For subsequent concentration studies, serial dilution was used.

6.6 Results and discussion

6.6.1 Microemulsion Formation

In this work, phase behaviour was investigated as a function of surfactant ratio (in wt %) and w value (w = [water] / [surfactant]) at various surfactant concentrations (Figure 6.7) and also as a function of temperature at constant surfactant concentration (Figure 6.8) in order to locate phase boundaries. Single-phase (1Φ) w/o microemulsions were identified (by visual inspection). Samples with faint turbidity or small water droplets settling out, were taken to be at the emulsification boundary (w_{max}).

D_2O-DDAB-*n*-heptane microemulsion systems have been studied before, exhibiting two distinct phase separations regions (WII and 1Φ).[17] By partially replacing DDAB with the single chain DTAB, Eastoe *et al.* showed that the single-phase region shifted to higher w, meaning that higher DTAB content both increased maximum water solubilization (w_{max}) and the amount of water required to stabilize the microemulsions (w_{min}). They demonstrated that microemulsion phase behaviour was affected by surfactant bulk composition and changes in the effective packing parameter as a result of surfactant mixing at the interface. The single-chained DTAB prefers to be curved toward the oil (positive curvature, $v/a_h l_c \sim 0.65$), whereas the double-chained surfactant curves towards water (negative curvature, $v/a_h l_c \sim 1.30$). Here curvature depends on both surfactant type but also on the interface. Replacing DDAB by DTAB decreases the average chain volume, whilst the area per surfactant head group remains almost constant. Hence the mean packing parameter of the surfactant mixture decreases.

Instead of using DTAB, our studies used the structurally analogues but magnetically-responsive surfactant DTAF. It is important to note that conductivity data and SANS show only small changes in physico-

chemical properties of these surfactants on changing the anion from Br^- to $FeCl_3Br^-$.

The phase behaviour of DDAB-DTAF systems (Figure 6.8) compares with the studies for DDAB-DTAB systems, and is almost independent of overall surfactant content[18]. Increasing DTAF content to around 35 wt% leads to w_{max} = 120 (for 0.050 M surfactant system) for a single-phase. Above the solubilization boundary, the w/o microemulsion is present in co-existence with an excess water phase (i.e. WII system).

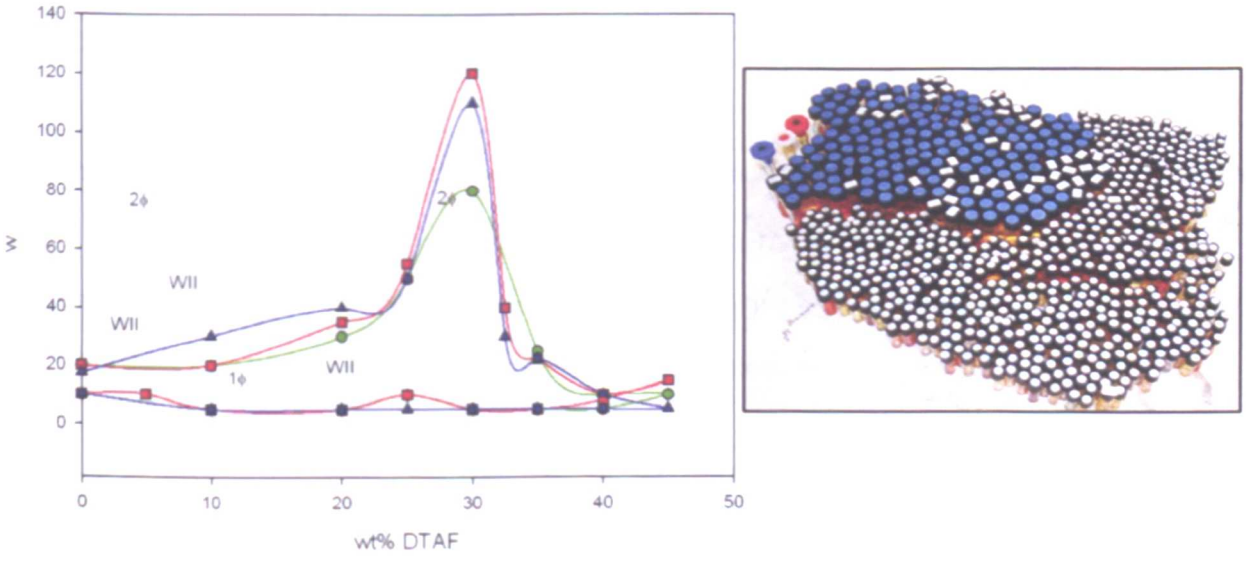

Figure 6.7: (left) Phase diagram as a function of surfactant ratio (DDAB:DTAF) , w value and total surfactant concentration at 25 °C. [$Surfactant_{total}$]: 0.100 M (green circle), 0.050 M (red square), 0.025 M (blue triangle); **(right)** Microemulsions prepared for the study.

There are two effects of temperature for ionic surfactant systems: (i) an increase in the electrostatic repulsions between the surfactant headgroups (due to higher counter-ion dissociation), causes an increase in film curvature; (ii) more gauche conformations are induced in the surfactant chains, which become more coiled, resulting in an decrease in curvature[16]. The combined effects are competitive with the electrostatic term believed to be slightly dominant, so curvature increases weakly with increasing temperature. The results in this chapter agree with this (Figure 6.8). For 0.10 M total surfactant concentration on increasing the temperature from -18 °C up to 25 °C the single phase region increases. However, on increasing the temperature further to 55 °C a dramatic decrease in the single phase region occurs. This is probably owing to a change in dominance whereby tail group conformation becomes more important.

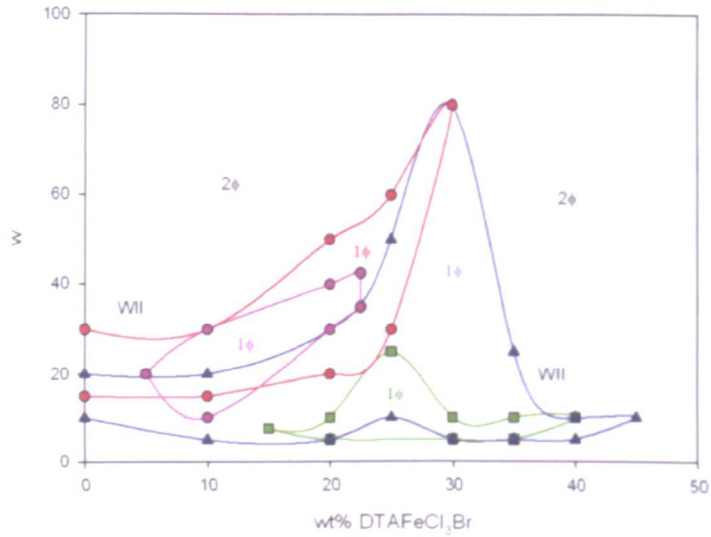

Figure 6.8: Phase diagram at constant surfactant concentration (0.10 M), as a function of surfactant ratio (DDAB:DTAF), *w* value and temperature.

Temperature: 55 °C(green square), 25 °C(blue triangle), 5 °C(red circle), -18 °C(pink circle).

6.6.2 Small-Angle Neutron Scattering

Small-angle neutron scattering (SANS) conclusively shows the structure of the microemulsions as a function of surfactant ratio at constant *w* value and overall surfactant concentration. The profiles are consistent with non-interacting rods (Figure 6.9, Table 6.5) whereby increasing the DTAF (single chain) content leads to a reduction in rod length. At high q the scaling of Q^{-4} indicates a sharp, smooth water/oil interface.

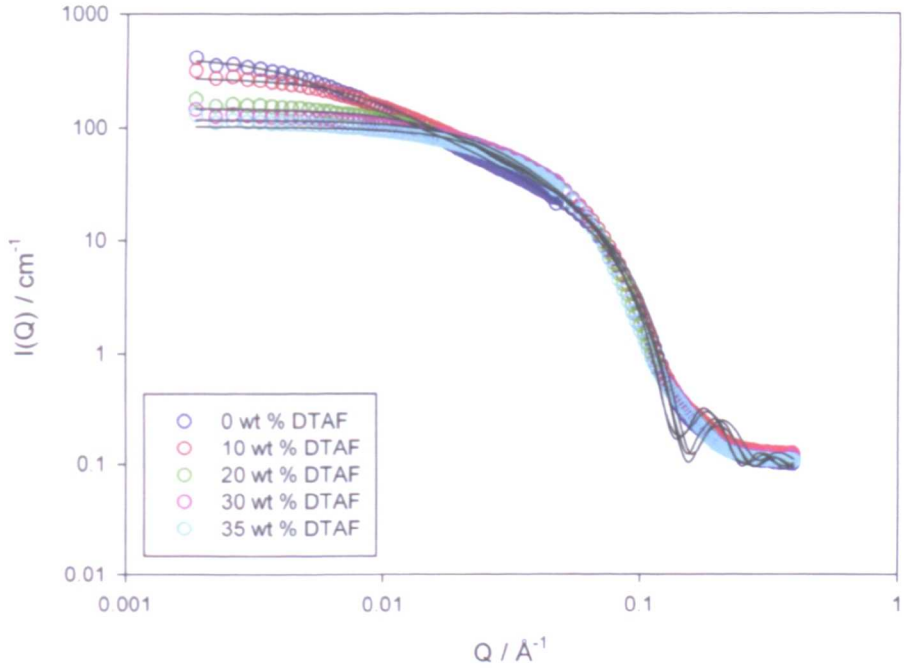

Figure 6.9: SANS profiles for H_2O-in-*d*-heptane mixed micelles using DDAB-DTAF at a fixed total surfactant concentration of 0.100 M surfactant at 25 °C.

wt % DTAF	*w*	Type	Shape	*R* / Å	*L* / Å
0	10	1Φ	rod	25	874
10	10	1Φ	rod	25	495
20	10	1Φ	rod	26	252
30	10	1Φ	rod	28	170
35	10	1Φ	rod	28	159

Table 6.5: Parameters fitted to SANS data using the model for rods.

SANS experiments were repeated in the presence of a 6.7 T magnetic field (set up shown in Figure 6.10). However, the anisotropic microemulsions appeared not to orientate themselves even in very large fields (6.5 T) as indicated by the SANS profiles, which remained consistent with those pre-field. This was an unexpected result but may potentially be that only orientation of spin occurs which does not lead to the movement of the microemulsion.

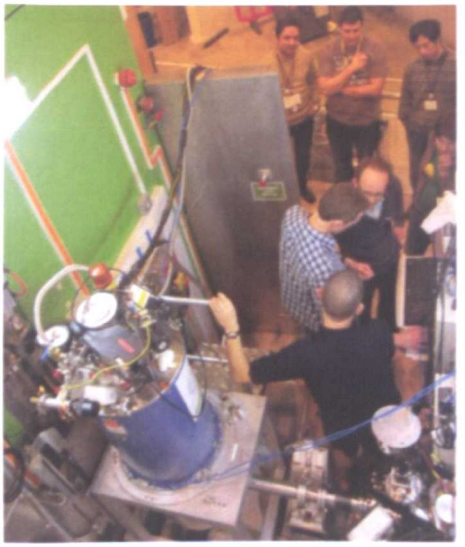

Figure 6.10: SANS set up using a 6.9 T cryomagnet on SANS 2D (ISIS, UK).

6.7 References

1. A. Kaiser; T. Liu; W. Richtering; A. M. Schmidt, *Langmuir,* 2009, *25*, 7335.
2. P. Brown; A. Bushmelev; C. P. Butts; J. Cheng; J. Eastoe; I. Grillo; R. K. Heenan; A. M. Schmidt, *Angew. Chem. Int. Ed.,* 2012, 2414.
3. S. Iglauer; Y. Wu; P. Shuler; Y. Tang; W. A. Goddard, *J. Pet. Sci. Eng.,* 2010, *71*, 23.
4. H. Zhang, Porous Materials by Templating of Small Liquid Drops. In *Hierarchically Structured Porous Materials*, Wiley-VCH Verlag GmbH & Co. KGaA: 2011; p. 209.
5. Y. Sakaguchi; H. Hayashi, *Chem. Phys.,* 1992, *162*, 119.
6. (a) M. Akimoto; Y. Morimoto, *Biomaterials,* 1983, *4*, 49; (b) R. T. Woodward; C. I. Olariu; E. A. Hasan; H. H. P. Yiu; M. J. Rosseinsky; J. V. M. Weaver, *Soft Matter,* 2011, *7*.
7. H. Sis; S. Chander, *Minerals Eng.,* 2003, *16*, 577.
8. P. Dames; B. Gleich; A. Flemmer; K. Hajek; N. Seidl; F. Wiekhorst; D. Eberbeck; I. Bittmann; C. Bergemann; T. Weyh; L. Trahms; J. Rosenecker; C. Rudolph, *Nat Nano,* 2007, *2*, 495.
9. M. Dobbelin; V. Jovanovski; I. Llarena; L. J. Claros Marfil; G. Cabanero; J. Rodriguez; D. Mecerreyes, *Polym. Chem.,* 2011, *2*, 1275.
10. G. R. Bernett; R. Atkin; S. Hicks; J. Eastoe, *Langmuir,* 2004, *20*, 5673
11. M. G. Steinmetz; C. Yu, *Organometallics,* 1992, *11*, 2686.
12. J. R. Rodríguez; A. González-Pérez; J. L. Del Castillo; J. Czapkiewicz, *J. Coll. Int. Sci.,* 2002, *250*, 438.
13. G. Corsico; L. Mattei; A. Roselli; C. Gommellini, *Poly(internal olefins) - Synthetic and high-performance functional fluids*. Marcel Dekker, 1999.
14. (a) D. Moon; J. Kim; M. S. Lah, *Bull. Korean. Chem. Soc.,* 2006, *27*, 1597; (b) H. Funasaka; K. Sugiyama; K. Yamamoto; T. Takahashi, *J. Phys. Chem.,* 1995, *99*, 1826.
15. B. P. Binks, *Modern Aspects of Emulsion Science*. Royal Society of Chemistry: 1998.
16. T. Cosgrove, *Colloid Science Principles, Methods and Applications*. 2nd Ed.; Wiley: London, 2010.
17. A. Bumajdad; J. Eastoe, *J. Coll. Int. Sci.,* 2004, *274*, 268.

18. (a) L. Magnus Bergström; V. M. Garamus, *J. Coll. Int. Sci.*, 2012, *381*, 89; (b) A. Y. E. A. Bumajdad. Phase structure and interfacial composition of mixed surfactant microemulsions. University of Bristol, Bristol, 2000.

Chapter 7

Microemulsions as Tunable Nanomagnets

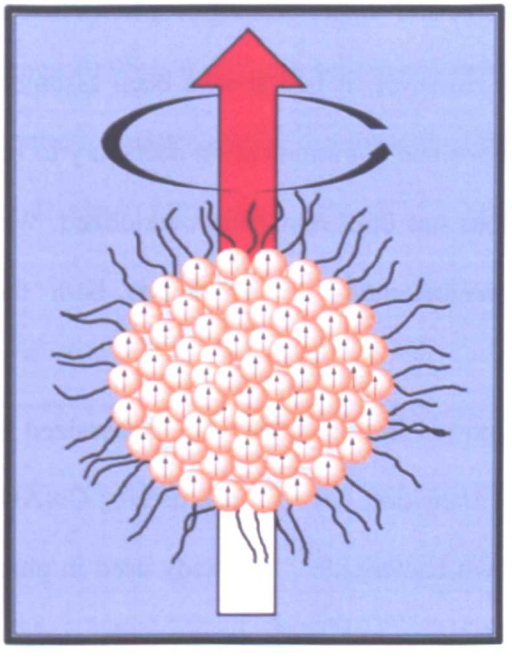

In Chapter 5 magnetic surfactants based on common surfactant ions with metal complexes were presented, and because they contain high effective concentrations of metal centres, they can be controlled non-invasively and reversibly simply by switching "on" and "off" an external magnetic field. In Chapter 6 magnetic emulsions and microemulsions were generated from cationic surfactants. In this chapter the first magnetic microemulsions from new anionic magnetic surfactants are investigated with particular emphasis placed on their intrinsic magnetic behaviour and how they may be thought of as molecular magnets.

Magnetic microemulsions comprising of magnetic surfactants exhibit monodomain magnetic behaviour intermediate between magnetic nanoparticles and molecular magnets. Importantly, due to partitioning of surfactant molecules at the water/oil interface only surface anisotropy is observed. These new systems allow for *in situ* tunability through composition and the solubilization of hydrophobic additives.

7.0 Introduction

Microemulsions have numerous technological applications[1], in part because of the ability to precisely control size and stability of the nano-domains. Microemulsions made from transition metal and lanthanide metal-based surfactants have been used as compartmentalized reaction media to prepare sub-micron or nano-sized particles with controlled size and shape, bearing properties relevant for applications such as high density magnetic recording media[2]. However, it had always been assumed that the metallic centres were isolated, lacking long range interactions and communication necessary to be magnetically-active and so the intrinsic magnetism of microemulsions has until now been overlooked. We have used small-angle neutron scattering (SANS) and SQUID magnetometry to investigate both the bulk "dry" surfactants and microemulsions.

The magnetic anionic surfactants reported in this chapter are synthesized from the commercially available commodity Aerosol-OT (AOT), and transition *d*- or *f*-block metals: $Co(AOT)_2$, $Mn(AOT)_2$, $Ce(AOT)_3$ and $Ho(AOT)_3$. Common AOT is a known bactericide[3], is already used in pharmaceutical formulations, offers better detergency than cationic surfactants and leads to magnetic surfactants which are less aggressive (lower Lewis acidity) than the cationic analogues. Non-radioactive lanthanides are classified as having low toxicity[4], having uses as catalysts[5] and superconductors[5b]. Lanthanide anionic surfactants have also been reported for spectroscopic studies because of intrinsic luminescence[6]. Significantly, certain lanthanides have the highest known effective magnetic moments, exhibiting ferro- or antiferromagnetism as well as paramagnetism.

7.1 Experimental

7.1.1 Materials and Synthesis

Aerosol-OT (Na-AOT) was purchased from Sigma and purified by Soxhlet extraction using dry acetone as the solvent followed by dissolving in the minimum amount of dry acetone and subjecting to repeat centrifugation. The purified Na-AOT was then dried *in vacuo* at 60 °C for two days. $Co(AOT)_2$ was prepared by exchanging Na^+ for $[Co(H_2O)_6]^{2+}$ using the following liquid-liquid extraction technique[2a].

A saturated aqueous solution (*ca.* 100 cm^3) of cobalt nitrate, (Sigma 98%) was prepared at 25°C and mixed with an ethanolic solution of Na-AOT, 150 cm^3 at 1 mol dm^{-3}. Diethyl ether (50 cm^3) was then added and

two phases appeared. The $Co(AOT)_2$ rich organic phase was separated and washed seven times with water (Elga, 18.2 MΩ cm) until clear. The organic solvent was then removed under reduced pressure and residual water removed *in vacuo* at 60 °C for 2 days.

The replacement of Na^+ by Co^{2+} was monitored using UV-visible absorbance (Nicolet evolution 300) at A = 510 nm using a range of concentrations (0.01 – 0.10 mol dm^{-3}) of $Co(NO_3)_2$ solutions as standards[7]. The efficiency of the counterion exchange (0.95 ± 0.05) was calculated from the ratio of the observed cation concentration ($M^{2+}{}_{obs}$) to the concentration expected ($M^{2+}{}_{ex}$) assuming that 1 mol of surfactant contained 1 mol of M^{2+} (Figure 7.1). The divalent ions used bear H_2O ligands, therefore the surfactant is $Co(AOT)_2.6H_2O$.

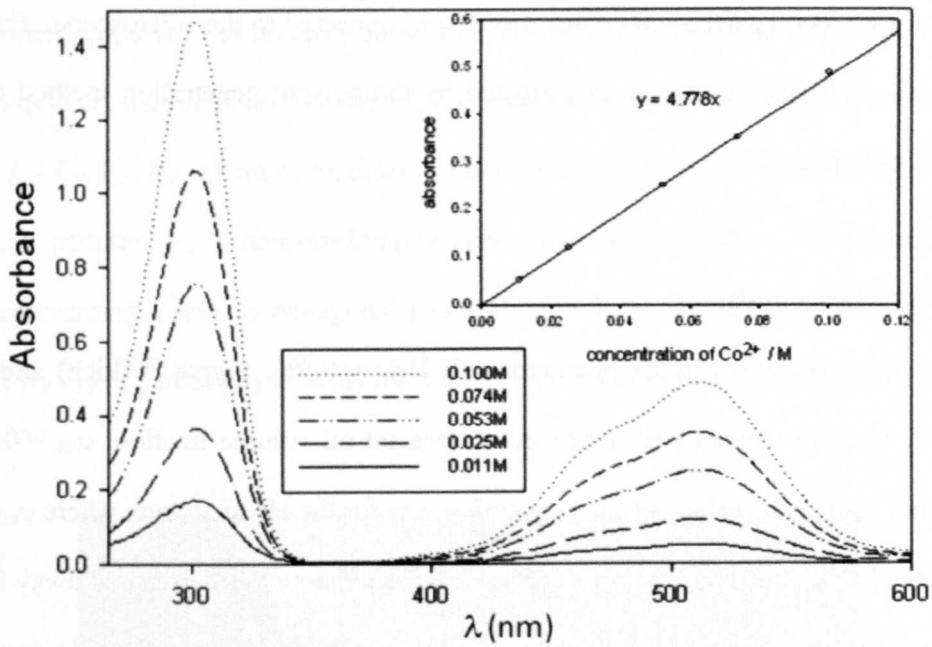

Figure 7.1: UV-visible absorbance spectra of the $Co(NO_3)_2$ solutions as standards.

Inset: Beer-Lambert type dependence of absorbance with concentration.

The UV-Visible spectrum for $Co(AOT)_2$ was characteristic of an octahedral complex. The efficiency of the counterion exchange was calculated from the ratio of the observed ($Co^{2+}{}_{obs}$) cation concentration to the concentration expected ($Co^{2+}{}_{ex}$) assuming that 1 mol of surfactant contained 1 mol of Co^{2+}. The value of $[Co^{2+}]_{obs}/[Co^{2+}]_{ex}$ was 0.95.

The Mn, Ce and Ho AOT analogues were prepared by the liquid-liquid ion exchange process. The appropriate metal chloride (Sigma + 99%) was solubilised in ethanol:H_2O (75:25 v/v). The appropriate equivalent of Na-AOT was then added and the solution stirred for 5 hours. The solvent was then removed under reduced pressure and the metal-surfactant was dried for *in vacuo* at 80°C for two days. The surfactant was then re-solubilised in a minimum amount of dry dicholoromethane and NaCl was filtered off. This was then followed by repeat centrifugation. The pure surfactant was then dried *in vacuo* at 80°C for two days. Analyses showed no chlorine or sodium present and so the synthesis was considered complete.

7.1.2 Polarizing Light Microscopy (PLM)

PLM was conducted with a Nikon Optiphot-2 microscope fitted with polarizing filters, and images were captured on a PC via a video camera and colour processor connected to the microscope. The liquid crystal phase progression of each surfactant was investigated by the solvent penetration method (i.e. phase cut) against pure water[8], or heptane.

7.1.3 Preparation of Microemulsions

Water in oil (w/o) microemulsions were prepared with D_2O (99.9%, Sigma Aldrich) and SiO_2-column-purified n-heptane[9]. Microemulsions were prepared at constant oil volume fraction, $\varphi_{oil} = 0.90$ assuming a density of 1.14 g mol^{-1} for each surfactant (one exception was for the Ho analogue, where $\varphi_{oil} = 0.96$) and at w ratios (w = [D_2O] / [surfactant]) so that the resulting microemulsions were prepared away from any phase boundaries. Microemulsions were characterized by visual inspection and small angle neutron scattering (SANS).

7.1.4 Small-Angle Neutron Scattering (SANS)

SANS was measured on the SANS2D diffractometer at the ISIS Facility, Rutherford Appleton Laboratory, UK, and the D22 diffractometer at ILL, Grenoble, France. SANS2D is a time-of-flight instrument using neutrons with an incident wavelength $2.2 < \lambda < 14$ Å, and with the 1 m^2 detector offset sideways and vertically by 150 mm, the resulting Q-range was $0.006 < Q < 0.7$ $Å^{-1}$. The D22 is a reactor-based

diffractometer, and a neutron wavelength of λ = 10 Å was employed at two different detector distances giving $0.0024 < Q < 0.37$ Å^{-1} (see Chapter 3 for more details).

7.1.5 SQUID Magnetometry

Magnetic properties were measured in a SQUID (superconducting quantum interference device) magnetometer (Quantum Design MPMS-5T) equipped with a 5T superconducting magnet. Liquid dispersions were transferred into the measuring capsule using a 100 µL Hamilton syringe.

7.2 Results and Discussion

7.2.1 Polarizing light microscopy

Polarizing light microscopy (PLM) textures show that the magnetic surfactants exhibit a transition from fluid micellar to liquid crystalline phases in water. The phase progression for Na(AOT) at 25 °C agrees with previous work[10]: L_1- L_α- V_2- H_2, where L_1 represents a non-birefringent micellar solution, L_α a lamellar phase with parallel streak patterns, V_2, a non-birefringent cubic bi-continuous phase, and finally, H_2, a fan-like mosaic texture representing a reverse hexagonal phase (Figure 7.2). In comparison, cobalt and manganese analogues exhibit less varied mesophase structure. Cerium and holmium showed only very limited solubility in water.

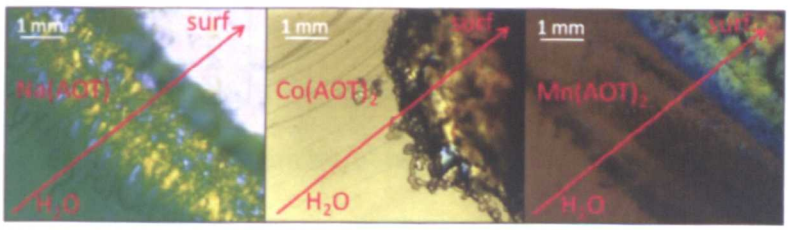

Figure 7.2: Optical textures of surfactants in water in phase penetration experiments (T = 25 °C). PLM textures show no mesophase formation in heptane; instead only a dilute L_2 phases (inverse micelles) are formed (Figure 7.3).

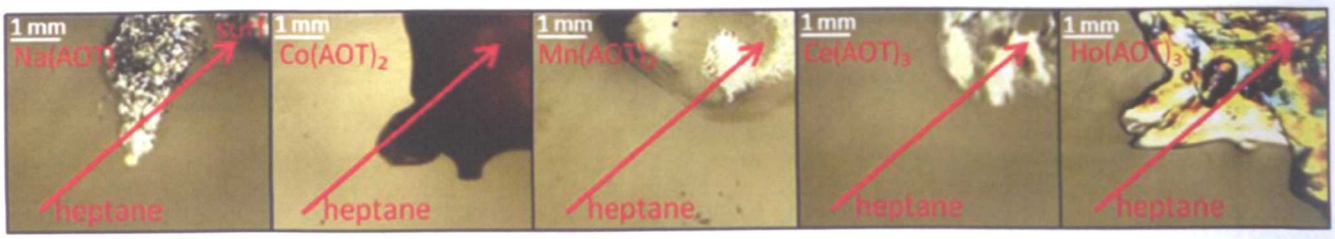

Figure 7.3: Optical textures of surfactants in heptane in phase penetration experiments (T = 25 °C).

7.2.2 Small-angle neutron scattering (SANS)

SANS conclusively shows that the compounds aggregate in water above critical micelle concentrations (cmcs) (Figure 7.4). Na(AOT) forms charged ellipsoidal micelles at 1 wt% in D_2O with a radius of 12 Å and aspect ratio, X = 2.1 (Figure 7.4). However, the structure in water is concentration dependant with scattering profiles consistent with mixed systems $(L_1 + L_\alpha)$[11] at higher concentrations. On the other hand, $Co(AOT)_2$ shows a scattering profile consistent with a collapsed lamellar phase, with a Bragg peak at around 31 Å (broadly independent of concentration). Finally, $Mn(AOT)_2$ was fitted to a model for multilamellar stacks [12], with a mean layer thickness of 25 Å and an interlamellar spacing of 58 Å. The SANS from $Mn(AOT)_2$ solutions depends greatly on increasing concentration, becoming more rigid as interbilayer distance decreases.

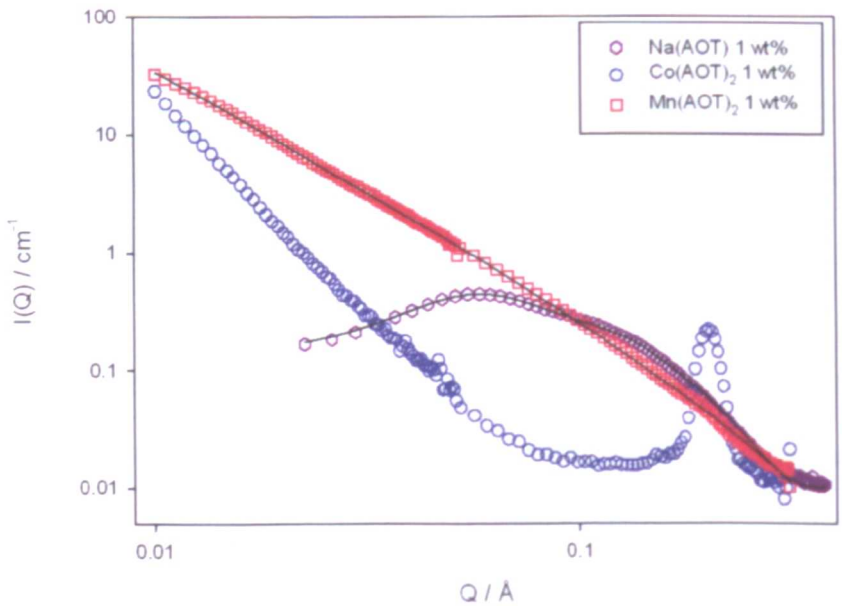

Figure 7.4: SANS profiles for Na, Co and Mn surfactants in D_2O at 1 wt% at 25 °C.

Lines through the data are fits.

In a typical organic solvent, heptane, SANS data (Figure 7.5, Table 7.1) show only minor changes in micellar size or shape on exchange of the metal ion and also with concentration.

At 1 wt % in heptane all profiles could be fitted to Schultz polydisperse spheres with radii between 17 Å to 20 Å. The slight difference in radius is assumed to be the result of the difference in ionic radii of the metal ions combined with different hydration numbers. The cobalt analogue was not soluble above 0.5 wt % but had a structure consistent with literature[2b]. An interesting feature of the profiles is the lack any obvious structure factor, (S(Q)), indicating only weak interactions.

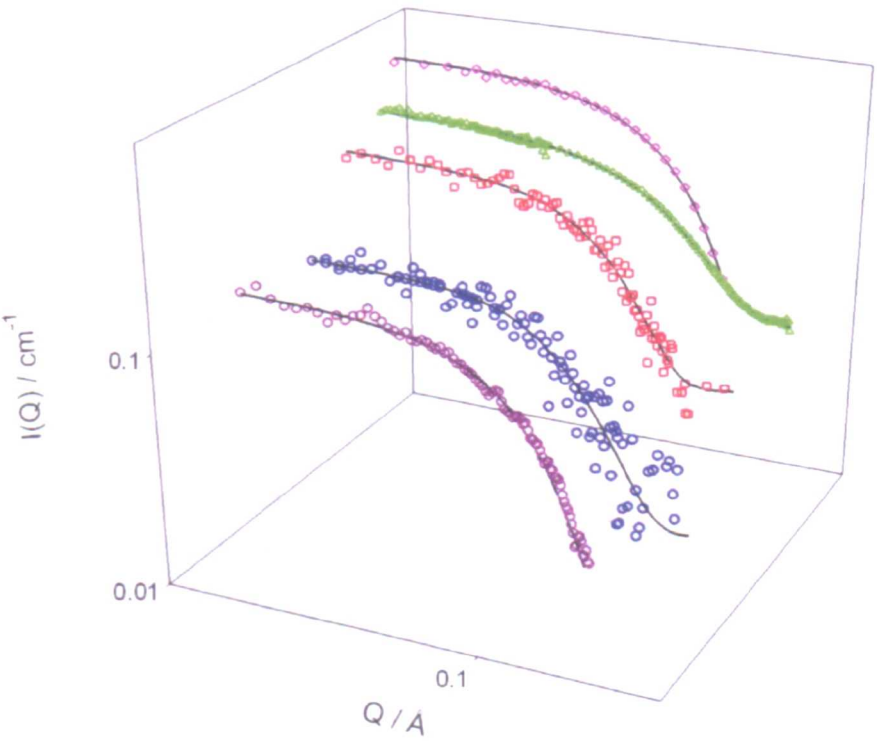

Figure 7.5: SANS profiles for surfactants in d_{16}-heptane at 1.0 wt% at 25 °C. Lines through the data are fits. $Co(AOT)_2$ is at 0. 5 wt% due to phase separation at higher concentrations. Na(AOT) (○), $Co(AOT)_2$ (○), $Mn(AOT)_2$ (□), $Ce(AOT)_3$ (△) $Ho(AOT)_3$ (○).

Compound	wt %	R_1 / Å
Na(AOT)	1.0	18
$Co(AOT)_2$	0.5	17
$Mn(AOT)_2$	1.0	20
$Ce(AOT)_3$	1.0	19
$Ho(AOT)_3$	1.0	18

Table 7.1: Parameters fitted to SANS data from reverse micelles of surfactants using polydisperse sphere model at 1 wt % in d_{16}-heptane, 25 °C.

7.2.3 SQUID magnetometry

SQUID Magnetometry between 5 K and 300 K on the pure surfactants (Figure 7.6, Table 7.2) indicates Co, Mn and Ho analogues are paramagnetic over most of the temperature range, with little noticeable deviation between field cooled (FC) and zero field cooled (ZFC) measurements (Figure 7.6).

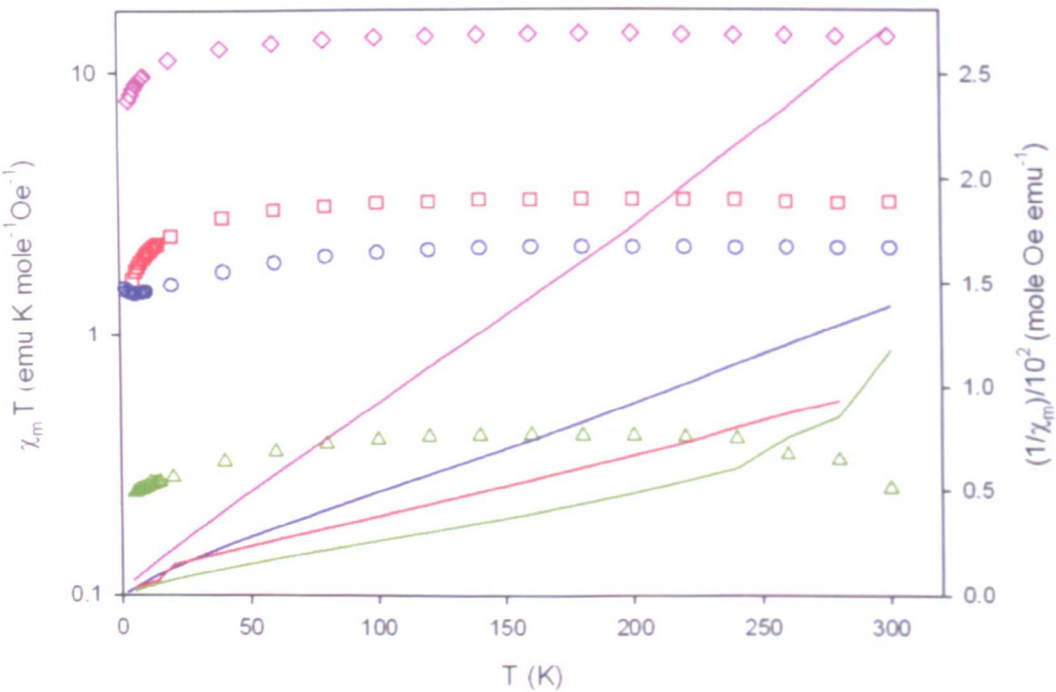

Figure 7.6: SQUID magnetometry data showing temperature dependence of $\chi_m T$ (symbols) and $1/\chi_m$ (lines) for each surfactant measured under 0.25 kOe. $Ho(AOT)_3$ ( ), $Mn(AOT)_2$ (□), $Co(AOT)_2$ (○), $Ce(AOT)_3$ (Δ).

Compound	Mw / (g mol^{-1})	$\chi_m T$ / (emu K mol^{-1} Oe^{-1})	μ_{eff} / (B. M.)	θ_p / K	T_N / K
Na(AOT)	444.25	-	-	-	-
$Co(AOT)_2$	901.45	2.16	4.15 (4.20[a])	-4.7	20
$Mn(AOT)_2$	897.46	3.22	5.07 (5.92[a])	-6.2	60
$Ce(AOT)_3$	1403.90	0.27	1.46 (2.54[b])	-	242
$Ho(AOT)_3$	1428.71	13.61	10.43 (10.60[b])	-0.1	-

Table 7.2. Results derived from SQUID magnetometry. Brackets indicate literature data.

[a]Spin-only moment. [b] Calculated moment.

The $Co(AOT)_2$ has a susceptibility $\chi_m T$ of 2.16 emu K mol^{-1} Oe^{-1} at room temperature (at field H = 0.25 kOe) corresponding to an effective paramagnetic moment μ_{eff} = 4.15 B.M. per Co^{2+} ion, which is consistent with literature for high spin d^7 Co(III) ions (S = 3/2)[13]. Above 20 K the magnetic susceptibility follows the

Curie-Weiss law with Weiss temperatures, θ_p, close to -4.7 K. This negative θ_p value together with the reduction of the effective magnetic moment observed on decreasing temperature suggests overall antiferromagnetic behavior at low T. Magnetization as a function H (Figure 7.7) at 2.0 K shows reversibility in the entire applied field range studied, $-50 \geq H$ (kOe) ≤ 50. With an increasing magnetic field, a linear dependence in magnetization from 0 to 6 kOe is observed and then the magnetization tends to saturate at around 30 kOe.

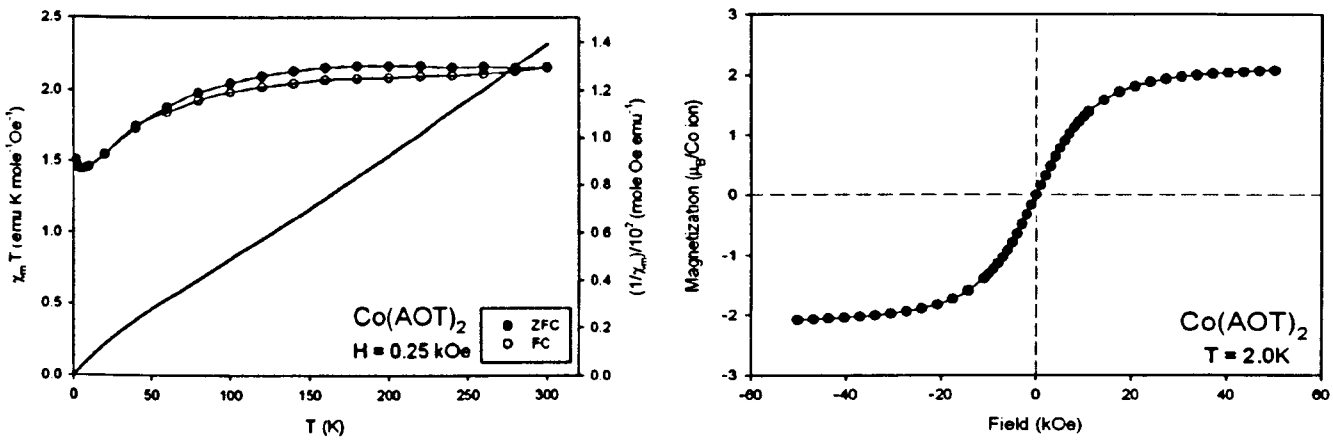

Figure 7.7: SQUID magnetometry data for $Co(AOT)_2$ showing **left**: temperature dependence of $\chi_m T$ and $1/\chi_m$ for each surfactant measured under 0.25 kOe; and **right**: magnetization versus applied magnetic field. The inset shows the detail of the low magnetic field region.

The magnetic behavior of $Mn(AOT)_2$ (Figure 7.8) is similar to $Co(AOT)_2$ (Figure 7.9) having $\chi_m T$ = 3.22 emu K mol^{-1} Oe^{-1} at room temperature corresponding to an effective paramagnetic moment μ_{eff} = 5.07 B.M. per Mn^{2+} ion, being a little lower than the spin only value (5.92 B.M.) expected for a S = 5/2 high spin d^5 complex[13]. Furthermore, $Mn(AOT)_2$ has a Neél temperature of T_N = 60 K and θ_p = -6.2 K implying the existence of slightly more short range interactions than the Co^{2+} analogue. Magnetization as a function of H at 5.0 K also shows reversibility over the entire applied field range studied, but lacking saturation up to the experimental limit of 50 kOe.

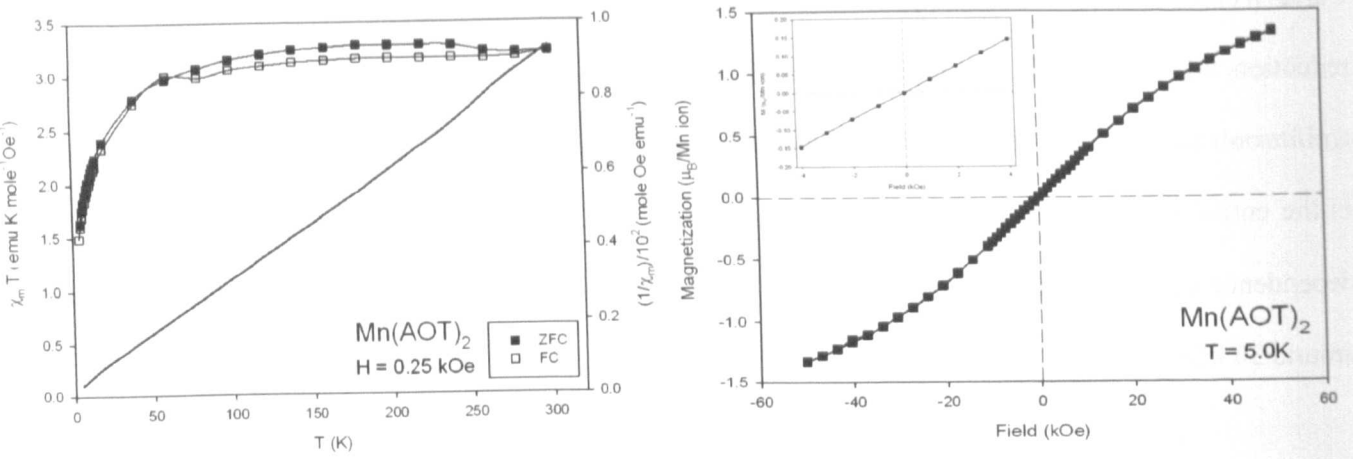

Figure 7.8: SQUID magnetometry data for $Mn(AOT)_2$ showing **left**: temperature dependence of $\chi_m T$ and $1/\chi_m$ for each surfactant measured under 0.25 kOe; and **right**: magnetization versus applied magnetic field. The inset shows the detail of the low magnetic field region.

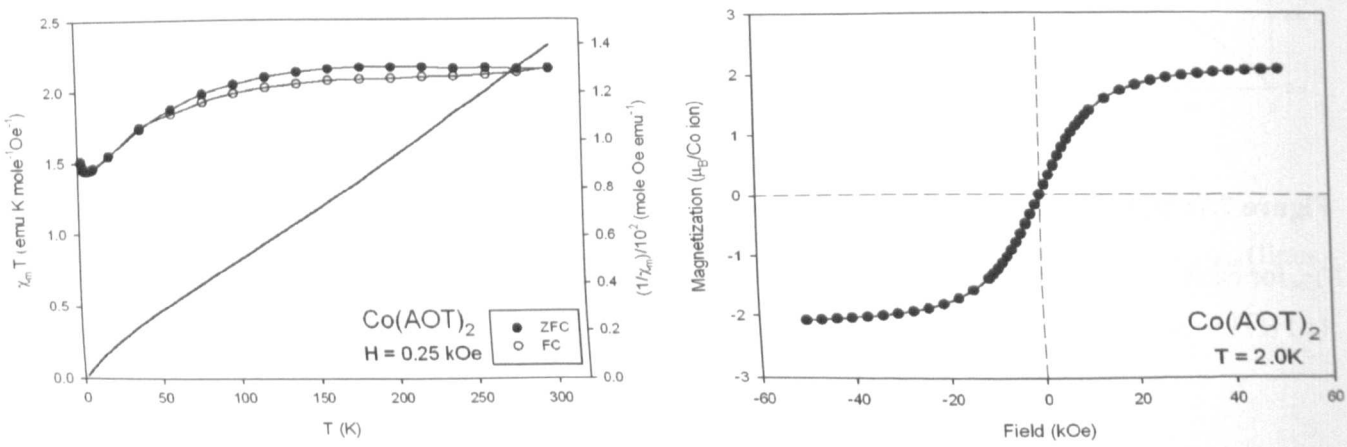

Figure 7.9: SQUID magnetometry data for $Co(AOT)_2$ showing **left**: temperature dependence of $\chi_m T$ and $1/\chi_m$ for each surfactant measured under 0.25 kOe; and **right**: magnetization versus applied magnetic field. The inset shows the detail of the low magnetic field region.

The $Ho(AOT)_3$ appears to be paramagnetic over the entire temperature range studied (Figure 7.10). Literature suggests T_N should be found at low temperatures (~19 K), although that was not observed with the surfactant. Holmium has the highest magnetic susceptibility of any metal and for $Ho(AOT)_3$ a $\chi_m T$ value of 13.61 emu K mol^{-1} Oe^{-1} at room temperature was observed corresponding to an effective paramagnetic moment μ_{eff} = 10.43 B.M. per Ho^{3+} ion.

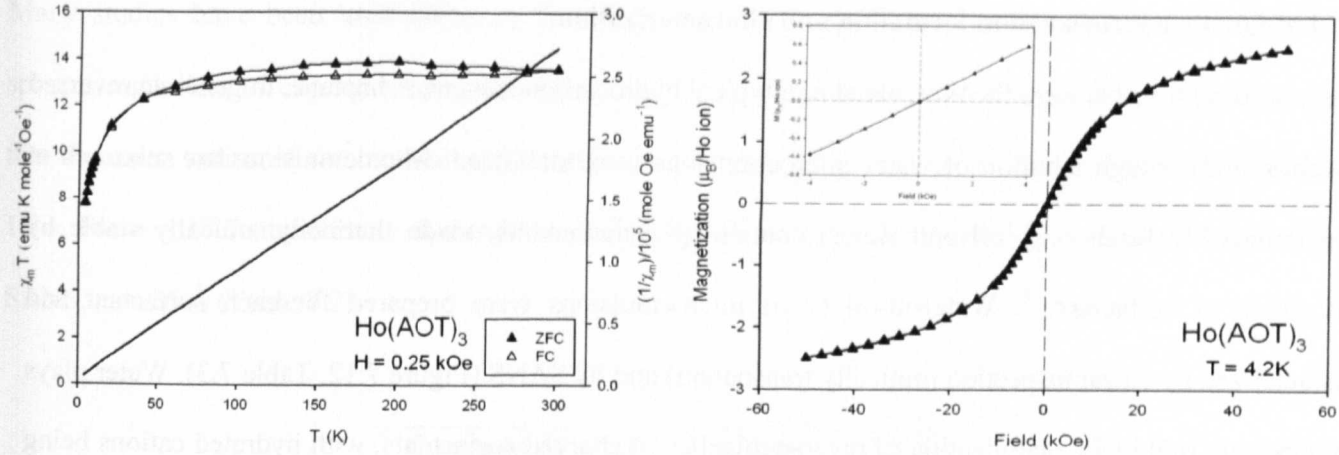

Figure 7.10: SQUID magnetometry data for $Ho(AOT)_3$ showing **left**: temperature dependence of $\chi_m T$ and $1/\chi_m$ for each surfactant measured under 0.25 kOe; and **right**: magnetization versus applied magnetic field. The inset shows the detail of the low magnetic field region

Finally, $Ce(AOT)_3$ behaves slightly differently as it does not follow the Curie-Weiss law (Figure 7.11), being superparamagnetic at low temperature, as evidenced by a $\theta_p = 0$ K with a transition to ferromagnetism at 20 K. There is another transition at 242 K that is possibly an antiferromagnetic phase.

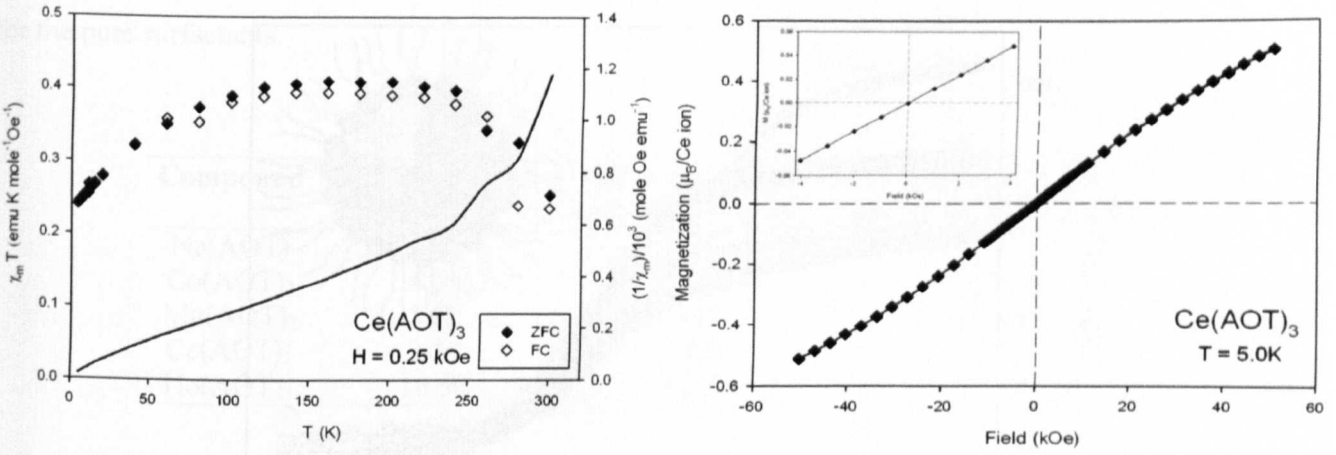

Figure 7.11: SQUID magnetometry data for $Ce(AOT)_3$ showing **left**: temperature dependence of $\chi_m T$ and $1/\chi_m$ for each surfactant measured under 0.25 kOe; and **right**: magnetization versus applied magnetic field. The inset shows the detail of the low magnetic field region.

7.2.4 Magnetic microemulsion formation and characterization

These surfactant solids were then dissolved in a typical hydrocarbon solvent, n-heptane, to generate reversed micelles, and through addition of water microemulsions were stabilized. Microemulsions are mixtures of two immiscible fluids (e.g. oil and water) containing nanodomains, made thermodynamically stable by adsorption of surfactants[14]. Water-in-oil (w/o) microemulsions were prepared for each surfactant and characterized by visual inspection (optically transparent) and by SANS (Figure 7.12, Table 7.3). Water plays an important role in the stabilization of reverse micelles of charged surfactants, with hydrated cations being ineffective at screening repulsions between head groups at low w values (w = [water] / [surfactant]). It is also known that metal counterion exchange can lead to significant changes in intermolecular interactions, which may result in sphere-to-rod micellar shape transitions[15]. However, for the systems studied here SANS data are consistent with spherical micelles, as has been found for other transition metal and lanthanide based AOT microemulsions[16]. The SANS analyses are consistent with only weakly polydisperse spheres (normalized standard deviation $\sigma/R \sim 0.20$), and it is recognized that quantum effects cannot be observed in widely polydisperse assemblies[17].

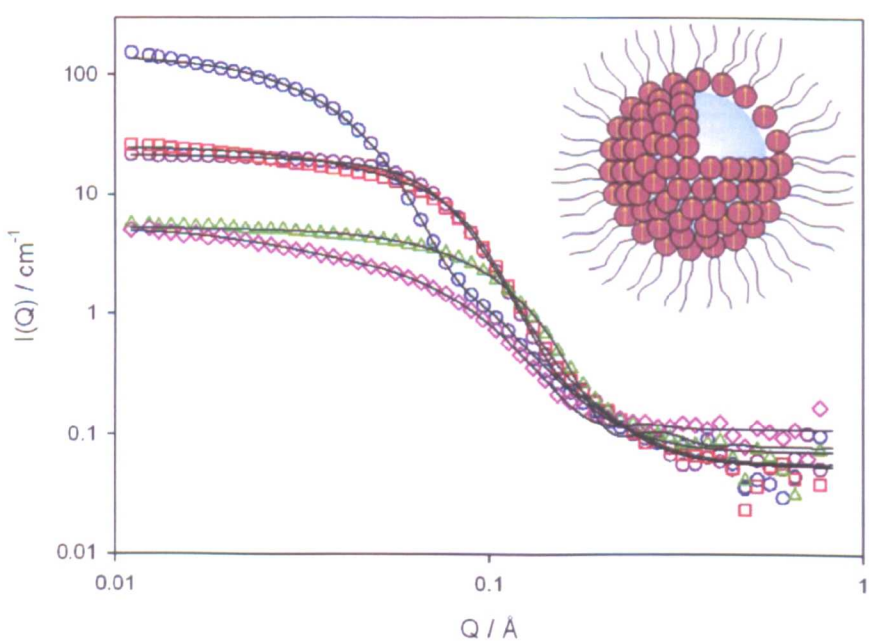

Figure 7.12: SANS profiles for D_2O-in-heptane microemulsions at 25 °C. Lines are model fits (parameters in Table 7.3). Na(AOT) (○), $Co(AOT)_2$ (○), $Mn(AOT)_2$ (□) $Ce(AOT)_3$ (△), $Ho(AOT)_3$ (◇). Inset is a schematic of a typical microemulsion droplet with aligning spins in a magnetic field.

Many studies have been undertaken on Na(AOT) w/o microemulsions, showing that it forms discrete spheres regardless of experimental conditions (*e.g.* pressure, temperature, surfactant chain length *etc.*) and that the mean radius of the internal water core, r_c, is directly related to the w value[15]. For Na(AOT), $r_c = 1.8w$. For $w = 13.7$ studied here, it should be expected that $r_c = 25$ Å agreeing with the value elucidated by SANS, $r_c = 26$ Å (Table 7.2).

Compound	w	Shape	R / Å
Na(AOT)	13.7	sphere	26 (30)
$Co(AOT)_2$	63.6	sphere	61[a] (57)
$Mn(AOT)_2$	27.8	sphere	25(28)
$Ce(AOT)_3$	24.6	sphere	21(21)
$Ho(AOT)_3$	26.7	sphere	21(22)

Table 7.3. Parameters fitted to SANS data from w/o microemulsions at 25 °C using polydisperse sphere model. [a]Guinier analysis. Bracketed values from Porod analysis.

The magnetic behaviour of these microemulsions was investigated with interesting results (Table 7.4). All the emulsions exhibit effective magnetic moments (calculated from molar susceptibilities) far above those for the pure surfactants.

Compound	Calculated μ_{eff} / B.M.	Observed μ_{eff} in surfactants / B.M.	Observed μ_{eff} in microemulsions / B.M.
Na(AOT)	0	-	-
$Co(AOT)_2$	4.20	4.15	9.83
$Mn(AOT)_2$	5.92	5.07	7.67
$Ce(AOT)_3$	2.54	1.46	6.23
$Ho(AOT)_3$	10.60	10.43	16.26

Table 7.4. Magnetic properties derived from SQUID magnetometry.

Effective magnetic moments for microemulsions calculated in a field of 10 kOe at 300 K.

A characteristic sigmoidal magnetization M-H curve is observed with M approaching saturation at high H (Figure 7.13, right). A $1/\chi_m$ *vs* T plot suggests that the Ho-based microemulsion is ferromagnetic below $T =$ 75 K but superparamagnetic above that. This is completely different to the magnetic phase behaviour

observed for the pure surfactant. However, similar results have been observed in literature for magnetite nanoparticle-based Pickering emulsions, whereby dry samples were ferromagnetic but colloidal samples were superparamagnetic[18]. The result may be due to magnetic anisotropy, preventing random fluctuations and fixing the spatial orientation of the magnetization (a magnetization reorientation barrier).

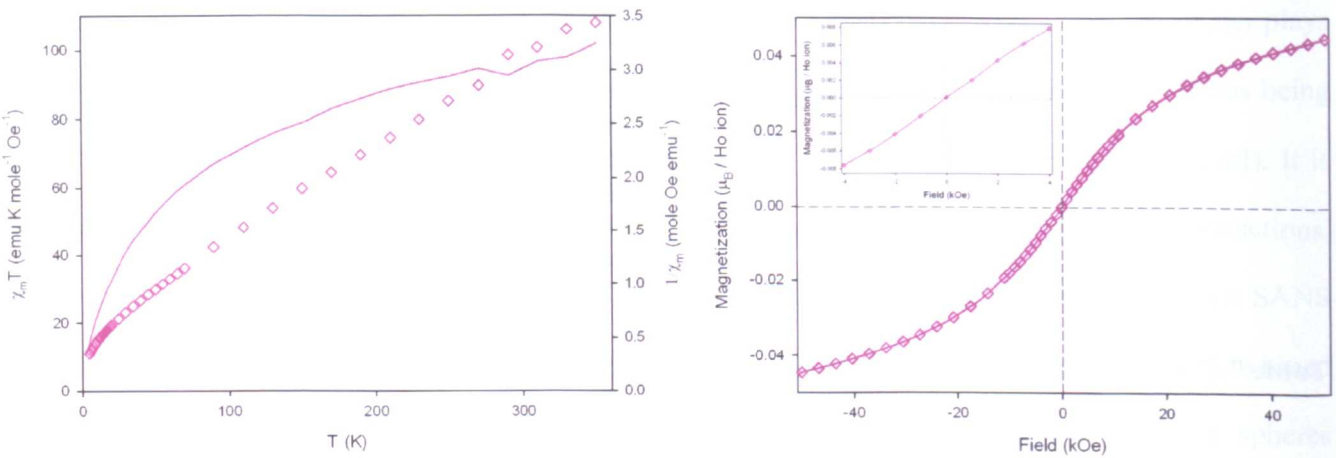

Figure 7.13: SQUID magnetometry data showing **left:** temperature dependence of $\chi_m T$ (symbols) and $1/\chi_m$ (line) for $Ho(AOT)_3$ measured under 0.50 kOe and **right:** magnetization versus applied magnetic field (inset shows the detail of the low magnetic field region).

Formation of microemulsions (typically $n = 75 - 150$ for the compounds studied here) or micelles ($n \sim 20$)[19] reduces the domain size and causes the magnetic moment of the "cluster" to become sensitive to thermal fluctuations (high dipole mobility), whereas the individual atomic moments maintain their ordered state relative to each other (high domain alignment)[17]. This leads to the anhysteretic, but still sigmoidal, *M–H* curve[20]. In comparison to magnetic anisotropy in MNPs arising from a contribution from both the bulk material (magnetocrystalline anisotropy) and the surface anisotropy[21], magnetic microemulsions only display surface anisotropy as all surfactant molecules are partitioned at the water/oil interface – displaying behaviour seemingly intermediate between MNPs and molecular magnets. The same effects can be seen for each surfactant and the respective microemulsion. Regardless of w/o water content and micelle volume fraction, the magnetic properties of the microemulsions are always much higher than those of the "dry" surfactant. This result is especially interesting because it demonstrates that magnetic surfactants behave like conventional surfactants in forming monolayers (e.g. microemulsions), but now the monolayers are

magnetic. These properties might allowing for routes to new Langmuir-Blodgett films, for the development of magnetic information storage, or as components in electronic or spintronic devices where interfacing magnetic material is essential[22].

7.3 Conclusions

In conclusion this chapter reports the synthesis of new anionic magnetic surfactants, which stabilize magnetic reversed micelles and microemulsions. These magnetic surfactants behave like typical $M^{n+}(AOT)_n$ compounds which are routinely used for the controlled synthesize (size and shape) of nanoparticles[2d].

Importantly, the intrinsic magnetic behaviour of microemulsions prepared form these lanthanide –based anionic surfactants were investigated for the first time and it was found that through the partitioning of metal ions at the oil/water interface unprecedented magnetic susceptibilities could be observed. The superparamagnetic behaviour not only suggests potential for new biomedical strategies, but also provides a new way to investigate evolution from molecular through to bulk solid-state magnetic limits simply by the tuning of composite volume fractions.

7.4 References

1. J. Klier; C. J. Tucker; T. H. Kalantar; D. P. Green, *Adv. Mat.*, 2000, *12*, 1751.
2. (a) J. Eastoe; D. C. Steytler; B. H. Robinson; R. K. Heenan; A. N. North; J. C. Dore, *J. Chem. Soc. Faraday Trans.*, 1994, *90*, 2497; (b) J. Eastoe; S. Stebbing; J. Dalton; R. K. Heenan, *Colloids Surf. A*, 1996, *119*, 123; (c) Y. Xing; M. Li; S. A. Davis; A. J. Patil; S. Mann, *Soft Matter*, 2006, *2*, 603; (d) M. P. Pileni, *Langmuir*, 1997, *13*, 3266.
3. W. L. Hough; M. Smiglak; H. Rodriguez; R. P. Swatloski; S. K. Spear; D. T. Daly; J. Pernak; J. E. Grisel; R. D. Carliss; M. D. Soutullo; J. J. H. Davis; R. D. Rogers, *New J. Chem.*, 2007, *31*, 1429.
4. I. McGill, *Rare Earth Elements*, Wiley-VCH: Weinheim, 2005.
5. (a) S. Arndt; J. Okuda, *Adv. Synth. Catal.*, 2005, *347*, 339; (b) J. C. G. Bünzli; V. J. Pecharsky, *Handbook on the Physics and Chemistry of Rare Earths*, Elsevier: Amsterdam, 2012; Vol. 42.
6. H. D. Burrows; M. J. Tapia, *Langmuir*, 2002, *18*, 6706.
7. K. Trickett; D. Xing; J. Eastoe; R. Enick; A. Mohamed; M. J. Hollamby; S. Cummings; S. E. Rogers; R. K. Heenan, *Langmuir*, 2009, *26*, 4732.
8. P. Brown; C. P. Butts; J. Eastoe; D. Fermin; I. Grillo; H.-C. Lee; D. Parker; D. Plana; R. M. Richardson, *Langmuir*, 2012, *28*, 2502.
9. G. Corsico; L. Mattei; A. Roselli; C. Gommellini, *Poly(internal olefins) - Synthetic and high-performance functional fluids*, Marcel Dekker: 1999.
10. J. Rogers; P. A. Winsor, *J. Coll. Int. Sci.*, 1969, *30*, 247.
11. Z. X. Li; A. Weller; R. K. Thomas; A. R. Rennie; J. R. P. Webster; J. Penfold; R. K. Heenan; R. Cubitt, *J. Phys. Chem. B*, 1999, *103*, 10800.
12. M. Kotlarchyk; S. M. Ritzau, *J. App. Cryst.*, 1991, *24*, 753.
13. J. A. Peters; J. Huskens; D. J. Raber, *Prog. Nucl. Magn. Reson. Spectrosc.*, 1996, *28*, 283.
14. I. Danielsson; B. Lindman, *Colloids Surf. A*, 1981, *3*, 391.
15. J. Eastoe; G. Fragneto; B. H. Robinson; T. F. Towey; R. K. Heenan; F. J. Leng, *J. Chem. Soc. Faraday Trans.*, 1992, *88*, 461.
16. (a) J. Eastoe; T. F. Towey; B. H. Robinson; J. Williams; R. K. Heenan, *J. Phys. Chem.*, 1993, *97*, 1459; (b) A. Beeby; I. M. Clarkson; J. Eastoe; S. Faulkner; B. Warne, *Langmuir*, 1997, *13*, 5816.

17. D. Gatteschi; R. Sessoli; J. Villain. *Molecular Nanomagnets*, 2006.

18. Z. Wang; C. Holm, *Phys. Rev., E* 2003, *68*, 041401.

19. I. M. Umlong; K. Ismail, *J. Coll. Int. Sci.*, 2005, *291*, 529.

20. Q. A. Pankhurst; J. Connolly; S. K. Jones; J. Dobson, *J. Phys. D: Appl. Phys.*, 2003, *36*, R167.

21. D. Gatteschi; M. Fittipaldi; C. Sangregorio; L. Sorace, *Angew. Chem. Internat. Ed.*, 2012, *51*, 4792.

22. D. R. Talham; M. W. Meisel, *Chem. Soc. Rev.*, 2011, *40*, 3356.

Chapter 8

Magnetizing DNA and proteins using responsive surfactants

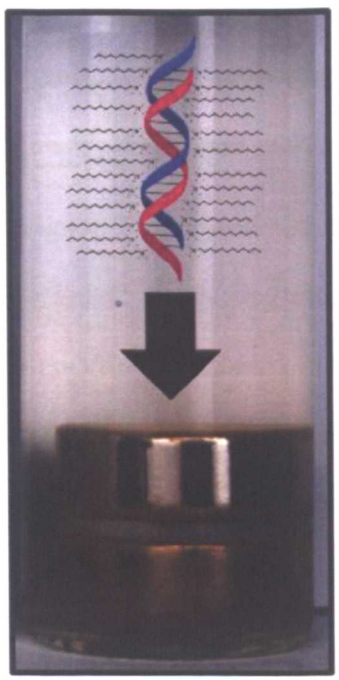

Chapter 8 investigates how DNA chains and their movement in solvent may now be controlled simply by surfactant binding and the switching "on" and "off" of a magnetic field adding a new paradigm to the study and control, condensation and manipulation of DNA (and other biomolecules). Such control is essential for biotechnological applications such as transfection and the regulation of gene suppression, as well as in materials science concerning soft molecular self-assemblies.

8.0 Introduction

One of the major challenges in biotechnology is the effective control over transport and delivery of biomolecules for the regulation of gene suppression[1], targeted drug delivery[1], and protein separation[2]. To date, magnetic field-based approaches using heterogeneous dispersions of magnetic particles have been used with some success[3], although for such systems to be employed efficiently, they must be able to inhibit sedimentation, be biocompatible, and nontoxic[4], The synthesis of ultrafine particles with these attributes is challenging, and interactions between particle surfaces and the associated biomolecules can often disrupt the native conformation and subsequent functions of the biomolecules[5], The advantages of employing magnetic surfactants[6] over nanoparticles include their facile fabrication (one-step synthesis), fast and effective binding (which can be readily tuned via alteration of the surfactant aliphatic groups and counterion[7]),and their good dispersibility and stability in solution, and the possibility of DNA-surfactant conjugate decompaction using either cyclodextrins[8] or via the formation of mixed micelles[9]. In this chapter, unprecedented low-strength magnetic field-induced migration of DNA and proteins via magnetic surfactant conjugation is presented. Moreover, near-native conformations of the biomolecules are maintained by careful control over the biomolecule: surfactant stoichiometry.

8.1 Experimental

8.1.1 Materials and Methods

Dodecyltrimethylammonium bromide (99%, DTAB), cetyltrimethylammonium bromide (99%, CTAB), iron trichloride (99.9%), gadolinium (III) trichloride hexahydrate, holmium (III) trichloride hexahydrate and Trizma® base (99.9% titration) were purchased from Sigma Aldrich and used without further purification. Dodecyltrimethylammonium trichloromonobromoferrate (DTAF) was synthesized according to chapter 4, by mixing equimolar amounts of DTAB with iron trichloride in methanol and stirring overnight at room temperature. The solvent was then removed and the product dried at reduced pressure at 80 °C overnight yielding brown/red solid. Dodecyltrimethylammonium trichloromonobromogadolinate (DTAG) and dodecyltrimethylammonium trichloromonobromoholminate (DTAH) were prepared in the same way yielding a white solid (Chapter 6)[6].

DNA (oligonucleotides from herring sperm, D-3159, <50bp) was purchased from Sigma. On preparing solutions, the final concentration of nucleic acid was 0.150 mM with respect to the phosphate groups. The DNA concentration was calculated according to the absorbance at 260 nm by using ε_{DNA} = 6600 M^{-1} cm^{-1} [10]. In all experiments, the DNA concentration was held constant at 0.150 mM and the surfactant to DNA base pair ratio was varied from X = 0 to X = 1.

Myoglobin (Mb, from equine heart) was purchased from Sigma Aldrich. Concentrations were calculated according to the absorbance at 409 nm by using ε_{Mb} = 171,000 M^{-1} cm^{-1} [11]. Cat-GFP was synthesized as follows: Escherichia coli host was transformed with a pET45b(+) plasmid vector, and used to express polyhistidine-tagged enhanced green fluorescent protein (eGFP), which was subsequently purified using a nickel nitriloacetic acid (Ni-NTA) column. The acidic residues of eGFP were covalently modified with DMPA, in a carbidiimide-mediated cationisation process to yield a protein with up to 44 cationic residues. Concentrations were calculated according to the absorbance at 277 nm by using ε_{GFP} = 55,000 M^{-1} cm^{-1} [12]. Purified water was used which had a high resistivity (18.2 MΩ cm) and a surface tension of 71.9 mN m^{-1} at 25 °C, in good agreement with literature values.

8.1.2 Critical micelle concentrations (cmcs)

Cmcs were determined though electrical conductivity measurements (Supporting Information): CTAB (0.8 mM, β = 0.14), DTAF (13.6mM, β = 0.81), DTAG (11.9mM, β = 0.59), DTAH (11.6 mM, β = 0.76).

8.1.3 pH

pH measurements of 0.1 M surfactant solutions in H_2O gave DTAF (pH 3.98), DTAG (pH 7.25) and DTAH (pH 7.27).

8.1.4 SQUID magnetometry

Magnetic properties were measured in a SQUID (superconducting quantum interference device) magnetometer (Quantum Design MPMS-5T) equipped with a 5T superconducting magnet. Theoretical values for high-spin d^5 Fe^{3+} (spin-only value = 5.92 B. M.[13]), Gd^{3+} (spin-only value = 7.94 B.M.[14]) and Ho^{3+} (calculated value = 10.60 B.M.[14]).

8.1.5 Stability Studies

The bulk behavior of aqueous mixtures of DNA (150mM)) and surfactant was investigated (by visual inspection) at 25 °C in order to determine appropriate concentrations for magnetic experiments. Stock solution of DNA was prepared by dissolving commercial nucleic acid in water and fragmenting by sonic vibration with a sonic probe (MSE Soniprep 150 (UK), 23 KHz, 1 min sonication time). The required amount of surfactant solution was then slowly added to avoid aggregation.

8.1.6 Dynamic Light Scattering (DLS)

DLS measurements were taken to define the boundaries at which DNA compaction occurred. Measurements were performed on a Malvern Instruments Zetasizer Nano ZS (Malvern, UK) using a constant scattering angle of 90° at 25 °C. All solutions were made dust-free by filtration through cellulose acetate membranes of 0.45 mm pore size (Millipore, USA).

4 mL of DNA solution containing appropriate amounts of surfactant were allowed to equilibrate for 5 hours. Measurements were taken on the same day as preparation for samples that had not precipitated.

8.1.7 Circular Dichroism

Synchrotron radiation circular dichroism (SRCD) spectra were collected at the Diamond Light Source on beamline B23 over a wavelength range of 330 to 200 nm with an integration time of 2 s and 1 nm data intervals. Samples were run in 1.0 cm quartz cuvette cells with 4 accumulations. Concentrations were chosen below the point of precipitation (50μM surfactant and 150μM DNA).

8.1.8 UV-Visible Spectrometry

UV-Vis absorption spectra were recorded on a Nicolet Eco 300 UV-Vis spectrometer. An aqueous solution (60 mL) of DTAG (0.05μM) and DNA (150μM) was placed in two specially built glass vials. One vial also contained a NdFeB magnet (12 mm x 3mm, N52) with a magnetic field density of 0.44 T on the surface and a gradient of about 36 mT mm^{-2}. The top 1.5 mL was removed for analysis over time and replaced carefully each time.

The UV-Vis experiments were also repeated using myoglobin and cationized green fluorescent protein (cat-GFP). For the myoglobin solutions DTAH was used was used and for cat-GFP, DTAG was used. [myoglobin] = 11.6 μM, [DTAH] = 3.03 mM; [cat-GFP] = 38 μM, [DTAG] = 687 μM.

8.2 Results and Discussion

8.2.1 DNA binding and magnetic manipulation

The magnetic cationic surfactants DTAF[6] ($[C_{15}H_{34}N]^+[FeCl_3Br]^-$), DTAG ($[C_{15}H_{34}N]^+[GdCl_3Br]^-$) and DTAH ($[C_{15}H_{34}N]^+[HoCl_3Br]^-$) were synthesized using commercially available compounds to contain high-spin Fe(III), Gd(III) and Ho(III)-based counterions, resulting in high effective spin-only magnetic moments of 5.09 B.M., 7.42 B.M. and 9.53 B.M. respectively. The addition of the surfactants to DNA (from herring sperm < 50 bp) and exposure to a magnetic field (0.44 T) resulted in effective migration of the DNA-surfactant complex to the magnet surface. This in turn increased the local concentration of the complex beyond the solubility limit, which resulted in deposition at the point of highest magnetic field density (Figure 8.1).

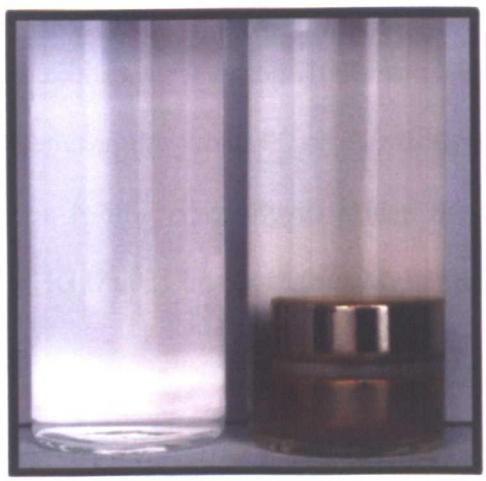

Figure 8.1: DNA-DTAG complex after 5 days in the absence of a magnetic field (left) and in the presence of a magnetic field (right). [DNA] = 150 μM, and [DTAG] = 50 μM.

UV-visible spectroscopy revealed a small reduction in the intensity of the characteristic absorbance maximum at 260 nm on mixing very low concentrations of DTAG (50 μM) and DNA (150 μM) in the

absence of a magnetic field, but importantly there was no evidence of aggregation over 96 hours (Figure 8.2a). Significantly, applying a small magnetic field (0.44T, gradient ~36 mT mm^{-2}) to stable aqueous solutions of DNA-surfactant complexes resulted in a notable reduction in the 260 nm peak intensity (Figure 8.2b), which equated to a decrease in DNA concentration of 48 % over four days. This was accompanied by a concomitant elevation of the baseline, which was indicative of aggregation due to the increased concentration of the complex adjacent to the magnet surface.

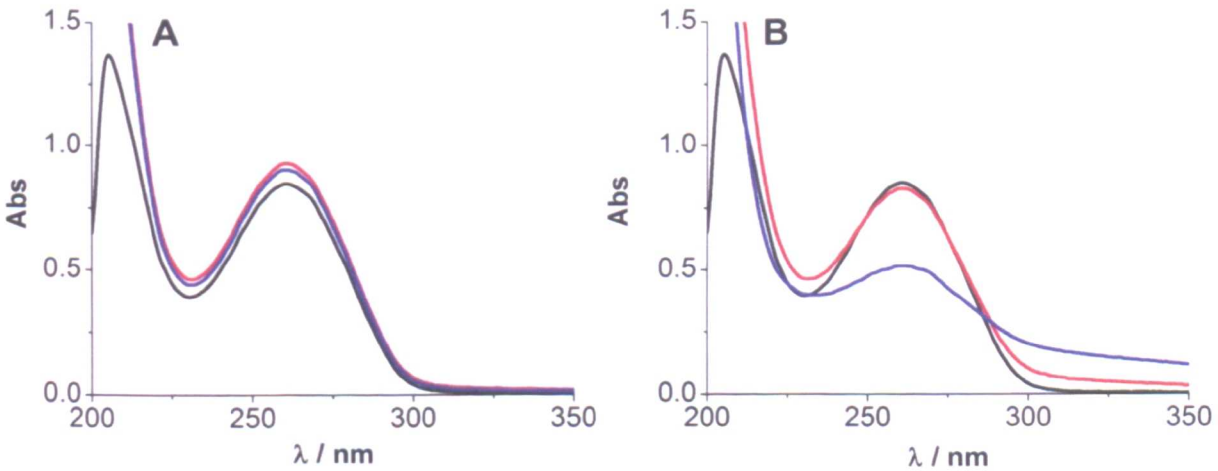

Figure 8.2: UV-Visible spectrum of the stable DNA-DTAG complex in (A) the absence of a magnetic field and (B) in the presence of an applied magnetic field. t = 0 (black line), t = 24 hrs (red line) and t = 96 hrs (blue line).

At higher DNA or magnetic surfactant concentrations, the strong attraction between DNA and DTAG (micelles) resulted in the formation of overcharged aggregates that led to macroscopic phase separation in less than one hour. These aggregates can be manipulated with small magnets (0.2T) (Figure 8.3 and 8.4), which, for *in vitro* applications may be useful as it may increase sedimentation of the complexes and the rate of transfection[1].

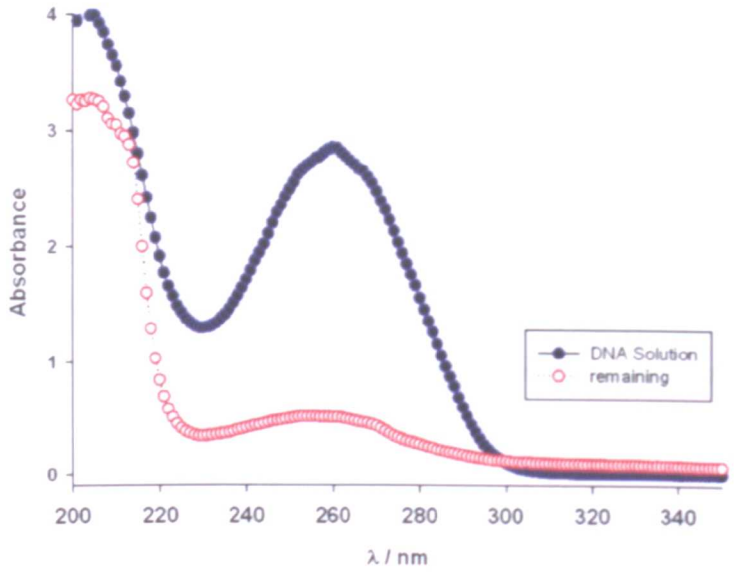

Figure 8.3: As an excess of DTAF (5.44 mM) is added to a DNA solution 0.43 mM DNA-DTAF complex precipitates reducing the amount of surfactant in the supernant by 81% in under 1 hour. The precipitate is magnetic (*c.f.* Figure 8.4).

Figure 8.4: The magnetization of DNA by DTAF (left) and DTAG (right).

The magnet is NdBFe (0.2 T).

8.2.2 Circular dichroism

The synchrotron radiation circular dichroism (SRCD) spectrum of DNA (Figure 8.5) showed the characteristic β-form with a negative peak at 248 nm due to helicity of the DNA, a positive peak at 285 nm due to base stacking, and a crossover peak at approximately 260 nm corresponding to the wavelength maximum for normal absorption. The inert CTAB (cetyltrimethylammonium bromide $C_{16}H_{33}N(CH_3)_3Br$)

and magnetic DTAG bind to the DNA duplex with no change in the peak positions, which indicated that the β-form persisted. Native DNA has no CD spectrum above 300 nm, however, the DNA-surfactant complexes still exhibited a positive signal up to 320 nm, which was indicative of the formation of globular structures (condensation)[15]. Moreover, the reduction in the peak intensity at 285 nm observed for the DNA- and DTAG-DNA complexes was consistent with alterations in the degree of helix hydration in the vicinity of phosphate and ribose ring due to changes in the local dielectric constant[16], *i.e.* exchange of the native sodium counterion with the hydrophobic cationic surfactant DTAG would have lead to such changes in the hydration near the phosphate group of the DNA helix[17]. The decreasing intensities of the 248 nm and 285 nm peaks also suggested that DNA compaction had occurred, resulting a reduction in the number of base pairs per helical period as the helical pitch shortens.

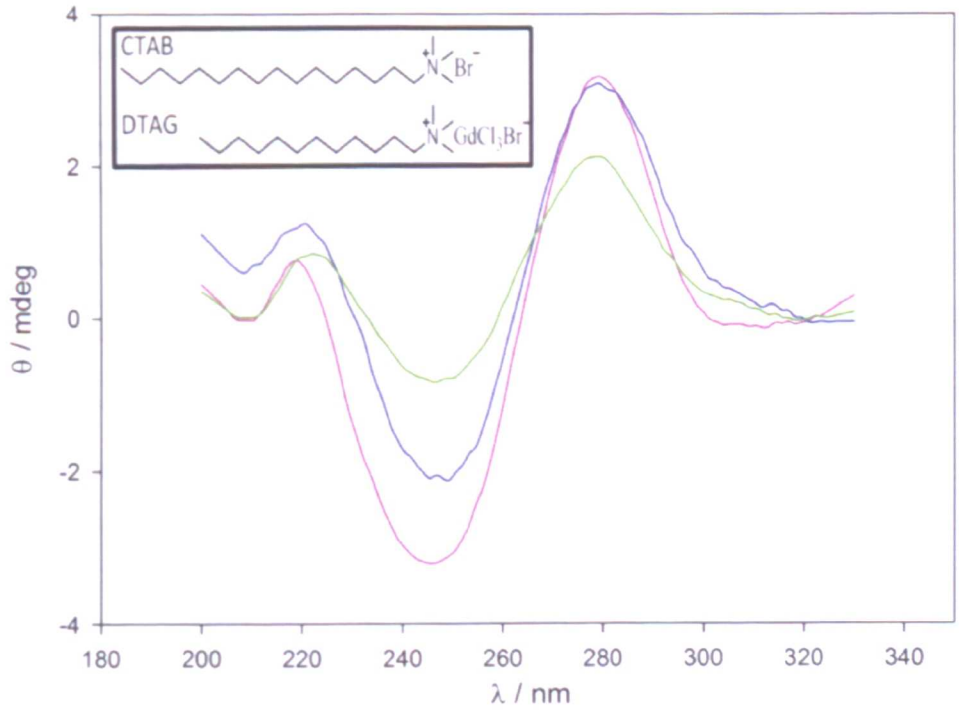

Figure 8.5: Synchrotron radiation circular dichroism (SRCD) spectra showing the effect of cationic surfactant addition on the conformation of herring sperm DNA. [DNA] = 150 μM; [surfactant] = 50 μM. Native DNA (pink line), DNA-CTAB (blue line), DNA-DTAG (green line).

8.2.3 Dynamic light scattering study of DNA compaction

It is well established that the helical structure of DNA and its effective compaction can be achieved by the addition of complexing cationic agents such as CTAB[18], whereby isolated DNA chains undergo a discrete

coil–globule transition in solution, upon the addition of even a very low concentration of surfactant (well below its critical micelle concentration, cmc)[19]. Initially the cationic surfactant interacts with DNA by electrostatic interactions, and it has been postulated that CTAB binds to DNA with one CTAB molecule bound per DNA phosphate group[20]. This is followed by hydrophobically-driven cooperative binding leading to a region of coexistence between unbound DNA chains and those saturated with surfactant[21]. This surfactant-induced compaction of DNA leads to a decrease in hydrodynamic radius, thereby changing its translational diffusion coefficient. Dynamic light scattering (DLS) measurements probe this change directly, showing coil-globule coexistence in bulk solution. Here, DNA extended coils diffuse slowly compared to surfactant-compacted DNA. At surfactant to DNA base pair ratios (X = [surf]/[PO_4^-]) greater than one (CTAB 5.2 – 36.3; DTAB 1.33 – 6.66) and relatively low DNA concentration (0.150 μM) (Figure 8.6 and Table 8.1) CTAB reduced the hydrodynamic radius of DNA by around 53% (232 nm to 108 nm).

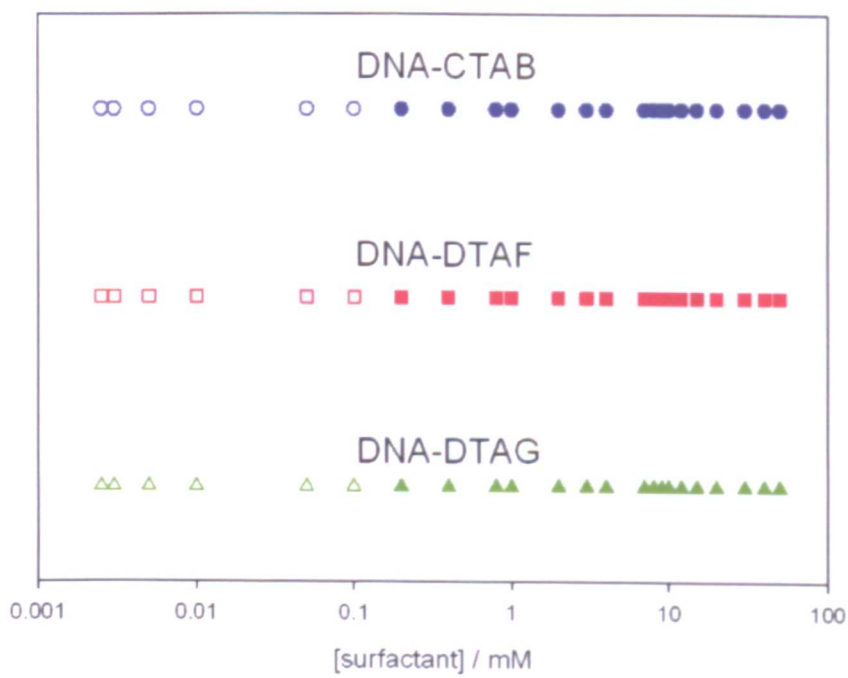

Figure 8.6: Phase map of aqueous mixture of DNA and surfactant presented as a function of surfactant concentration at 25 °C after 5 days. Open symbols represent clear stable samples, whereas filled symbols represent macroscopically phase separated samples.

Compound	[DNA] / mM	[surfactant] / mM	X	Size / nm	Size reduction / %
DNA	0.150	0.00	-	232	-
DNA-CTAB	0.150	5.44	36.27	105	77.4
DNA-CTAB	0.150	2.72	18.13	111	76.0
DNA-CTAB	0.150	1.36	9.07	100	78.3
DNA-CTAB	0.150	1.09	7.27	107	77.0
DNA-CTAB	0.150	0.73	4.87	117	74.7
DNA-DTAF	0.150	1.00	6.67	66	85.8
DNA-DTAF	0.150	0.80	5.33	63	86.3
DNA-DTAF	0.150	0.60	4.00	63	86.4
DNA-DTAF	0.150	0.40	2.67	63	86.3
DNA-DTAF	0.150	0.20	1.33	63	86.3

Table 8.1: Apparent DNA-surfactant size (nm) as a function of surfactant concentration (at high concentration) determined by DLS. X = [surfactant]/[PO_4^-]

This was similar to results reported by Cardenas *et al.*[22], who showed that CTAB induced a transition of the DNA hydrodynamic radius from about 100 nm to about 50 nm (~50%). In comparison, DTAF compacted DNA even more efficiently, resulting in a 72% reduction in hydrodynamic radius (64 nm), which was almost half that of CTAB. Solutions of DNA-DTAG were not stable for long periods at this concentration, and stability studies showed that the CTAB and DTAF complexes of DNA also precipitated after 1 day. Lower surfactant to DNA base pair ratios (0.006 – 1) yielded DNA-surfactant complexes that were stable in solution over five days, and DLS again showed a maximum in surfactant-induced compaction at X = 0.33 for all surfactants (Figure 8.7).

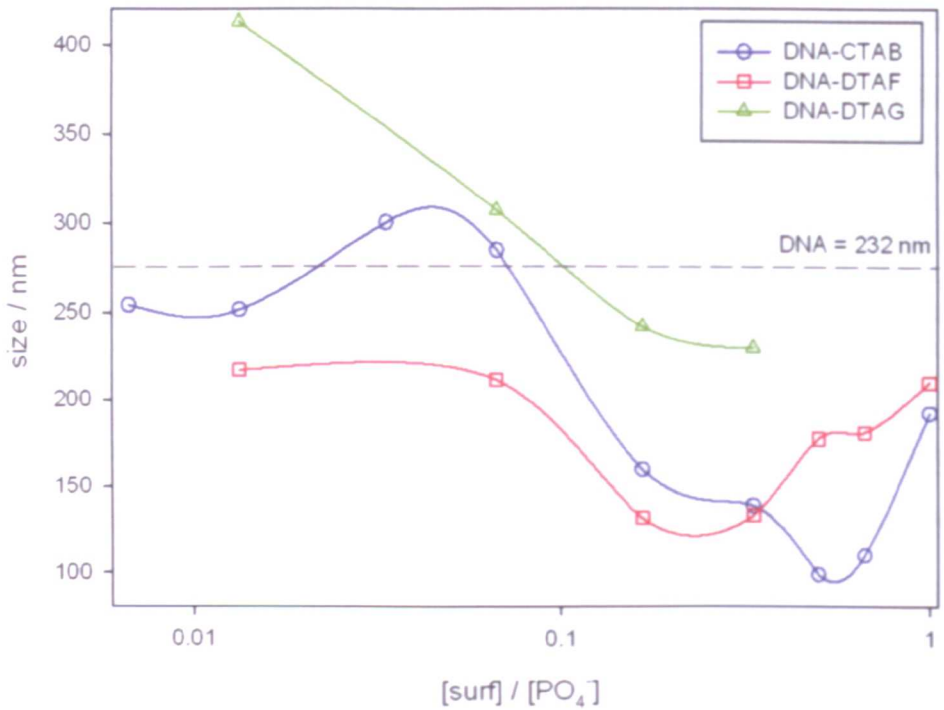

Figure 7: DNA compaction by inert CTAB and magnetic DTAF and DTAG as a function of the surfactant to DNA-phosphate molar charge ratio, *X*, at 25 °C.

8.2.4 Magnetic manipulation of biomolecules

The ability to control the migration of DNA using magnetic surfactants was also extended to myoglobin and green fluorescent protein (GFP). The UV-visible spectrum of the myoglobin surfactant complexes (Figure 8.8) gave an intense Soret band at 409 nm, as well as Q_α and Q_β bands at 641 nm and 502 nm respectively. These three adsorption bands were indicative of metmyoglobin with a low-spin (diamagnetic) heme group and a six-coordinate geometry with a strongly bound water molecule[23]. It is well known that ionic surfactants can denature myoglobin via strong binding to the charged and hydrophobic side chains[24], but adding DTAH below the cmc did not result in a shift in the positions of the characteristic adsorption bands, suggesting that there were no significant changes in the tertiary structure in the vicinity of the heme prosthetic group. Similar findings have been made after addition of anionic surfactants to myoglobin without denaturation[25]. With no magnetic field present, the myoglobin surfactant complex concentration remained constant, but after application of the magnetic field there was a reduction in concentration by approximately 60 % (11.6 μM to 4.64 μM) over five days.

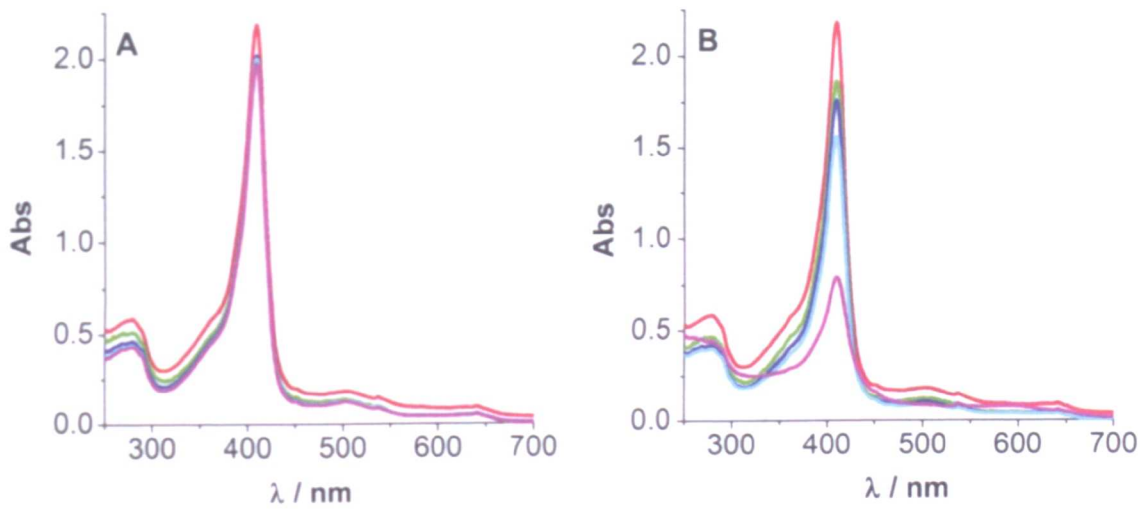

Figure 8.8: UV-Visible spectra of myoglobin-DTAH in (A) the absence of a magnetic field and (B) in the presence of a magnetic field. [Mb] = 11.6 μM; [DTAH] = 3.03 mM. t = 0 (red line), t = 12 hrs (green line), t = 36 hrs (light blue line), t = 50 hrs (dark blue line), t = 120 hrs (pink line).

The UV-visible spectrum from the Cat-GFP-DTAG complex (Figure 8.9) also showed no variation from the native protein, exhibiting the characteristic fluorophore absorbance at 277 nm (due to aromatic residues in the polypeptide side chain) and a broad band at around 500 nm (resulting from absorption at the Cat-GFP chromophore), which indicated that the presence of the surfactant corona had little or no effect on the protein structure. Exposure of the complex to the magnetic field results in aggregation (as can be seen by a rise in the peak at 277 nm). This aggregation occurs concomitantly with migration towards the magnet surface lowering the overall Cat-GFP at concentration by an estimated 25 % over 150 hrs (as seen by a reduction in 277 nm peak beginning after 110 hrs).

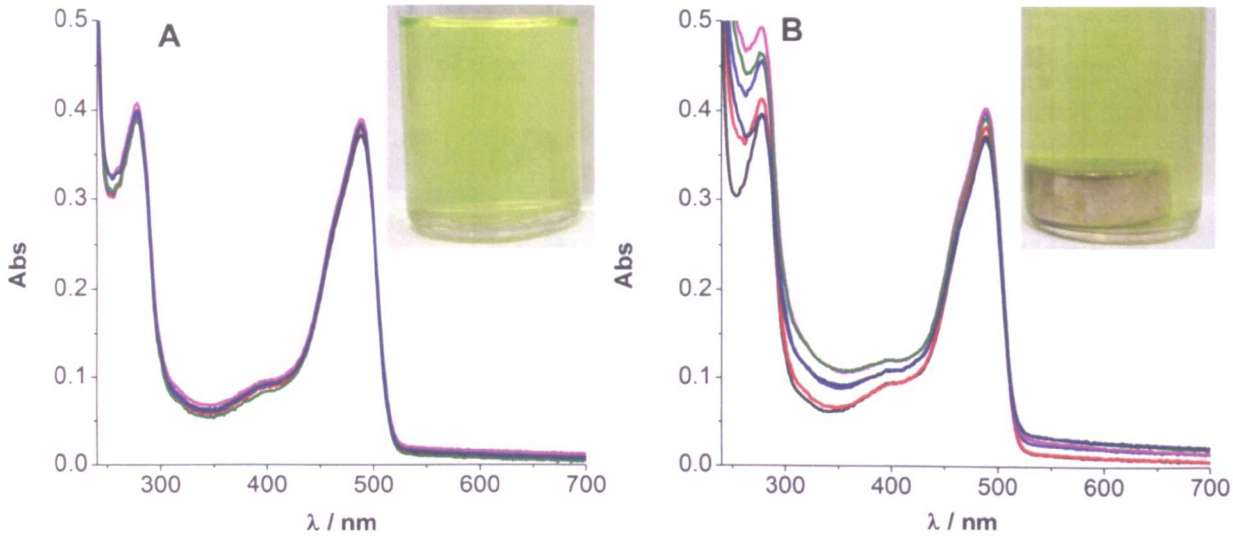

Figure 8.9: UV-Visible spectra of Cat-GFP-DTAG in (A) the absence of a magnetic field and (B) in the presence of a magnetic field. [catGFP] = 38 μM, [DTAG] = 687 μM. t = 0 (black line), t =18 hrs (red line), t = 36 hrs (light blue line), t = 60 hrs (pink line), t = 110 hrs (green line) and t = 150 hrs (dark blue line).

Exposure of the complex to the magnetic field also resulted in migration, as evidenced by a 25% reduction in the 277 nm peak intensity over 150 hrs. The concentration gradient also resulted in aggregation (as can be seen by a rise in the peak at 277 nm). Aggregates and unimers are then drawn towards the magnet surface lowering the overall GFP concentration after 150 hrs (*c.f.* decrease in 277 nm peak after 110 hrs).

8.3 Conclusions

In conclusion, this chapter demonstrates how novel magnetic surfactants compact DNA and bind to proteins just like conventional surfactants, and how they allow DNA-surfactant and protein-surfactant complexes to be manipulated by an external magnetic field. Until now all magnetic approaches have involved magnetic nanoparticles[3], which are often difficult to synthesis with potential toxic effects. Other methods of DNA and protein manipulation such as electrophoresis have widespread application in diagnostics[26] but have disadvantages such as toxicity and degradation of DNA/protein molecules; disadvantages which may be avoided with a magnetic approach.

This new paradigm for controlling biomolecules is significant as the studies suggest a strategy that can be applied to a diverse range of systems cheaply and non-invasively and could be readily developed for a wide range of biological structures and techniques.

8.4 References

1. J. Dobson, *Gene Ther.*, 2006, *13*, 283.
2. I. S. Lee; N. Lee; J. Park; B. H. Kim; Y.-W. Yi; T. Kim; T. K. Kim; I. H. Lee; S. R. Paik; T. Hyeon, *J. Am. Chem. Soc.*, 2006, *128*, 10658.
3. (a) S. C. McBain; H. Yiu; J. Dobson, *Int. J. Nanomed.*, 2008, *3*, 169 ; (b) O. Mykhaylyk; D. Vlaskou; N. Tresilwised; P. Pithayanukul; W. Möller; C. Plank, *J. Magn. Magn. Mat.*, 2007, *311*, 275; (c) C. Plank; O. Zelphati; O. Mykhaylyk, *Adv. Drug Delivery Rev.*, 2011, *63*, 1300.
4. P. Tartaj; M. P. Morales; T. González-Carreño; S. Veintemillas-Verdaguer; C. J. Serna, *J. Magn. Magn. Mat.*, 2005, *290–291*, 28.
5. I. Lynch; K. A. Dawson, *Nano Today*, 2008, *3*, 40.
6. P. Brown; A. Bushmelev; C. P. Butts; J. Cheng; J. Eastoe; I. Grillo; R. K. Heenan; A. M. Schmidt, *Angew. Chemie Int. Ed.*, 2012, 2414.
7. V. M. Jadhav; R. Valaske; S. Maiti, *J. Phys. Chem. B*, 2008, *112*, 8824.
8. A. Bilalov; J. Carlstedt; E. Krivtsova; B. Lindman; U. Olsson, *Soft Matter*, 2012, *8*, 4988.
9. R. S. Dias; B. Lindman; M. G. Miguel, *J. Phys. Chem. B*, 2002, *106*, 12608.
10. G. Cosa; K. S. Focsaneanu; J. R. N. McLean; J. P. McNamee; J. C. Scaiano, *Photochem. Photobiol.*, 2001, *73*, 585.
11. D. Puett; W. t. t. a. o. E. Friebele; B. K. Wasserman, *J. Biol. Chem.*, 1973, *248*, 4623.
12. S. R. McRae; C. L. Brown; G. R. Bushell, *Protein Expr. Purif.*, 2005, *41*, 121.
13. D. Moon; J. Kim; M. S. Lah, *Bull. Korean. Chem. Soc.*, 2006, *27*, 1597.
14. J. A. Peters; J. Huskens; D. J. Raber, *Prog. Nucl. Magn. Reson. Spectrosc.*, 1996, *28*, 283.
15. J. Kypr; I. Kejnovská; D. Renčiuk; M. Vorlíčková, *Nucleic Acids Res.*, 2009, *37*, 1713.
16. S. Hanlon; S. Brudno; T. T. Wu; B. Wolf, *Biochemistry*, 1975, *14*, 1648.
17. C. H. Spink; J. B. Chaires, *J. Am. Chem. Soc.*, 1997, *119*, 10920.
18. R. Dias; S. Mel'nikov; B. Lindman; M. G. Miguel, *Langmuir* 2000, *16*, 9577.
19. S. Marchetti; G. Onori; C. Cametti, *J. Phys. Chem. B*, 2006, *110*, 24761.
20. A. Bonincontro; S. Marchetti; G. Onori; A. Rosati, *Chem. Phys.*, 2005, *312*, 55.

21. D. M. McLoughlin; J. O'Brien; J. J. McManus; A. V. Gorelov; K. A. Dawson, *Bioseparation*, 2000, *9*, 307.

22. M. Cardenas; K. Schillen; T. Nylander; J. Jansson; B. Lindman, *Phys. Chem. Chem. Phys.*, 2004, *6*, 1603.

23. (a) M. Ikeda-Saito; H. Hori; L. A. Andersson; R. C. Prince; I. J. Pickering; G. N. George; C. R. Sanders; R. S. Lutz; E. J. McKelvey; R. Mattera, *J. Biol. Chem.*, 1992, *267*, 22843; (b) E. Antonini; M. Brunori, *Hemoglobin and myoglobin in their reactions with ligands*, North-Holland Publishing Company Amsterdam: London, 1971.

24. K. K. Andersen; P. Westh; D. E. Otzen, *Langmuir*, 2007, *24*, 399.

25. A. W. Perriman; A. P. S. Brogan; H. Cölfen; N. Tsoureas; G. R. Owen; S. Mann, *Nat Chem.*, 2010, *2*, 622.

26. A. L. Shapiro; E. Viñuela; J. V. Maizel Jr, *Biochem. Biophys. Res. Commun.*, 1967, *28*, 815.

Chapter 9
Conclusions and Future Work

9.0 Project conclusions

There has been much interest recently in ionic liquids (ILs) as not only do they have significant effects on reaction rates[1] and stereoselectivity[2, 3] of certain organic reactions they also promise greener alternatives to conventional molecular solvents[4]. However, most ionic liquids are based on imidazolium and halides which have unknown toxicity, and are not suitable for use with strong bases and Grignard reagents, they are also not especially cheap. For this reason new surfactant ionic liquids (SAILs) were developed and characterized that are more straightforward to synthesize (through ion exchange), more environmentally friendly (halide and imidazolium free), and potentially much less toxic and cheaper than almost all ionic liquids that have come before[5]. By compiling a matrix of compounds spanning the threshold between standard solid surfactants and the newer class of surfactant ionic liquids, and through detailed small-angle neutron scattering (SANS) studies it was shown that there is no magic switch in behaviour as traditional crystalline surfactants are transformed into surfactant ionic liquids, and that ionic liquid nature confers no special properties on SAILs. However, SAILs do offer advantages over conventional (microheterogeneous) ionic liquids.

A detailed investigation into SAILS based on organic surfactant anions and imidazolium cations[6] (again through facile synthesis and allowing for tunability of physico-chemical properties) showed that structuring of pure ionic liquid, aggregation in dilute aqueous solution and the possibility of switching between the two might have potential applications catalytic reaction control, but also in electrochemistry, battery design and supercapacitors owing to high capacitances, low densities and the ability to partition on an electrode surface depending on applied potential and concentration. Interestingly, these SAILs exhibited large electrochemical windows even though some residual water was present.

Surfactant ionic liquids were then developed to be magneto-responsive[7]. Only recently have magnetic ILs been discovered[8] because although ILs containing transition metals had been known it was always thought that long range communication between metal centres necessary for exhibiting magnetism did not exist. Unexpectedly, the new magnetic SAILs presented in this thesis were not only magnetic in the pure ionic

liquid phase but also in dilute aqueous solution. SANS showed that these new nanoparticle-free ferrofluids aggregated just like normal surfactants, though surprisingly large changes in counterion resulted in only minor changes in micellar shape. Importantly their physico-chemical behaviour could be controlled by the switching "on" and "off" of a magnetic switch. For example, interfacial tensiometry showed that these compounds are not only more efficient at reducing interfacial tension than their inert parent analogues, but are also bifunctional, exhibiting a further reduction in an applied magnetic field.

In order to optimize the magnetic surfactants different metal counterions (mainly lanthanides) were also considered producing surfactants with larger magnetic susceptibilities and more complicated magnetic phase behaviour. SQUID magnetometry was applied to investigate the full magnetic phase behaviour of these new magnetic surfactants as a function of temperature.

To demonstrate some "out of the laboratory" applications, emulsions were generated from brine, lubrication oil, heptane and/or water and investigated using dynamic light scattering (DLS)[9]. DLS results showed little difference between magnetic and inert emulsion droplets. However, the magnetic emulsions could be manipulated in a magnetic field, overcoming gravity and solvent viscosity. Emulsions could also be produced that respond to magnetic fields considered appropriate for targeted drug delivery[10]. All approaches so far have relied on Pickering emulsions[11] and this should be regarded as the first nanoparticle-free approach to drug delivery. This is an important approach as it has advantages over current methods, being more biocompatible, easier to fabricate (control of emulsion size and shape through appropriate surfactant selection and volume fractions of the two immiscible phases is well established) and could potentially be less toxic.

Whilst emulsions are commercially very useful, microemulsions are much easier to study due to their long term stability. Full phase diagrams were produced for some of the cationic magnetic surfactants but most important were the microemulsions formed from anionic magnetic surfactants. Some of these compounds were new but others were known for over 20[12, 13]. Surprisingly their intrinsic magnetic properties had never been investigated and their use was limited to aid control of nanoparticle synthesis. These microemulsions exhibited superparamagnetism with effective magnetic moments far above those expected for the solid surfactant. It was postulated that this effect arises from a lack of bulk anisotropy as all magnetic surfactants are partitioned at the water/oil interface. Typically nanomagnets are produced either by nanoparticle

synthesis (with a minimum size of ~400 metal centres) or through molecular magnets (with a maximum size of ~20 metal centres)[14]. Now it should be possible to control the size of nanomagnets and their magnetic properties to bridge this gap and simply by altering volume fractions of the component parts.

If microemulsion formation allows for the close proximity of metal centres while allowing for thermal fluctuations to play a role then this should also be the case for micelles. In fact the anionic microemulsions studied are simple inverse micelles. For this it was attempted to establish whether a critical micelle concentration could be determined through magnetometry. The results are a little ambiguous as only small effects are expected to be seen with the cationic surfactants studied, owing to large dissociation constants. Further work must be carried out spanning a range of surfactant types and using more sensitive techniques.

A final application of these magnetic surfactant ionic liquids concerned biochemistry[15]. To-date all attempts of controlling DNA and biomolecules with a magnetic field have relied on addition of pre-prepared nanoparticles. This has been used with some success[16, 17], however for such systems to be employed efficiently, they must be able to inhibit sedimentation, be biocompatible and non-toxic. Now a surfactant approach is possible which does not rely on the difficult synthesis of ultrafine particles, nor upset the native conformations and subsequent functions of biomolecules. The magnetic surfactants reported in this thesis can bind to and compact DNA and bind to biomolecules just like conventional surfactants, and also allow for their transportation and manipulation in a magnetic field. For example, over 5 days a solution of DNA could be reduced in concentration by up to 60% simply by surfactant binding and an applied magnetic field. This could have wide ranging implications for biotechnology and be applied to a diverse range of systems cheaply and non-invasively.

9.1 Future work

There are many ways in which the work presented in this thesis could be continued and extended to both resolve some of the fundamental questions raised and also further applications.

Firstly, it would be of great interest to ascertain whether the switching between pure ionic liquid phase to a surfactant mesophase for organic reactions in SAILS could lead to control of reaction pathways. This is especially exciting when considering magnetic SAILS where both partitioning into a mesophase and

enrichment of catalysts induced by internal magnetic field effects (due to faster proton transfer) could have a part to play[18].

Magnetic surfactants have shown remarkable properties but the basis for them is still poorly understood. Bifunctionality of these surfactants at reducing surface tension reduction may relate to an instability of the air/water interface[19] but may also be down to packing parameter arguments. Attempts to investigate this using neutron reflectivity were unsuccessful, however a mathematical approach combining Maxwell equations with those of Laplace have already been applied to ferrofluids[19] and may prove useful for surfactant systems. The use of muons and polarized neutrons should provide complementary results giving an indication as to the origin of magnetism in these systems as well as the effect of molecular ordering.

Magnetic ionic liquids suitable for drug delivery have been presented. However, the work only shows *in vitro* proof of principle and should be extended to solubilising various drugs and the replication of *in vivo* conditions. In this vein, the use of surfactant-biomolecule binding for transfection and other biomedical applications should also be investigated and improved.

In this thesis microemulsions have demonstrated unprecedented magnetic behaviour and this should work should be furthered to produce full phase diagrams for both surfactant mixing (to create "microemulsion alloys") and as a function of w value. It is also interesting to ask whether it is possible to build monolayers of surfactant which also exhibit superparamagnetism and could potentially find application in data storage, and what are the boundary conditions to observing this unusual magnetic behaviour (*c.f.* micellization effects in Chapter 5) and would the synthesis of non-ionic magnetic surfactants improve the situation further.

9.2 References

1. R. Sheldon, *Chem. Commun.*, 2001, 2399-2407.
2. C. Chiappe, D. Capraro, V. Conte and D. Pieraccini, *Org. Lett.*, 2001, 3, 1061-1063.
3. T. Welton, *Chem. Rev.*, 1999, 99, 2071-2084.
4. J. D. Holbrey and K. R. Seddon, *Clean Tech. Environ. Policy*, 1999, 1, 223-236.
5. P. Brown, C. Butts, R. Dyer, J. Eastoe, I. Grillo, F. Guittard, S. Rogers and R. Heenan, *Langmuir*, 2011, 27, 4563-4571.
6. P. Brown, C. P. Butts, J. Eastoe, D. Fermin, I. Grillo, H.-C. Lee, D. Parker, D. Plana and R. M. Richardson, *Langmuir*, 2012, 28, 2502-2509.
7. P. Brown, A. Bushmelev, C. P. Butts, J. Cheng, J. Eastoe, I. Grillo, R. K. Heenan and A. M. Schmidt, *Angew. Chem. Int. Ed.*, 2012, 2414-2416.
8. S. Hayashi and H. Hamaguchi, *Chem. Lett.*, 2004, 33, 1590-1591.
9. P. Brown, C. P. Butts, J. Cheng, J. Eastoe, C. A. Russell and G. N. Smith, *Soft Matter*, 2012, 8, 7545-7546.
10. B. P. Binks, ed., *Modern Aspects of Emulsion Science*, Royal Society of Chemistry, 1998.
11. A. Kaiser, T. Liu, W. Richtering and A. M. Schmidt, *Langmuir*, 2009, 25, 7335-7341.
12. H. D. Burrows and M. J. Tapia, *Langmuir*, 2002, 18, 6706-6708.
13. A. Beeby, I. M. Clarkson, J. Eastoe, S. Faulkner and B. Warne, *Langmuir*, 1997, 13, 5816-5819.
14. D. Gatteschi, M. Fittipaldi, C. Sangregorio and L. Sorace, *Angew. Chem. Int. Ed.*, 2012, 51, 4792-4800.
15. P. Brown, A. M. Khan, J. P. K. Armstrong, A. W. Perriman, C. P. Butts and J. Eastoe, *Adv. Mat.*,2012, DOI: 10.1002/adma.201202685
16. C. Plank, O. Zelphati and O. Mykhaylyk, *Adv. Drug Deliv. Rev.*, 2011, 63, 1300-1331.
17. O. Mykhaylyk, D. Vlaskou, N. Tresilwised, P. Pithayanukul, W. Möller and C. Plank, *J. Magn. Magn. Mater.*, 2007, 311, 275-281.
18. Y. Sakaguchi and H. Hayashi, *Chem.Phys.*, 1992, 162, 119-129.
19. R. E. Rosensweig, *Ferrohydrodynamics*, Dover Publications, New York, 1997.

Appendix A1

A1.0 Quaternary Ammonium-Based SAILS as Reaction Media

Many synthetic efforts have been devoted over the years toward finding reagents that could efficiently promote glycosidic bond formation[1]. The use of 1-butyl-3-methylimidazolium triflate ([bmim][OTf]) as a mild, recyclable, and versatile IL solvent/promoter of room temperature (rt) glycosylation reactions using trichloroacetimidate and thiophenyl glycoside donors has recently been reported[2]. It was shown that [bmim][OTf] could selectively activate "armed" glycosyl donors in the presence of "disarmed" ones and its applicability in regio- and chemoselective glycosylation reactions and in reactivity-based one-pot coupling reactions has been demonstrated[3]. Studies showed that the choice of counterion in the IL is key to promote these types of reactions, while modifications on the imidazolium cation did not have a significant effect on the IL reactivity toward the glycosylation reaction or on the stereoselectivity of the products[4].

Although the use of imidazolium-based ILs offers many attractive features, it is important to consider other ionic liquids that are cheaper, less toxic and compatible with reactions involving active metals or strong bases. The new class of ionic liquids mentioned in this thesis (quaternary ammonium cations and bis(2-ethyl-1-hexyl) sulfosuccinate (AOT) anions) have been used in combination with *N*-Iodosuccinimide (NIS) as a selective and mild promoter in glycosylation reactions with thiophenyl glycoside donors (Figure A1) that can be generally applied to oligosaccharide synthesis (applicable to both laboratory and industrial-scale preparation); being compatible with a range of hydroxyl-protecting groups, such as acetates, benzyl ethers, and acetals, and are also amenable to NH_2-masking strategies, that is, trichloroethylcarbamate (Troc)[5].

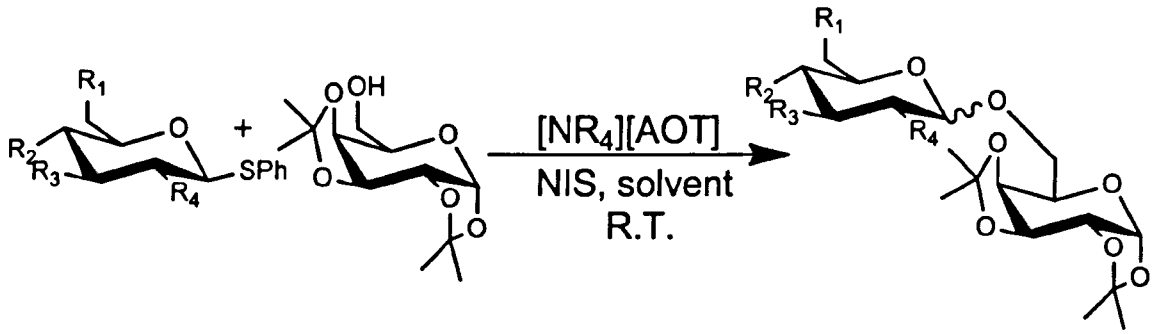

Figure A1.1: Glycosylation reaction with thioglycoside donor and model acceptor in the presence of SAIL /NIS at rt to yield disaccharide.

Mechanistically, $[NR_4][AOT]$ is a more reactive activator than [mim][OTf] while still discerning the less active (peracetylated) donors. Importantly, the anomeric outcome of the glycosylation reaction using glycosyl donors with no participating group at C-2 could be tuned by switching the solvent from DCM to MeCN.

A1.1 References

1. (a) M. C. Galan; D. Benito-Alifonso; G. M. Watt. *Org. Biomol. Chem.*, 2011, *9*, 3598; (b) J. T. Smoot; A. V. Demchenko. Chapter 5 Oligosaccharide Synthesis: From Conventional Methods to Modern Expeditious Strategies. In *Advances in Carbohydrate Chemistry and Biochemistry*, Derek, H., Ed. Academic Press: 2009; Vol. 62, pp 161; (c) X. Zhu; R. R. Schmidt. *Angew. Chem. Int. Ed.*, 2009, *48*, 1900.
2. M. C. Galan; C. Brunet; M. Fuensanta. *Tetrahedron Lett.*, 2009, *50*, 442.
3. M. C. Galan; A. T. Tran; S. Whitaker. *Chem. Commun.*, 2010, *46*, 2106.
4. M. C. Galan; K. Jouvin; D. Alvarez-Dorta. *Carbohyd. Res.* 2010, *345*, 45.
5. M. C. Galan; A. T. Tran; J. Boisson; D. Benito; C. Butts; J. Eastoe; P. Brown. *J. Carbohyd. Chem.*, 2011, *30*, 486.

Appendix A2

A2.0 Reactions in Surfactant Ionic Liquids

In Chapter 2 solvent effects of ionic liquids (ILs) were reviewed. It was concluded that the development of surfactant ionic liquids (SAILs) is advantageous as it presents the opportunity to combine the catalytic properties of surfactant systems with those unique to ILs, especially for separations and extractions. They also offer the possibility to switch between a "pure" IL solvent, with favourable solvating properties, and an IL mesophase which may confer different selectivity and kinetics for reactions occurring in the matrix.

To investigate this a Diels-Alder (DA) condensation was studied (Figure A2.1) as it is an important carbon-carbon bond forming reaction in organic synthesis[1]. The reaction is that of cyclopentadiene with diethylmaleate, which leads to a mixture of *exo* and *endo* products. This reaction has been widely investigated in a range of solvents (molecular and ionic) and solvent influences on the *endo/exo* selectivity of the reaction are well understood.

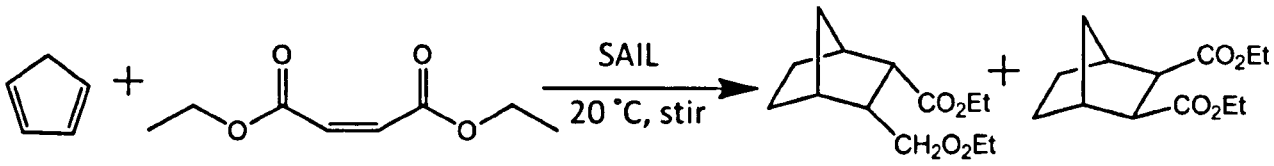

Figure A2.1: DA reaction of cyclopentadiene with diethylmaleate dienophile.

Solvent	Phase	*endo*	*exo*	Technique
none	-	97	3	^{1}H-NMR
H_2O	-	86 (84)	14 (16)	^{1}H-NMR (GC)
EtOH[2]	-	88	12	-
[bmim][Otf][3]	100 wt %	76	24	GC
[bmim][AOT]	100 wt %	73	27	GC
[bmim][DS]	100 wt %	79 (77)	21 (23)	^{1}H-NMR (GC)
[bmim][DS]	50 wt % in H_2O, L_α	61	39	GC
SDS	50 wt % in H_2O, L_α	83	17	GC
$[C_{14}H_{29}imH][Cl]$[2]	L_α	46	54	-

Table A2.1: Effect of solvent on endo/exo selectivity and the technique used for measurements. GC stands for gas chromatography.

In water the *endo/exo* selectivity is 97:02 and in ethanol the reaction gives 88:12[2]. As expected[4], on altering the IL counterion there were small changes in *endo/exo* selectivity (Table A2.1). All IL gave endo values lower than those for the molecular solvents. This might be due to partitioning of the reactants due to slight

structuring of the solvent. Lin *et al.* reported that using a liquid crystalline phase of 1-tetradecyl-3-methylimidazolium chloride, $[C_{14}H_{29}imH][Cl]$, dramatically affects selectivity (though the method insists upon using highly concentrated HCl, which is doubtful). Here, by using a lamella mesophase for SDS (as elucidated by polarizing light microscopy) the endo/exo ratio increases whereas using [bmim][DS] decreases the endo/exo ratio significantly. This could again be due to partitioning of cyclopentadiene in the IL which isn't possible in the SDS. It might be expected that SDS simply concentrates the reactants and affects only kinetics. Firm conclusions can not be drawn and the data is quite scarce, however there is an indication that switching between a "neat" IL and a mesophase leads to different results that are not solely attributable to salt effects and requiring further study.

The Diels-Alder reaction above has some drawbacks for investigation, as the reaction begins before complete mixing can occur in the viscous ILS. Also the reactants are symmetrical and so the full effects of partitioning may not be observable. Therefore a different reaction was sought. Recently enantiodifferentiation of a [4 + 4] photodimerization was reported in a chiral IL[5] (Figure A2.2). Microemulsions of an imidazolium based ionic liquids have also been used as microreactors for photocycloaddition with regioselectivity attributed to partitioning of reactants at the micellar interface[6]. Importantly, this partitioning of reactants occurs before the reaction commences.

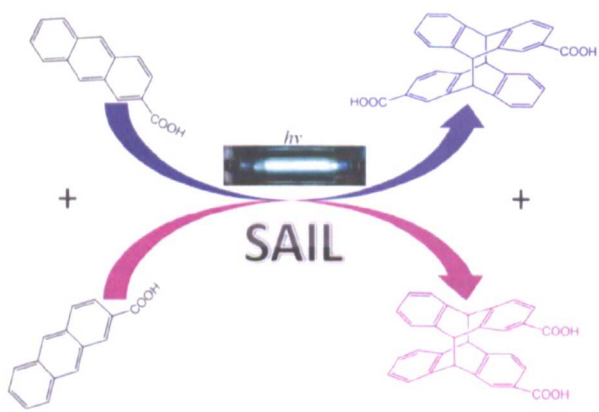

Figure A2.2: Photochemical dimerization of 2-anthrecene carboxylic acid. Enantiomeric excess determined by liquid chromatography–mass spectrometry (LC-MS).

For the first time, it was attempted to compare the effects of "neat" SAIL with that of its mesophase. Results indicate that [bmim][AOT] based solvents induce a selectivity which might be mapped against mesophase structure. Here "neat" SAIL confers no great effect whereas in aqueous solution an enantiomeric excess is observed, however with four possible enantiomers differentiation and quantitative analysis was not possible with the techniques used. Another interesting point is that using [bmim][AOT] allows the products to be easily extracted and the solvent recycled.

A2.1 References

1. J. Sauer; R. Sustmann, *Angew. Chem. Int. Ed.*, 1980, *19*, 779.
2. C. K. Lee; H. W. Huang; I. J. B. Lin, *Chem. Commun.*, 2000, 1911.
3. M. J. Earle; P. B. McCormac; K. R. Seddon, *Green Chem.*, 1999, *1*, 23.
4. A. Aggarwal; N. L. Lancaster; A. R. Sethi; T. Welton, *Green Chem.*, 2002, *4*, 517.
5. G. Fukuhara; C. Chiappe; A. Mele; B. Melai; F. Bellina; Y. Inoue, *Chem. Commun.*, 2010, *46*, 3472.
6. X. W. Li; J. Zhang; L. Q. Zheng; B. Chen; L. Z. Wu; F. F. L; B. Dong; C. H. Tung, *Langmuir*, 2009, *25*, 5484.

Appendix A3

A3.0 Magnetizing Graphene

A3.1 Introduction

Two-dimensional (2D) nanomaterials such as graphene have recently attracted attention as they have exceptional physical properties and a wide-range of potential applications in the areas of electronics, sensors and energy storage[1]. There are various methods to produce graphene. However, few show promise as efficient pathways to produce processable single layer graphene flakes in significant quantities for application[2]. Chemical oxidation (Hummers method[3]) is one solution, (whereby graphite is oxidized to exfoliated graphene oxide, followed by chemical reduction in the presence of stabilizers) but this route disrupts the electronic structure of graphene and introduces many carbonyl groups (-C=O), hydroxy groups (-OH), and epoxides in the sheets[2]. A non-chemical approach involves the sonication of graphite in various organic solvents[4], however sheets produced via these methods show agglomeration (through re-stacking) and often require the use of toxic solvents. By combining non-covalent functionalization through surfactants and ultrasonication, graphene may be exfoliated and dispersed successfully; even in water[5]. In this work DTAG (introduced in chapter 5) acted as an effective stabilizer. Importantly this study also shows some evidence that by selecting a magnetic surfactant, graphene sheets may be manipulated in a magnetic field. The graphene-DTAG systems were characterized by AFM, TEM and UV-visible spectroscopy, and stabilization studies were also carried out.

A3.2 Results and discussion

In this study, powdered graphite was dispersed in water below the critical micelle concentration (cmc) of DTAG. It is well known that the dispersed concentration is heavily dependent on surfactant content, however, concentration was not optimized for this system. The concentration of graphene remaining dispersed after centrifugation was calculated from the adsorption spectra using an extinction coefficient of 6600 ml^{-1} g^{-1} at 265 nm[6] and found to be 0.128 mM (Figure A3.5). Importantly there was no disruption in electronic structure.

It is expected that the DTAG molecules get adsorbed onto the electron rich graphene surface through van der Waals interactions with the hydrophobic interaction of the alkyl tails helping to prevent re-stacking. In aqueous media there is dissociation of the surfactant head group leading to an effective charge over the flake, causing electrostatic repulsion and stabilization. The electric potential at the edge of the layer of bound ions is called the zeta potential (ζ), and can be measured easily for aqueous dispersions. The magnitude of ζ has a bearing on the graphene concentration that can be obtained. For CTAB coated graphene ζ = + 49 mV, in agreement with literature[7] showing good stability. For DTAG this value falls to + 35 mV (moderate stability). It is important to note that the accepted value for colloidal stability is considered to be around +/- 30 mV.

TEM samples were prepared by pipetting a few millilitres of dispersion onto a carbon mesh grid (400 mesh). TEM analysis revealed a large quantity of flakes of various types as shown in Figure A3.1. The majority of these flakes were multilayers and very disordered. The disorder suggests that these flakes formed by re-aggregation of smaller flakes.

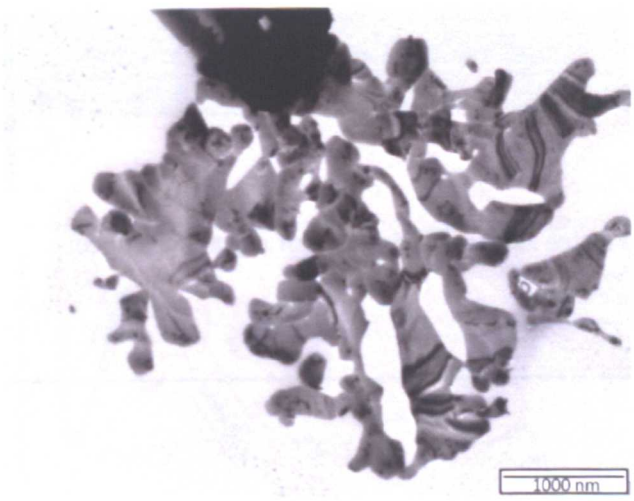

Figure A3.1: TEM image of surfactant stabilized graphene flakes

The morphology and the thickness of the flakes were further investigated using AFM. Figure A3.2 and A3.3 represent the AFM image graphene flakes and a height profile (relating to the scan across the white line in Figure A3.2) respectively. The contrast difference between the edge and the centre of the graphene

nanoflake clearly shows the sharp edge of a flake. The height of the flake was found to be ~ 3.0 nm, corresponding to ~ 5 graphene layers. However the increase in thickness could also be attributed to excess surfactant on the surface. AFM images clearly show that most flakes were < 1μm. Conventionally AFM samples of graphene are prepared through spin-coating. However this was not done in this study nor a detailed statistical analysis of flake dimensions.

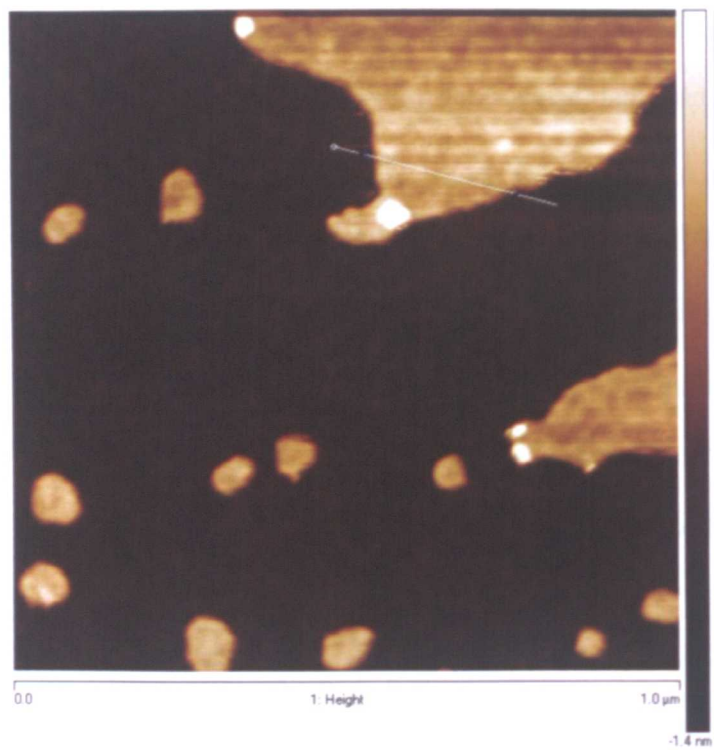

Figure A3.2: AFM image of a graphene sheets.

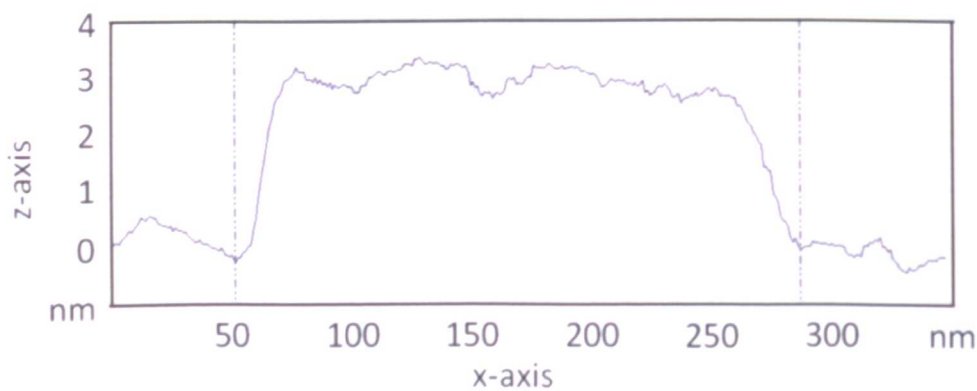

Figure A3.3: Height profile of graphene sheet in figure 2 marked by a white line.

A stable graphene solution was separated into two homemade vials; one of which contained a magnet (0.37 T on the surface, Figure A3.4). The characteristic peak at 265 nm was measured. After one day both dispersions showed moderate sedimentation (reducing the initial concentration by approximately 6.4 %). After a further 5 days the concentration of graphene in the absence of a magnetic field decrease by ~ 2% and in the presence of a magnetic field a decrease of ~5% was observed.

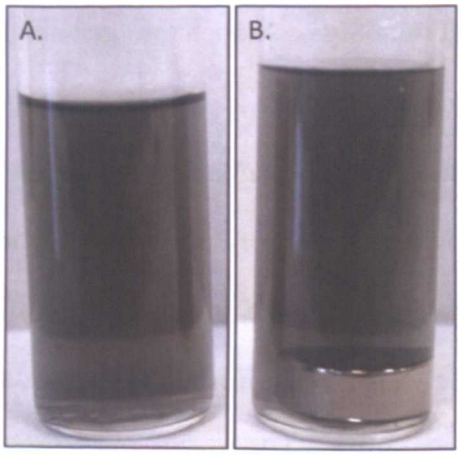

Figure A3. 4: Experimental set up for UV-Visible spectroscopy experiments (**A**) without a magnetic field and (**B**) in a magnetic field.

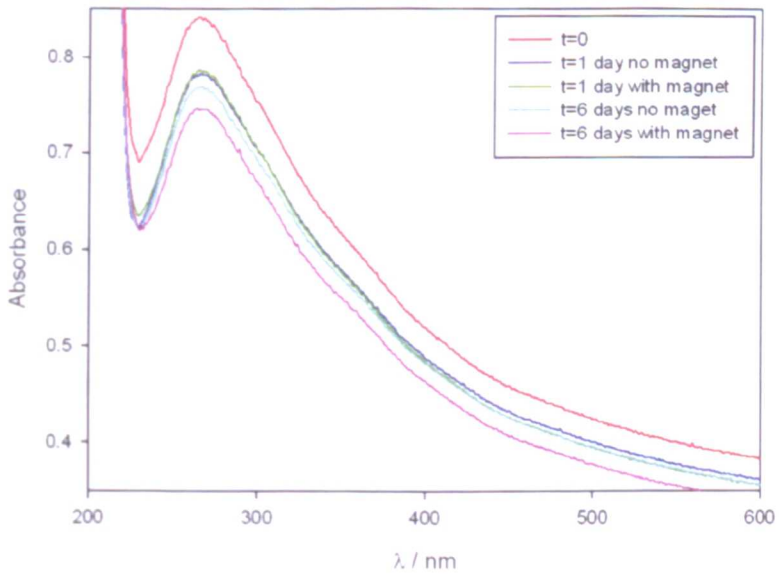

Figure A3.5: UV-Visible spectra of graphene dispersions with and without the presence of a magnetic field at 25 °C.

In conclusion we have shown that DTAG acts like a conventional cationic surfactant in stabilizing graphene flakes. In addition to this it may be that a strong enough magnetic field can manipulate graphene sheets in solution. The results here are tentative but indicate further research should be carried out to optimize surfactant loading and stabilization and to see if greater effects can be observed.

A3.3 Materials and methods

500 mg of graphite powder, purchased from Sigma Aldrich (product number 332461), was added to 100 ml of aqueous surfactant solution (0.1 mg ml^{-1} surfactant (DTAG) concentration) to give an initial graphitic concentration of 5 mg ml^{-1}. This mixture was sonicated using a sonic tip (MSE Soniprep 150 (UK), 23 KH) for 30 mins at 70 % of maximum power (i.e. 75% of 750 W nominal maximum power). This dispersion then cooled for 30 minutes and the process as repeated two more times. This solution was left overnight and then the top 20 ml was removed into a vial and centrifuged for 60 mins at 1700 rpm. The top 10 ml of this solution was the collected for measurements. For UV-Visible spectroscopy in a magnetic field this process was repeated three times and the final volumes of surfactant mixed together.

Zeta potential measurements were recorded on a Brookhaven Instruments Zeta-PALS apparatus (Brookhaven Instruments Corporation, Holtsville, NY) The zeta potential was calculated from the electrophoretic mobility, μ, using the Smoluchowski expression: $\zeta = \eta\mu\varepsilon$, where η is the solution viscosity and ε is the solution permittivity ($\varepsilon = \varepsilon_r/\varepsilon_0$).

TEM samples were prepared by pipetting a few millilitres of dispersion onto a carbon mesh (400 mesh) and images taken using a JEOL 2100.

AFM samples were also prepared by drop-casting a few millilitres of solution onto a fresh mica surface, which was allowed to dry overnight. Measurements were taken on a Dimension 3100 AFM, with Nanoscope IV controller (Veeco Instruments, Plainview, NY) in tapping mode with a resonance frequency of .

UV-Visible spectra were recorded on a Nicolet Eco 300 UV-Vis spectrometer at 25 °C.

A3.4 References

1. A. K. Geim; K. S. Novoselov, *Nat. Mater.*, 2007, *6*, 183.
2. S. Vadukumpully; J. Paul; S. Valiyaveettil, *Carbon,* 2009, *47*, 3288.
3. W. S. Hummers; R. E. Offeman, *J. Am. Chem. Soc.*, 1958, *80*, 1339.
4. A. B. Bourlinos; V. Georgakilas; R. Zboril; T. A. Steriotis; A. K. Stubos, *Small,* 2009, *5*, 1841.
5. M. Lotya; Y. Hernandez; P. J. King; R. J. Smith; V. Nicolosi; L. S. Karlsson; F. M. Blighe; S. De Wang; I. T. McGovern; G. S. Duesberg; J. N. Coleman, *J. Am. Chem. Soc.,* 2009, *131*, 3611.
6. M. Lotya; P. J. King; U. Khan; S. De; J. N. Coleman, *ACS Nano,* 2010, *4*, 3155.
7. R. J. Smith; M. Lotya; J. N. Coleman, *New J. Phys.*, 2010, *12*, 125008.

Appendix B

Techniques

B1.0 Small-Angle Neutron Scattering (SANS)

B1.1 Introduction

To investigate the size, shape, structural organization and interactions within colloidal dispersions the super-sensitive specialist technique called small-angle neutron scattering (SANS) has proven invaluable. Like any scattering experiment, it relies on the interaction of a beam of radiation with the sample of interest; for SANS this is specifically the atomic nuclei of the sample. This is possible as the wavelengths associated with neutron beams for these experiments are typically between 0.10 and 1.0 nm, much shorter than those of visible light (400 - 800 nm).

B1.2 Basic Principles[1]

The schematic representation of a small-angle scattering experiment is shown in Figure B1. An incoming neutron beam is shone onto the sample of interest; this beam can be viewed as a stream of free of particles in the same direction and with the same speed (on a monochromatic steady-state reactor source).

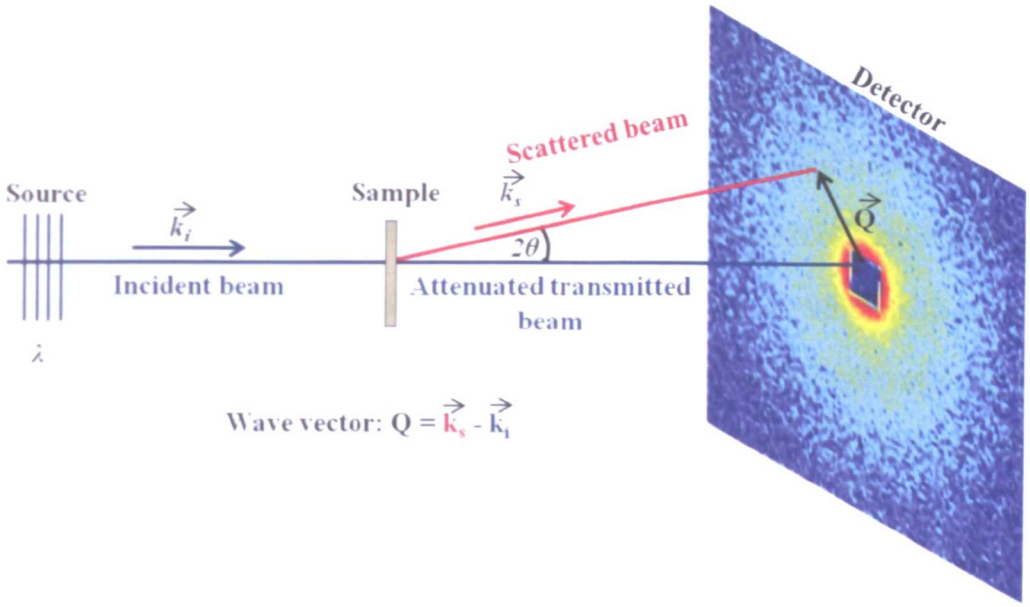

Figure B1: Schematic representation of a small-angle neutron scattering experiment. The incident $\mathbf{k_i}$ and scattered $\mathbf{k_s}$ wave vectors are shown, and the resultant scattering vector **Q**, which is in the plane of the detector.

Because of the de Broglie relationship ($\lambda = h/m$) linking particle momentum, m, and the associated wavelength, the beam can be thought of as a planar monochromatic wave with a wavelength λ, having an incident wave vector k_i. The free neutrons in the beam interact with the bound nuclei of atoms in the sample, resulting in scattering of the beam: these scattered neutrons are recorded by a position-sensitive detector set perpendicular. In SANS experiments the interactions between free neutrons in the beam and bound nuclei in the samples cause the incident beam to be deflected through an angle 2θ. Technically, only coherent elastic interactions (whereby energy is conserved) between the neutron beam and the sample nuclei are considered. The net result of these interactions is to knock the beam off course, and this change in direction (momentum) defines the scattered wave vector k_s. The resultant vector between incident and scattered beam is called the wave vector q, and mathematically $Q = k_s - k_i$. The magnitude of Q defines the spatial resolution, and hence the radius R of the particle sizes which can be studied. The units of Q are nm^{-1} (i.e. a reciprocal length), and because of this large particles scatter predominantly to low values of Q, where as smaller particles result in signals collected at larger Q values. Q is related to both the scattering angle, θ, and the incident neutron wavelength, λ:

$$Q = \frac{4\pi}{\lambda} sin\frac{\theta}{2} \qquad \text{Eq. B1}$$

The intensity, I, of scattered neutrons is recorded on the position-sensitive detector as a function of Q, and the collected $I(Q)$ pattern is computer-analyzed using mathematical models to find the size, the shape and the structure of the particles. The magnitude of the interaction between the incoming neutron beam and the nucleus is also proportional to the concentration of particles and to a parameter which is directly linked to the chemical composition of the molecules in the sample, and is called scattering length density, b. For bulk materials it is more convenient to use a summation of the scattering lengths for all atoms per volume. This property is known as the scattering length density, ρ, and is calculated as:

$$\rho = \frac{DN_A}{M_R}\sum_i b_i = \frac{\sum_i b_i}{V_m} \qquad \text{Eq. B2}$$

where D is the bulk density, M_R is the molar mass, N_A is Avagadro's number and V_m is the molecular volume.

A major feature of neutron scattering is a notable difference of scattering length densities between hydrogen and deuterium (remember hydrogen has only one proton, and deuterium is an isotope of hydrogen containing one proton and one neutron). Surfactants, polymers and biological molecules possess many hydrogen atoms, and if these molecules are dissolved in heavy water (D_2O), rather than normal light water (H_2O) then strong scattering of the neutron beam is seen, resulting in patterns on the detector. So an easy way to boost the scattering signal is to replace the normal hydrogen solvent by an isotopically labeled deuterated solvent. In fact this idea can be extended, and using modern chemical methods it is possible to make not just deuterium-containing solvents, but also deuterium-labeled surfactants, polymers and even proteins. This kind of isotopic substitution is now a powerful tool for looking at heterogeneous particles, as for example in soap micelles with oily cores, dissolved in water. Obviously, there are three components, surfactant, oil and water: now specific deuteration allows us to firstly highlight selectively the internal oily cores, or in a separate experiment the soap-coated shells alone. These experiments give different forms of $I(Q)$ scattering patterns which can be readily distinguished by computer-analyses. As can be seen in Figure B2, it becomes possible to gain a detailed picture of the internal structure of the micelle soap particles.

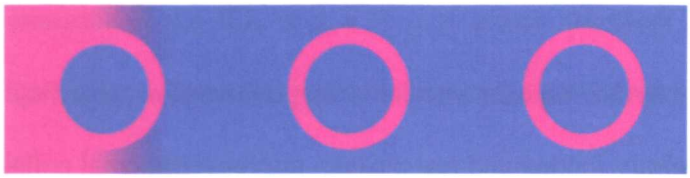

Figure B2: Illustration of isotopic substitution with heterogeneous particles, which can be used to highlight the cores only (left), or the separately the shells alone (right).

In neutron scattering experiments (as shown in Figure B1), the amplitude of the scattered wave, A_s, can be obtained as

$$A_s(\mathrm{Q}) = \frac{A_i b}{r} \exp\left[i(k_i \cdot r - \mathrm{Q} \cdot R)\right] \qquad \text{Eq. B3}$$

Here, A_i is the amplitude of the incident neutron beam, r is the distance between the scatterers, k_i the incident neutron wave vector and R the position for an atom at a certain position from the origin. For a realistic case of a very large ensemble of atoms, the total scattered amplitude is then written as

$$A_s(\mathrm{Q}) = \frac{A_i}{r} \exp\left(ik_i \cdot r0 \sum_i b_i \cdot \exp(-i\mathrm{Q} \cdot R_i)\right) \qquad \text{Eq. B4}$$

The scattered intensity, I_s measured at the detector, is simply the squared modulus of the amplitude

$$I_s = \langle |A_s(\mathrm{Q})|^2 \rangle \qquad \text{Eq. B5}$$

For an ensemble of n identical particles, the scattering averaged over all orientations, o, and shapes, s, this becomes

$$I_s(\mathrm{Q}) = \langle \langle |A_s(\mathrm{Q})|^2 \rangle_o \rangle_s \qquad \text{Eq. B6}$$

B1.3 Data Collection

Because neutrons are needed SANS experiments can only performed at large facilities, in Europe these are done at mega-laboratories, jointly funded and run through intergovernmental collaborations, such as ISIS in UK and ILL in France.

ISIS uses a spallation source to generate neutrons by bombarding a high-energy proton beam into a heavy-metal target (e.g. Ta). This method produces a large range of neutron wavelengths (a "white beam") and so the time-of-flight technique is used to measure their energy, and a fixed detector is used. The detectors are housed inside a large vacuum tube.

Figure B3: SANS2D instrument at ISIS (UK).

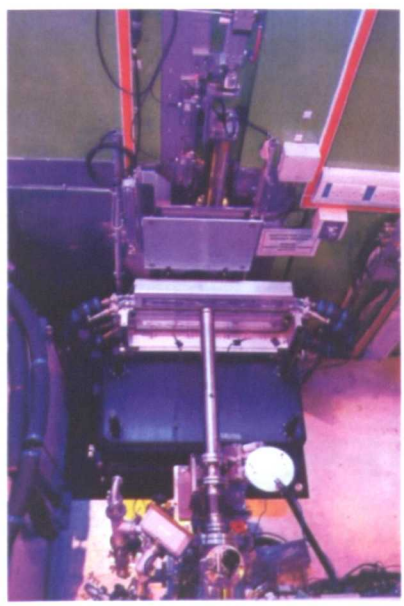

Figure B4: Inside the SANS2D sample position at ISIS (UK).

In contrast the D22 diffractometer at the ILL uses a reactor source (through fission) and a narrowly-distributed incident wavelength, selected by a mechanical chopper (velocity selector, Figure B5).

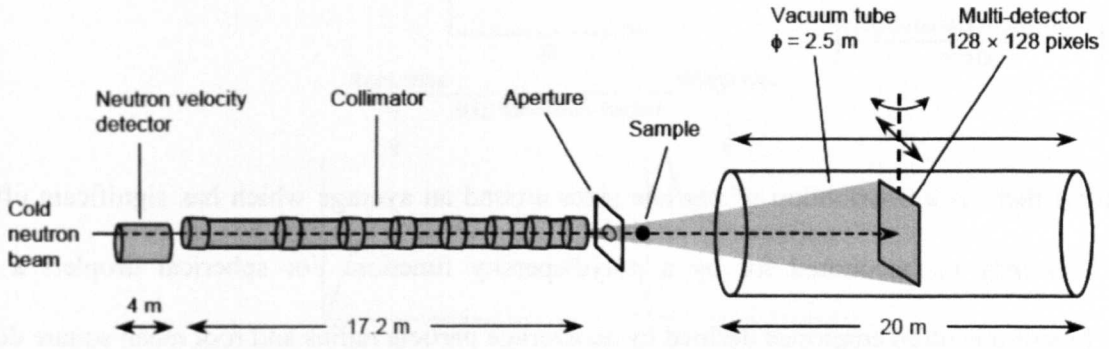

Figure B5: D22 instrument layout[1d].

B1.4 Data Analysis

Here only spherical particles will be considered. However, this is typical of many systems studied by SANS (such as micelles and microemulsion droplets). For monodisperse homogeneous spherical particles of radius R, volume V_p, number density n_p (cm^{-3}) and coherent scattering length density ρ_p dispersed in a medium of density ρ_m, the normalised SANS intensity $I(Q)$ (cm^{-1}) may be written as

$$I(Q) = n_p \Delta\rho^2 V_p^2 P(Q,R) S(q) + B_{inc} \qquad \text{Eq. B7}$$

where $\Delta\rho = \rho_p - \rho_m$, $P(Q,R)$ and $S(Q)$ are the form factor and structure factor, and B_{inc} is the incoherent background. The proportionality factor which relates the intensity to the form and structure factor is known as the scale factor, S_F

$$S_F = n_p(\rho_p - \rho_m)^2 V_p^2 = \varphi_p \cdot \Delta\rho^2 \cdot V_p \qquad \text{Eq. B8}$$

where φ_p is the volume fraction of the particles. S_F is a measure of the validity and consistency when modelling SANS data, as it can be separately calculated and fitted.

The form factor, $P(Q)$, gives information of the size and shape of particles. An approximate representation of the form factor for spheres is shown in Figure B6. For homogeneous spheres of radius R is may be written

$$P(Q,R) = \left[\frac{3(\sin(QR) - QR\cdot\cos(QR))}{(QR)^3}\right]^2 \qquad \text{Eq. B9}$$

In real systems there is a distribution of particle sizes around an average which has significant effects on scattering. This may be accounted for by a polydispersity function. For spherical droplets a Schultz distribution function is often employed defined by an average particle radius and root mean square deviation

$$\sigma = \frac{R^{av}}{(Z+1)^{1/2}} \qquad \text{Eq. B10}$$

where R^{av} is the average particle radius, and Z is a width parameter.

The structure factor, $S(Q)$, describes inter-particle scattering and depends on the interactions in the system, i.e. excluded volume, repulsive or attractive. When attractive interactions are minimal a hard sphere interaction potential is often appropriate

$$S(Q) = \frac{1}{[1 - n_p]\cdot f(r_d,\varphi_p)} \qquad \text{Eq. B11}$$

Figure B6 shows how important $S(Q)$ is at low Q values where it reduces the scattering intensity and produces a peak in $I(Q)$ profile at $Q_{max}=2\pi/D$, with I the nearest neighbour distance in the sample. For interacting systems, an effective way of reducing $I(Q)$ is by diluting the system.

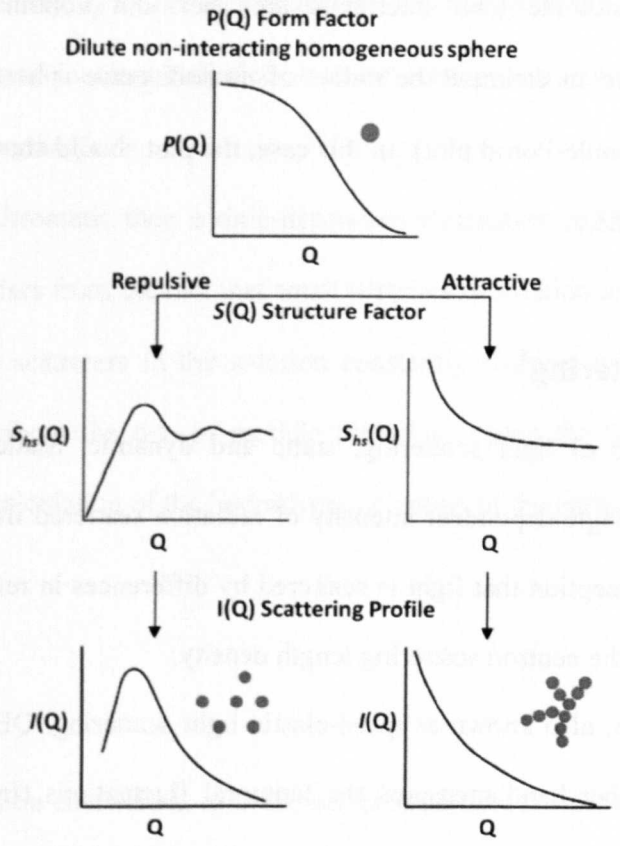

Figure B6: Schematic representation of the particle form factor (P(Q,R) and structure factor S(Q) for attractive and repulsive homogeneous spheres, and their contribution to the scattered intensity I(Q)[1d].

B1.5 Guinier and Porod Analysis

At low Q (Guinier regime), scattered intensity is sensitive to different particle shapes. The Guinier approximation relates the Guinier regime to a radius of gyration R_g of the particle. For dilute systems the single particle form factor P(Q, R) can be simplified to[2]

$$P(Q,R) = 1 - \frac{Q^2 {R_g}^2}{3} \qquad \text{Eq. B12}$$

At high Q, scattered intensity is sensitive to the total interfacial area in a system. Porod's law presents this relation as[3]

$$I(Q) = 2\pi\delta\rho^2 \left(\frac{S}{V}\right) Q^{-4} \qquad \text{Eq. B13}$$

Here the (S/V) term represents the total interfacial area per unit volume of solution. The Porod approximation can also be used to estimate the radius of monodisperse spheres of radius r, by plotting $I(q)\cdot q^4$ against Q (known as a Soulé-Porod plot). In this case, the plot should show an initial maximum at Q $\approx 2.7/r$ and a minimum at Q $\approx 4.5/r$.

B2.0 Dynamic Light Scattering[4]

There are two different types of light scattering, static and dynamic. Static light scattering involves measuring the time-averaged angle-dependent intensity of radiation scattered from a sample, analogous to how SANS works, with the exception that light is scattered by differences in refractive index and neutrons are scattered by differences in the neutron scattering length density.

Dynamic light scattering (DLS, also known as quasi-elastic light scattering, QELS and photon correlation spectroscopy, PCS) on the other hand measures the temporal fluctuations (from Brownian motion) in intensity of laser light scattered by a sample at a fixed angle. The scattered light depends on the diffusion of the particles which can itself dependant on particle size. A basic DLS setup can be seen in Figure B7.

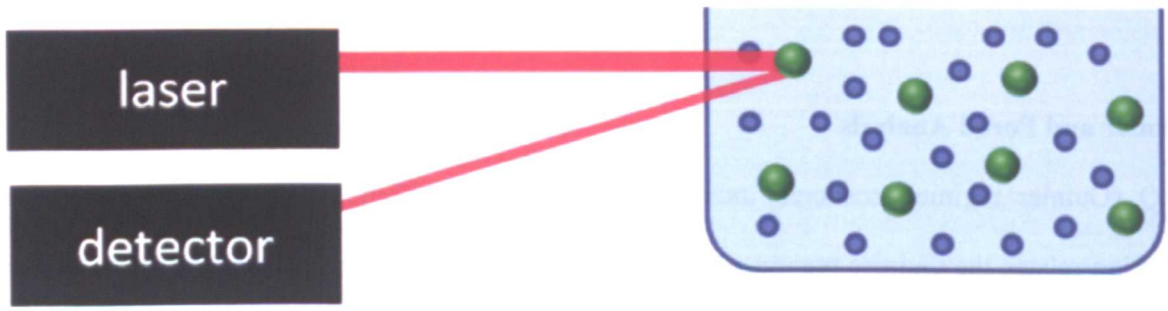

Figure B7: Schematic diagram of a basic DLS setup.

B2.1 Basic Principles

When light hits a small particles it scatters in all directions. This is known as Rayleigh scattering and occurs only when the particles are considerably smaller than the wavelength of the light source (often ~ 600 nm). The scattered light from one particle can be described by the Rayleigh equation

$$I_s = I_0 \frac{8\pi^4 r^6}{R^2 \lambda^4} \left[\frac{n^2-1}{n^2+2}\right]^2 (1 + cos^2\theta) \qquad \text{Eq. B14}$$

where I_s is the scattered intensity, I_0 the incident intensity, r is the particle radius, R is the distance to the particle, λ is the wavelength of incident radiation, n is the relative refractive index of the particle in the medium and θ is the scattering angle.

If the light source is monochromatic then a time-dependent fluctuation in the scattering intensity can be observed. This fluctuation arises from the fact that small particles in solution undergo Brownian motion, and so the distance between the scatterers in the solution constantly changes with time and so the recorded fluctuation contains details about the rate of particle diffusion. Using the Stokes-Einstein equation, this diffusion coefficient allows calculation of the hydrodynamic radius of the particles:

$$D = \frac{k_B T}{6\pi\eta r_H} \qquad \text{Eq. B15}$$

where D is the particle diffusion coefficient, r_H is the solvated particle radius, k_B is the Boltzmann constant, T is the temperature in Kelvin and η is the viscosity of the solvent.

The dynamic information is collected from an autocorrelation function of the intensity trace comparing the intensity signal at a given time t ($I(t)$) with that a small time $t + \tau$ later. The rate of change of signal intensity is proportional to the speed at which the particles are diffusing. The correlation function, $g(\tau)$, describes this rate of change:

$$G(\tau) = \langle I(t) \cdot I(t+\tau) \rangle \qquad \text{Eq. B16}$$

B3.0 Surface and interfacial tensiometry[1a, 1d]

A surface free energy is associated with an interface due to the different environment of molecules located as an interface as compared to those in a bulk phase either side. The surface free energy per unit area is defined as the surface tension, γ_0 and is the minimum amount of isothermal work, W_{min}, required to create a new area of that interface, ΔA

$$W_{min} = \gamma_0 \times \Delta A \qquad \text{Eq. B17}$$

A surfactant adsorbs preferentially at an interface and changes the amount of work need to expand that interface, therefore reducing the interfacial tension.

In solution above the cmc surfactant monomers are present as free monomers and micellized surfactant in the bulk and as an adsorbed monolayer. Below the cmc, however, there are no micelles, just monomers adsorbing and desorbing at the surface. This is known as dynamic surface tension. Depending on the surfactant structure and concentration adsorption takes place at different rates but over a certain period of time an equilibrium surface tension value is observed.

Dynamic surface tension is of interest for many industrially and biologically relevant applications, however only static surface tension was considered in this thesis.

The surface excess, Γ, is the concentration of surfactant in a surface plane, relative to that of a similar plane in the bulk. Gibbs proposed[5] that in an ideal model the two phases, α and β meet with a surface phase of zero thickness. However in reality although bulk concentrations of α and β remain constant, the concentrations of components in the interfacial region will gradually vary from the bulk concentration of α to the bulk concentration of β over the distance x. This is illustrated in Figure B8.

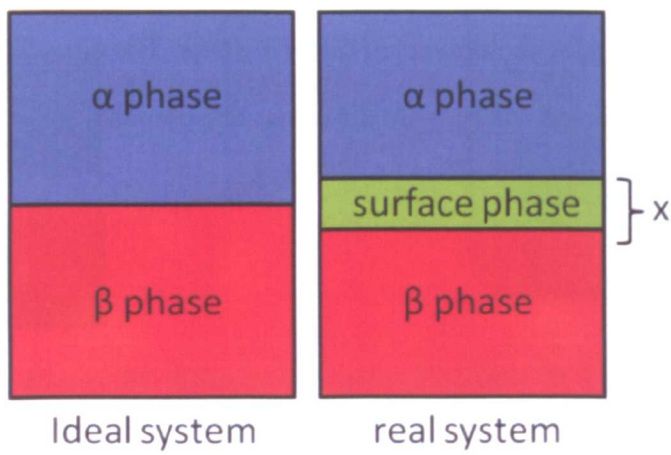

Figure B8: Comparison between the real and idealized model of a surface.

The Gibbs dividing surface is arbitrarily chosen so that the surface excess adsorption of a solvent is zero. Therefore, the surface excess concentration of component i over the interfacial area A can be described as

$$\Gamma_i^{\sigma} = \frac{n_i^{\sigma}}{A} \qquad \text{Eq. B18}$$

Where n_i^σ is the amount of component i in the surface phase σ. Either side of the surface only bulk media exists with no change in concentration.

Considering the internal energy, U, of the system, for any infinitesimal change in temperature, T, entropy, S, interfacial area, A, or chemical potential, μ, and an amount of component, n, the change in internal can be defined as

$$dU = TdS^\sigma + S^\sigma dT + \gamma dA + Ad\gamma + \sum_i \mu_i dn_i^\sigma + \sum_i n_i^\sigma d\mu_i \quad \text{Eq. B19}$$

And for a small reversible change the differential total internal energy in the interfacial region is

$$dU = TdS^\sigma + \gamma dA + \sum_i \mu_i dn_i^\sigma \quad \text{Eq. B20}$$

Subtracting Eq. B20 from Eq. B19 gives

$$S^\sigma dT + Ad\gamma + \sum_i \mu_i dn_i^\sigma = 0 \quad \text{Eq. B21}$$

Then at constant temperature the Gibbs equation is defined as

$$d\gamma = -\sum_i \Gamma_i^\sigma d\mu_i \quad \text{Eq. B22}$$

For a system comprising of a solvent, 1, and solute, 2 this becomes

$$d\gamma = -\Gamma_1^\sigma d\mu_1 - \Gamma_2^\sigma d\mu_2 \quad \text{Eq. B23}$$

As the Gibbs dividing interface is chosen so that $\Gamma_1^\sigma = 0$ the above reduces to

$$d\gamma = -\Gamma_2^\sigma d\mu_2 \quad \text{Eq. B24}$$

where Γ_2^σ is the solute surface excess.

The chemical potential is defined as

$$d\mu_i = RTdlna_i + dRTlna_i \qquad \text{Eq. B25}$$

At constant temperature the second term becomes zero and Eq. B25 becomes

$$(d\mu_i)_T = RTdlna_i \qquad \text{Eq. B26}$$

Then applying this to Eq. B24 gives the Gibbs equation for non-dissociating compounds

$$d\gamma = -\Gamma_2^\sigma RTdlna_2 \qquad \text{Eq. B27}$$

Rearrangement gives

$$\Gamma_2^\sigma = -\frac{1}{RT}\frac{d\gamma}{dlna_2} \qquad \text{Eq. B28}$$

For dissociating solutes, such as ionic surfactants of the form R^-M^+ and assuming ideal behaviour below the cmc, Eq. B27 becomes

$$d\gamma = -\Gamma_R^\sigma d\mu_R - \Gamma_M^\sigma d\mu_M \qquad \text{Eq. B29}$$

Electroneutrality of the interface requires that, if no electrolyte is added, $\Gamma_R^\sigma = \Gamma_M^\sigma$. Using mean ionic activities so that $a_2 = (a_R a_m)^{1/2}$ and substituting into Eq. B29 gives the Gibbs equation for 1:1 dissociating compounds:

$$\Gamma_2^\sigma = -\frac{1}{2RT}\frac{d\gamma}{dlna_2} \qquad \text{Eq. B30}$$

It should be noted that Eq. B28 and Eq. B30 are valid for dilute surfactant systems and so concentration can be substituted for activity without great loss of accuracy.

Finally, the area per molecule, a_s, which gives a description of the packing and orientation of the adsorbed surfactant molecules at the interface can be described by:

$$a_s = \frac{1}{\Gamma N_A} \qquad \text{Eq. B31}$$

B4.0 References

1. (a) T. Cosgrove, *Colloid Science Principles, Methods and Applications*. 2nd Ed.; Wiley, London, 2010; (b) D. S. Sivia, *Elementary Scattering Theory For X-ray and Neutron Users*, Oxford University Press: Oxford, 2011; (c) I. Grillo, Small-Angle Neutron Scattering and Applications in Soft Condensed Matter

   Soft Matter Characterization. Borsali, R.; Pecora, R., Eds. Springer Netherlands: 2008, p 723; (d) J. Eastoe, *Surfactant Chemistry*, Wuhan University Press, Wuhan, 2005.

2. A. Guinier, *Annales de Physique*, **1939,** *12*, 161.

3. (a) G. Porod, *Koll. Z.* **1951,** *124*, 82; (b) L. Auvray; P. Auroy, *Neutron, X-ray and Light Scatterin*. Elsevier Science Publishers, Holland, 1991.

4. (a) B. J. Berne; R. Pecora, *Dynamic Light Scattering: With Applications to Chemistry, Biology, and Physics*, Wiley-VCH, New York, 2000; (b) P. N. Pusey; R. J. A. Taugh, *Dynamic Light Scattering and Velocimetry: Applications of PCS*, Plenum Press, 1982.

5. J. W. Gibbs, *The Collected Works of J. W. Gibbs*, Longmans, New York, 1931, Vol. 1.